Measurement of prompt charm production and the decay $D^0 \to K^+\pi^-\pi^+\pi^-$ at LHCb

by

Thomas R. Hampson

A thesis submitted to the University of Bristol for the degree of Doctor of Philosophy

in the
Faculty of Science
School of Physics

June 2013

Abstract

Prompt charm production in pp collisions at a centre-of-mass energy of 7 TeV is measured with the decay $D^0 \to K^-\pi^+\pi^-\pi^+$, using an integrated luminosity of $15.0\,\text{nb}^{-1}$ collected by the LHCb detector at CERN. The measurement is carried out in two-dimensional bins of D^0 rapidity and transverse momentum in the region $2.0 < y < 4.5$ and $0 < p_\text{T} < 8\,\text{GeV}/c$. The results are found to have excellent agreement with those measured using the decay $D^0 \to K^-\pi^+$.

With $1.0\,\text{fb}^{-1}$ of integrated luminosity, the time dependent ratio of $D^0 \to K^+\pi^-\pi^+\pi^-$ to $D^0 \to K^-\pi^+\pi^-\pi^+$ decays is used to determine the ratio of doubly Cabibbo suppressed to Cabibbo favoured decay rates

$$r_D^2 = (0.341 \pm 0.017 \pm 0.006)\,\%$$

where the first uncertainty is statistical and the second is systematic. This is a previously unmeasured quantity, and can be used to measure the branching fraction of the doubly Cabibbo suppressed decay $D^0 \to K^+\pi^-\pi^+\pi^-$

$$\mathcal{B}\left(D^0 \to K^+\pi^-\pi^+\pi^-\right) \text{ via DCS } = (2.75 \pm 0.14 \pm 0.05 \pm 0.07) \times 10^{-4}$$

where the final uncertainty is from the branching fraction of the Cabibbo favoured decay $D^0 \to K^-\pi^+\pi^-\pi^+$. In addition, the no-mixing hypothesis is excluded with a probability that corresponds to 2.8 standard deviations, and the time-integrated mixing rate is measured as $R_M = (0.04 \pm 0.88) \times 10^{-4}$.

Declaration of authorship

I, Thomas Hampson, declare that the work in this dissertation was carried out in accordance with the requirements of the University's Regulations and Code of Practice for Research Degree Programmes and that it has not been submitted for any other academic award. Except where indicated by specific reference in the text, the work is the candidate's own work. Work done in collaboration with, or with the assistance of, others, is indicated as such. Any views expressed in the dissertation are those of the author.

Signed: _____

Date: _____

Acknowledgements

I would like to take this opportunity to thank a few of the people who have helped me over the past few years. Without them, I don't think any of this work would have been possible.

Firstly, I would like to thank Jonas Rademacker for his excellent supervision. Jonas provided me with countless opportunities, was always full of new ideas, and was always there to help me out and answer my questions.

Thank you to Nick Brook, Matt Coombes, and Anatoly Solomin for all their help with my work on the RICH alignment selection. I particularly enjoyed all of the long discussions with Anatoly. Thank you also to Chris Jones for helping me with the RICH reconstruction software.

Thank you for the hard work of the members of the $K3\pi$ task force; Philip Hunt, Paras Naik, Andrew Powell, and Jonas. It took a while, but we finally measured those cross-sections!

A big thank you to Vava Gligorov who helped me understand the trigger software, and whose encouragement led to the four-body charm trigger. Thank you to Patrick Spradlin for writing the two-body part of the trigger algorithm.

Thanks to Sam Harnew who took over a large part of the analysis that forms Chapter 5. We will publish it eventually...

Thank you to the friends I made in Bristol and at CERN for making the last four years unforgettable. There are too many of you to list here.

Thank you to all of my family, especially my parents, for their continuing love and support.

Finally, thank you to Cathryn for putting up with my long absences, and for keeping me fed while I was writing up. I could not have done this without you.

Author's contribution

Much of the work presented in this thesis was carried out with the assistance of members of the Bristol particle physics group, and other members of the LHCb collaboration. The following list outlines the Author's specific contributions.

- Chapter 3: event selection algorithm.
- Chapter 4: event selection, yield extraction, fiducial acceptance and reconstruction/selection efficiency calculations, many of the systematic uncertainties (yield extraction, fiducial acceptance, selection/reconstruction efficiency, Dalitz model, multiple candidates, peaking background, and the final combination of all uncertainties), and the calculation of the cross-sections, as well as the comparison with the other decay mode.
- Chapter 5: trigger, event selection, yield extraction, secondary background correction, and the systematic uncertainties.

Contents

Introduction

The Standard Model of particle physics represents one of the greatest achievements of modern science. It aims to fully describe the fundamental particles that make up the Universe, and the laws that govern their interactions. The LHCb detector is one of the four main experimental machines placed at intersection points around the Large Hadron Collider at CERN. It has been designed to exploit the exceptional b and c quark production rate of the LHC to study heavy flavour physics with unprecedented precision, and has already recorded some of the largest samples of $b-$ and $c-$meson decays to date.

In this thesis, the production of D mesons is studied using the decay to the final state $K3\pi$. The same final state is used, along with its charge-conjugate, to investigate $D^0-\overline{D}^0$ oscillations, and perform a first measurement of the ratio of doubly Cabibbo suppressed to Cabibbo favoured decay rates. A discussion of the alignment of the LHCb RICH mirrors is also given, for which an event selection is developed. The alignment plays a vital role in the performance of RICH particle identification, which is crucial for the measurements presented here.

Chapter 1 begins with a brief introduction to the Standard Model, before introducing the mixing formalism for multi-body decays of D^0 mesons, which is relevant later in the thesis. Chapter 2 outlines the LHCb detector, including all of the various sub-detectors. In Chapter 3, the method used to align the LHCb RICH mirror segments is outlined, before a selection algorithm, designed to speed up the procedure, is discussed.

Chapter 4 describes an analysis which measures the production of promptly produced charm mesons, using some of the earliest LHCb data recorded with a centre-of-mass energy of 7 TeV (with additional figures in Appendix A). Chapter 5 describes a time

dependent analysis which uses the full 2011 dataset to search for neutral charm meson oscillations, and measure the ratio of doubly Cabibbo suppressed to Cabibbo favoured decay rates for $D \to K3\pi$ decays. Additional figures relevant to this chapter are placed in Appendix B.

Chapter 1

The Standard Model

1.1 Introduction

The Standard Model (SM) of particle physics is a mathematical description of the fundamental matter particles and their interactions. Within the SM there are twelve spin-$\frac{1}{2}$ matter particles (fermions), divided into two groups: quarks and leptons. For each of the quarks and leptons there is a corresponding antiquark or antilepton. Three forces describe the interactions between fermions: the weak force; the strong force; and electromagnetism. The interactions between fermions are transmitted via the exchange of spin-1 force mediators (bosons), but only if the fermions posses the type of charge associated with the given force. The strong interaction is mediated by gluons, which act on "colour" charge; the electromagnetic force is mediated by the photon, which acts on electric charge; and the weak force is mediated by the $W^{\pm}$ and Z^0 bosons, which act on "weak isospin" and "weak hypercharge". Quarks carry all three types of charge, so they can take part in all three interactions. The charged leptons can interact via the weak or electromagnetic interactions, and the neutrinos interact only weakly. A summary of the fundamental particles is shown in Figure 1.1.

The SM also predicts the existence of the spin-0 "Higgs" boson, which is required for electroweak symmetry breaking, and gives mass to the fermions via their interactions with the Higgs field (called Yukawa interactions). Recently, both the CMS and ATLAS

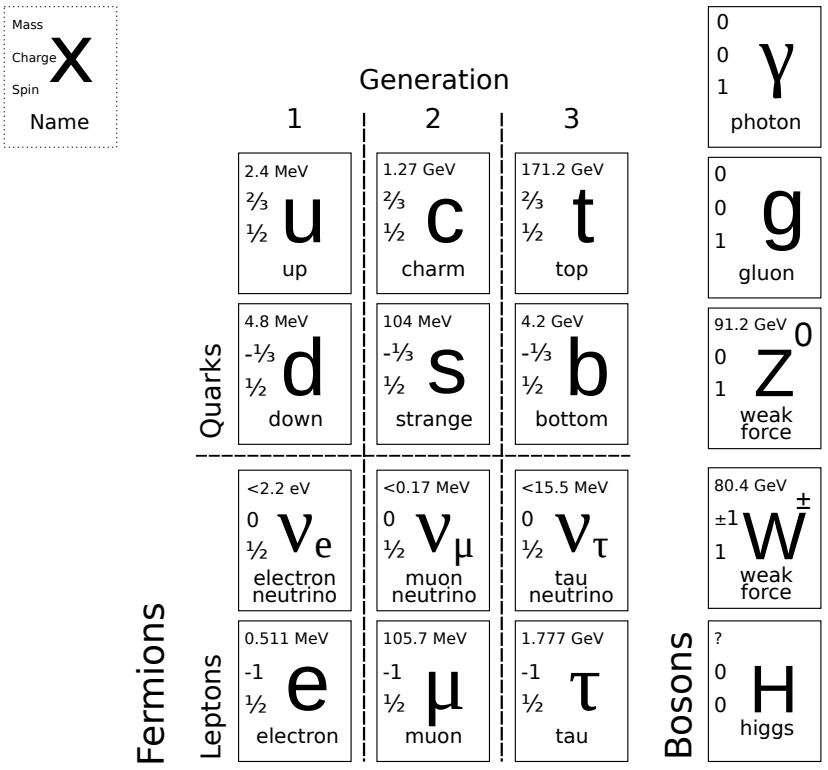

Figure 1.1: Fundamental particles of the Standard Model, showing their masses, electric charges, and spins [1]. Masses of the $u-$, $d-$ and $s-$quarks are "current quark mass" estimates, while the $c-$ and $b-$quark masses are "running" masses. Values are taken from [2].

collaborations reported observations of a neutral boson with a mass of $\sim 125\,\mathrm{GeV}/c^2$, consistent with a SM Higgs boson [3, 4].

The dynamics of the fundamental particles within the SM are described in terms of their kinetic and potential energy by the SM Lagrangian[1]

$$\mathcal{L}_{\mathrm{SM}} = \mathcal{L}_{\mathrm{EW}} + \mathcal{L}_{\mathrm{QCD}} + \mathcal{L}_{\mathrm{Higgs-Yukawa}}. \tag{1.1}$$

The Lagrangian is invariant under certain local transformations, or gauge transformations, resulting in the conservation of certain charges carried by the particles (following Noether's theorem). Transformations between different gauges are represented by a mathematical group, the generators of which correspond to gauge fields that are needed to ensure gauge invariance. It is the quanta of these fields that represent the gauge bosons.

[1]Here, the word "Lagrangian" actually refers to the Lagrangian density.

The SM Lagrangian is invariant under local gauge transformations of the symmetry group

$$\mathrm{SU(3)_C} \otimes \mathrm{SU(2)_I} \otimes \mathrm{U(1)_Y} \tag{1.2}$$

where $\mathrm{SU(3)_C}$ is the symmetry group for the strong interaction, and $\mathrm{SU(2)_I} \otimes \mathrm{U(1)_Y}$ is the symmetry group of the electroweak interaction. This results in the conservation of the charges C (colour), I (weak isospin), and Y (weak hypercharge). Since the electric charge is derived from the weak hypercharge and the third component of weak isospin, $Q = \mathrm{Y} + \mathrm{I}^3$, it is also conserved.

A brief description of the mathematical theory of the SM (including each of the terms in Equation 1.1) is presented below. A more detailed account can be found in Reference [5], for example.

1.2 Quantum electrodynamics

Quantum ElectroDynamics (QED) is the relativistic Quantum Field Theory (QFT) that describes the interactions between photons and charged spin-$\frac{1}{2}$ fermions. It can be shown that all of electrodynamics is generated by requiring that the free Dirac Lagrangian is invariant under local phase (or "gauge") transformations.

Free fermions are described by the Dirac Lagrangian[2]

$$\mathcal{L} = i\bar{\psi}\gamma^{\mu}\partial_{\mu}\psi - m\bar{\psi}\psi \tag{1.3}$$

where ψ is the Dirac spinor that describes the free fermion field, m is the fermion mass, and γ_{μ} are the gamma matrices. The Dirac Lagrangian is invariant under the global gauge transformation

$$\psi \longrightarrow e^{i\theta}\psi \tag{1.4}$$

where θ is any real number. If θ is a function of space-time, Equation 1.4 becomes the local gauge transformation

$$\psi \longrightarrow e^{i\theta(x)}\psi \tag{1.5}$$

[2]In this chapter we use the "natural units" $c = \hbar = 1$.

under which the Dirac Lagrangian picks up an extra term of the form

$$\bar{\psi}\gamma^{\mu}\psi\partial_{\mu}\theta\left(x\right). \tag{1.6}$$

In other words, the Lagrangian is not invariant under local gauge transformations. However, invariance can be restored by introducing a gauge field, A_{μ}, to the Lagrangian so that

$$\mathcal{L} = i\bar{\psi}\gamma^{\mu}\partial_{\mu}\psi - m\bar{\psi}\psi + q\bar{\psi}\gamma^{\mu}\psi A_{\mu} \tag{1.7}$$

where A_{μ} transforms under local gauge transformations as

$$A_{\mu} \longrightarrow A_{\mu} + \frac{1}{q}\partial_{\mu}\psi\left(x\right). \tag{1.8}$$

The last term in Equation 1.7 represents the interaction between the fermion current $\bar{\psi}\gamma^{\mu}\psi$ and the gauge field A_{μ} with the coupling strength q.

Finally, a "free" term for the gauge field is added to complete the electromagnetic Lagrangian:

$$\mathcal{L}_{\mathrm{EM}} = i\bar{\psi}\gamma^{\mu}\partial_{\mu}\psi - m\bar{\psi}\psi + q\bar{\psi}\gamma^{\mu}\psi A_{\mu} - \frac{1}{4}F^{\mu\nu}F_{\mu\nu} \tag{1.9}$$

where $F^{\mu\nu} \equiv \partial^{\mu}A^{\nu} - \partial^{\nu}A^{\mu}$ is the electromagnetic field tensor. Note that a mass term for the gauge field, $m_A^2 A_{\mu}A^{\mu}$, is not included because it is not invariant under the local gauge transformation (Equation 1.8). This leads to the conclusion that the gauge field must be massless.

1.3 Quantum chromodynamics

Quantum ChromoDynamics (QCD) is the QFT that describes strong interactions between quarks and gluons, and is responsible for binding quarks into hadrons, as well as holding protons and neutrons together within the nucleus. Gluons act on "colour" charge, of which there are three types: "red", "green", and "blue". Gluons themselves carry colour charge, which gives rise to gluon self-interactions. Similarly to QED, the dynamics of the strong force can be shown to result from requiring local gauge invariance.

The Dirac Lagrangian for one particular quark flavour is

$$\mathcal{L} = \left(i\bar{\psi}_r\gamma^\mu\partial_\mu\psi_r - m\bar{\psi}_r\psi_r\right) + \left(i\bar{\psi}_g\gamma^\mu\partial_\mu\psi_g - m\bar{\psi}_g\psi_g\right) + \left(i\bar{\psi}_b\gamma^\mu\partial_\mu\psi_b - m\bar{\psi}_b\psi_b\right) \quad (1.10)$$

which can be written more compactly as

$$\mathcal{L} = i\bar{\psi}\gamma^\mu\partial_\mu\psi - m\bar{\psi}\psi. \quad (1.11)$$

This is the same as the free fermion Lagrangian in Equation 1.3, except that now ψ is a three component vector of Dirac spinors:

$$\psi \equiv \begin{pmatrix} \psi_r \\ \psi_g \\ \psi_b \end{pmatrix}, \quad \bar{\psi} = \begin{pmatrix} \bar{\psi}_r & \bar{\psi}_g & \bar{\psi}_b \end{pmatrix}, \quad (1.12)$$

one for each colour charge. The three-component Lagrangian is invariant under the global transformation

$$\psi \longrightarrow e^{iH}\psi \quad (1.13)$$

where H is a 3×3 Hermitian matrix which can be written as

$$H = \theta\,\mathbf{I} + \boldsymbol{\lambda}\cdot\mathbf{a}. \quad (1.14)$$

Here θ is a real number, $\mathbf{I}$ is the 3×3 identity matrix and

$$\boldsymbol{\lambda}\cdot\mathbf{a} \equiv \lambda_1 a_1 + \cdots + \lambda_8 a_8 \quad (1.15)$$

where $a_1, \cdots, a_8$ are real numbers, and $\lambda_1, \cdots, \lambda_8$ are the Gell-Mann matrices. The gauge transformation can be split into two parts, $e^{iH} = e^{i\theta}e^{i\boldsymbol{\lambda}\cdot\mathbf{a}}$, the first of which is a phase transformation that was discussed for QED. Demanding that the Dirac Lagrangian be invariant under the local gauge transformation

$$\psi \longrightarrow e^{iq\boldsymbol{\lambda}\cdot\phi(x)} \quad \text{where} \quad \phi\,(x) \equiv \frac{\mathbf{a}\,(x)}{q} \quad (1.16)$$

requires an extra term (underlined):

$$\mathcal{L} = i\bar{\psi}\gamma^{\mu}\partial_{\mu}\psi - m\bar{\psi}\psi - \underline{\left(q\bar{\psi}\gamma^{\mu}\boldsymbol{\lambda}\psi\right)\cdot\mathbf{G}_{\mu}} \tag{1.17}$$

that accounts for the colour interaction between the quarks and the eight gauge (gluon) fields $\mathbf{G}_{\mu}$, with a coupling strength q. Finally, the free gluon Lagrangian is added to give the complete QCD Lagrangian[3]:

$$\mathcal{L}_{\mathrm{QCD}} = i\bar{\psi}\gamma^{\mu}\partial_{\mu}\psi - m\bar{\psi}\psi - \left(q\bar{\psi}\gamma^{\mu}\boldsymbol{\lambda}\psi\right)\cdot\mathbf{G}_{\mu} - \frac{1}{4}\mathbf{G}^{\mu\nu}\mathbf{G}_{\mu\nu} \tag{1.18}$$

where the gluon field strength tensor is

$$\mathbf{G}^{\mu\nu} = \partial^{\mu}\mathbf{G}^{\nu} - \partial^{\nu}\mathbf{G}^{\mu} - q\left(\mathbf{G}^{\mu}\times\mathbf{G}^{\nu}\right). \tag{1.19}$$

Here, each of the eight components, i, of the "cross product" is given by

$$\left(\mathbf{G}^{\mu}\times\mathbf{G}^{\nu}\right)_{i} = \sum_{j,k=1}^{8} f_{ijk}G_{j}^{\mu}G_{k}^{\nu} \tag{1.20}$$

where f_{ijk} are the SU(3) structure constants. The additional term in the field strength tensor accounts for gluon self-interactions with a coupling strength q, the same as between quarks and gluons. The coupling constant is more often referred to in terms of α_s, defined as

$$\alpha_{\mathrm{s}} = \frac{q}{4\pi}. \tag{1.21}$$

Self-interaction occurs because gluons posses a colour charge, unlike in the case of QED where the photon is chargeless.

In QED, the electric charge of a particle is screened by the polarisation of surrounding virtual particle/antiparticle pairs. This leads to a coupling strength that depends on the energy scale of the interaction - at high energies an interacting particle is able to penetrate through the cloud of virtual particles to feel more of the bare electric charge. The same is true for QCD: virtual quark/antiquark pairs produced near a bare quark will screen the colour charge. However, gluon self-interactions introduce an

[3]There are actually six versions of this Lagrangian: one for each of the different quark flavours.

"antiscreening" effect which outweighs the screening from the quark/antiquark pairs. Therefore, for QCD, at higher energies the coupling strength decreases. This gives rise to two interesting phenomena: confinement and asymptotic freedom.

Confinement is a physical phenomenon that prevents the existence of isolated colour charges; quarks can only bind together in colourless combinations to form hadrons. As the separation between two quarks increases, α_s increases until it becomes energetically more favourable to produce a new quark-antiquark pair. The new quarks will form colourless combinations with the original pair; a process referred to as "hadronisation" (or "fragmentation"). At high energies (or small distances), the size of the coupling constant decreases and the quarks behave more like free particles. This is known as asymptotic freedom.

1.4 Electroweak interactions

The weak force is the only fundamental interaction that violates parity. The $W^{\pm}$ bosons couple only to left-handed fermion states, while the Z^0 boson couples to left- and right-handed states with different strengths.

Under SU(2) (the symmetry group of the weak interaction), the left-handed fermions form doublets

$$\psi_{\mathrm{L}} = \begin{pmatrix} \nu_{\mathrm{L}} \\ l_{\mathrm{L}} \end{pmatrix} , \quad \begin{pmatrix} u_{\mathrm{L}} \\ d'_{\mathrm{L}} \end{pmatrix} \tag{1.22}$$

while the right-handed fermions form singlets

$$\psi_{\mathrm{R}} = l_{\mathrm{R}} , \;\; u_{\mathrm{R}} , \;\; d_{\mathrm{R}}. \tag{1.23}$$

Here, the prime on the down-type quark represents the flavour eigenstate, which is different to the mass eigenstate (see Section 1.6).

The ElectroWeak (EW) interaction is the unification of the weak force and electromagnetism [6], with the symmetry group

$$\mathrm{SU(2)_I} \otimes \mathrm{U(1)_Y}, \tag{1.24}$$

which gives rise to three weak isospin bosons (W_μ^α) and one weak hypercharge boson (B_μ). After requiring local gauge invariance and introducing a gauge invariant kinetic term for the bosons, the EW Lagrangian[4] is given by

$$\mathcal{L}_{\mathrm{EW}} = \bar{\psi}_{\mathrm{R}} \gamma^\mu \left(\partial_\mu - i g_{\mathrm{Y}} \frac{Y_{\mathrm{R}}}{2} B_\mu \right) \psi_{\mathrm{R}} \tag{1.25}$$

$$+ \bar{\psi}_{\mathrm{L}} \gamma^\mu \left(\partial_\mu - i g_{\mathrm{Y}} \frac{Y_{\mathrm{L}}}{2} B_\mu - i g_{\mathrm{W}} \frac{\sigma^\alpha}{2} W_\mu^\alpha \right) \psi_{\mathrm{L}} \tag{1.26}$$

$$- \frac{1}{4} W_{\mu\nu}^\alpha W^{\alpha\mu\nu} - \frac{1}{4} B_{\mu\nu} B^{\mu\nu} \tag{1.27}$$

where g_{Y} is the weak hypercharge coupling constant, g_{W} is the weak isospin coupling constant, $Y_{\mathrm{L,R}}$ are the weak hypercharges of the left- and right-handed fermions, and σ^α are the Pauli matrices. The field strength tensors are given by

$$W_{\mu\nu}^\alpha = \partial_\mu W_\nu^\alpha - \partial^\alpha W_\mu^\alpha + g_{\mathrm{W}} \varepsilon_{\alpha\beta\gamma} W_\mu^\beta W_\mu^\gamma \tag{1.28}$$

and

$$B_{\mu\nu} = \partial_\mu B_\nu - \partial_\nu B_\mu \tag{1.29}$$

where $\varepsilon_{\alpha\beta\gamma}$ are the SU(2) structure constants. Note that because right-handed fermion fields are invariant under local $\mathrm{SU(2)_I}$ transformations, they do not couple to the W_μ^α gauge fields, whereas the left-handed fermion fields interact with both the W_μ^α and B_μ gauge fields (this is parity violation).

As with the QED and QCD Lagrangians, local gauge invariance requires that the gauge fields are massless. However, observations have shown that all of the electroweak bosons except for the photon are massive [7, 8]. Furthermore, it is not possible to simply add a mass terms of the form

$$m\psi\bar{\psi} = m \left(\bar{\psi_{\mathrm{L}}} \psi_{\mathrm{R}} + \bar{\psi_{\mathrm{R}}} \psi_{\mathrm{L}} \right) \tag{1.30}$$

[4]Note that this is for one generation only.

for the fermion fields because it is not invariant under an $SU(2)_I$ local gauge transformation.

1.5 The Higgs mechanism

The masses of the EW gauge bosons are explained by their interaction with the Higgs field, which is a weak isospin doublet of scalar fields,

$$\phi = \begin{pmatrix} \phi_+ \\ \phi_0 \end{pmatrix} = \begin{pmatrix} \phi_1 + i\phi_2 \\ \phi_3 + i\phi_4 \end{pmatrix} \tag{1.31}$$

and which has a potential of the form

$$V\left(\phi^\dagger\phi\right) = -\mu^2\left(\phi^\dagger\phi\right) + \frac{\lambda\left(\phi^\dagger\phi\right)^2}{2}. \tag{1.32}$$

If $\mu^2 < 0$ then the minimum of the potential trivially corresponds to $\phi = 0$. However, for $\mu^2 > 0$ the minimum of the potential occurs at

$$\phi^\dagger\phi = \frac{\mu^2}{2\lambda} \equiv \left(\frac{v}{\sqrt{2}}\right)^2. \tag{1.33}$$

Here, the vacuum is said to be degenerate (*i.e.* there are an infinite number of states with the same minimum potential). The vacuum expectation value is chosen to be

$$\langle\phi\rangle_0 = \frac{1}{\sqrt{2}}\begin{pmatrix} 0 \\ v \end{pmatrix} \tag{1.34}$$

which breaks the $SU(2)_I \otimes U(1)_Y$ symmetry while leaving the $U(1)_{QED}$ symmetry unbroken (spontaneous symmetry breaking). Expanding around this vacuum expectation values gives

$$\phi = \frac{1}{\sqrt{2}}\begin{pmatrix} 0 \\ v + H \end{pmatrix} \tag{1.35}$$

where H, which is the excitation of the Higgs field from the vacuum expectation value, is the Higgs boson. Here, we have chosen $\phi_1 = \phi_2 = \phi_4 = 0$ in the ground state. Using this

particular gauge (the "unitary" gauge [9]) leaves only one scalar degree of freedom (the Higgs field), while the other three degrees of freedom act as longitudinal polarisation components of the three massive weak bosons. Without this choice of gauge, we would be left with non-existent, massless "Goldstone" bosons [10].

The Lagrangian that describes the kinematics of the Higgs field, and its interaction with the EW gauge fields is given by

$$\mathcal{L}_{\text{Higgs}} = \left(\mathcal{D}^{\mu}\phi\right)^{\dagger}\left(\mathcal{D}_{\mu}\phi\right) - V\left(\phi^{\dagger}\phi\right) \tag{1.36}$$

where the covariant derivative, $\mathcal{D}_{\mu}$, is defined as

$$\mathcal{D}_{\mu} \equiv \partial_{\mu} - ig_{\text{Y}}\frac{Y}{2}B_{\mu} - ig_{\text{W}}\frac{\sigma^{\alpha}}{2}W_{\mu}^{\alpha}. \tag{1.37}$$

EW symmetry breaking leads to the consequence that the photon is massless while the weak gauge bosons acquire the masses

$$m_{W} = \frac{vg_{\text{W}}}{2} \quad \text{and} \quad m_{Z} = \frac{m_{\text{W}}}{\cos\theta_{\text{W}}} \tag{1.38}$$

where θ_{W} is the Weinberg angle, given by $\tan\theta_{\text{W}} = g_{\text{Y}}/g_{\text{W}}$. The physical weak boson states (and the photon) are related to the massless states by:

$$\begin{pmatrix} Z_{\mu} \\ A_{\mu} \end{pmatrix} = \begin{pmatrix} \cos\theta_{\text{W}} & \sin\theta_{\text{W}} \\ -\sin\theta_{\text{W}} & \cos\theta_{\text{W}} \end{pmatrix} \begin{pmatrix} W_{\mu}^{3} \\ B_{\mu} \end{pmatrix} \tag{1.39}$$

and

$$\begin{pmatrix} W_{\mu}^{+} \\ W_{\mu}^{-} \end{pmatrix} = \begin{pmatrix} 1 & i \\ 1 & -i \end{pmatrix} \begin{pmatrix} W_{\mu}^{1} \\ W_{\mu}^{2} \end{pmatrix}. \tag{1.40}$$

In the SM, fermion fields acquire their masses via Yukawa interactions with the Higgs field. For each fermion field, the Yukawa Lagrangian is of the form

$$\mathcal{L}_{\text{Yukawa}} = c\left(\bar{\psi_{\text{L}}}\phi\psi_{\text{R}} + \bar{\psi_{\text{R}}}\phi^{\dagger}\psi_{\text{L}}\right) \tag{1.41}$$

where c is the Yukawa coupling (different for each fermion state) and ϕ is given by Equation 1.35. This leads to fermion masses of

$$m = \frac{cv}{\sqrt{2}}, \tag{1.42}$$

but because the Yukawa couplings are not known, the masses are not predicted by the SM.

1.6 Quark mixing and the CKM matrix

The Yukawa coupling terms for all three quark generations can be written as

$$\mathcal{L}^{q}_{\text{Yukawa}} = -\left(1 + \frac{H}{v}\right)\left(\bar{\mathbf{d}}'_{\text{L}} M'_d \mathbf{d}'_{\text{R}} + \bar{\mathbf{u}}'_{\text{L}} M'_u \mathbf{u}'_{\text{R}}\right) + \text{h.c.} \tag{1.43}$$

where $\mathbf{u}'_{\text{R,L}}$ and $\mathbf{d}'_{\text{R,L}}$ are up- and down-type quark flavour space vectors; and M'_u and M'_d are complex 3×3 flavour space matrices that allow mixing of different quark flavour states. In order to obtain the physical quark states (mass eigenstates), the matrices must be diagonalised:

$$M'_u = S^{\dagger}_{u\text{L}} M_u S_{u\text{R}} \ , \quad M'_d = S^{\dagger}_{d\text{L}} M_d S_{d\text{R}} \tag{1.44}$$

where S are unitary matrices, $M_u = \text{diag}\,(m_u, m_c, m_t)$, and $M_d = \text{diag}\,(m_d, m_s, m_b)$. For left-handed quarks, the transformations from the weak states to the mass states are given by

$$u^i_{\text{L}} \longrightarrow S^{ij}_{u\text{L}} u^j_{\text{L}} \quad \text{and} \quad d^i_{\text{L}} \longrightarrow S^{ij}_{d\text{L}} d^j_{\text{L}}. \tag{1.45}$$

Note that because the matrices S are unitary, the transformations have no effect on neutral current interactions: $\bar{d}^i d^i \longrightarrow \bar{d}^i S_d \left(S_d\right)^{\dagger} d^i \equiv \bar{d}^i d^i$. Therefore flavour changing neutral currents do not exist at the tree level within the SM. Charged current interactions

transform as

$$u^i_{\mathrm{L}}\gamma^\mu d^i_{\mathrm{L}} \longrightarrow u^i_{\mathrm{L}}\gamma^\mu \left(S_{u\mathrm{L}}\left(S_{d\mathrm{L}}\right)^\dagger\right) d^i_{\mathrm{L}} \tag{1.46}$$

$$d^i_{\mathrm{L}}\gamma^\mu u^i_{\mathrm{L}} \longrightarrow d^i_{\mathrm{L}}\gamma^\mu \left(S_{d\mathrm{L}}\left(S_{u\mathrm{L}}\right)^\dagger\right) u^i_{\mathrm{L}} \tag{1.47}$$

where $\left(S_{u\mathrm{L}}\left(S_{d\mathrm{L}}\right)^\dagger\right) \equiv V_{\mathrm{CKM}}$ is the Cabibbo-Kobayashi-Maskawa (CKM) matrix, given by

$$V_{\mathrm{CKM}} = \begin{pmatrix} V_{ud} & V_{uc} & V_{ub} \\ V_{cd} & V_{cs} & V_{cb} \\ V_{td} & V_{ts} & V_{tb} \end{pmatrix} \tag{1.48}$$

which is a mixing matrix that relates the weak flavour eigenstates to the mass eigenstates:

$$\begin{pmatrix} d' \\ s' \\ b' \end{pmatrix} = \begin{pmatrix} V_{ud} & V_{uc} & V_{ub} \\ V_{cd} & V_{cs} & V_{cb} \\ V_{td} & V_{ts} & V_{tb} \end{pmatrix} \begin{pmatrix} d \\ s \\ b \end{pmatrix}. \tag{1.49}$$

Each element V_{ij} represents the coupling strength for a quark transition from state i to state j. Diagonal elements are all close to one, while the off diagonal terms, which represent transitions between different generations, are small.

The CKM matrix can be parameterised in many different ways. One example is the Wolfenstein parameterisation [11]

$$V_{\mathrm{CKM}} = \begin{pmatrix} 1-\frac{1}{2}\lambda^2 & \lambda & \lambda^3 A\left(\rho - i\eta\right) \\ -\lambda & 1-\frac{1}{2}\lambda^2 & \lambda^2 A \\ \lambda^3 A\left(1-\rho-i\eta\right) & -\lambda^2 A & 1 \end{pmatrix} + \mathcal{O}\left(\lambda^4\right) + \cdots \tag{1.50}$$

where

$$\lambda = \frac{|V_{us}|}{\sqrt{|V_{us}|^2 + |V_{ud}|^2}}, \qquad A\lambda^2 = \left|\frac{V_{cb}}{V_{us}}\right|, \qquad A\lambda^3\left(\rho + i\eta\right) = V^*_{ub}. \tag{1.51}$$

The parameter λ may also be written in terms of the Cabibbo angle, $\lambda = \sin\theta_C \simeq 0.23$. In the Wolfenstein parameterisation, the complex phase responsible for CP violation is represented by $i\eta$.

1.6.1 CP violation

The invariance of physics under the exchange of particles for antiparticles (charge conjugation), and the reversal of spatial coordinates (parity flipping), is referred to as CP symmetry. While CP is conserved by electromagnetic and strong interactions, the symmetry is violated in weak interactions. In the SM, CP violation is accommodated by a complex phase in the CKM matrix, leading to $V_{ij} \neq V_{ij}^*$. In other words, the Yukawa Lagrangian is not invariant under CP transformations. There are three different types of CP violation:

1. CP violation in decay (referred to as "direct CP violation"). This occurs when the amplitude for a decay and its CP conjugate have different magnitudes, and is present in both charged and neutral decays.

2. CP violation in mixing (or "indirect CP violation"). The mass eigenstates of a neutral meson may be written in terms of the flavour eigenstates:

$$|P_1\rangle = p\left|P^0\right\rangle + q\left|\overline{P}^0\right\rangle \tag{1.52}$$

$$|P_2\rangle = p\left|P^0\right\rangle - q\left|\overline{P}^0\right\rangle \tag{1.53}$$

   where p and q are complex numbers that satisfy $|p|^2 + |q|^2 = 1$. If p and q are the same then the mass eigenstates are CP eigenstates. CP violation occurs if $|q/p| \neq 1$, when the mass eigenstates are not CP eigenstates.

3. CP violation in the interference between mixing and decay.

1.6.2 The unitarity triangle

The unitarity of the CKM matrix leads to six the constraints $\sum_k V_{ik}V_{jk}^* = 0$ for $i \neq j$, which can be represented as triangles on the complex plane (called unitarity triangles). In particular, the condition

$$V_{ub}^* V_{ud} + V_{cb}^* V_{cd} + V_{tb}^* V_{td} = 0 \tag{1.54}$$

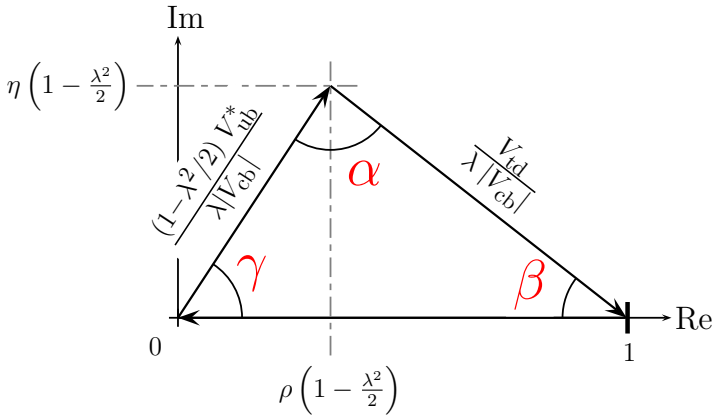

Figure 1.2: The unitarity triangle in the Wolfenstein parameterisation [12]. The lengths of the sides are normalised to $V_{cd}V_{cb}^*$.

results in a triangle with angles

$$\alpha \equiv \arg\left(-\frac{V_{td}V_{tb}^*}{V_{ud}V_{ub}^*}\right), \quad \beta \equiv \arg\left(-\frac{V_{cd}V_{cb}^*}{V_{td}V_{tb}^*}\right), \quad \gamma \equiv \arg\left(-\frac{V_{ud}V_{ub}^*}{V_{cd}V_{cb}^*}\right), \tag{1.55}$$

and which is referred to as *the* unitarity triangle (shown in Figure 1.2) because all of the sides are of the same order (λ^3)[5]. One of the main goals of the LHCb experiment is to perform a precise measurement of the angle γ, in order to test the unitarity of the CKM matrix. Any deviation from unitarity would provide clear evidence for physics beyond the SM.

It is possible to measure γ by considering the interference between $B^- \to D^0 K^-$ and $B^- \to \overline{D}^0 K^-$ decays (and of course between their charge conjugates), where the D^0 decays via the mode $D^0 \to K^\pm\pi^\mp\pi^+\pi^-$ [12, 13]. The functional forms of the decay rates are

$$\Gamma\left(B^- \to \left(K^-\pi^+\pi^-\pi^+\right)_D K^-\right) \propto 1 + (r_B r_D)^2 + 2R_D r_B r_D \cos\left(\delta_B - \delta_D - \gamma\right) \tag{1.56}$$

$$\Gamma\left(B^- \to \left(K^+\pi^-\pi^+\pi^-\right)_D K^-\right) \propto r_B^2 + r_D^2 + 2R_D r_B r_D \cos\left(\delta_B + \delta_D - \gamma\right) \tag{1.57}$$

where r_B is the ratio of magnitudes of the two B decays and δ_B is the strong phase difference between the B decays. The parameters r_D, δ_D and R_D relate to the decay

[5]Triangles resulting from four of the other conditions have very unequal sides, making CP violation measurements very difficult. The other remaining condition results in a triangle that coincides with the unitarity triangle up to $\mathcal{O}\left(\lambda^3\right)$.

of the D, and are discussed in Section 1.7. Measurements of the D parameters provide constraints vital for the extraction of the CP violating phase γ.

1.7 Mixing in multi-body D decays

This section follows the derivation found in [14]. The mass eigenstates of the neutral D meson can be written in terms of the flavour eigenstates as follows:

$$\begin{aligned} |D_1\rangle &= p\left|D^0\right\rangle + q\left|\overline{D}^0\right\rangle \\ |D_2\rangle &= p\left|D^0\right\rangle - q\left|\overline{D}^0\right\rangle . \end{aligned} \tag{1.58}$$

The time evolution of these states is governed by the Schrödinger equation, resulting in

$$\begin{aligned} |D_1(t)\rangle &= p\left|D^0(t)\right\rangle + q\left|\overline{D}^0(t)\right\rangle = e^{-iM_1t-\frac{1}{2}\Gamma_1 t}\left[\, p\left|D^0\right\rangle + q\left|\overline{D}^0\right\rangle \,\right] \\ |D_2(t)\rangle &= p\left|D^0(t)\right\rangle - q\left|\overline{D}^0(t)\right\rangle = e^{-iM_2t-\frac{1}{2}\Gamma_2 t}\left[\, p\left|D^0\right\rangle - q\left|\overline{D}^0\right\rangle \,\right] \end{aligned} \tag{1.59}$$

where $M_{1,2}$ and $\Gamma_{1,2}$ are the masses and widths of the mass eigenstates $D_{1,2}$. This can be rearranged to give

$$\left|D^0(t)\right\rangle = f_+(t)\left|D^0\right\rangle + \frac{q}{p}f_-(t)\left|\overline{D}^0\right\rangle \tag{1.60}$$

$$\left|\overline{D}^0(t)\right\rangle = \frac{p}{q}f_-(t)\left|D^0\right\rangle + f_+(t)\left|\overline{D}^0\right\rangle \tag{1.61}$$

where $f_+(t)$ and $f_-(t)$ are defined as

$$f_+(t) = e^{-iMt-\frac{1}{2}\Gamma t}\cos\left(\frac{1}{2}\Delta M t - \frac{i}{4}\Delta\Gamma t\right) \tag{1.62}$$

$$f_-(t) = e^{-iMt-\frac{1}{2}\Gamma t} i \sin\left(\frac{1}{2}\Delta M t - \frac{i}{4}\Delta\Gamma t\right). \tag{1.63}$$

Here

$$M = \frac{M_1 + M_2}{2} \quad \text{and} \quad \Gamma = \frac{\Gamma_1 + \Gamma_2}{2} \tag{1.64}$$

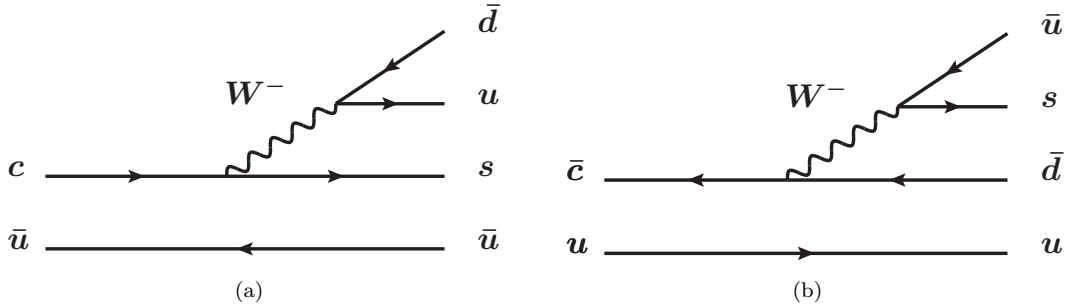

Figure 1.3: Feynman diagrams for (a) Cabibbo favoured and (b) doubly Cabibbo suppressed $D \to K3\pi$ decays (showing only the resonant part of the decay, for example $D \to a_1^+(1260)K^-$). The DCS decay is heavily suppressed compared to the CF decay because each of the weak vertices introduces a factor of λ.

are the average mass and width of the two mass eigenstates, while

$$\Delta M = M_2 - M_1 \quad \text{and} \quad \Delta\Gamma = \Gamma_2 - \Gamma_1 \tag{1.65}$$

are their differences.

The four probability amplitudes,

$$\begin{aligned} \mathcal{A}(\mathbf{p}) &= \left\langle f_{\mathbf{p}} \left| \hat{H} \right| D_0 \right\rangle & \bar{\mathcal{A}}(\mathbf{p}) &= \left\langle \bar{f}_{\mathbf{p}} \left| \hat{H} \right| \overline{D}_0 \right\rangle \\ \mathcal{B}(\mathbf{p}) &= \left\langle f_{\mathbf{p}} \left| \hat{H} \right| \overline{D}_0 \right\rangle & \bar{\mathcal{B}}(\mathbf{p}) &= \left\langle \bar{f}_{\mathbf{p}} \left| \hat{H} \right| D_0 \right\rangle \end{aligned} \tag{1.66}$$

are defined, where $f_{\mathbf{p}}$ and $\bar{f}_{\mathbf{p}}$ are CP conjugate final states, and $\mathbf{p}$ parameterises the five-dimensional space that is accessible by the four-body final state. We choose $\bar{\mathcal{A}}(\mathbf{p})$ to represent the Doubly Cabibbo Suppressed (DCS) decay $\overline{D}^0 \to K^-\pi^+\pi^-\pi^+$, which means $\bar{\mathcal{B}}(\mathbf{p})$ is the Cabibbo Favoured (CF) decay $D^0 \to K^-\pi^+\pi^-\pi^+$ (see Figure 1.3).

Using Equations 1.60, 1.61 and 1.66, the amplitudes for flavour eigenstates (with the flavour "tagged" at time $t = 0$) decaying to given final states are given by

$$\left\langle f_{\mathbf{p}} \left| \hat{H} \right| D_0(t) \right\rangle = f_+(t)\mathcal{A}(\mathbf{p}) + \frac{q}{p} f_-(t)\mathcal{B}(\mathbf{p}) \tag{1.67}$$

$$\left\langle \bar{f}_{\mathbf{p}} \left| \hat{H} \right| D_0(t) \right\rangle = f_+(t)\bar{\mathcal{B}}(\mathbf{p}) + \frac{q}{p} f_-(t)\bar{\mathcal{A}}(\mathbf{p}) \tag{1.68}$$

$$\left\langle \bar{f}_{\mathbf{p}} \left| \hat{H} \right| \overline{D}_0(t) \right\rangle = f_+(t)\bar{\mathcal{A}}(\mathbf{p}) + \frac{p}{q} f_-(t)\bar{\mathcal{B}}(\mathbf{p}) \tag{1.69}$$

$$\left\langle f_{\mathbf{p}} \left| \hat{H} \right| \overline{D}_0(t) \right\rangle = f_+(t)\mathcal{B}(\mathbf{p}) + \frac{p}{q} f_-(t)\mathcal{A}(\mathbf{p}). \tag{1.70}$$

Measurable quantities are given by squaring the above amplitudes and integrating over phase space. Decay rates will therefore be given in terms of the following expressions

$$\begin{aligned}
&\int \mathcal{A}(\mathbf{p})\mathcal{A}^*(\mathbf{p})\mathrm{d}\mathbf{p} = \mathcal{A}^2 && \int \bar{\mathcal{A}}(\mathbf{p})\bar{\mathcal{A}}^*(\mathbf{p})\mathrm{d}\mathbf{p} = \bar{\mathcal{A}}^2 \\
&\int \mathcal{B}(\mathbf{p})\mathcal{B}^*(\mathbf{p})\mathrm{d}\mathbf{p} = \mathcal{B}^2 && \int \bar{\mathcal{B}}(\mathbf{p})\bar{\mathcal{B}}^*(\mathbf{p})\mathrm{d}\mathbf{p} = \bar{\mathcal{B}}^2 \\
&\int \mathcal{A}(\mathbf{p})\mathcal{B}^*(\mathbf{p})\mathrm{d}\mathbf{p} = \mathcal{A}\mathcal{B}R_D e^{-i\delta_D} && \int \bar{\mathcal{A}}(\mathbf{p})\bar{\mathcal{B}}^*(\mathbf{p})\mathrm{d}\mathbf{p} = \bar{\mathcal{A}}\bar{\mathcal{B}}\bar{R}_D e^{-i\bar{\delta}_D}
\end{aligned} \tag{1.71}$$

where R_D is the "coherence factor" and δ_D is the average strong phase difference between the DCS and CF modes. The coherence factor takes a value between 0 and 1 and describes the degree of coherence between the two different amplitudes. If the decay proceeds via a single resonance the coherence factor will be high.

It is convenient to introduce the following definitions

$$\left|\frac{q}{p}\right| \equiv r_{cp}\,, \qquad \arg\left(\frac{q}{p}\right) \equiv \phi_{cp}\,, \qquad x = \frac{\Delta M}{\Gamma}\,, \qquad y = \frac{\Delta\Gamma}{2\Gamma} \tag{1.72}$$

where the complex numbers p and q are used to parameterise CP violation in the D sector, and x and y are dimensionless mixing parameters.

Substituting Equations 1.71 and 1.72 into Equations 1.67–1.70, followed by squaring, and then integrating over phase space results in the rates

$$\Gamma\left(D_0(t)\to f_{\mathbf{p}}\right) = \frac{1}{2}\mathcal{B}^2 e^{-\Gamma t}\Big\{r_D^2\left(\cosh y\Gamma t + \cos x\Gamma t\right) + r_{cp}^2\left(\cosh y\Gamma t - \cos x\Gamma t\right) \\ +\ 2R_D r_D r_{cp}\big[\cos(\delta_D+\phi_{cp})\sinh(y\Gamma t) - \sin(\delta_D+\phi_{cp})\sin(x\Gamma t)\big]\Big\}$$

$$\Gamma\left(D_0(t)\to \bar{f}_{\mathbf{p}}\right) = \frac{1}{2}\bar{\mathcal{B}}^2 e^{-\Gamma t}\Big\{\left(\cosh y\Gamma t + \cos x\Gamma t\right) + \bar{r}_D^2 r_{cp}^2\left(\cosh y\Gamma t - \cos x\Gamma t\right) \\ +\ 2\bar{R}_D \bar{r}_D r_{cp}\big[\cos(-(\bar{\delta}_D-\phi_{cp}))\sinh(y\Gamma t) - \sin(-(\bar{\delta}_D-\phi_{cp}))\sin(x\Gamma t)\big]\Big\}$$

$$\Gamma\left(\overline{D}_0(t)\to \bar{f}_{\mathbf{p}}\right) = \frac{1}{2}\bar{\mathcal{B}}^2 e^{-\Gamma t}\Big\{\bar{r}_D^2\left(\cosh y\Gamma t + \cos x\Gamma t\right) + \frac{1}{r_{cp}^2}\left(\cosh y\Gamma t - \cos x\Gamma t\right) \\ +\ 2\bar{R}_D \frac{\bar{r}_D}{r_{cp}}\big[\cos(\bar{\delta}_D-\phi_{cp})\sinh(y\Gamma t) - \sin(\bar{\delta}_D-\phi_{cp})\sin(x\Gamma t)\big]\Big\}$$

$$\Gamma\left(\overline{D}_0(t)\to f_{\mathbf{p}}\right) = \frac{1}{2}\mathcal{B}^2 e^{-\Gamma t}\Big\{\left(\cosh y\Gamma t + \cos x\Gamma t\right) + \frac{r_D^2}{r_{cp}^2}\left(\cosh y\Gamma t - \cos x\Gamma t\right) \\ +\ 2R_D \frac{r_D}{r_{cp}}\big[\cos(-(\delta_D+\phi_{cp}))\sinh(y\Gamma t) - \sin(-(\delta_D+\phi_{cp}))\sin(x\Gamma t)\big]\Big\}.$$

Here $r_D = \mathcal{A}/\mathcal{B}$ and $\bar{r}_D = \bar{\mathcal{A}}/\bar{\mathcal{B}}$, so r_D^2 is the ratio of DCS to CF decay rates. Using a second order Taylor expansion for t, the rates can be approximated as

$$\Gamma\left(D_0(t)\to f_{\mathbf{p}}\right) \simeq \frac{1}{2}\mathcal{B}^2 e^{-\Gamma t}\left(r_D^2 + r_{cp}r_D R_D y'_{\beta_+}\Gamma t + \left[\frac{\left(r_{cp}^2 - r_D^2\right)}{4}x^2 + \frac{\left(r_{cp}^2 + r_D^2\right)}{4}y^2\right](\Gamma t)^2\right)$$

$$\Gamma\left(D_0(t)\to \bar{f}_{\mathbf{p}}\right) \simeq \frac{1}{2}\bar{\mathcal{B}}^2 e^{-\Gamma t}\left(1 + r_{cp}\bar{r}_D \bar{R}_D y'_{\beta_-}\Gamma t + \left[\frac{\left(1 + r_{cp}^2\bar{r}_D^2\right)}{4}y^2 - \frac{\left(1 - r_{cp}^2\bar{r}_D^2\right)}{4}x^2\right](\Gamma t)^2\right)$$

$$\Gamma\left(\overline{D}_0(t)\to \bar{f}_{\mathbf{p}}\right) \simeq \frac{1}{2}\bar{\mathcal{B}}^2 e^{-\Gamma t}\left(\bar{r}_D^2 + \frac{\bar{r}_D}{r_{cp}}\bar{R}_D y'_{\bar{\beta}_+}\Gamma t + \left[\frac{\left(\frac{1}{r_{cp}^2} - \bar{r}_D^2\right)}{4}x^2 + \frac{\left(\frac{1}{r_{cp}^2} + \bar{r}_D^2\right)}{4}y^2\right](\Gamma t)^2\right)$$

$$\Gamma\left(\overline{D}_0(t)\to f_{\mathbf{p}}\right) \simeq \frac{1}{2}\mathcal{B}^2 e^{-\Gamma t}\left(1 + \frac{r_D}{r_{cp}}R_D y'_{\bar{\beta}_-}\Gamma t + \left[\frac{\left(1 + \frac{r_D^2}{r_{cp}^2}\right)}{4}y^2 - \frac{\left(1 - \frac{r_D^2}{r_{cp}^2}\right)}{4}x^2\right](\Gamma t)^2\right)$$

where $y'_\beta = y\cos(\beta) - x\sin(\beta)$ is the mixing parameter rotated by β. The four values of β are

$$\beta_+ = \delta_D + \phi_{cp} \qquad \bar{\beta}_+ = \bar{\delta}_D - \phi_{cp} \tag{1.73}$$

$$\beta_- = -\bar{\delta}_D + \phi_{cp} \qquad \bar{\beta}_- = -\delta_D - \phi_{cp} \tag{1.74}$$

Assuming no CP violation in the D sector leads to

$$r_D = \bar{r}_D\,, \quad \bar{\delta}_D = \delta_D\,, \quad R_D = \bar{R}_D\,, \quad r_{cp} = 1\,, \quad \phi_{CP} = 0\,, \quad \beta_+ = \bar{\beta}_+\,, \quad \beta_- = \bar{\beta}_-\,,$$

which results in the two rate equations (the CP conjugates are identical now),

$$\Gamma\left(D_0(t) \to f_{\mathbf{p}}\right) \simeq \frac{1}{2}\mathcal{B}^2 e^{-\Gamma t}\left(r_D^2 + r_D R_D y'_+ \Gamma t + \left[\frac{(1-r_D^2)}{4}x^2 + \frac{(1+r_D^2)}{4}y^2\right](\Gamma t)^2\right)$$

$$\Gamma\left(\overline{D}_0(t) \to f_{\mathbf{p}}\right) \simeq \frac{1}{2}\mathcal{B}^2 e^{-\Gamma t}\left(1 + r_D R_D y'_- \Gamma t + \left[\frac{(1+r_D^2)}{4}y^2 - \frac{(1-r_D^2)}{4}x^2\right](\Gamma t)^2\right).$$

Another second order Taylor expansion for t gives

$$\Gamma\left(D_0(t) \to f_{\mathbf{p}}\right) \simeq \frac{1}{2}\mathcal{B}^2 e^{-\Gamma t}\left(r_D^2 + r_D R_D y'_+ \Gamma t + \frac{x^2+y^2}{4}(\Gamma t)^2\right) \tag{1.75}$$

$$\Gamma\left(D_0(t) \to \bar{f}_{\mathbf{p}}\right) \simeq \frac{1}{2}\mathcal{B}^2 e^{-\Gamma t}\left(1 + r_D R_D y'_- \Gamma t + \frac{y^2-x^2}{4}(\Gamma t)^2\right). \tag{1.76}$$

Here $y'_\pm = y\cos(\delta_D) \mp x\sin(\delta_D)$, is the mixing parameter rotated by the strong phase. The rate in Equation 1.75 is referred to as the Wrong Sign (WS) rate, while Equation 1.76 is referred to as the Right Sign (RS) rate. The first term in the WS rate equation is due to DCS decays and the last term is due to the D^0 oscillating to a $\overline{D}^0$ before decaying

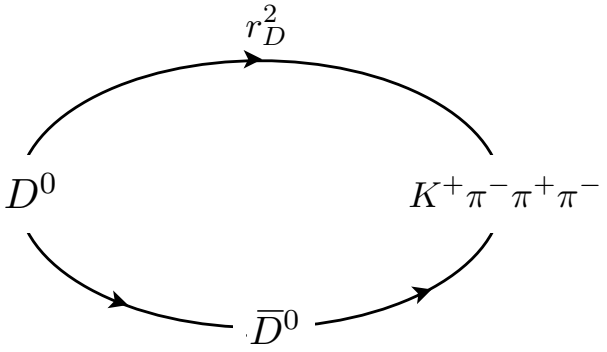

Figure 1.4: A D^0 may decay directly via the DCS process, or it may first oscillate to a $\overline{D}^0$ and decay via the CF process.

via the CF process (see Figure 1.4). The second term is due to interference between the two paths.

The time dependent WS/RS ratio, $R(t)$, is obtained by dividing Equation 1.75 by Equation 1.76 and performing another second order Taylor expansion for t:

$$R(t) = \frac{\Gamma\left(D_0(t) \to f_{\mathbf{p}}\right)}{\Gamma\left(D_0(t) \to \bar{f}_{\mathbf{p}}\right)} \simeq r_D^2 + r_D R_D y'_+ \Gamma t + \frac{x^2+y^2}{4}\left(\Gamma t\right)^2 . \tag{1.77}$$

The third term is often referred to as the rate of mixing (but divided by two), $R_M = \frac{x^2+y^2}{2}$, which is independent of the D^0 decay mode. It is important to note that r_D, R_D and δ_D (from $y'_+ = y\cos\left(\delta_D\right) - x\sin\left(\delta_D\right)$) are the same as the parameters that appear in Equation 1.56. For any two body final state $R_D = 1$, while for any CP self-conjugate final state $\delta_D = 0$ and $r_D = 1$ (in the absence of direct CP violation).

Chapter 2

The LHCb detector

2.1 The Large Hadron Collider

The Large Hadron Collider (LHC) [15], located at the CERN laboratory near Geneva, is the most powerful particle accelerator on Earth. At depths ranging between 45 m and 170 m, it is housed in the tunnel that was once home to the Large Electron Positron (LEP) collider, straddling the Swiss-French border with a 27 km circumference.

At the start of the LHC injector chain is a cylinder of hydrogen gas which acts as a source of protons, produced by ionising the gas. The protons are fed into the LINear ACcelerator 2 (LINAC2) where they reach an energy of 50 MeV before they are injected into the Proton Synchrotron Booster (PSB). Once the protons reach an energy of 1.4 GeV they are fed into the Proton Synchrotron (PS) followed by the Super Proton Synchrotron (SPS) where they are accelerated to energies of 25 GeV and 450 GeV respectively. They are then injected into the LHC in two counter rotating beams, where they are steered and accelerated by a total of 1232 superconducting dipole magnets up to a maximum energy of 7 TeV per beam. The protons complete their long journey when they are brought to collide at one of the four intersection points where the two beam lines cross. It is at these intersection points that the four main LHC experiments are placed to record the remains of the collisions: two general purpose detectors, ATLAS [16] and CMS [17]; ALICE [18], which is designed to study collisions between relativistic heavy ions; and

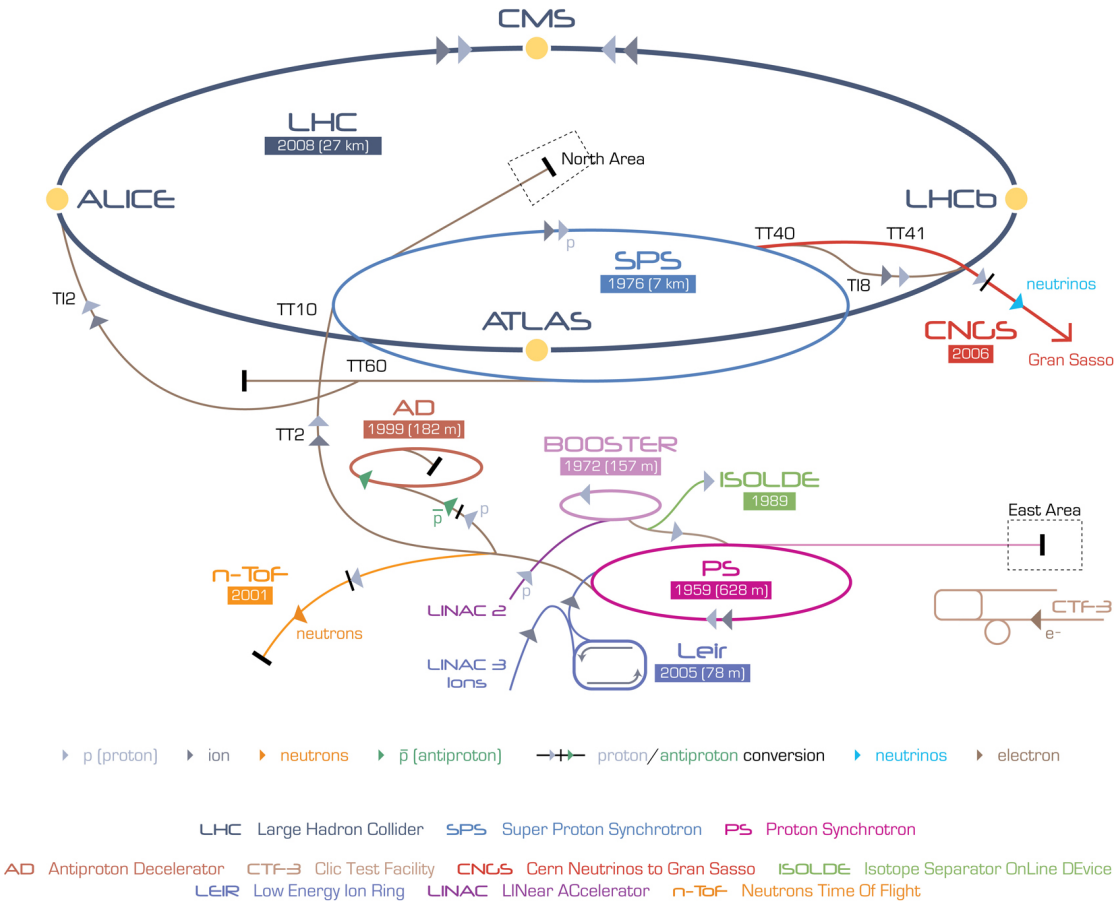

Figure 2.1: The CERN accelerator complex.

LHCb [19], an experiment dedicated to exploring the field of heavy flavour physics. A pictorial representation of the CERN accelerator complex is shown in Figure 2.1.

Although the maximum design centre-of-mass energy of the LHC is 14 TeV, data recorded during 2010 and 2011 was produced with a centre-of-mass energy of 7 TeV. For data taken during 2012 the centre-of-mass energy was increased to 8 TeV.

2.2 LHCb

The Large Hadron Collider Beauty (LHCb) experiment is designed to take advantage of the copious production of B mesons at the LHC. The production cross-section, $\sigma(pp \to b\bar{b}X)$, has been measured by LHCb as $75.3 \pm 5.4 \pm 13.0\,\mu\text{b}$ at $\sqrt{s} = 7\,\text{TeV}$ [20]. This

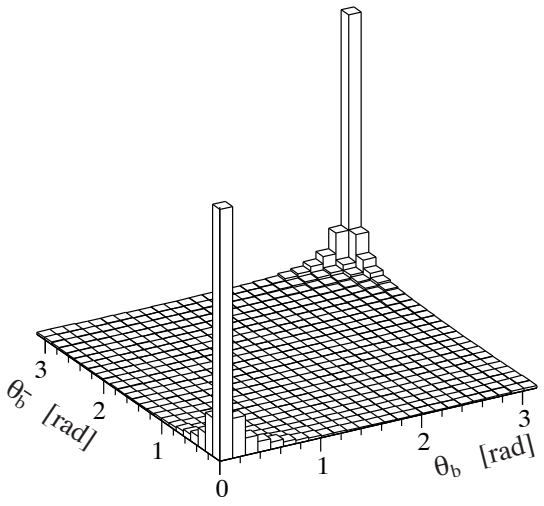

Figure 2.2: PYTHIA simulation of the angles formed with respect to the beam axis by hadrons created from $b\bar{b}$ pairs.

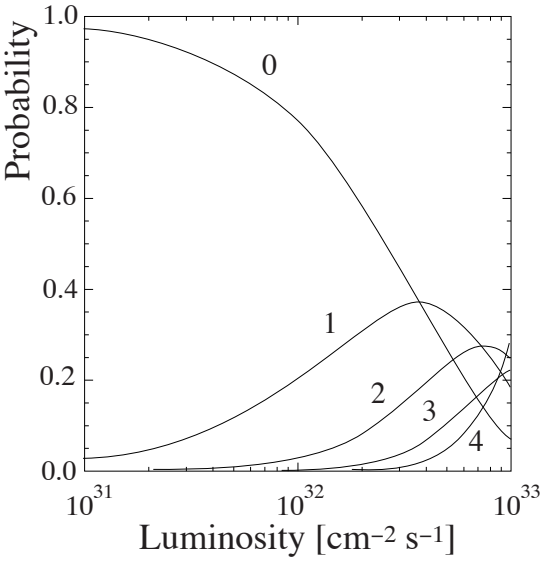

Figure 2.3: Probabilities of different numbers of inelastic pp collisions per bunch crossing as a function of luminosity.

can be compared with a value of 1.3 µb as measured by CDF[1] in $p\bar{p}$ collisions at $\sqrt{s} =$ 1.96 TeV [21].

Because $b\bar{b}$ pairs are produced predominantly with highly correlated trajectories and are so highly boosted at LHC energies, the resulting B hadrons typically travel close to the beam axis in a common direction (demonstrated in Figure 2.2, where PYTHIA [22] is used to simulate pp collisions at the LHC design energy of 14 TeV). To take advantage of this, the LHCb detector is a single arm spectrometer with a small forward angular acceptance of 10 mrad to 300 mrad in the horizontal plane and 10 mrad to 250 mrad in the vertical plane.

The LHC is designed to collide protons with a peak luminosity of $10^{34}\,\mathrm{cm}^{-2}\mathrm{s}^{-1}$. However, at LHCb it is advantageous to run with a much lower luminosity of $2 \times 10^{32}\,\mathrm{cm}^{-2}\mathrm{s}^{-1}$, which can be achieved by defocussing the beams. Figure 2.3 shows that, at this value, the probability of having only one inelastic pp collision dominates the probabilities of multiple interactions. This leads to a cleaner environment (or lower track multiplicity) allowing for more precise reconstruction of multi-body decays. Additionally, a lower luminosity reduces the radiation damage to the front end electronics, as well as the various

[1] A detector at the previous highest energy accelerator - the Tevatron.

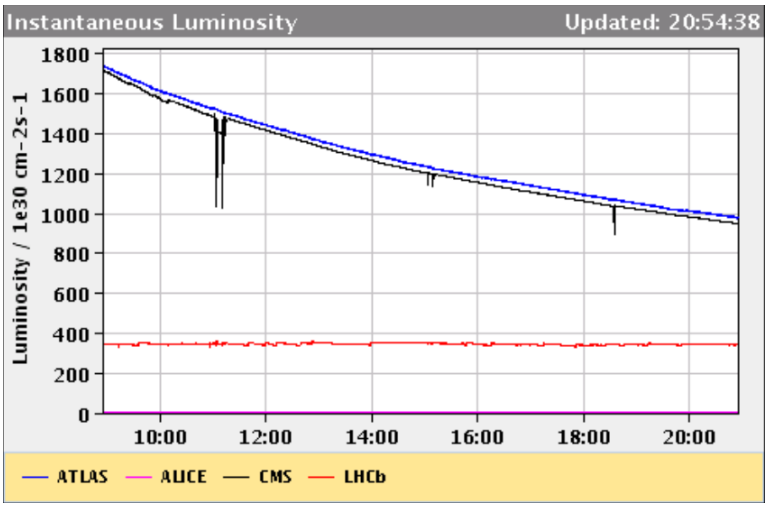

Figure 2.4: Luminosity levelling at LHCb. At LHCb the luminosity is kept constant, unlike at ATLAS and CMS where the luminosity diminishes over the course of a fill.

sub-detectors. Despite these concerns, excellent sub-detector and trigger performance meant it was possible to run with a luminosity of more than $3 \times 10^{32}\,\mathrm{cm}^{-2}\mathrm{s}^{-1}$ for most of the 2011 data taking period. The instantaneous luminosity at LHCb can be tuned by altering the beam focus at the interaction point, allowing an approximately constant luminosity throughout a single run (shown in Figure 2.4), or indeed throughout the life of the detector.

The LHCb detector is comprised of many sub-detectors, each described in the following sections. Figure 2.5 shows the layout of the sub-detectors.

2.2.1 Vertex locator

The LHCb VErtex LOcator (VELO) [23] is a silicon microstrip vertex detector designed to provide precise track coordinate measurements close to the interaction region. This allows reconstruction of both primary and secondary vertices, the latter being especially important for $b-$ and $c-$hadrons which have characteristically long lifetimes. In addition, the VELO is used to provide precise impact parameter measurements for all charged tracks.

The VELO consists of two sets of 21 modules, located on either side of the beam line (the layout of the modules is shown in Fgure 2.6). Some modules are placed to the left

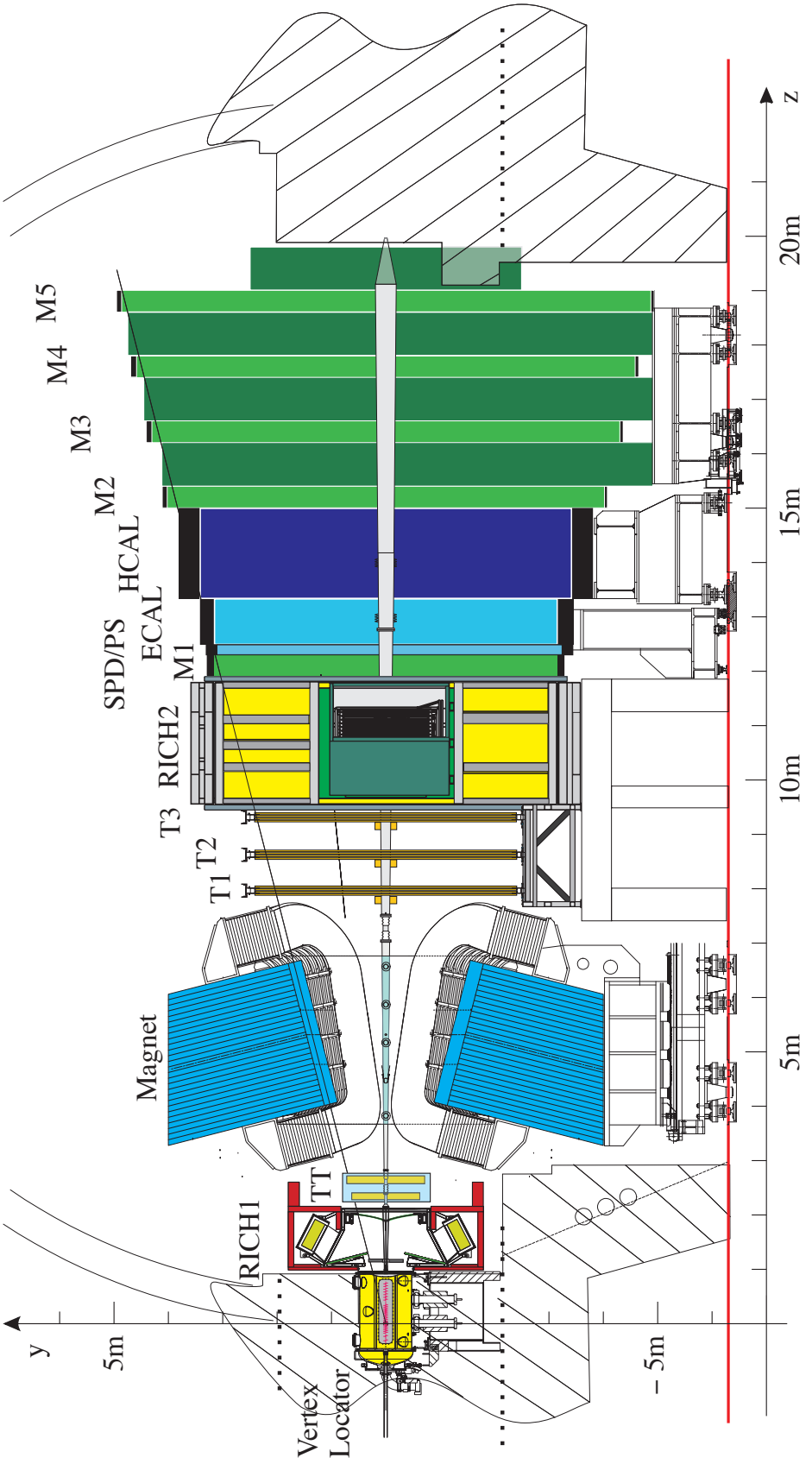

Figure 2.5: A side view of the LHCb detector.

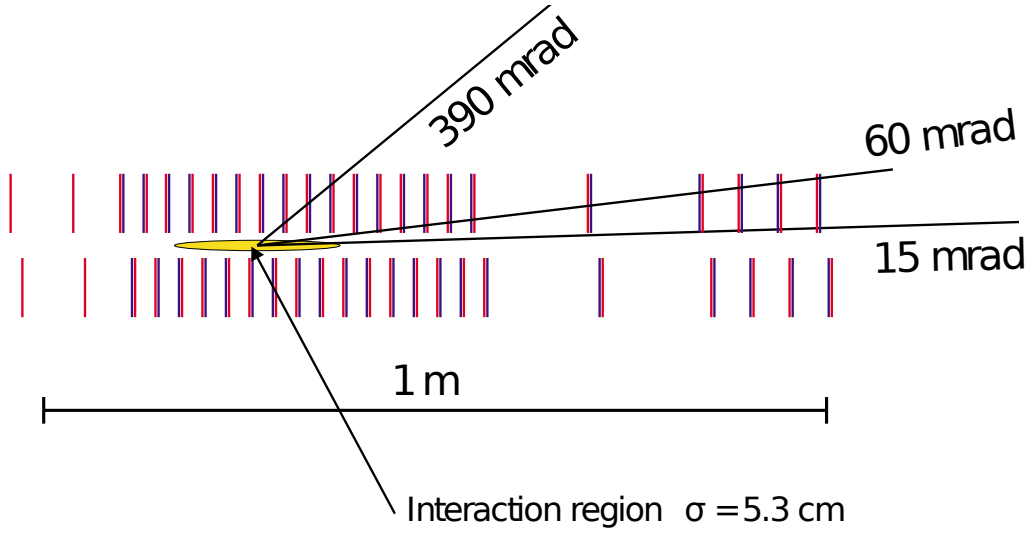

Figure 2.6: The layout of the VELO R (red) and ϕ (blue) sensors shown in the (x, z) plane. A $\pm 2\sigma$ area around the nominal interaction point is shown in yellow. Lines drawn at 390 mrad and 15 mrad represent the maximum and minimum angular coverage, while the line at 60 mrad shows the average track angle in minimum bias events.

of the primary interaction point because of the uncertainty (~ 5 cm) on its z coordinate. Each module comprises two semicircular sensors (one R sensor and one ϕ sensor), each approximately 300 µm in thickness and with a diameter of 84 mm. The R sensors are embedded with silicon in concentric semicircles centred on the beam axis, allowing for determination of the r coordinates of track points. The orthogonal coordinates are supplied by the ϕ sensors in which the silicon strips run radially out from the beam axis. A hole in each sensor with a radius of 8 mm allows safe passage of the beam. Both types of sensor are shown in Figure 2.7.

During LHC injection, the width of the beam increases significantly. Therefore it is necessary to horizontally retract each half of the VELO by ~ 3 cm to avoid damage to the sensors. Once the beam is stable, the aperture reduces to ~ 100 µm and the two halves are moved back together so that they overlap slightly in order to ensure coverage of the full azimuthal acceptance and to aid with module alignment. A vacuum is maintained within the VELO to minimise interactions before charged particles reach the silicon microstrips.

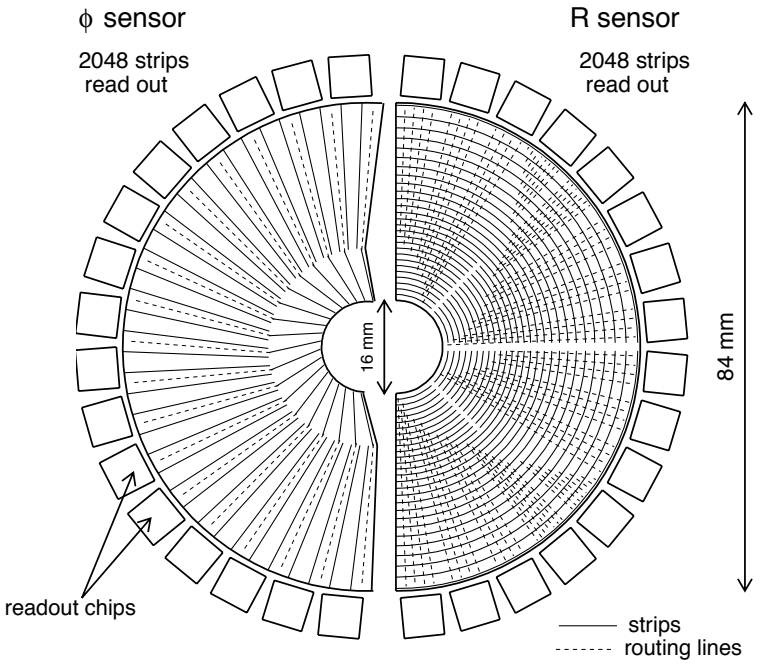

Figure 2.7: Schematic diagram of an R sensor (right) and a ϕ sensor (left).

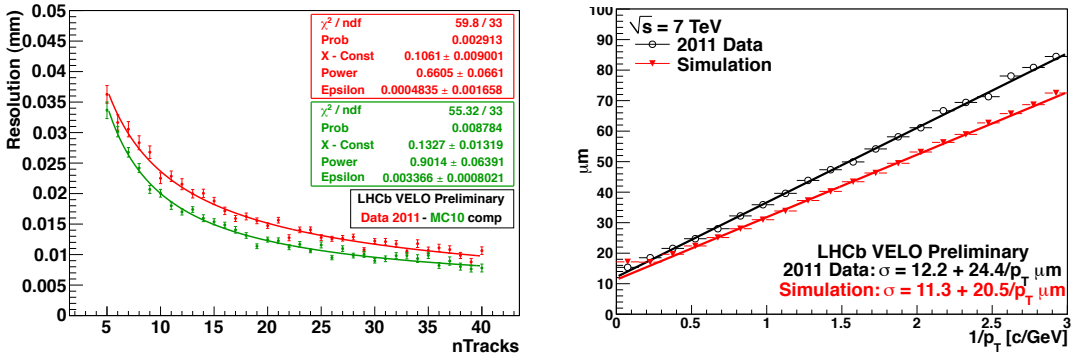

(a) (b)

Figure 2.8: Impact parameter resolution in the $x-$direction, as a function of (a) the number of tracks coming from the primary vertex, and (b) the inverse of the track transverse momentum.

2.2.1.1 Performance

The spatial resolution in the $x-$direction is shown in Figure 2.8 as a function of the number of tracks coming from the primary vertex, and the inverse of track transverse momentum. In the $x-$ and $y-$ directions, the best achieved impact parameter resolution is $\sim 13\,\mu$m, while in the $z-$direction it is $\sim 70\,\mu$m. The resolution is $\sim 18\%$ worse than the Monte Carlo prediction.

2.2.2 Particle ID

One essential design feature of the LHCb detector is its ability to distinguish different final state charged particles. This is especially important for discriminating between decays that are topologically equivalent but differ only by the species of their final state charged particles. An example of particular importance to this thesis is the doubly Cabibbo suppressed decay $D^0 \to K^+\pi^-\pi^+\pi^-$, for which the Cabibbo favoured decay $D^0 \to K^-\pi^+\pi^-\pi^+$ is a major background.

Particle IDentification (PID) is achieved at LHCb by the use of two Ring Imaging CHerenkov (RICH) detectors, a calorimeter system and a muon detector, designed to cover all of the common charged particles (e, μ, π, K, p). Electrons are largely identified by the calorimeter system, muons by the muon detector and charged hadrons by the RICH detectors. The likelihoods for different particle species are formed by combining the likelihoods from the various sub-detectors as follows [24]:

$$\mathcal{L}_e = \mathcal{L}_e^{\mathrm{RICH}}\mathcal{L}_e^{\mathrm{CALO}}\mathcal{L}_{\mathrm{non}-\mu}^{\mathrm{MUON}} \tag{2.1}$$

$$\mathcal{L}_\mu = \mathcal{L}_\mu^{\mathrm{RICH}}\mathcal{L}_{\mathrm{non}-e}^{\mathrm{CALO}}\mathcal{L}_\mu^{\mathrm{MUON}} \tag{2.2}$$

$$\mathcal{L}_h = \mathcal{L}_h^{\mathrm{RICH}}\mathcal{L}_{\mathrm{non}-e}^{\mathrm{CALO}}\mathcal{L}_{\mathrm{non}-\mu}^{\mathrm{MUON}} \tag{2.3}$$

where h represents a charged hadron (π, K, p). Rather than using the absolute likelihood values, it is more efficient to compute the relative difference between the hypotheses of two particle types. For distinguishing between pions and kaons, the difference between the logarithms of their likelihoods, or the Delta Log Likelihood (DLL), is defined as

$$\Delta \log \mathcal{L}(K - \pi) \equiv \log \mathcal{L}_K - \log \mathcal{L}_\pi \tag{2.4}$$

Here, a positive DLL means that a particle is more likely to be a kaon than a pion, and a negative DLL indicates the opposite.

2.2.3 Ring imaging Cherenkov detectors

A charged particle traversing through a dielectric medium faster than the speed of light in that medium will emit Cherenkov radiation at an angle, θ_{C} (called the *Cherenkov angle*), relative to the particle's direction of propagation. The Cherenkov angle is given by

$$\cos\left(\theta_{\mathrm{C}}\right) = \frac{1}{n\beta} \tag{2.5}$$

where n is the refractive index of the medium (also called the radiator) and $\beta = v/c$ is the velocity of the particle divided by the speed of light in a vacuum. Equation 2.5 is easily written as

$$\cos\left(\theta_{\mathrm{C}}\right) = \frac{1}{n}\sqrt{1 + \left(\frac{m}{p}\right)^2} \tag{2.6}$$

where m and p are the mass and momentum of the particle. Here it becomes apparent that knowledge of the refractive index of the radiator, along with measurements of the particle's momentum and the Cherenkov angle of its emitted radiation, enables determination of its mass and, therefore, particle type. This is, in essence, the principle employed by Cherenkov detectors. Figure 2.9(a) is a histogram showing the result of combining every Cherenkov photon in one event with every track in the same event (with some simple selection criteria), repeated for a few thousand events, using the RICH1 sub-detector. Despite the large continuum of background, which results from Cherenkov photons that are combined with the wrong tracks, kaon and proton peaks are clearly observable. Calculating the average of all the mass values for each track results in a much cleaner distribution (the proton peak is shown Figure 2.9(b)). Although this method is not used for PID at LHCb, it demonstrates the ability to reconstruct particle masses using the RICH detectors.

Hadron identification at LHCb is achieved primarily with two RICH detectors [25], RICH1 and RICH2 (both shown in Figure 2.10). Three radiators are used to provide discrimination between kaons and pions in the momentum range $1 - 100\,\mathrm{GeV}/c$. RICH1

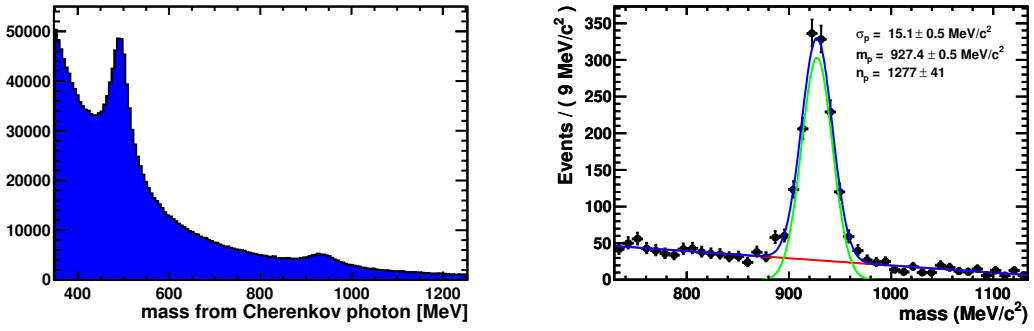

(a) (b)

Figure 2.9: Mass of charged particles traversing through the RICH1 sub-detector. In (a) all Cherenkov photons in an event are combined with all tracks passing through RICH1 and each entry represents one of these combinations. In (b) each entry represents the average mass value for one track when combined with all Cherenkov photons.

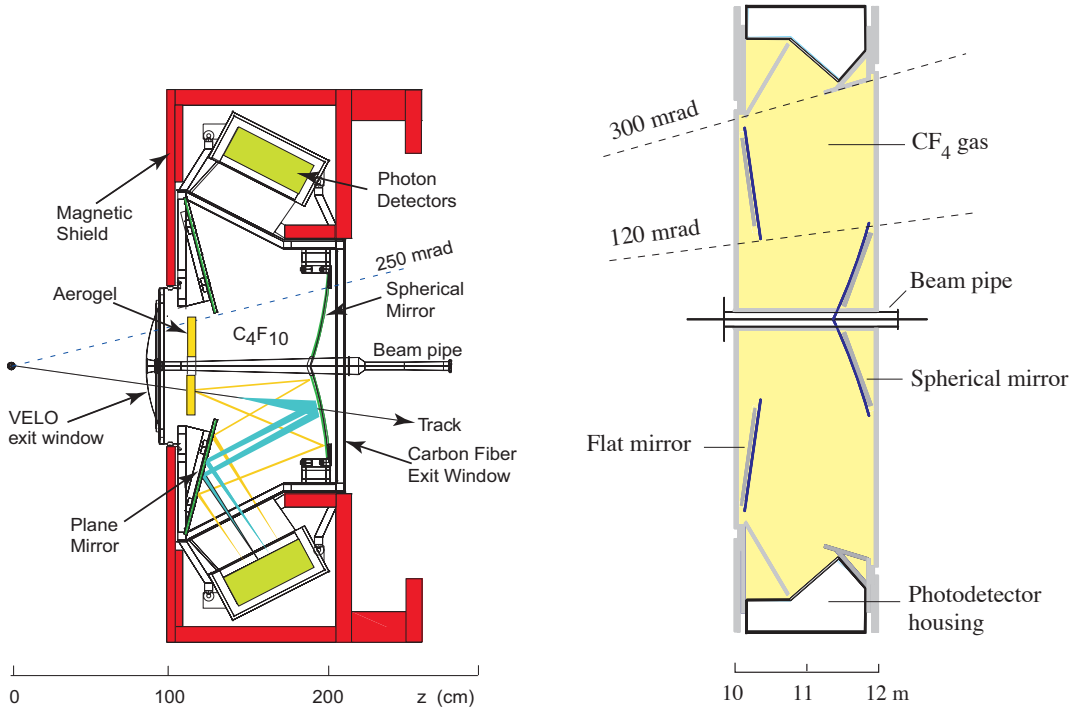

(a) (b)

Figure 2.10: Schematic diagrams of the (a) RICH1 and (b) RICH2 sub-detectors. RICH1 is shown from the side, while RICH2 is shown from above.

contains two radiators: silica aerogel for tracks with momenta up to $\sim 10\,\mathrm{GeV}/c$, and C_4F_{10} gas for tracks up to $\sim 60\,\mathrm{GeV}/c$. Higher momentum tracks ($\sim 15 - 100\,\mathrm{GeV}/c$) are covered by RICH2 which contains CF_4 gas as its radiator.

Each of the two RICH detectors incorporates a similar optical layout. Cherenkov photons are focused into rings by spherical mirrors and reflected onto two flat mirror planes

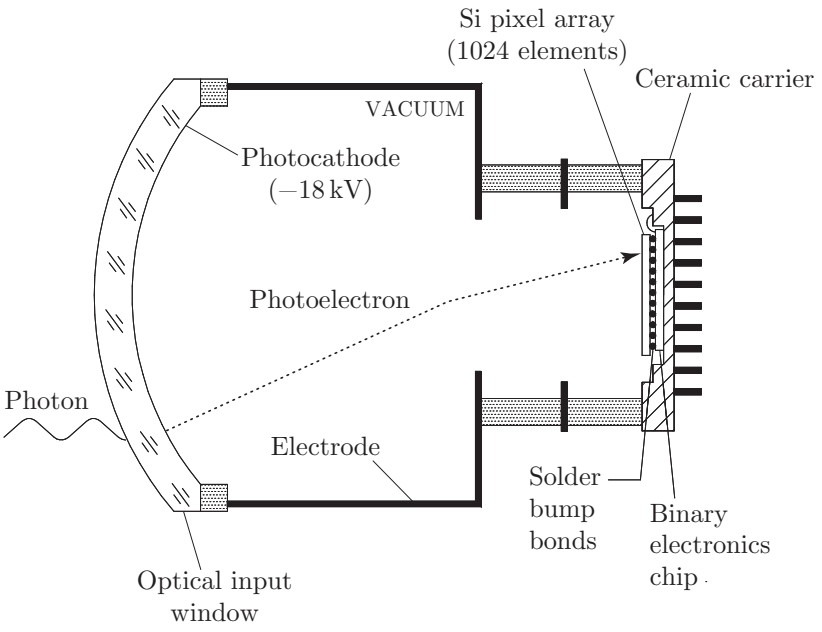

Figure 2.11: Schematic representation of one of the HPDs used in both of the RICH detectors.

(one either side of the beam pipe). The photons are then reflected onto two arrays of hexagonally close packed Hybrid Photon Detectors (HPDs) which are located outside of the detector acceptance and surrounded by iron housings to shield them from the field produced by the LHCb dipole magnet.

Photoelectrons are created when Cherenkov photons incident on the surface of an HPD strike the photocathode. The photoelectrons are then accelerated by a high voltage of $\sim 18\,\mathrm{kV}$ through a vacuum onto a silicon pixel detector consisting of an array of 1024 pixels. This is shown schematically in Figure 2.11.

HPD hits are used to calculate Cherenkov angles with respect to reconstructed tracks by using knowledge of the RICH optical layouts. RICH PID is then performed by comparing the reconstructed Cherenkov angle distribution with the expected distributions for different particle species, by using either a "local" or "global" analysis. In the local analysis the likelihood for different particle hypotheses is calculated for each track individually. The majority of background photons come from neighbouring tracks. Using the global technique is much more accurate because it accounts for this background. Here all tracks in an event are examined simultaneously and a global likelihood is maximised by varying the all of the particles' hypotheses. In LHCb the reconstruction uses

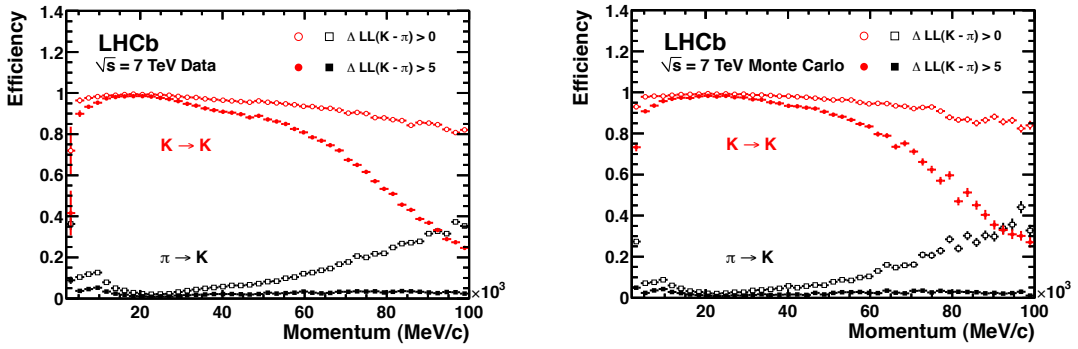

(a) (b)

Figure 2.12: Kaon identification efficiency (red), and pion misidentification rate (black), shown for (a) real data and (b) Monte Carlo.

the global technique by default.

2.2.3.1 Performance

The kaon identification efficiency and pion misidentification rate are shown as a function of momentum in Figure 2.12(a) for two different PID requirements. Over the momentum range $2 < p < 100\,\text{GeV}/c$, for $\Delta \log \mathcal{L}(K - \pi) > 0$ (*i.e.* when the likelihood of the kaon hypothesis is larger than that of the pion hypothesis), the kaon PID efficiency is $\sim 95\%$ and the pion misidentification rate is $\sim 10\%$. Over the same momentum range the kaon PID efficiency drops to $\sim 85\%$ for $\Delta \log \mathcal{L}(K - \pi) > 5$, but the pion misidentification rate improves to $\sim 3\%$. The kaon PID efficiency and pion misidentification rates are shown for Monte Carlo data in Figure 2.12(b).

2.2.4 Calorimeters

The LHCb calorimetry system [26] adopts the classical layout of an Electromagnet Calorimeter (ECAL) followed by a Hadronic Calorimeter (HCAL). The calorimeters are designed to measure the energy and location of photons, electrons and hadrons, providing information for the Level-0 trigger and, ultimately, PID. Two additional sub-detectors, the Scintillating Pad Detector (SPD) and Pre-Shower (PS) are placed before the ECAL to help reject pion backgrounds for signal photons and electrons.

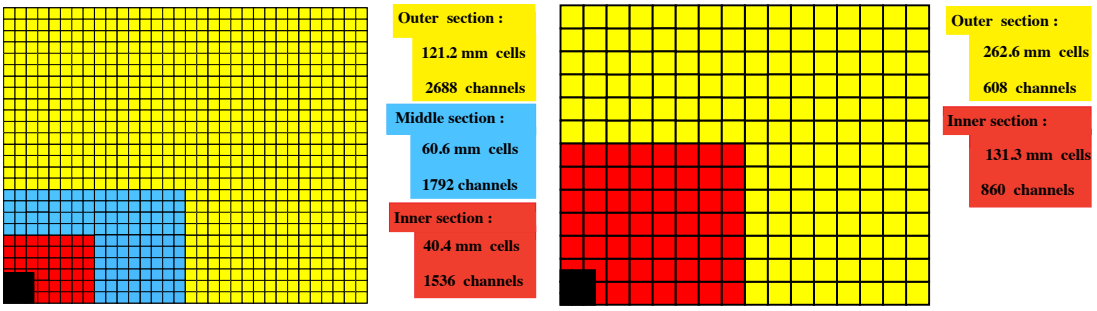

Figure 2.13: Segmentation of the ECAL (left), and HCAL (right). The segmentation of the SPD and PS are the same as the ECAL, but the dimensions are slightly smaller. The black area is a gap for the beam pipe.

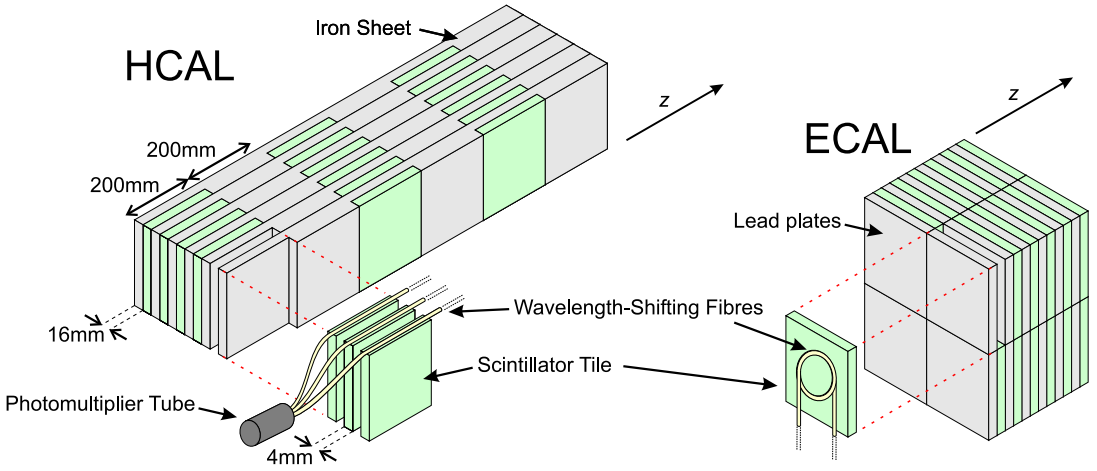

Figure 2.14: Internal structure of the HCAL (left), and ECAL (right). Scintillator tiles and iron absorbers run parallel to the beam axis in the HCAL, while lead absorbers and scintillator tiles are perpendicular to the beam axis in the ECAL.

Each of the four component sub-detectors is laterally segmented with a cell size that increases with the distance from the beam pipe (see Figure 2.13) to account for the varying particle multiplicity across the (x, y) plane (about two orders of magnitude). Although the layout of the segments is identical for the SPD, PS and ECAL, their areas differ slighty because of the projectivity of the LHCb detector.

The same basic principle is employed by each of the calorimeters: a charged particle passing through a polystyrene scintillator emits light which is transferred via Wavelength Shifting (WLS) fibres to Photo-Multiplier Tubes (PMT). In the case of the SPD and PS, single fibres are connected to multianode PMTs for read out.

SPD and PS. The SPD and PS are two almost identical planes of scintillator pads, separated by a 15 mm thick lead converter, equal to 2.5 radiation lengths ($2.5X_0$). The

role of the SPD is to detect charged particles, and when used together with the ECAL, provides rejection of π^0 and γ backgrounds to e^- signal candidates. In addition, SPD information is used by the Level-0 trigger to reject high multiplicity events. The PS is designed to detect electromagnetic particles which shower in the lead plate (primarily e^- and γ because of their comparatively short interaction lengths) and is used in conjunction with the ECAL to reject $\pi^\pm$ backgrounds to e^- signal candidates.

ECAL. The ECAL is a shashlik[2] calorimeter, comprising 66 layers, each of which incorporates a 2 mm thick lead absorber and 4 mm thick scintillator tile. The total thickness of the ECAL is $25X_0$ so that it can fully contain electromagnetic showers.

HCAL. The HCAL is formed of alternating layers of iron absorber and scintillator. However, unlike the ECAL, the scintillator tiles and iron absorbers run parallel to the beam axis instead of perpendicular to it, each with a length corresponding to the hadron interaction length (λ_I) in steel. Adjacent tiles are separated in the lateral direction by 1 cm thick iron. The total thickness of the HCAL in the z direction corresponds to $5.6\lambda_\mathrm{I}$. Figure 2.14 shows a comparison between the internal structures of the HCAL and ECAL sub-detectors.

2.2.4.1 Performance

Using test beam data, the energy resolution of the ECAL is determined to be

$$\frac{\sigma_E}{E} = \frac{(8.5 - 9.5)\,\%}{\sqrt{E}} \oplus 0.8\%$$

where E is measured in GeV and $\oplus$ represents the sum in quadrature. For the HCAL, the energy resolution is measured as

$$\frac{\sigma_E}{E} = \frac{(69 \pm 5)\,\%}{\sqrt{E}} \oplus (9 \pm 2)\,\%.$$

[2]most likely named after a popular Russian kebab

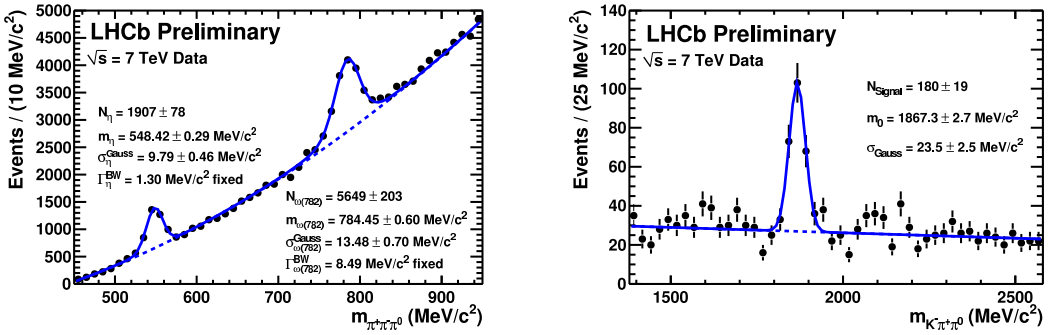

(a) (b)

Figure 2.15: Invariant mass plots for (a) $\eta/\omega \to \pi^+\pi^-\pi^0$ decays, and (b) $D^0 \to K^-\pi^+\pi^0$ decays. Both are reconstructed with a π^0 in the final state, making use of calorimeter information.

Figure 2.15 shows invariant mass distributions which demonstrate the ability to reconstruct particle masses using calorimeter information.

2.2.5 Dipole magnet

Charged particle momentum measurements at LHCb are facilitated by a warm dipole magnet [27], consisting of two ~ 25 ton saddle-shaped aluminium coils supported by a ~ 1500 ton iron yoke (see Figure 2.16). The aperture of the magnet follows the full LHCb acceptance of ± 250 mrad vertically and ± 300 mrad horizontally. An integrated magnetic field of 4 Tm for tracks traversing 10 m provides opposite bending for positive and negative particles in the horizontal plane, allowing $\sim 0.5\%$ momentum resolution for tracks up to 200 GeV/c.

2.2.6 Tracking

Tracking at LHCb is important not only for precise momentum measurements, but also for providing tracks with which to associate Cherenkov rings and calorimeter clusters, as well as providing precise impact parameter measurements for separating primary and secondary vertices. It consists of the VELO (see Section 2.2.1) and the Tracker Turicensis (TT) located before the magnet, and the Tracking stations, T1, T2 and T3, placed after the magnet. Each of the stations T1-T3 comprise an Inner Tracker (IT) [28]

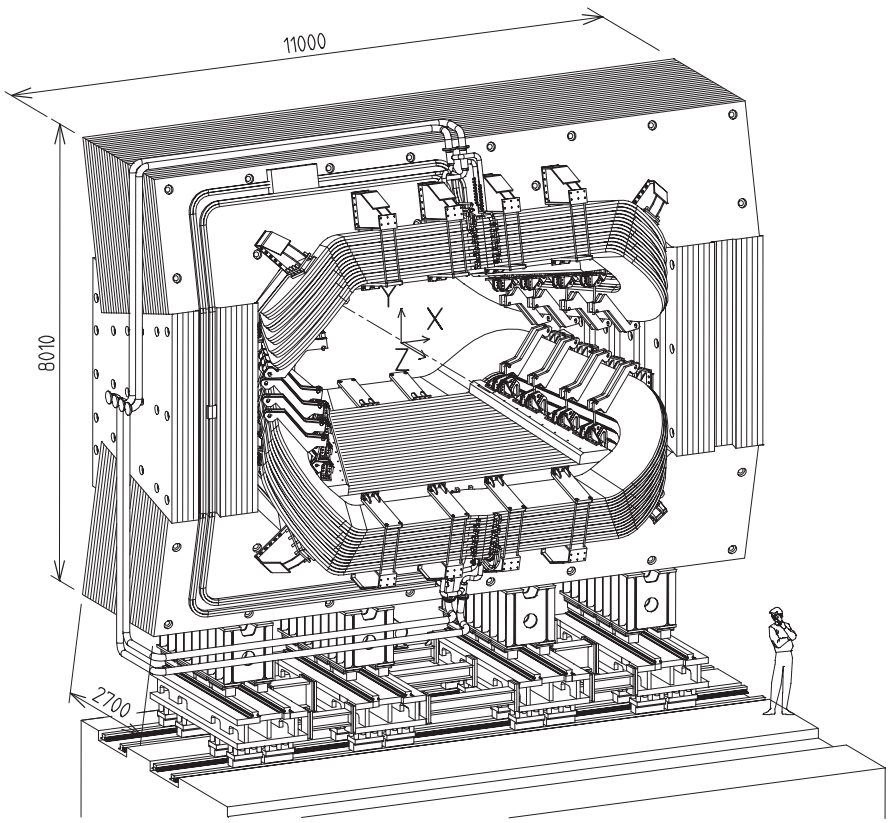

Figure 2.16: Perspective view of the dipole magnet used at LHCb, shown in front of the collision point. Measurements are shown in mm.

and an Outer Tracker (OT) [29]. The TT and IT are collectively known as the Silicon Tracker (ST) because they share the same silicon sensor technology.

ST. Each of the ST stations (the TT and the IT regions of T1-T3) is made from four planes of silicon detectors consisting of microstrips with a pitch of 200 µm. The outer two layers contain vertical microstrips, while the second and third layers contain microstrips rotated with stereo angles of $+5^\circ$ and -5° respectively, enabling determination of the transverse components of a track's geometry. Figure 2.17 shows a vertical layer of the IT and the second plane of the TT, with a $+5^\circ$ rotation. The TT covers the full acceptance, whereas the IT covers only about 2% of the total area of T1-T3.

OT. The OT is a drift tube detector which completes the coverage of the stations T1-T3. The boundary with the IT is chosen to limit the occupancy to less than 10% at the nominal LHCb luminosity. The four layers of each OT station follow the same geometry as the IT with the inner two layers rotated by $+5^\circ$ and -5°. To ensure a

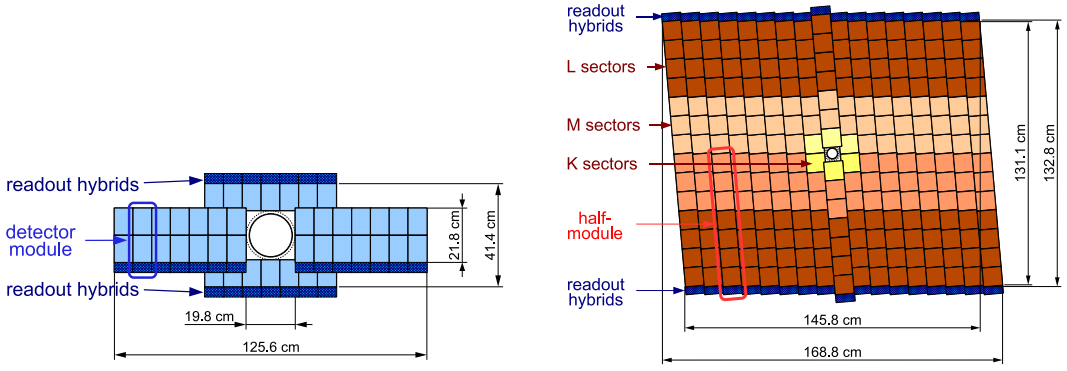

(a) (b)

Figure 2.17: Schematic diagrams of (a) one of the IT outer layers, and (b) the second TT layer, with its +5° rotation.

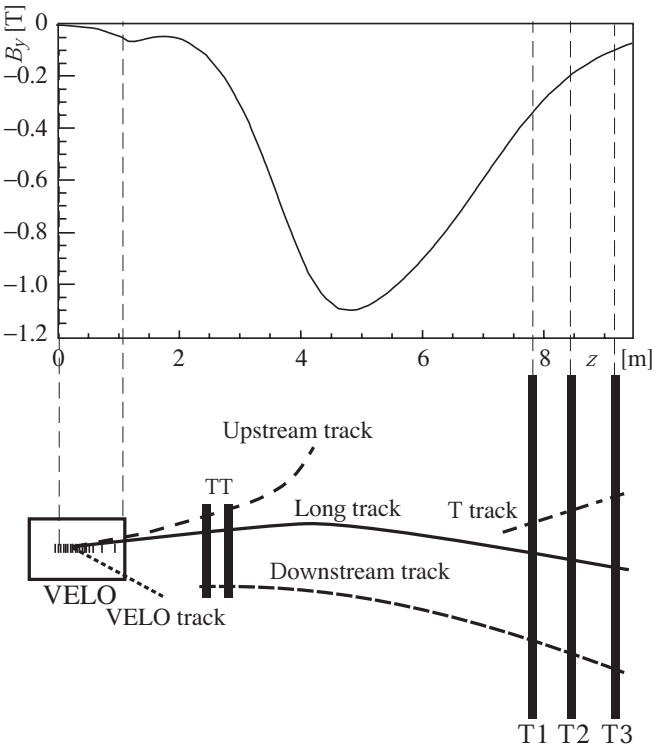

Figure 2.18: A schematic representation of the five different track types at LHCb. Above, the y component of the magnetic field is shown as a function of z.

maximum drift time of 50 ns (the time taken for two proton bunch crossings), the tubes contain a mixture of 70% argon and 30% carbon dioxide, and have an inner diameter of 4.9 mm.

Track types. At LHCb, the reconstruction software classifies tracks depending on which sub-detectors they leave hits in (see Figure 2.18). The five track types are:

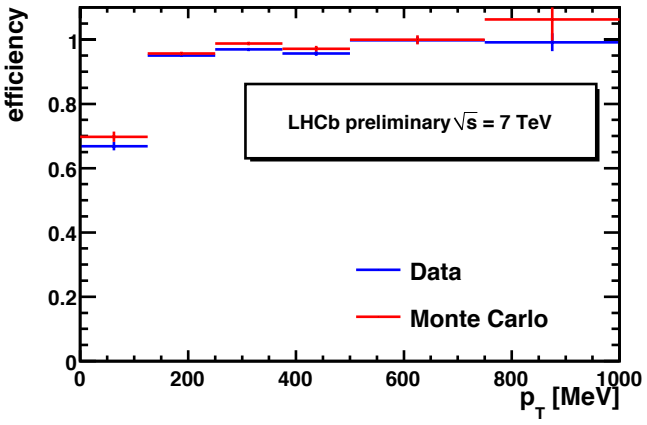

Figure 2.19: Tracking efficiency measured with $K^0_S \to \pi^+\pi^-$ decays as a function of track transverse momentum.

- **VELO tracks** leave the fiducial acceptance after passing through the VELO and are typically used for primary vertex reconstruction.
- **Upstream tracks** typically have low momenta and traverse the VELO and TT before they are swept out of acceptance by the magnet.
- **Long tracks** travel through all of the tracking detectors, from the VELO to T3, and consequently have the most precise momenta measurements.
- **Downstream tracks** only traverse the TT and the T stations. Since they are not recorded by the VELO, these tracks are predominantly produced from decays of long-lived neutral particles.
- **T tracks** pass through only the T stations.

2.2.6.1 Performance

Using the tag and probe method, the tracking efficiency is measured with $K^0_S \to \pi^+\pi^-$ decays as a function of track transverse momentum. The resulting distribution for long tracks is shown in Figure 2.19, where it is compared to the Monte Carlo prediction. The tracking efficiency is above 95% for all tracks with a transverse momentum larger than 100 MeV/c.

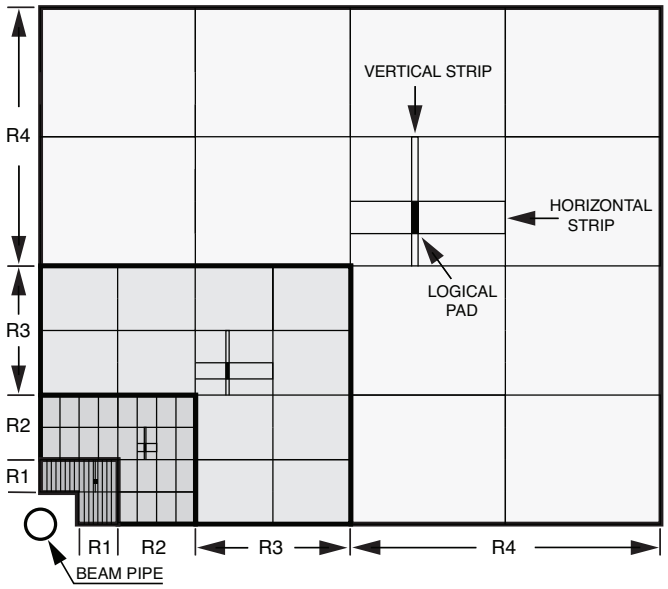

Figure 2.20: One quarter of the M2 (or M3) station, shown from the front.

2.2.7 Muon chambers

Although it is not particularly relevant for this thesis, muon detection is vital for any analyses which contain one or more muons in the final state. The most notable, perhaps, is the search for the flavour changing neutral current decay $B_s^0 \to \mu^+\mu^-$ [30]. Five muon stations [31] (M1-M5) are used to provide reconstructed muon tracks for these analyses. In addition, the muon stations are used to search for high transverse momentum tracks for the Level-0 trigger. The M1 station is placed before the calorimeters, while the stations M2-M5 are located after the calorimeter and are each separated by 80 cm iron absorbers. The iron plates amount to a thickness of $20\lambda_{\mathrm{I}}$ and are designed to remove any hadronic background that exits the HCAL. Consequently, to penetrate through to M5, muons must have a momentum of at least 6 GeV/c.

The muon chambers increase in size from M1 to M5 to maintain an acceptance of ± 306 mrad in the horizontal plane and ± 258 mrad in the vertical plane. Each of the muon chambers is divided into regions of different chamber and logical pad size, increasing in size further from the beam pipe (see Figure 2.20). The M1, M2 and M3 stations have a higher spatial resolution in the bending plane in order to precisely measure the trajectory and transverse momentum of a muon candidate. M4 and M5 must simply identify any tracks which penetrate the iron layers.

All of the muon stations use Multi-Wire Proportional Chambers (MWPC), except for the inner region (R1) of M1 (where the particle flux is too high) which employs triple-GEM (Gas Electron Multiplier) detectors, chosen because of their higher radiation tolerance. Both types of chamber use a mixture of $Ar - CO_2 - CF_4$ gas.

2.2.8 Trigger

The LHCb trigger system [32] is designed to reduce the 10 MHz rate of visible interactions down to 3 kHz for offline storage. This is achieved by selecting events that contain tracks with high transverse momentum (p_T), high transverse energy (E_T), and which have large impact parameters with respect to the primary collision vertex. These are features common to decays of both $b-$ and $c-$hadrons, which have relatively large masses and fly significant distances before decaying. The trigger system employs a Level-0 (L0) hardware trigger to reduce the rate to about 1 MHz, followed by two stages of software trigger, called the High Level Triggers (HLT1 and HLT2), which reduce the rate down to 3 kHz.

2.2.8.1 Level-0 trigger

The L0 hardware trigger consists of separate parts: the calorimeters, and the muon chambers. Information from each of these sub-detectors is fed into the L0 decision unit (L0DU), which makes the final decision for each bunch crossing.

The calorimetry system identifies e^-, γ, and charged hadron candidates by using information from the SPD, PS, ECAL and HCAL. The E_T of each candidate is calculated by measuring the E_T deposits in clusters of 2×2 cells. The highest E_T value for each particle species is recorded and given to the L0DU.

Muon tracks are located by searching for hits in the muon chambers that form straight lines pointing back to the interaction point. The p_T of muon candidates is calculated using only the first two muon stations which yields a resolution of $\sim 20\%$. The two highest-p_T muons are recorded in each quadrant and sent to the L0DU.

In addition, global event variables are used in the selection of events: a minimum requirement on the total HCAL energy is imposed to ensure that only visible interactions are selected, and an upper limit is placed on the number of SPD hits, which removes events with excessively high track multiplicities in order to reduce the average processing time per event.

2.2.8.2 High level trigger

The HLT is a two-stage software trigger in the form of a C++ application, with several different trigger lines running in parallel for both HLT1 and HLT2. The HLT has access to all data from the detector, so could in principle perform the full offline reconstruction. However, timing constraints limit this. For example, there is no RICH reconstruction, and a much faster track fitting algorithm is used which increases the tracking uncertainty (lowers the momentum resolution) from 0.35% to $\sim 1\%$.

The job of HLT1 is to reconstruct particles using the VELO and tracking stations, using L0 candidates as an input, and output events at a rate of 30 kHz. Of particular importance for this thesis is the highly inclusive HLT1 1-track trigger line [33], which accepts events that contain at least one track with high momentum, high p_{T}, good track fit quality and a large impact parameter with respect to the primary vertex, taking advantage of the characteristics of $b-$ and $c-$hadron decays.

In the HLT2 algorithms, tracks are combined to create composite particles. The example most relevant for this thesis is the *HLT2CharmHadD02HHHH* trigger line (see Section 5.3) which searches for $D^0 \to hhhh$ candidates, where $hhhh$ represents any neutral combination of charged kaons or pions (with the exception of $D^0 \to K^+K^+K^-K^-$ which is kinematically forbidden). The 3 kHz output rate of HLT2 is divided evenly between $b-$hadrons decaying to charged hadrons, $b-$hadrons decaying to leptons, and decays of charm hadrons.

2.2.9 Software

The bulk of the LHCb software (from event generation to physics analysis) is built using the C++ GAUDI framework [34]. The software is split into two main parts: the simulation phase (which includes digitisation), and the reconstruction phase, which is identical for both Monte Carlo simulation and real data. The main stages are outlined below.

Simulation. This is handled by the GAUSS application, which is responsible for event generation, and the subsequent decays of particles, as well as their interactions with the detector material. Particle generation is provided by PYTHIA [22]. decays of $b-$ and $c-$hadrons are modelled using EVTGEN [35], and final state radiation is simulated with PHOTOS [36]. Material interactions are simulated with GEANT4 [37], along with use of the Detector Description Database (DDDB) which contains the geometry of the detector.

Digitisation. The digitisation phase is provided by BOOLE, which digitises the response of the detector. Background from the LHC is included, as well as any imperfections and resolutions of the sub-detectors. BOOLE takes simulated events from GAUSS and outputs them in a format identical to that of real data read out of the LHCb detector, except that Monte Carlo truth information is included.

Reconstruction. BRUNEL is responsible for the reconstruction of physics objects including tracks, Cherenkov photons, and calorimeter clusters. As input, BRUNEL accepts output from either BOOLE or the LHCb detector, and makes use of the DDDB, as well as the Conditions Database (CondDB) which contains information such as calibration and alignment parameters.

Analysis. The final stage in the reconstruction chain is the DAVINCI application. It creates objects like composite particles and decay chains, and supplies information including kinematic and PID variables, which are necessary for event selection. DAVINCI

provides a wide range of algorithms useful for physics analyses, including a Monte Carlo background categorisation tool (described below).

2.2.9.1 Background classification

When performing an analysis on a particular particle decay, it is useful to study potential sources of background in detail. The Monte Carlo background categorisation algorithm [38] provides classification of Monte Carlo simulated events and separates them into different (mutually exclusive) categories. A reconstructed charged track and a true Monte Carlo track are considered to be correctly matched if they share at least 70% of their sub-detector hits. The different background categories are summarised below:

- **Signal:** All of the particles in the decay chain are correctly matched to Monte Carlo particles with the same PIDs. Particles decaying via intermediate resonances are also considered to be signal candidates, and are distinguished from non-resonant decays. For example, the non-resonant decay $D^0 \to K^-\pi^+\pi^-\pi^+$ and the decay $D^0 \to \overline{K}^{*0}(892)\,\rho^0 \to K^-\pi^+\pi^-\pi^+$ are both signal decays to the same final state.

- **Fully reconstructed physics background:** All reconstructed particles are correctly matched to Monte Carlo particles, except for the mother.

- **Reflection:** Any of the daughter particles is incorrectly identified. For example, $D^0 \to K^+\pi^-\pi^+\pi^-$ being incorrectly reconstructed as $D^0 \to \pi^+\pi^-\pi^+\pi^-$. This background can be largely suppressed by imposing PID requirements on the daughter particles and a tight mass window around the reconstructed D^0 mass.

- **Partially reconstructed physics background:** A fragment of a decay has been identified as signal. For example, a $D^0 \to K^-\pi^+$ decay reconstructed from a true $D^0 \to K^-\pi^+\pi^-\pi^+$ decay. This background can also include reflections.

- **Low mass background:** A special case of partially reconstructed physics background where there is no mis-identification, resulting in systematically low reconstructed masses.

- **Ghost background:** At least one of the reconstructed final state particles has no associated Monte Carlo particle.

- **Primary vertex background:** At least one of the reconstructed final state particles comes directly from the primary collision vertex. This background is suppressed by the use of impact parameter requirements.

- **Badly reconstructed primary vertex:** A special case of primary vertex background in which all of the reconstructed final state particles are from the primary collision vertex.

- **Pileup background:** The final state reconstructed particles originate from more than one primary collision vertex.

- $\boldsymbol{b\bar{b}}$ **background:** Background which is not in any of the categories above, with at least one reconstructed final state particle with a mother that contains a b quark.

- $\boldsymbol{c\bar{c}}$ **background:** Background which is not in any of the categories above, with at least one reconstructed final state particle with a mother that contains a c quark.

- $\boldsymbol{uds}$ **background:** Background that is not categorised by any of the above.

Chapter 3

Event selection for RICH mirror alignment

3.1 Introduction

Good separation of different particle types is essential for distinguishing between topologically equivalent decay modes whose final states differ only by particle type. Using the derivations found in [12, 39], for small Cherenkov angles and large momenta ($p \gg m$), Equation 2.6 can be approximated by

$$1 - \frac{\theta_{\mathrm{C}}^2}{2} = \frac{1}{n}\left(1 + \frac{m^2}{2p^2}\right). \tag{3.1}$$

For two charged particles with different masses but the same momenta, the difference between the squares of their Cherenkov angles, θ_1 and θ_2, is

$$\theta_2^2 - \theta_1^2 = -\frac{1}{n}\frac{\Delta\left(m^2\right)}{p^2} \tag{3.2}$$

where $\Delta\left(m^2\right) = m_1^2 - m_2^2$, is the difference between the squares of the masses of the two particles. This can be rewritten as

$$\Delta\theta_{\mathrm{C}} \cdot (\theta_1 + \theta_2) = -\frac{1}{n}\frac{\Delta\left(m^2\right)}{p^2} \tag{3.3}$$

where $\Delta\theta_{\mathrm{C}} = \theta_2 - \theta_1$. For $p \gg m$, Equation 3.1 becomes

$$\theta_{\mathrm{C}} = \sqrt{2\left(1 - \frac{1}{n}\right)} \simeq \sqrt{2\,(n-1)} \tag{3.4}$$

where the approximation has been made for $n - 1 \ll 1$. Therefore

$$(\theta_1 + \theta_2) = 2\sqrt{2\,(n-1)} \tag{3.5}$$

which can be substituted into Equation 3.3 to give

$$\Delta\theta_{\mathrm{C}} = \frac{1}{2n\sqrt{2\,(n-1)}} \cdot \frac{\Delta\left(m^2\right)}{p^2}. \tag{3.6}$$

Assuming the Cherenkov angles follow a Gaussian distribution with a width σ_θ, the number of standard deviations separating two different particle species, each with momentum p, is given by

$$n_\sigma = \frac{\Delta\theta_{\mathrm{C}}}{\sigma_\theta} = \frac{1}{2n\sigma_\theta\sqrt{2\,(n-1)}} \cdot \frac{\Delta\left(m^2\right)}{p^2}. \tag{3.7}$$

Here, it is evident that the PID performance of the RICH detectors is dependent upon the Cherenkov angle resolution. There are four sources that dominate the resolution:

- **Emission point error:** Because the spherical mirrors are tilted, the position of the Cherenkov photons on the HPD plane depends on how far along the track trajectory they are emitted. All photons are assumed to have been emitted at the centre point of the track segment within the radiator. This leads to a smearing of the reconstructed Cherenkov angle.

- **Chromatic dispersion:** The refractive index of the radiator (and therefore the Cherenkov angle) varies with the wavelength of the Cherenkov photon. Since the wavelength of an emitted photon is unknown, this leads to an uncertainty on the Cherenkov angle.

- **HPD resolution:** The finite HPD pixel size limits the Cherenkov angle resolution.

Table 3.1: The four main sources of Cherenkov angle uncertainty, shown for each of the three RICH radiators. The refractive index of each of the radiators is shown at 0° C, 101.325 kPa and 400 nm.

$\sigma(\theta_C)$ (mrad)	Aerogel	C_4F_{10}	CF_4
Emission point	0.4	0.8	0.2
Chromatic dispersion	2.1	0.9	0.5
HPD resolution	0.5	0.6	0.2
Tracking	0.4	0.4	0.4
Total	2.6	1.5	0.7
Refractive index	1.03	1.0014	1.0005

- **Tracking resolution:** Since the Cherenkov angle is measured with respect to a charged track, uncertainty on the track direction leads to an uncertainty on the measured Cherenkov angle.

Table 3.1 gives a summary of the effects of each of these sources in all three of the RICH radiators, along with the total resolutions which is the sum in quadrature of the individual contributions.

Because of their large size, each of the RICH mirror planes consists of an array of mirror segments: the RICH1 mirrors consists of 4 spherical segments and 16 flat segments, while the RICH2 mirrors comprise 56 spherical segments and 40 flat segments. The segmentation and numbering scheme of the mirrors in the left-hand side of RICH2 is shown in Figure 3.1. Imperfect alignment of a mirror segment will result in a discrepancy between the trajectory of a track and the centre of its photon ring on the HPD plane (illustrated in Figure 3.2). This leads to an error on the measured Cherenkov angle.

The goal of the mirror alignment is to reduce the uncertainty on the Cherenkov angle measurement caused by misaligned mirror segments to less than 0.1 mrad, so that it is small compared to the irreducible sources of error.

3.2 Alignment method

The RICH mirror segments are aligned with collision data, employing a method similar to that developed by HERA-B [42]. A misalignment results in the displacement of a Cherenkov ring with respect to the track trajectory (see Figure 3.3), leading to the

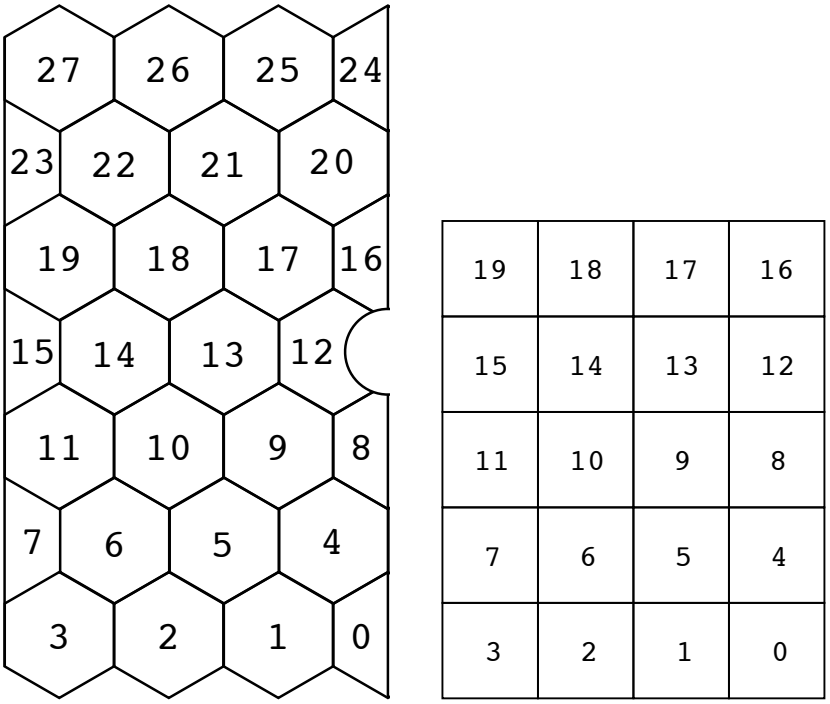

Figure 3.1: Mirror numbering convention for (a) the spherical mirror plane, and (b) the flat mirror plane in the left-hand side of RICH2. The gap next to spherical mirror 12 is for the beam pipe.

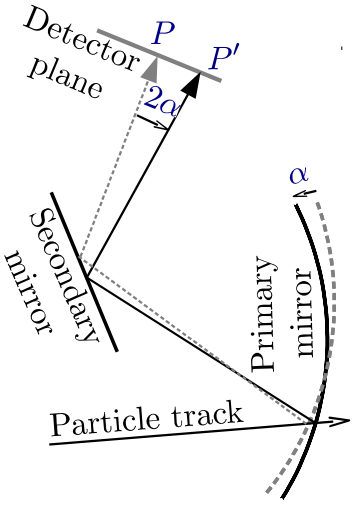

Figure 3.2: The effect of a tilted mirror segment. A small tilt causes a shift of the Cherenkov photon on the HPD plane, resulting in a translation of the photon ring [40].

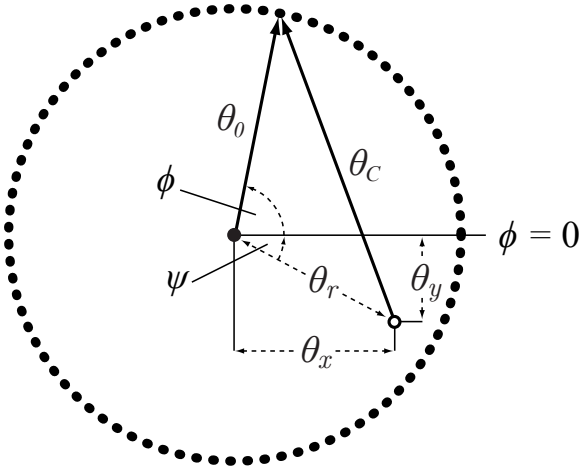

Figure 3.3: A schematic representation of a Cherenkov ring misalignment. Here θ_{C} is the reconstructed Cherenkov angle and θ_0 is the expected Cherenkov angle. The ring is displaced by θ_r from the reconstructed track trajectory (shown as an empty circle). θ_x and θ_y are the horizontal and vertical displacements. The misalignment is exaggerated for illustrative purposes. [41]

measured Cherenkov angle having a dependence on the azimuthal angle, ϕ, around the ring. Starting with Figure 3.3 and using trigonometric identities, the difference between the expected Cherenkov angle, θ_0, and the measured Cherenkov angle, θ_{C},

$$\Delta\theta = \theta_{\mathrm{C}} - \theta_0 \tag{3.8}$$

can be expressed in terms of ϕ, following the derivation in [41]. First, the relationship between θ_0, θ_{C}, and the displacement of the ring with respect to the track, θ_r, is given by the cosine rule

$$\theta_{\mathrm{C}}^2 = \theta_0^2 + \theta_r^2 - 2\theta_0\theta_r \cos(\phi + \psi) \tag{3.9}$$

where ψ is the angle between θ_r and the line $\phi = 0$. Inserting the expression from Equation 3.8 gives

$$(\theta_0 + \Delta\theta)^2 = \theta_0^2 + \theta_r^2 - 2\theta_0\theta_r \cos(\phi + \psi) \tag{3.10}$$

which, when rearranged, leads to

$$\begin{aligned} \Delta\theta + \frac{1}{2\theta_0}\left(\Delta\theta^2 - \theta_r^2\right) &= -\theta_r \cos(\phi + \psi) \\ &= -\theta_r \left(\cos\phi\cos\psi - \sin\phi\sin\psi\right). \end{aligned} \tag{3.11}$$

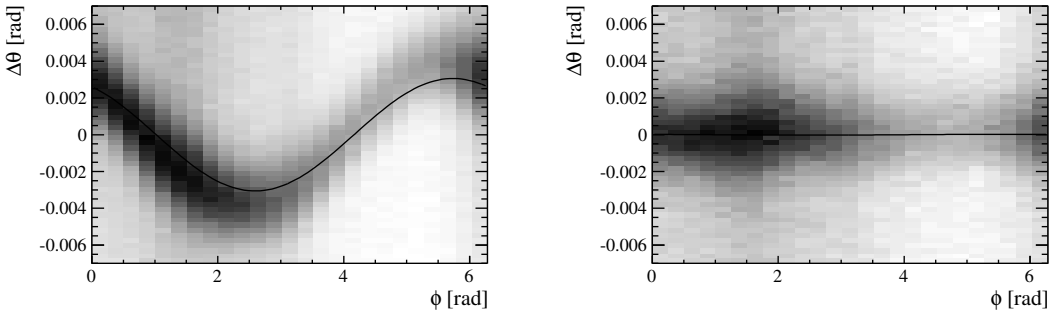

(a) (b)

Figure 3.4: $\Delta\theta$ vs. ϕ histograms for one of the RICH1 mirror pairs (a) before and (b) after mirror alignment [40].

Using the relations

$$\cos\psi = \frac{\theta_x}{\theta_r} \quad \text{and} \quad \sin\psi = \frac{\theta_y}{\theta_r}\,, \tag{3.12}$$

Equation 3.11 can be written as

$$\Delta\theta + \frac{1}{2\theta_0}\left(\Delta\theta^2 - \theta_r^2\right) = -\theta_r\left(\frac{\theta_x}{\theta_r}\cos\phi - \frac{\theta_y}{\theta_r}\sin\phi\right) = \theta_y\sin\phi - \theta_x\cos\phi. \tag{3.13}$$

Making the assumption that misalignments are small, *i.e.* $\Delta\theta$, $\theta_r \ll \theta_0$, Equation 3.13 becomes

$$\Delta\theta = \theta_y\sin\phi - \theta_x\cos\phi. \tag{3.14}$$

Here θ_x and θ_y represent the combined tilts of spherical and flat mirrors about the x and y axes[1]. Such a distribution can be seen in Figure 3.4 for photons reflecting from one spherical segment and one flat segment in RICH1, before and after mirror alignment, using real collision data.

To measure misalignments of all of the individual mirror segments, a system of simultaneous equations is used [40], each of which represents a "mirror pair" (a pairing of a spherical and a flat segment, for example, spherical mirror 12 and flat mirror 9 in RICH2, referred to as mirror pair 1209). The list of mirror pairs is chosen so that each flat mirror is paired with at least two spherical mirrors.

[1] θ_x and θ_y also incorporate "magnification coefficients" which relate the displacement of the Cherenkov rings to physical mirror tilts.

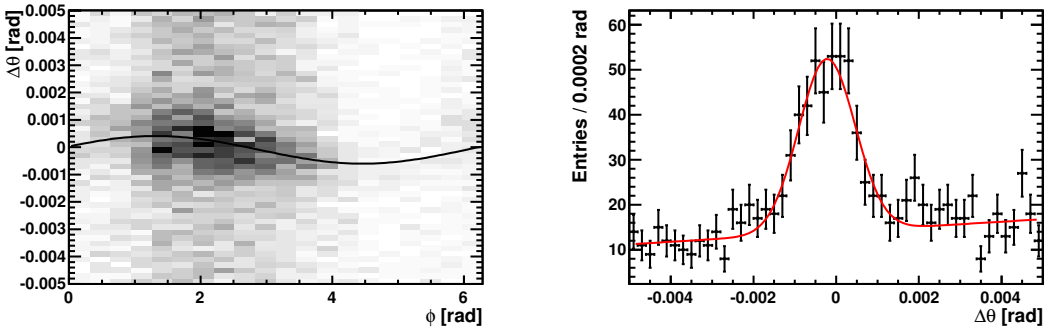

(a) (b)

Figure 3.5: (a) A sinusoidal fit to the ϕ distribution of the $\Delta\theta$ peak positions for RICH2 mirror pair 2218. (b) A fit to the ϕ slice between 162° and 180° degrees.

Each of the $\Delta\theta$ vs. ϕ distributions (one per mirror pair) is divided into twenty slices in ϕ. To find the $\Delta\theta$ peak position of each ϕ slice, the $\Delta\theta$ projections are fit with a Gaussian signal component plus a first order polynomial background component. An example is shown in Figure 3.5 for mirror pair 2218 in RICH2. Once all of the peak positions are found, their ϕ distribution is fit with a sinusoidal function of the form shown in Equation 3.14, allowing extraction of misalignment parameters.

To enable accurate estimation of the expected Cherenkov angle, θ_0, only high momentum tracks are used. This is because as momentum increases, the Cherenkov angle values of different particle species tend towards the same saturation value. Therefore all high momentum tracks can be assumed to be pions (Equation 3.4 shows that the Cherenkov angle is independent of the particle mass at high momentum). In addition, only "unambiguous" photons are used to populate the histograms. A photon is declared unambiguous if the reconstruction results in it reflecting off the same pair of mirrors regardless of how far along the track it is emitted. This is useful for removing background from the $\Delta\theta$ vs. ϕ histograms.

The alignment procedure is iterative: at the end of each iteration, the misalignment parameters are entered into the CondDB. Subsequent iterations use the updated parameters from previous iterations. The procedure ends when all of the x and y tilt corrections for every mirror pair are less than 0.1 mrad.

3.3 Event selection

Because the photon population of the mirror pairs is very heavily biased towards the mirrors closest to the beam axis (illustrated in Figure 3.6), to achieve adequate populations in all of the peripheral mirror pairs it is necessary to reconstruct $\sim$ 5M events for alignment of the RICH2 mirrors. The mirror alignment employs an iterative procedure, therefore the same $\sim$ 5M events need to be reconstructed several times (once per iteration), using a significant amount of CPU time. An event selection that picks out events with highly populated peripheral pairs is used to significantly reduce the number of events needed to fewer than 100k for RICH2.

For each alignment histogram ($\Delta\theta$ vs. ϕ for a particular mirror pair), most of the twenty ϕ bins must be populated sufficiently for successful convergence of the fitting procedure. Testing reveals that each ϕ bin requires at least 300 entries, and that the fit can cope with up to four insufficiently filled ϕ bins. Therefore, events are selected so that all ϕ bins in all alignment histograms contain at least 300 entries. The selection procedure is described in following text.

During the reconstruction of an event, if there are any photons within an alignment histogram ϕ bin which is not already full enough (*i.e.* containing at least 300 entries), the event is accepted. In general, events will contribute to many of the ϕ bins, so the population of each ϕ bin in all of the alignment histograms is incremented appropriately for any accepted events. If an event is found to contain no photons which add to any of the empty (*i.e.* fewer than 300 entries) ϕ bins, that event is discarded and all of the photons are ignored.

Because of the location of some of the mirror pairs, their ϕ distributions can be extremely non-uniform (see Figure 3.5(a) for an example) and in some cases it is practically impossible to reconstruct the number of events needed to fill all of the ϕ bins. However, the mirror pairs used in the alignment procedure are chosen so that this problem is avoided. After the selection there are enough sufficiently full ϕ bins for the fitting procedure to successfully converge. Figure 3.7 shows the number of insufficiently filled ϕ bins for each

mirror pair. The mirror pair using spherical mirror 2 and flat mirror 3 is not used in the alignment procedure.

3.4 Conclusions

An event selection has been developed that selects events to more evenly populate the mirror planes in the LHCb RICH detectors. It is used to reduce the number of events required for the mirror alignment by a factor of ~ 50, significantly speeding up the procedure and saving valuable computing resources (RICH reconstruction for a typical event lasts ~ 1 s).

Using the alignment procedure on data collected in 2011, the Cherenkov angle resolution for the gaseous radiator in RICH1 improves from 13.96 mrad to 1.60 mrad, while in RICH2, the Cherenkov angle resolution is improved from 0.73 mrad to 0.63 mrad [40]. The resolutions measured with collision data are now very close to their Monte Carlo predictions of 1.5 mrad for RICH1 and 0.6 mrad for RICH2 (in fact, the RICH2 resolution is slightly better than the Monte Carlo prediction). This has resulted in excellent PID performance [43].

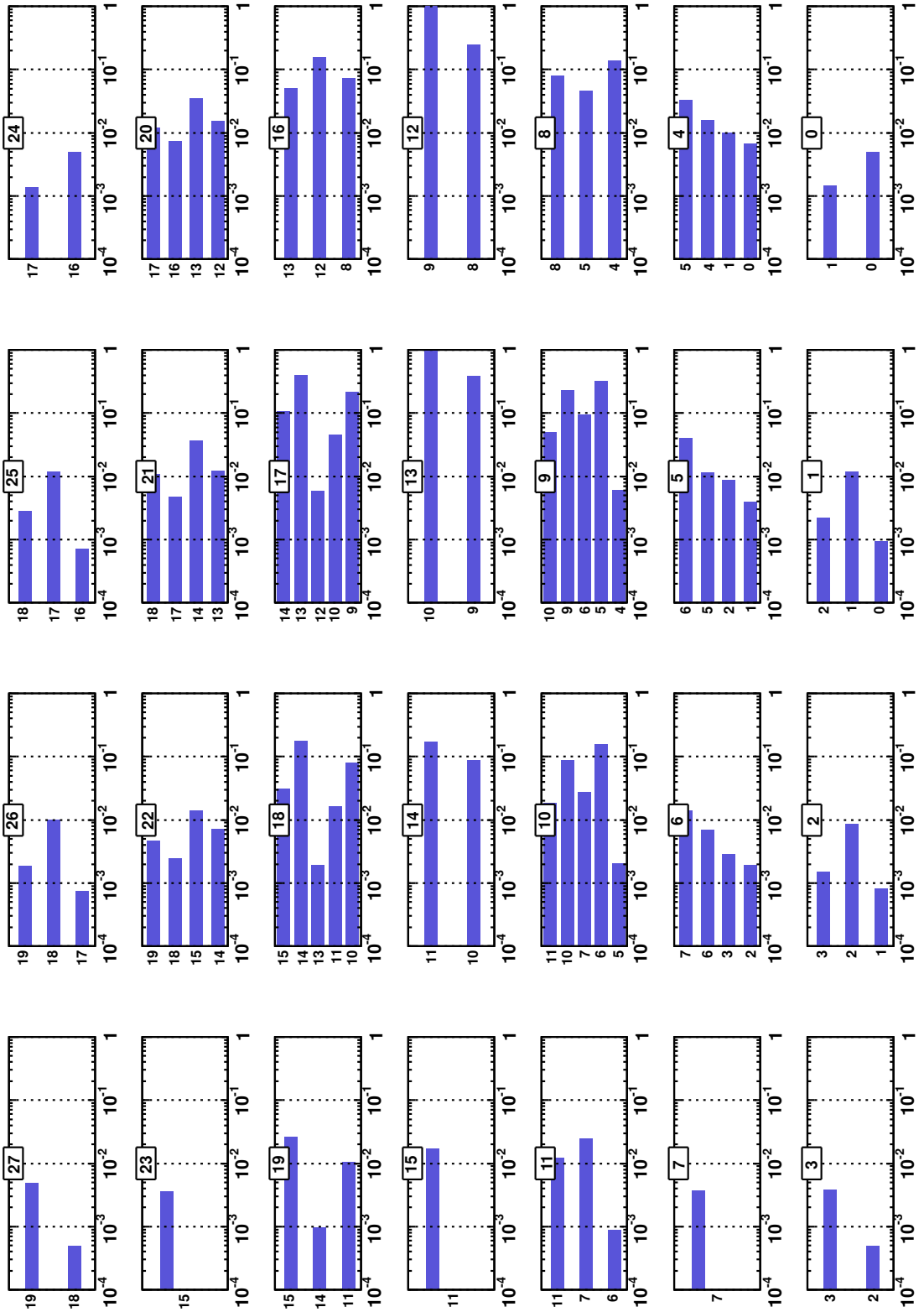

Figure 3.6: Population of mirror pairs in the left-hand side of RICH2, normalised to the largest population. The title of each of the plots represents a spherical mirror segment, and the $y-$axis labels show the flat mirror segments with which they are paired. Spherical mirror 12 has the highest photon population because it is closest to the beam pipe.

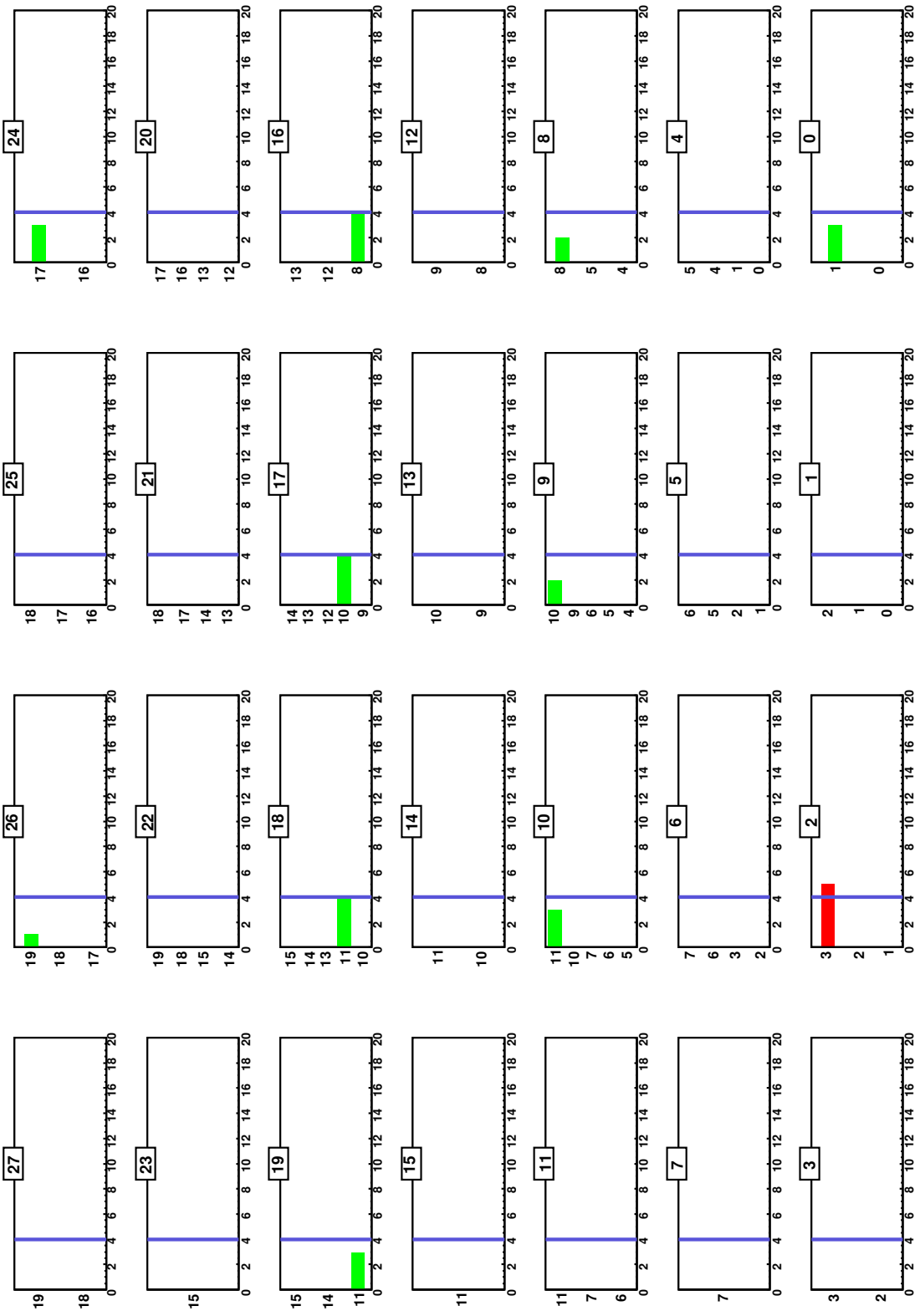

Figure 3.7: Number of incompletely filled ϕ bins per histogram for the left-hand side of RICH2. Green bars (or no bars) show mirror pairs with an acceptable number of incompletely filled ϕ slices. Not all of the mirror pairs shown here are used in the alignment procedure, including the pair containing spherical mirror 2 and flat mirror 3.

Chapter 4

Prompt charm production in pp collisions at $\sqrt{s} = 7\,\text{TeV}$

4.1 Introduction

This chapter describes the measurement of prompt D^0 production[1] using $15.0 \pm 0.5\,\text{nb}^{-1}$ of low pileup pp collision data taken in 2010[2] with the LHCb detector at a centre of mass energy of 7 TeV. The analysis is performed using the Cabibbo-favoured decay mode $D^0 \to K^-\pi^+\pi^-\pi^+$ mainly as a systematic cross-check to the more abundant $D^0 \to K^-\pi^+$ mode. Agreement between the two sets of results provides a powerful validation of the analysis techniques used and demonstrates a good understanding of the various efficiencies involved in the cross-section calculations.

Production of D^0 mesons can occur either promptly or from the decays of b-hadrons (referred to as "secondary" charm). "Prompt" D^0 mesons may be produced either directly in the pp collision or by the immediate decay of excited charm resonances. The measurement of prompt D^0 production is a means to test QCD predictions and can be used to provide estimates of expected event yields for various future analyses.

[1] Throughout this chapter, unless otherwise stated, the charge conjugate modes are implied.
[2] The reason for the choice of dataset is explained in Section 4.6.2.

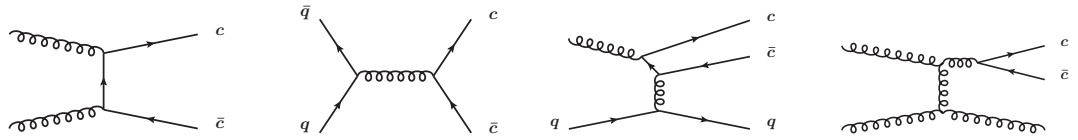

(a) (b) (c) (d)

Figure 4.1: Feynman diagrams illustrating the main charm production mechanisms at the LHC: (a) gluon-gluon fusion, (b) $q\bar{q}$ annihilation, (c) flavour excitation, and (d) gluon splitting.

4.2 Charm production mechanisms

Three mechanisms contribute to charm production at the LHC:

- **Flavour creation:** This is a hard QCD scattering process which refers to two lowest-order production diagrams; gluon-gluon fusion (Figure 4.1(a)), and $q\bar{q}$ annihilation (Figure 4.1(b)).
- **Flavour excitation:** This is a semi-hard process that corresponds to diagrams in which a $c\bar{c}$ pair is excited into the final state from the sea of quarks in the proton. This happens when one of the partons from the other colliding proton undergoes a hard QCD interaction with one of the c quarks (Figure 4.1(c)).
- **Gluon splitting:** A soft QCD process where the $c\bar{c}$ pair is produced from the splitting of a gluon ($g \rightarrow c\bar{c}$) in either the initial or final state. Here, neither of the charm quarks participate in a hard scattering (Figure 4.1(d)).

Measuring the production of charm over a large p_{T} range is important for testing QCD predictions because it helps with disentangling the contributions from each of the different production mechanisms. Heavy flavour production has been measured by other proton and electron colliders, where significant discrepancies were found between the data and Next-to-Leading-Order (NLO) QCD predictions (for an example, see the Tevatron Run I results [44]). Therefore, measurements of heavy flavour production at 7 TeV provide an extremely useful tool for testing theoretical predictions. At the end of this chapter, we compare our results with two different NLO QCD models, and reasonable agreement is found, although there is not enough discriminating power to distinguish between the two.

4.3 Analysis strategy

The production cross-section of D^0 mesons is measured in two-dimensional bins of rapidity, $y = \frac{1}{2}\ln\left(\frac{E+p_z}{E-p_z}\right)$, and transverse momentum, $p_\text{T} = \sqrt{p_x^2 + p_y^2}$, where the D^0 momentum four-vector, (E, p_x, p_y, p_z), is measured in the pp collision centre of mass frame. The measurement is performed (where possible) in eight uniformly spaced transverse momentum bins between $0 < p_\text{T} < 8\,\text{GeV}$ and five uniformly spaced rapidity bins between $2.0 < y < 4.5$, taking advantage of LHCb's unique acceptance.

In each bin, i, the cross-section is measured using

$$\sigma_i\left(D^0\right) = \frac{N_i\left(D^0 \to K^-\pi^+\pi^-\pi^+\right)}{\varepsilon_{i,\text{tot}} \cdot \mathcal{B}\left(D^0 \to K^-\pi^+\pi^-\pi^+\right) \cdot \mathcal{L}_\text{int}}, \tag{4.1}$$

where $N_i\left(D^0 \to K^-\pi^+\pi^-\pi^+\right)$ is the yield of prompt charm decays, $\mathcal{B}\left(D^0 \to K^-\pi^+\pi^-\pi^+\right)$ is the branching fraction of the Cabibbo-favoured decay mode $D^0 \to K^-\pi^+\pi^-\pi^+$, $\mathcal{L}_\text{int}$ is the integrated luminosity used for the measurement, and $\varepsilon_{i,\text{tot}}$ is a product of the components, given by

$$\varepsilon_{i,\text{tot}} = \varepsilon_{i,\text{acc}} \cdot \varepsilon_{i,\text{trig|acc}} \cdot \varepsilon_{i,\text{sel|trig}} \cdot \varepsilon_{i,\text{PID|sel}}\,. \tag{4.2}$$

Here

- $\varepsilon_{i,\text{acc}}$ is the efficiency for all four final state tracks to be within the fiducial acceptance of the LHCb detector
- $\varepsilon_{i,\text{trig|acc}}$ is the efficiency for the trigger to fire on the event given that the final state tracks are within the fiducial acceptance
- $\varepsilon_{i,\text{sel|trig}}$ is the efficiency for the event to pass all selection and reconstruction criteria given that the event is triggered on
- $\varepsilon_{i,\text{PID|sel}}$ is the efficiency for all four final state tracks to pass particle identification (PID) requirements given that the D^0 candidate is reconstructed and that the event passes all selection criteria.

The trigger efficiency is taken as uniform across all analysis bins (i.e. there is no y or p_{T} dependence - see Section 4.6.2) which makes it convenient to rewrite Equation 4.1 as

$$\sigma_i\left(D^0\right) = \frac{N_i\left(D^0 \to K^-\pi^+\pi^-\pi^+\right)}{\varepsilon_{i,\text{acc}} \cdot \varepsilon_{i,\text{sel|trig}} \cdot \varepsilon_{i,\text{PID|sel}} \cdot \mathcal{B}\left(D^0 \to K^-\pi^+\pi^-\pi^+\right) \cdot \mathcal{L}_{\text{eff}}}, \tag{4.3}$$

where $\mathcal{L}_{\text{eff}} \equiv \mathcal{L}_{\text{int}}\varepsilon_{\text{trig}}$ is an effective integrated luminosity, discussed in Section 4.6.2.

4.4 Event selection using a genetic algorithm

Reconstructing hadronic decays of D^0 mesons is a big challenge in a hadronic environment, particularly when there are four tracks in the final state. Without a tight set of selection criteria the combinatorial background alone is overwhelming and completely buries any signal peak that may be present (see Figure 4.8(a)). However, choosing selection criteria that are too strict will result in a very low signal yield.

The task of finding optimal selection criteria is complicated by the fact that many of the kinematic variables used in the selection have non-trivial correlations. Cutting on one variable distribution will affect the shape of others. Therefore it is important to consider the point at which the variable distributions are cut simultaneously, not individually. For the sake of significantly simplifying the efficiency calculations (including systematics and correction factors), no multivariate technique is used. Instead we use a genetic algorithm to optimise a set of one-dimensional selection cuts.

4.4.1 Selection variables

The variables used in the analysis are described in the following paragraphs.

Daughter track p_{T}. Because the D^0 mass is much larger than that of its decay products, at least one daughter kaon or pion is expected to have a large transverse momentum (here measured in the lab frame, perpendicular to the beam axis). By ordering the four daughter p_{T} and cutting on each in turn, much greater discriminating

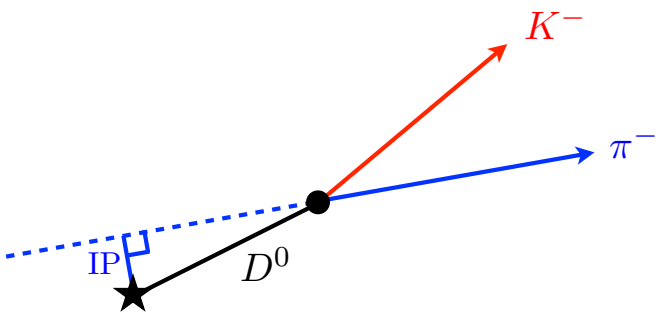

Figure 4.2: A schematic representation of a $D^0 \to K^-\pi^+$ decay, where the D^0 originates from the primary vertex (represented by the star). The impact parameter of a pion track with respect to the primary vertex is the perpendicular distance between the primary vertex and the extrapolated track.

power is achieved compared with simply asserting that all daughters must have p_{T} greater than some value (which is equivalent to cutting on only the lowest daughter p_{T}). For example, a tighter cut can be applied to the track with the largest p_{T} value than the others with a smaller effect on the signal efficiency. Simulated distributions of the three largest daughter p_{T} variables are shown in Figure 4.3.

Track fit χ^2/N_{dof}. All final state tracks are required to be reconstructed with an upper limit on the track fit χ^2 per degree of freedom.

Track clone distance. Occasionally, the tracking pattern recognition will reconstruct multiple tracks using detector hits from just one particle. These "clone" tracks can result in multiple reconstructed $D^0 \to K^-\pi^+\pi^-\pi^+$ decay candidates per event. The Kullback-Liebler distance [45] (or clone distance) is essentially a measure of the difference in information content between two tracks and is used to identify and remove clone tracks. All tracks with a Kullback-Liebler distance > 5000 with respect to every other track (*i.e.* not clone-like) are accepted. Additionally, tracks which are the best of a group of all possible clones (based on the number of hits and the track fit χ^2/N_{dof}) are accepted.

Daughter track *IP* χ^2 with respect to the primary vertex (PV). Sometimes referred to as the "impact parameter significance", this variable is defined as the magnitude of the impact parameter divided by its uncertainty. The impact parameter of a particle with respect to the PV is defined as the distance between the PV and the

trajectory of the particle at its point of closest approach to the PV (see Figure 4.2). One characteristic of D^0 mesons are their long lifetimes which result in significant distances of flight from the PV. Consequently, the daughter tracks should not point back to the PV and will have *IP* χ^2s with respect to the PV that differ significantly from zero. As with the daughter p_{T} variables, the four daughters' *IP* χ^2s are ordered in each event and used as separate variables in the selection (see Figure 4.4).

Track type. All tracks used in the analysis are "long" tracks (see Section 2.2.6).

Particle identification (PID). PID is provided at LHCb by combining track information from the two RICH detectors, the calorimeters, and the muon system. This information is used to form a global likelihood hypothesis for each particle type (e, μ, π, K, p). Here we exploit the difference between the logarithm of the kaon and pion likelihoods ($\log\mathcal{L}_K - \log\mathcal{L}_\pi$) to distinguish between the two particle types. This variable is used to suppress background from combinations of pions which are produced copiously in the primary interaction, as well as significantly reducing any background from misidentifying a pion as a kaon or vice-versa. Backgrounds with muons misidentified as pions are ignored. This is because either they contain a neutrino in the final state (specifically, the decay $D^0 \to K^-\pi^+\pi^-\mu^+\nu_\mu$) and peak far from the mass of the D^0 when reconstructed as $D^0 \to K^-\pi^+\pi^-\pi^+$ decays, or the decays are flavour-changing neutral current processes that are highly supressed in the SM ($D^0 \to K^-\pi^+\mu^-\mu^+$ for example).

D^0 vertex χ^2/N_{dof}. Used as a measure of the vertex quality, this variable is extremely powerful for suppressing combinatorial background. Low values are consistent with all four daughter tracks emerging from a common decay vertex.

Daughter track maximum distance of closest approach (*DoCA*). Defined as the largest distance of closest approach between any of the two daughter track combinations. Like the D^0 vertex χ^2/N_{dof}, the *DoCA* is very effective at removing combinatorial background.

Flight distance (FD) χ^2 with respect to the PV. This variable is defined as the flight distance divided by its uncertainty. Because of the relatively long D^0 lifetime, requiring a signifcant D^0 vertex separation from the PV is useful to remove any background originating from the PV. An upper limit of $\ln\left(FD\chi^2\right) < 10$ is also applied to remove reconstructed candidates with unphysical high lifetimes.

D^0 lifetime τ. All decay candidates are require to have a positive lifetime.

Cosine of the direction angle ($DIRA$). The cosine of the angle between the reconstructed D^0 momentum vector and the vector of displacement from the PV to the decay vertex. For a promptly produced D^0 the value will be very close to one.

D^0 $\log_{10}(IP\chi^2)$. The D^0 $\log_{10}(IP\chi^2)$ is a useful parameter for distinguishing between prompt D^0 decays and those from decays of b hadrons. Any D^0 which was produced promptly will have a low $\log_{10}(IP\chi^2)$. The variable is used (along with the invariant mass) to extract the yield of prompt charm decays (see Section 4.5).

4.4.2 Event selection optimisation

After a very loose selection (see the "Stripping" column in Table 4.2), variables (and ranges) are carefully chosen to have minimal impact on both the fraction of secondary charm and the distribution of the D^0 p_T (Table 4.1 shows the full list of chosen variables). A genetic algorithm is then used to optimise an event selection using these variables within the given ranges. Because the cross-section is measured all the way down to the bins between $0 < p_\text{T} < 1\,\text{GeV}$, it is important that none of the selection cuts remove the events with small D^0 p_T values. Additionally, the use of any variables significantly correlated with the D^0 $\log_{10}(IP\chi^2)$ is avoided where possible because this variable is used later to discriminate between prompt and secondary decays. In some cases (for example the cut of $FD\chi^2 > 16$) only very loose cuts are applied in the stripping selection to minimise biasing effects. Simulated distributions of the ten variables chosen for the optimisation are shown in Figures 4.3, 4.4 and 4.5 where one can see clear differences

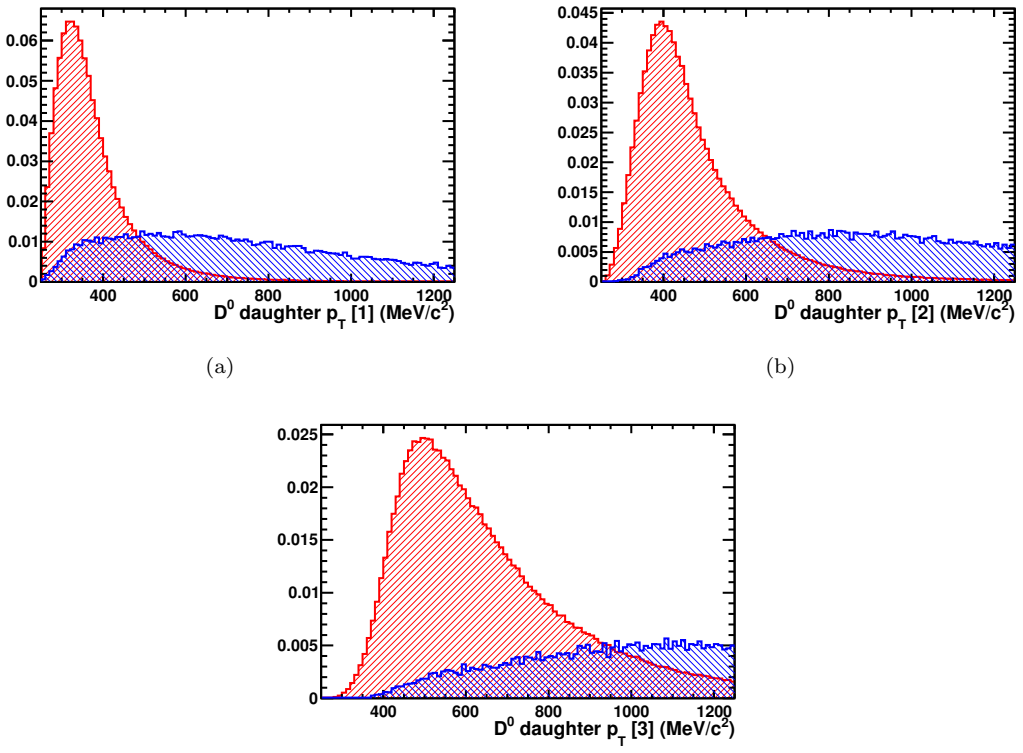

(a) (b)

(c)

Figure 4.3: Normalised distributions of (a) the second smallest, (b) second largest, and (c) largest D^0 daughter p_{T} for signal (blue) and inclusive $c\bar{c}$ reconstructed Monte Carlo decay candidates. Note that the normalisation takes into account any entries outside of the histogram range.

between signal and background shapes. Here we use a sample of Monte Carlo simulated signal events to model the signal distributions and a sample of inclusive $c\bar{c}$[3] Monte Carlo events to model the background.

The optimisation ranges of the three ordered D^0 daughter p_{T} variables are chosen so that any resulting cuts will have only a small impact on the p_{T} distribution of the D^0. For the upper ranges, two-dimensional Monte Carlo signal distributions of D^0 p_{T} vs. the D^0 daughter p_{T} variables are examined and values are chosen so that the majority of low D^0 p_{T} events remain, even if the upper limits were used in the selection (see Figure 4.6).

Similarly, the optimisation ranges of the four ordered D^0 daughter $IP\chi^2$s and the D^0 *DIRA* are chosen to have a minimal impact on the D^0 $\log_{10}(IP\chi^2)$. Two dimensional distributions of D^0 $\log_{10}(IP\chi^2)$ vs. D^0 *DIRA* are shown for prompt and secondary

[3] A sample of Monte Carlo data that contains at least one charmed hadron pair per event.

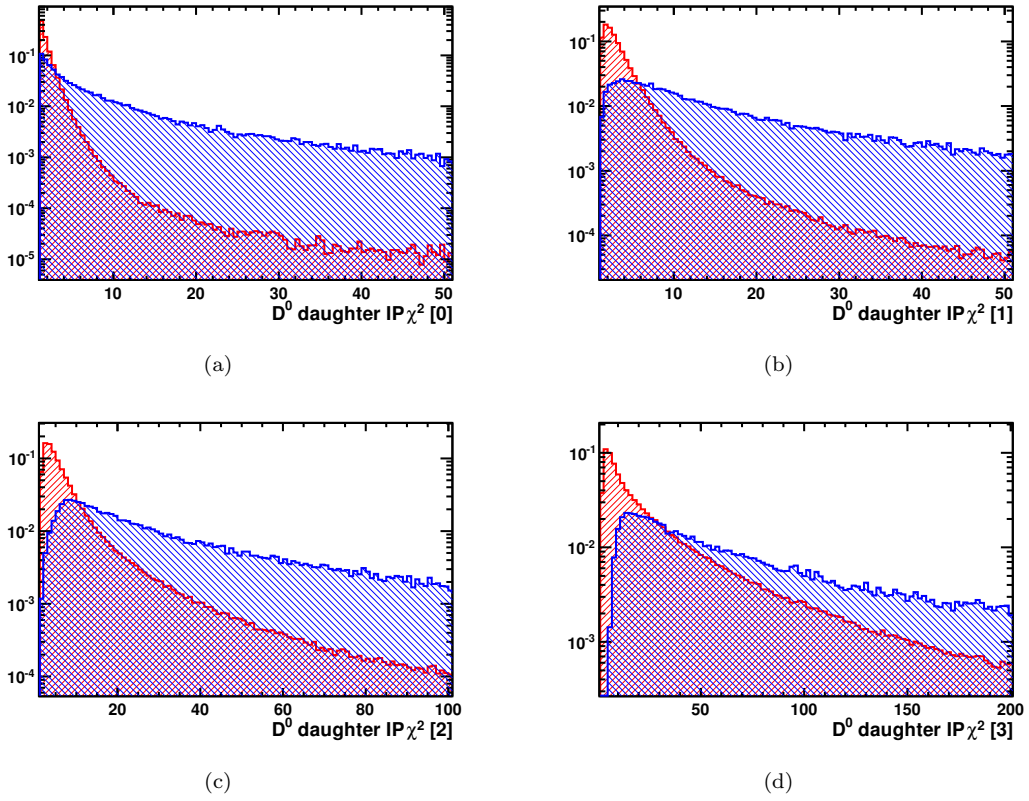

(a) (b) (c) (d)

Figure 4.4: Normalised distributions of (a) the smallest, (b) second smallest, (c) second largest, and (d) largest D^0 daughter $IP\chi^2$ for signal (blue) and inclusive $c\bar{c}$ reconstructed Monte Carlo decay candidates. Note that the normalisation takes into account any entries outside of the histogram range.

decays in Figure 4.7. Here, the upper limit is chosen so that the majority of both prompt and secondary events remain, in order to help with the yield extraction. The same procedure is applied to the D^0 daughter $IP\chi^2$s.

Table 4.1: Variables used in the genetic algorithm optimisation, shown with the lower and upper allowed limits, as well as the resolution used by the algorithm.

	Variable name	Lower limit	Upper Limit	Resolution
D^0	vertex χ^2/N_{dof}	0.0	20.0	1.0
	$DoCA$	0.20	0.50	0.01
	$DIRA$	0.99950	0.99980	0.00001
$h^\pm$	smallest IP χ^2	1.0	9.0	0.5
	3$^{\text{rd}}$ largest IP χ^2	1.0	16.0	0.5
	2$^{\text{nd}}$ largest IP χ^2	1.0	36.0	1.0
	largest IP χ^2	2.0	80.0	2.0
	3$^{\text{rd}}$ largest p_{T}	250.0 GeV/c	300.0 GeV/c	10.0 GeV/c
	2$^{\text{nd}}$ largest p_{T}	250.0 GeV/c	350.0 GeV/c	10.0 GeV/c
	largest p_{T}	250.0 GeV/c	400.0 GeV/c	10.0 GeV/c

To train the selection a sample of Monte Carlo signal events is used, along with a sample

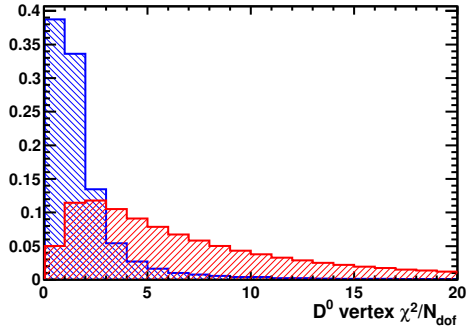

(a)

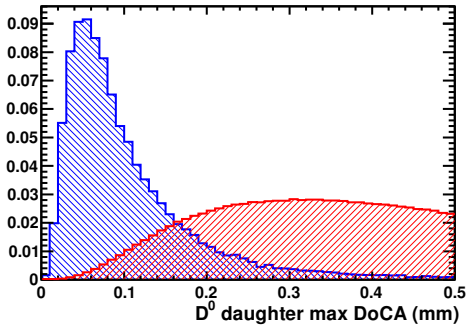

(b)

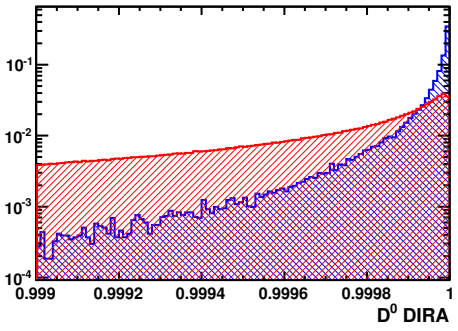

(c)

Figure 4.5: Normalised distributions of (a) the D^0 vertex χ^2/N_{dof}, (b) the D^0 daughter maximum *DoCA*, and (c) the D^0 *DIRA* for signal (blue) and inclusive $c\bar{c}$ reconstructed Monte Carlo decay candidates. Note that the normalisation takes into account any entries outside of the histogram range.

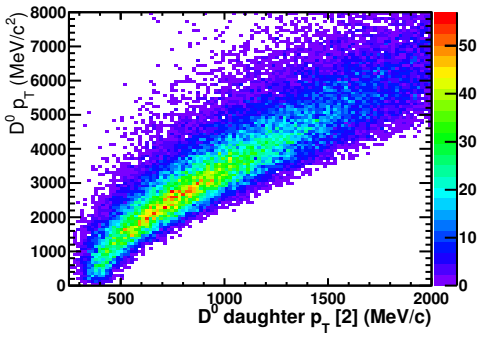

(a)

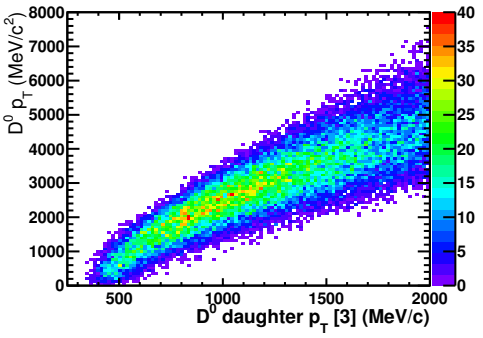

(b)

Figure 4.6: Monte Carlo signal distributions of D^0 p_{T} vs. (a) second largest and (b) largest D^0 daughter track *pt*. To avoid loss of low D^0 p_{T} events, upper limits of 350 MeV/c and 400 MeV/c are chosen for the optimisation.

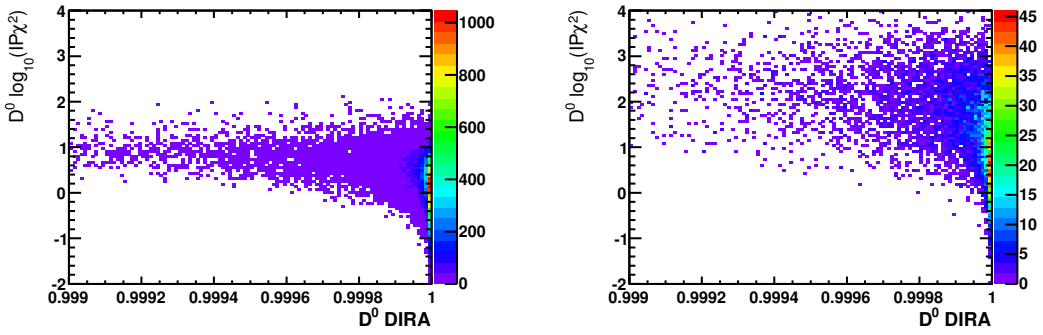

(a) (b)

Figure 4.7: Monte Carlo distributions of D^0 $\log_{10}(IP\chi^2)$ vs. D^0 *DIRA* for (a) prompt and (b) secondary D^0 decays. An upper limit of 0.99980 is chosen for the optimisation so that the majority of both prompt and secondary decays remain.

of inclusive $c\bar{c}$ (the same samples used to produce Figures 4.3, 4.4 and 4.5). Both are passed through the same reconstruction software as the real data. The genetic algorithm used to optimise the selection cuts is described in the following text.

Initialisation

To begin, each member of a starting population of twenty cut sets is assigned a random value for each of the ten cut variables. The random values are chosen to be within the predefined variable ranges. Each variable can be thought of as a "gene". The resolution of the variables can be seen in Figures 4.3, 4.4 and 4.5), although the ranges are somewhat smaller than depicted. Table 4.1 shows the ranges and resolutions used for each variable.

Reproduction

The population is then split into ten random pairs, each of which is made to "reproduce" twice so that the population doubles in size. Each of the genes in an "offspring" cut set has an equal probability of inheritance from either parent.

Mutation

To avoid stagnation all offspring genes then have a 10% probability of "mutating" to a new random value. This prevents the algorithm from becoming stuck in a local minimum.

Natural selection

Each member of the population represents a set of selection criteria. The criteria are tested using Monte Carlo simulated signal and background data, using the signal significance $\left(\frac{\text{signal}}{\sqrt{\text{signal+background}}}\right)$ as the figure of merit. The entire population (offspring and parents) is then ordered by the signal significance and the half that perform the worst are terminated.

Convergence

The whole process (from reproduction to natural selection) is repeated for as many generations as required (the number depends on how many cut variables are used, as well as the resolution of each of them). In this case the number of required generations was found to be around 100 by closely observing the output and looking for any further improvements. To ensure convergence the algorithm is left to run for 1000.

4.4.3 Final selection criteria

The final list of selection criteria can be found in Table 4.2, where the optimised variable cuts are shown (along with the clone distance cut and high cut on the D^0 *FD* χ^2) in the "Offline" column.

4.5 Yield extraction

The yield of prompt D^0 mesons is extracted in each of the (y, p_{T}) bins by performing an unbinned maximum likelihood fit to the two dimensional mass - $\log_{10}(IP\chi^2)$ plane. We use the $\log_{10}(IP\chi^2)$ variable to discriminate between the prompt signal and secondary

Table 4.2: Selection criteria used to isolate $D^0 \to K^-\pi^+\pi^-\pi^+$ signal candidates. The symbol $h^\pm$ is used to represent either a pion or kaon daughter track. The "Stripping" column lists a set of very loose criteria applied prior to the analysis, and the "Offline" column lists the cuts which are optimised using a genetic algorithm, along with the clone distance and $\ln\left(FD\chi^2\right)$ criteria. If four values are present, the first is a requirement for all of the daughter tracks, the second is required of at least three of the daughter tracks, the third of at least two of the daughter tracks, and the final requirement is only necessary for one of the daughter tracks.

	Variable name	Stripping	Offline
$h^\pm$	Track χ^2/N_{dof}	< 5	—
	Track type	Long	—
	Clone distance	—	> 5000 or "best clone"
	IP χ^2	> 1	$> 1.5, 6, 9, 16$
	p_{T}	$> 250\,\text{MeV}/c$	$>$ —, 300, 350, 400 MeV/c
	$\lvert\vec{p}\rvert$	$> 3\,\text{GeV}/c$	—
K^-	$\log\left(\mathcal{L}_K/\mathcal{L}_\pi\right)$	> 0	—
$\pi^\pm$	$\log\left(\mathcal{L}_K/\mathcal{L}_\pi\right)$	< 5	—
D^0	Vertex χ^2/N_{dof}	< 20	< 3
h_ih_j pair	*DoCA*	< 0.5 mm	< 0.21 mm
	FD χ^2	> 16	—
	Signed *FD*	$> 0\,\text{mm}$	—
	τ	$> 0\,\text{ps}$	—
	$\ln\left(FD\chi^2\right)$	—	< 10
	DIRA	—	> 0.99979
	Mass window	$\lvert m - m_{\text{PDG}}\rvert < 75\,\text{MeV}/c^2$	—

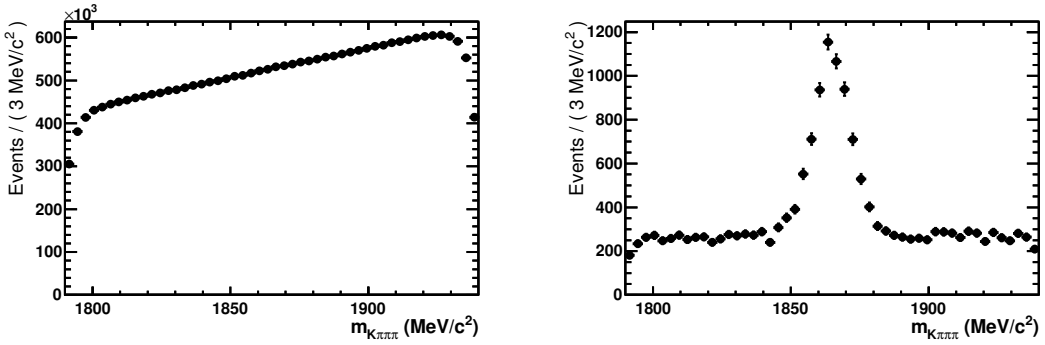

(a) (b)

Figure 4.8: Invariant mass distribution of reconstructed $D^0 \to K^-\pi^+\pi^-\pi^+$ candidates after (a) the stripping selection and (b) the full selection.

background. The PDF used for the fit is a sum of three two-dimensional components: prompt signal, secondary background, and combinatorial background. In the mass projection, the prompt signal and secondary background are described by a common Crystal

Ball[4] [46] function, and the combinatorial background is modelled by a first order polynomial. The Crystal Ball function is useful for fitting the signal invariant mass shape because it accounts for the radiative tail. In the $\log_{10}(IP\chi^2)$ projection, each of the three components is described by an asymmetric Gaussian with exponential tails. This function is defined as

$$P(x) \propto \begin{cases} \exp\left(\frac{\rho_L^2}{2} + \frac{x-\mu}{\sigma(1-\varepsilon)}\rho_L\right) & \text{if } \frac{x-\mu}{\sigma(1-\varepsilon)} < -\rho_L \\ \exp\left(\frac{\rho_R^2}{2} - \frac{x-\mu}{\sigma(1+\varepsilon)}\rho_R\right) & \text{if } \frac{x-\mu}{\sigma(1+\varepsilon)} > \rho_R \\ \exp\left(-\frac{(x-\mu)^2}{2\sigma^2(1-\varepsilon)^2}\right) & \text{if } -\rho_L < \frac{x-\mu}{\sigma(1-\varepsilon)} < 0 \\ \exp\left(-\frac{(x-\mu)^2}{2\sigma^2(1+\varepsilon)^2}\right) & \text{if } 0 < \frac{x-\mu}{\sigma(1+\varepsilon)} < \rho_R \end{cases} \tag{4.4}$$

where μ is the mean of the distribution, σ is the width, ε is an asymmetry parameter, and ρ_L and ρ_R are the number of σ from the left or right of the mean where the exponential behaviour begins. When $-\rho_L < x < \rho_R$ the form is reduced to an asymmetric Gaussian. For the secondary and combinatorial background $\log_{10}(IP\chi^2)$ fits, the PDF is reduced to its symmetric form (*i.e.* the conditions $\varepsilon = 0$ and $\rho_L = \rho_R = \rho$ are imposed). The function is chosen because it describes the Monte Carlo signal, and data background (from the D^0 mass sidebands) very well. Examples can be seen in Figure 4.10.

Many of the (p_T, y) bins contain only a small number of events (~ 100). Therefore, in order to improve fit stability, some fit parameters are shared between neighbouring bins, which are grouped into big bins with the boundaries shown in Figure 4.9. The individual (p_T, y) bins within a big bin are fit simultaneously, sharing parameters that are expected to vary slowly with p_T and y (ε, ρ_L and ρ_R for the prompt component of the $\log_{10}(IP\chi^2)$ distribution, ρ for both the secondary and background components of the $\log_{10}(IP\chi^2)$ distribution, the Crystal Ball tail parameters for the invariant mass distribution, and the fraction of secondary charm events $\left(\frac{\text{secondary}}{\text{prompt+secondary}}\right)$, while leaving all others free to float in each of the small bins.

[4]Named after the Crystal Ball Collaboration, this function consists of a Gaussian with a power-law tail.

In order to set initial values for the fit parameters used in the two-dimensional fit, initially a series of one-dimensional fits are performed. First, the $\log_{10}(IP\chi^2)$ distributions of both prompt and secondary Monte Carlo signal decays are fit individually (see Figure 4.10(a)). Then the $\log_{10}(IP\chi^2)$ distribution of data taken from the D^0 mass sidebands ($m_{K\pi\pi\pi} > 1895\,\text{MeV}/c^2$ or $m_{K\pi\pi\pi} < 1835\,\text{MeV}/c^2$) is fit (see Figure 4.10(b)). Finally, the one-dimensional invariant mass distribution is fit. Once all of the parameters have been seeded, some are fixed (ε, σ, ρ_L and ρ_R for the prompt $\log_{10}(IP\chi^2)$ distribution, and σ, ρ and μ for the secondary $\log_{10}(IP\chi^2)$ distribution) to improve the fit stability. Finally the two-dimensional fits to the mass - $\log_{10}(IP\chi^2)$ plane are performed to extract the prompt charm yields (see Table 4.3 for the yields in each bin). Projections of the two-dimensional fit are shown for a fit to the full (p_{T}, y) range in Figure 4.11. Fits for all of the analysis bins are shown in Appendix A, and the χ^2 per degree of freedom of the mass and $\log_{10}(IP\chi^2)$ projections for each bin are shown in Tables 4.4 and 4.5.

To test the fitter a toy study is performed using Monte Carlo with a range of secondary fractions: 10%, 6%, 3% and 0%. No bias is found in any of the fit parameters, and the measured secondary fractions agree well with their simulated values [47].

A systematic uncertainty that accounts for both the two-dimensional fit method, and the choice of signal and background PDFs is detailed in Section 4.7.1.

Table 4.3: Prompt yields of $D^0 \to K\pi\pi\pi$ signal events in the data, shown with statistical uncertainties.

p_t	y				
(GeV/c)	(2.0, 2.5)	(2.5, 3.0)	(3.0, 3.5)	(3.5, 4.0)	(4.0, 4.5)
(0, 1)	—	—	47.8 ± 12.6	39.2 ± 13.6	—
(1, 2)	—	61.4 ± 17.3	157.8 ± 24.8	136.6 ± 23.1	—
(2, 3)	21.1 ± 4.7	190.6 ± 18.8	400.6 ± 30.7	242.0 ± 26.6	77.5 ± 15.4
(3, 4)	35.2 ± 6.1	323.3 ± 22.7	446.8 ± 27.2	295.5 ± 23.7	30.8 ± 7.2
(4, 5)	59.8 ± 7.9	276.6 ± 18.3	310.4 ± 20.5	201.5 ± 16.6	31.7 ± 6.7
(5, 6)	44.3 ± 7.4	210.8 ± 15.5	201.7 ± 16.2	100.2 ± 11.5	16.1 ± 4.6
(6, 7)	37.6 ± 6.3	115.6 ± 11.3	104.8 ± 10.9	59.5 ± 8.8	12.8 ± 3.5
(7, 8)	35.4 ± 5.9	79.1 ± 9.4	71.5 ± 8.7	33.1 ± 6.1	2.7 ± 1.6

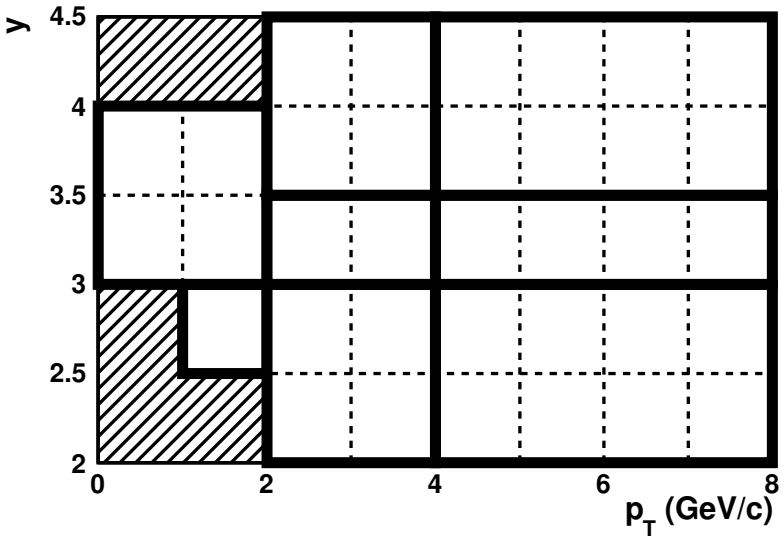

Figure 4.9: Grouping of bins for the simultaneous fits. Boundaries between the big bins are shown by thick solid lines, while the boundaries between the individual bins are shown with dashed lines. The hashing shows bins which are not used in the analysis.

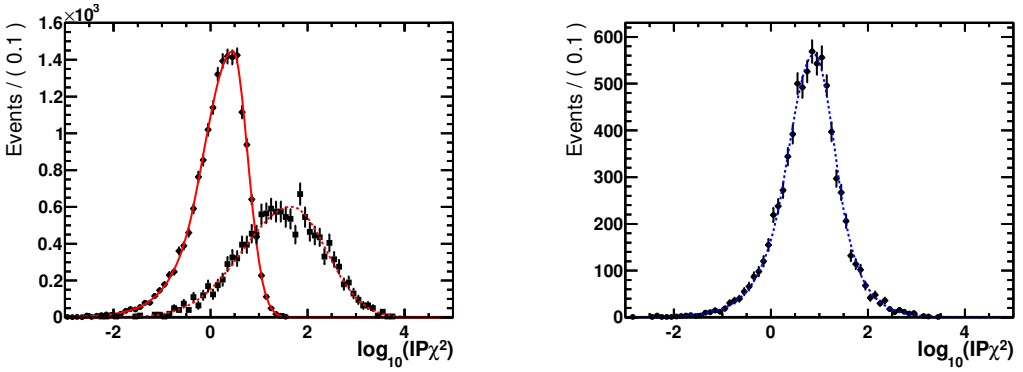

(a) (b)

Figure 4.10: Fits to the $\log_{10}(IP\chi^2)$ distributions for (a) Monte Carlo and (b) data sidebands to extract parameters to be used in the two-dimensional mass - $\log_{10}(IP\chi^2)$ fit. In (a) the solid line represents a fit to the prompt signal (shown with circular points) and the dashed line shows a fit to the secondary background (shown with square points). The secondary Monte Carlo data and fit line are both scaled by a factor of five.

4.6 Efficiency corrections

To provide a more realistic representation of the four-body phase space, all MC signal events are re-weighted so that the daughter four-momenta more closely match the distributions predicted by the Mark III amplitude model [48].

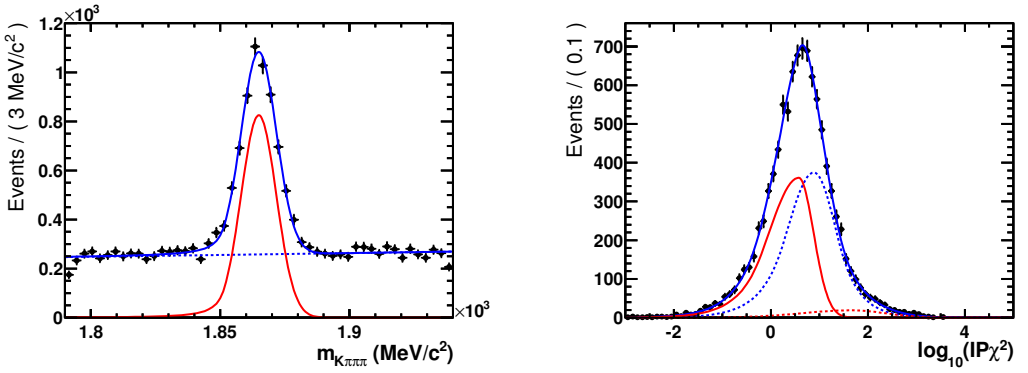

(a) (b)

Figure 4.11: (a) Mass and (b) $\log_{10}(IP\chi^2)$ projections of the two-dimensional fit to the data for the full (p_{T}, y) range. The solid red line in (a) represents the contribution from D^0 signal decays (either prompt or secondary), combinatorial background is shown in dashed blue in both (a) and (b), and the prompt and secondary D^0 $\log_{10}(IP\chi^2)$ contributions are shown in (b) by red solid and dashed lines respectively.

Table 4.4: Fit χ^2 per degree of freedom for the mass projection in each of the bins.

p_t	y				
(GeV/c)	(2.0, 2.5)	(2.5, 3.0)	(3.0, 3.5)	(3.5, 4.0)	(4.0, 4.5)
(0, 1)	—	—	1.46	1.87	—
(1, 2)	—	1.74	1.51	1.63	—
(2, 3)	0.33	1.11	2.04	1.11	1.45
(3, 4)	0.26	1.78	1.24	1.37	0.88
(4, 5)	0.29	0.79	1.05	0.95	0.47
(5, 6)	0.29	0.40	0.87	0.99	0.31
(6, 7)	0.23	0.32	0.41	0.59	0.10
(7, 8)	0.15	0.86	0.25	0.32	0.03

4.6.1 Fiducial acceptance

To measure the efficiencies of the detector acceptance, $\varepsilon_{i,\mathrm{acc}}$, a sample of generator-level signal Monte Carlo events is used (events which have not been passed through the detector simulation and reconstruction phases). For each (y, p_{T}) bin we sum the weights of events in which all D^0 daughters are within the fiducial volume and divide by the sum of weights for all events. The resulting efficiencies are shown in Table 4.6.

Table 4.5: Fit χ^2 per degree of freedom for the $\log_{10}(IP\chi^2)$ projection in each of the bins.

p_t	y				
(GeV/c)	(2.0, 2.5)	(2.5, 3.0)	(3.0, 3.5)	(3.5, 4.0)	(4.0, 4.5)
(0, 1)	—	—	0.66	0.45	—
(1, 2)	—	0.41	1.00	1.33	—
(2, 3)	0.16	0.57	1.36	0.82	0.79
(3, 4)	0.27	0.86	0.70	0.61	0.68
(4, 5)	0.46	0.62	1.77	0.87	0.33
(5, 6)	0.36	0.76	0.86	0.74	0.10
(6, 7)	0.18	0.73	0.37	0.49	0.09
(7, 8)	0.32	0.33	0.55	0.27	0.06

Table 4.6: The fraction of events with all daughters within fiducial acceptance. For simplicity, binomial errors are used.

p_t	y				
(GeV/c)	(2.0, 2.5)	(2.5, 3.0)	(3.0, 3.5)	(3.5, 4.0)	(4.0, 4.5)
(0, 1)	0.667 ± 0.007	0.910 ± 0.005	0.924 ± 0.005	0.746 ± 0.008	0.499 ± 0.008
(1, 2)	0.747 ± 0.006	0.952 ± 0.004	0.946 ± 0.004	0.868 ± 0.007	0.663 ± 0.009
(2, 3)	0.834 ± 0.007	0.976 ± 0.003	0.973 ± 0.004	0.945 ± 0.006	0.801 ± 0.012
(3, 4)	0.881 ± 0.009	0.997 ± 0.002	0.997 ± 0.002	0.980 ± 0.005	0.893 ± 0.014
(4, 5)	0.954 ± 0.008	1.000 ± 0.001	0.994 ± 0.004	0.985 ± 0.007	0.946 ± 0.015
(5, 6)	0.960 ± 0.010	1.000 ± 0.001	0.994 ± 0.006	0.989 ± 0.009	0.995 ± 0.006
(6, 7)	0.991 ± 0.006	1.000 ± 0.000	0.992 ± 0.007	0.988 ± 0.012	0.936 ± 0.030
(7, 8)	1.000 ± 0.000	1.000 ± 0.000	1.000 ± 0.000	1.000 ± 0.000	1.000 ± 0.000

4.6.2 Trigger efficiency and effective luminosity

The data used in this analysis were collected in May 2010 when pileup[5] was low. Two trigger configurations were used, both employing "micro-bias" triggers[6] which accept events leaving track segments in either the VELO or the tracking stations. In the first configuration, all events that pass the micro-bias triggers are accepted. An integrated luminosity of $(1.87 \pm 0.07)\ \text{nb}^{-1}$ was collected with an efficiency of $\varepsilon_{\text{trig}} = 100\%$ for events within the detector acceptance. In the second configuration, rate limits and prescales were applied to the mico-bias triggers in order to suppress the data rate. Here, $(13.09 \pm 0.46)\ \text{nb}^{-1}$ were collected but with an effective efficiency (determined using the known prescale and rate limits) of $\varepsilon_{\text{trig}} = (23.99 \pm 0.19)\,\%$. It then follows that the total effective integrated luminosity is the sum over the different trigger configurations (T):

[5]The average number of *pp* collisons per event.

[6]So-named because of their almost non-existent biasing effects, these triggers have an efficiency of 100% on the reconstructed signal decays.

$$\begin{aligned} \mathcal{L}_{\text{eff}} &= \sum_{\text{T}} \varepsilon^{\text{T}}_{\text{trig}}\, \mathcal{L}^{\text{T}}_{\text{int}} \\ &= (5.01 \pm 0.18)\ \text{nb}^{-1}. \end{aligned} \tag{4.5}$$

Because the trigger selects all signal events within the fiducial volume, no contribution to the systematic uncertainty is introduced. Increasing the sample size would require the use of data selected by non-trivial trigger configurations, which would not select 100% of the signal events, and determination of the trigger efficiency would introduce a systematic uncertainty (mainly because of the difficulty in simulating the hardware trigger). Since the total systematic uncertainty is already larger than the statistical uncertainty in almost all of the (y, p_{T}) bins, we use only data which were triggered by the micro-bias triggers.

4.6.3 Reconstruction and selection efficiency

The reconstruction and selection efficiency in each (y, p_{T}) bin, $\varepsilon_{i,\text{sel|trig}}$, is measured using a sample of Monte Carlo data which use the full event and detector simulation. In each bin the efficiency is calculated as

$$\varepsilon_{i,\text{sel|trig}} = \frac{N_{i,\text{sel}}}{N_{i,\text{gen}}} \tag{4.6}$$

where $N_{i,\text{sel}}$ is the sum of weights of events which pass all selection and reconstruction criteria (excluding PID requirements) and $N_{i,\text{gen}}$ is the sum of weights of events which are generated with all daughters within the fiducial volume. The reconstruction and selection efficiency in each (y, p_{T}) can be found in Table 4.7.

4.6.4 PID efficiency

Because the PID variable $\log(\mathcal{L}_K/\mathcal{L}_\pi)$ is not particularly well described by the Monte Carlo simulation, the efficiencies, $\varepsilon_{i,\text{PID|sel}}$, are determined using data. Calibration

Table 4.7: Efficiency of reconstruction and selection for events with all daughters inside the fiducial volume, shown as percentages.

p_t	y				
(GeV/c)	(2.0, 2.5)	(2.5, 3.0)	(3.0, 3.5)	(3.5, 4.0)	(4.0, 4.5)
(0, 1)	—	0.01 ± 0.00	0.08 ± 0.00	0.07 ± 0.00	0.02 ± 0.00
(1, 2)	—	0.12 ± 0.00	0.51 ± 0.00	0.40 ± 0.00	0.13 ± 0.00
(2, 3)	0.06 ± 0.00	0.96 ± 0.00	2.08 ± 0.01	1.93 ± 0.01	0.54 ± 0.00
(3, 4)	0.35 ± 0.00	2.89 ± 0.01	5.02 ± 0.02	4.25 ± 0.02	1.55 ± 0.01
(4, 5)	1.17 ± 0.01	5.12 ± 0.03	7.82 ± 0.05	6.95 ± 0.06	2.58 ± 0.03
(5, 6)	1.57 ± 0.01	7.22 ± 0.06	10.65 ± 0.10	9.31 ± 0.10	3.01 ± 0.04
(6, 7)	3.16 ± 0.03	9.66 ± 0.11	11.89 ± 0.15	10.52 ± 0.16	3.17 ± 0.07
(7, 8)	4.03 ± 0.06	10.68 ± 0.15	13.31 ± 0.23	11.97 ± 0.24	2.22 ± 0.06

samples of pion and kaon tracks are obtained from reconstructing $K^0_S \to \pi^+\pi^-$ and $\phi \to K^+K^-$ decays respectively. Each K^0_S is reconstructed without any PID requirement on the pion tracks. Background suppression is achieved in the case of the ϕ decay by requiring just one of the daughter kaons to have a tight PID requirement, thus halving the available sample size. For consistency, both decay channels are reconstructed from the same $14.96\,\text{nb}^{-1}$ of collision data as used in the D^0 yield extraction.

To extract the signal $\log(\mathcal{L}_K/\mathcal{L}_\pi)$ distributions, the ${}_s\mathcal{P}lot$ [49] technique is used, exploiting the different shapes of the signal and background distributions in invariant mass. It is then possible to determine the identification and misidentification rates for pions and kaons for a given PID requirement.

To determine the overall PID efficiency for the D^0 decays, one must have knowledge of both the dependance of the PID selection upon the daughter track kinematics ($|\vec{p}|$ and η), and the correlations between the kinematic variables of the daughter tracks. The former is achieved with the calibration samples of pions and kaons. The latter are determined using a signal Monte Carlo sample to model the daughter track distributions. In reality, since the samples are finite, these dependancies are measured in bins of daughter track $|\vec{p}|$ and η. So for each D^0 (y, p_T) bin, the efficiency is determined using

$$\varepsilon_{\text{PID|sel}} = \sum_{\alpha,\beta,\gamma,\delta=1}^{n} \varepsilon_1^\alpha \cdot \varepsilon_2^\beta \cdot \varepsilon_3^\gamma \cdot \varepsilon_4^\delta \cdot f_{1234}^{\alpha\beta\gamma\delta} \tag{4.7}$$

where ε_k^ω represents the PID efficiency within the kinematic bin ω for daughter track k, n is the total number of kinematics bins, and f is the fraction of events with daughters that lie within the given kinematic bins.

The following kinematic constraints are applied to both the calibration and D^0 data samples:

- $2 < |\vec{p}| < 100\,\text{GeV}/c$,
- $2 < \eta < 5$,
- $p_\text{T} < 5\,\text{GeV}$.

Additionally, a few of the daughter track $(|\vec{p}|, \eta)$ bins are vetoed because they do not contain enough events in the calibration samples to calculated an efficiency.

The resulting PID efficiencies are shown in Table 4.8.

Table 4.8: Efficiency of the PID selection for events passing reconstruction and selection criteria, shown with statistical uncertainties only. For simplicity, binomial errors are used.

p_t	y				
(GeV/c)	(2.0, 2.5)	(2.5, 3.0)	(3.0, 3.5)	(3.5, 4.0)	(4.0, 4.5)
(0, 1)	—	0.821 ± 0.002	0.787 ± 0.001	0.761 ± 0.001	0.761 ± 0.002
(1, 2)	0.859 ± 0.006	0.824 ± 0.001	0.810 ± 0.000	0.791 ± 0.000	0.771 ± 0.001
(2, 3)	0.858 ± 0.001	0.847 ± 0.000	0.842 ± 0.000	0.820 ± 0.000	0.762 ± 0.001
(3, 4)	0.873 ± 0.001	0.868 ± 0.000	0.866 ± 0.000	0.836 ± 0.000	0.752 ± 0.001
(4, 5)	0.889 ± 0.001	0.886 ± 0.000	0.883 ± 0.000	0.845 ± 0.000	0.743 ± 0.001
(5, 6)	0.902 ± 0.001	0.898 ± 0.000	0.891 ± 0.000	0.839 ± 0.001	0.727 ± 0.001
(6, 7)	0.916 ± 0.001	0.908 ± 0.001	0.890 ± 0.001	0.836 ± 0.001	0.748 ± 0.002
(7, 8)	0.921 ± 0.001	0.916 ± 0.001	0.895 ± 0.001	0.835 ± 0.001	0.732 ± 0.003

4.7 Systematic uncertainties and correction factors

4.7.1 Yield extraction

To estimate the systematic uncertainty arising from the yield extraction we perform two alternative fits for each (p_T, y) bin.

The first alternative yield extraction procedure is identical to the method detailed in Section 4.5 except that different PDFs are used to describe the data. For the mass projection we use a common Gaussian for the prompt signal and secondary background, and a first order polynomial for the combinatorial background. For the $\log_{10}(IP\chi^2)$ projection, a separate "Bukin" PDF is used for each of the components. The Bukin PDF is defined as

$$P(x) \propto \exp\left(-\ln 2\left[\frac{\ln\left(1+2\xi\sqrt{\xi^2+1}\,\frac{x-\mu}{\sigma\sqrt{2\ln 2}}\right)}{\ln\left(1+2\xi^2-2\xi\sqrt{\xi^2+1}\right)}\right]^2\right) \tag{4.8}$$

for $x_1 < x < x_2$ and

$$P(x) \propto \exp\left(\frac{\xi\sqrt{\xi^2+1}\,(x-x_i)\,\sqrt{2\ln 2}}{\sigma\left(\sqrt{\xi^2+1}-\xi\right)^2\ln\left(\sqrt{\xi^2+1}+\xi\right)} + \rho_i\left(\frac{x-x_i}{\mu-x_i}\right)^2 - \ln 2\right) \tag{4.9}$$

with $\rho_i = \rho_1$ and $x_i = x_1$ when $x < x_1$, and $\rho_i = \rho_2$, and $x_i = x_2$ when $x > x_2$. Here x_1 and x_2 are defined as

$$x_{1,2} = \mu + \sigma\sqrt{2\ln 2}\left(\frac{\xi}{\sqrt{\xi^2+1}} \mp 1\right). \tag{4.10}$$

The free parameters μ and σ are the position and width of the peak, ρ_1 and ρ_2 are left and right exponential tail parameters, and ξ parameterises the asymmetry. Examples of the Bukin PDF can be seen in Figure 4.12. Projections of the two-dimensional fit to the mass–$\log_{10}(IP\chi^2)$ plane are shown in Figure 4.13 for the full (y, p_{T}) range.

The second alternative yield extraction procedure involves the use of binned background subtraction to produce a signal distribution for the $\log_{10}(IP\chi^2)$ variable, instead of performing a two-dimensional fit. Signal and background PDFs (a Gaussian and a first order polynomial, respectively) are fitted to the invariant mass distribution. The background $\log_{10}(IP\chi^2)$ shape is taken from the invariant mass sidebands, defined as $1790 < m_{K\pi\pi\pi} < 1835\,\text{MeV}/c^2$ and $1895 < m_{K\pi\pi\pi} < 1940\,\text{MeV}/c^2$. This shape is scaled

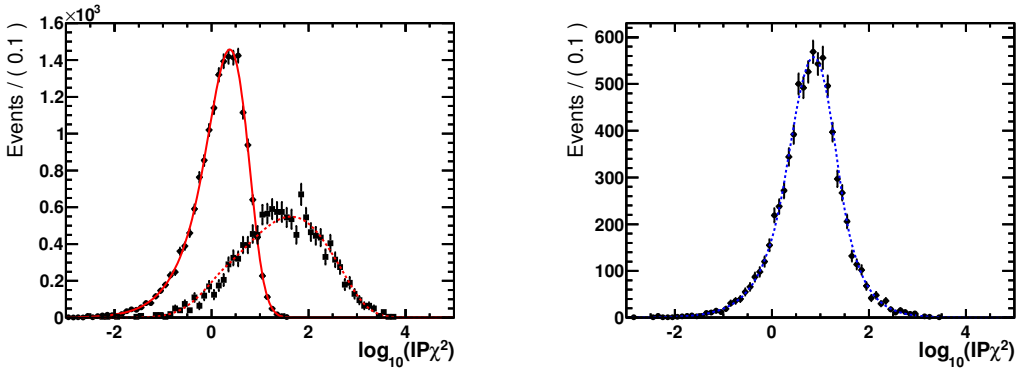

(a) (b)

Figure 4.12: Bukin PDF fits to the $\log_{10}(IP\chi^2)$ distributions for (a) Monte Carlo and (b) data sidebands to extract parameters to be used in the two-dimensional mass - $\log_{10}(IP\chi^2)$ fit. In (a) the solid line represents a fit to the prompt signal (shown with circular points) and the dashed line shows a fit to the secondary background (shown with square points). The secondary Monte Carlo data and fit line are both scaled by a factor of five.

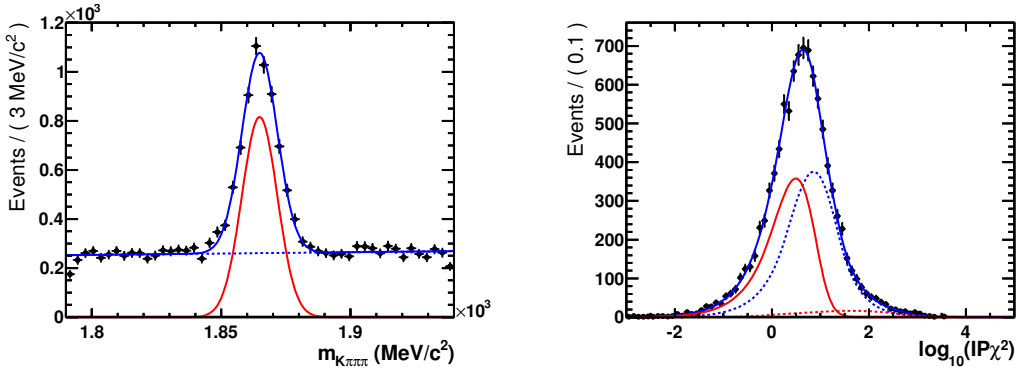

(a) (b)

Figure 4.13: (a) Mass and (b) $\log_{10}(IP\chi^2)$ projections of the two-dimensional fit to the data for the full (p_{T}, y) range, using the alternative PDFs. The solid red line in (a) represents the contribution from D^0 signal decays (either prompt or secondary), combinatorial background is shown in dashed blue in both (a) and (b), and the prompt and secondary D^0 $\log_{10}(IP\chi^2)$ contributions are shown in (b) by red solid and dashed lines respectively.

to match the background yield under the signal peak (three standard deviations either side of the measured mass peak) and is then subtracted from the $\log_{10}(IP\chi^2)$ distribution underneath the same peak, leaving an unfolded prompt and secondary $\log_{10}(IP\chi^2)$ distribution. This is fitted with Bukin PDFs (one for prompt and one for secondary) to extract a fraction of prompt charm decays.

The largest absolute yield difference between the main fit result and each of the two alternative yield extractions is used as a systematic uncertainty for the yield extraction

procedure. Table 4.9 shows the uncertainties in each of the (p_{T}, y) bins.

Table 4.9: Systematic uncertainties arising from the yield extraction procedure, shown as percentages.

p_t	y				
(GeV/c)	(2.0, 2.5)	(2.5, 3.0)	(3.0, 3.5)	(3.5, 4.0)	(4.0, 4.5)
(0, 1)	—	—	11.63	35.49	—
(1, 2)	—	19.66	2.60	8.24	—
(2, 3)	6.38	2.51	8.71	11.90	27.50
(3, 4)	6.90	2.81	6.02	9.53	19.95
(4, 5)	16.37	8.90	8.16	2.40	4.06
(5, 6)	11.34	7.33	8.92	1.04	25.08
(6, 7)	9.09	12.13	6.66	1.04	26.07
(7, 8)	6.98	3.99	14.16	5.48	19.13

4.7.2 Fiducial acceptance

Since the Monte Carlo sample used to measure the detector efficiencies is inevitably finite, there is a statistical uncertainty associated with the calculation (which is binomial in nature and can be reduced by increasing the Monte Carlo sample size). This is taken as a systematic uncertainty, shown in (p_{T}, y) bins, in Table 4.10.

Table 4.10: Systematic uncertainties arising from the limited Monte Carlo statistics available for the fiducial acceptance study, shown as percentages.

p_t	y				
(GeV/c)	(2.0, 2.5)	(2.5, 3.0)	(3.0, 3.5)	(3.5, 4.0)	(4.0, 4.5)
(0, 1)	—	—	0.54	1.04	—
(1, 2)	—	0.38	0.42	0.77	—
(2, 3)	0.89	0.35	0.41	0.65	1.45
(3, 4)	1.01	0.18	0.19	0.54	1.61
(4, 5)	0.85	0.10	0.37	0.75	1.63
(5, 6)	1.06	0.12	0.57	0.88	0.60
(6, 7)	0.65	0.00	0.75	1.26	3.21
(7, 8)	0.00	0.00	0.00	0.00	0.00

4.7.3 Selection and reconstruction efficiency

Identically to the fiducial acceptance systematic, a binomial uncertainty is calculated based on the number of Monte Carlo events used to study the selection and reconstruction efficiency in each (p_{T}, y) bin. These are shown in Table 4.11.

Table 4.11: Systematic uncertainties arising from the limited number of Monte Carlo events available for the reconstruction and selection efficiency calculation, shown as percentages.

p_t	y				
(GeV/c)	(2.0, 2.5)	(2.5, 3.0)	(3.0, 3.5)	(3.5, 4.0)	(4.0, 4.5)
(0, 1)	—	—	0.27	0.30	—
(1, 2)	—	0.24	0.26	0.29	—
(2, 3)	0.31	0.33	0.35	0.40	0.47
(3, 4)	0.42	0.45	0.50	0.56	0.69
(4, 5)	0.58	0.63	0.68	0.80	1.01
(5, 6)	0.80	0.84	0.94	1.12	1.46
(6, 7)	1.04	1.12	1.26	1.54	2.09
(7, 8)	1.39	1.45	1.71	2.03	2.89

4.7.4 PID efficiency

To asses the systematic uncertainty originating from the PID efficiency determination, a Monte Carlo simulated calibration sample is used. The entire PID calibration procedure (discussed in Section 4.6.4) is repeated, using the Monte Carlo calibration sample instead of the real data, to produce distributions of efficiencies as a function of a cut on $\log(\mathcal{L}_K/\mathcal{L}_\pi)$ for each of the daughter tracks. These distributions are then compared with the true distributions from a Monte Carlo signal sample. The largest difference between the two distributions within ± 5 of the $\log(\mathcal{L}_K/\mathcal{L}_\pi)$ cut used is taken as the systematic uncertainty. The uncertainties from the four tracks are added in quadrature. In addition there is a statistical uncertainty resulting from the finite size of the Monte Carlo and calibration samples used to calculate the PID efficiencies. This is added in quadrature with the other uncertainty. The combined systematics for all bins can be found in Table 4.12.

4.7.5 Dalitz model

Each of the amplitudes and phases of the resonances in the Mark III $D^0 \to K^-\pi^+\pi^-\pi^+$ Dalitz model (the model we use is shown in Table 4.13) are varied randomly to produce ten random variations of the amplitude model. Each amplitude is multiplied by a uniformly generated random number between 0.5 and 2.0, and the phases are chosen

Table 4.12: Systematic uncertainties arising from the PID efficiency determination, shown as percentages.

p_t	y				
(GeV/c)	(2.0, 2.5)	(2.5, 3.0)	(3.0, 3.5)	(3.5, 4.0)	(4.0, 4.5)
(0, 1)	—	—	9.27	11.45	—
(1, 2)	—	7.72	6.09	6.18	—
(2, 3)	10.17	7.35	5.82	4.19	7.84
(3, 4)	9.99	5.77	3.20	3.45	7.56
(4, 5)	8.36	2.93	1.87	2.97	10.07
(5, 6)	6.03	2.92	2.84	4.18	11.99
(6, 7)	4.24	3.00	3.56	6.98	11.65
(7, 8)	4.32	2.34	6.13	7.94	11.91

Table 4.13: The implementation of the Mark III amplitude model used to re-weight Monte Carlo signal events.

Decay chain	Fraction	Amplitude	Phase
non-resonant	0.22	0.97	2.07
$D^0 \to a_1^+(1260)K^-, a_1^+(1260) \to \rho^0(770)\pi^+$	0.47	1.0	0.0
$D^0 \to K_1^-(1270)\pi^+, K_1^-(1270) \to \rho^0(770)K^-$	0.032	0.13	0.71
$D^0 \to K_1^-(1270)\pi^+, K_1^-(1270) \to \overline{K}^{*0}(1430)\pi^-$	0.021	0.57	3.85
$D^0 \to K_1^-(1270)\pi^+, K_1^-(1270) \to \overline{K}^{*0}(892)\pi^-$	0.013	0.040	0.1
$D^0 \to \overline{K}^{*0}(892)\pi^+\pi^-$	0.13	0.93	6.21
$D^0 \to \rho^0(770)K^-\pi^+$	0.088	0.5464	2.84
$D^0 \to \overline{K}^{*0}(892)\rho^0(770)$	0.29	0.1232	1.69
$D^0(D-\text{wave}) \to \overline{K}^{*0}(892)\rho^0(770)$	0.13	0.1963	1.96

randomly between 0 and 2π. This produces a much more significant range of variation than one would expect, leading to a conservative systematic uncertainty.

The product of the fiducial acceptance, selection, reconstruction, and PID efficiencies is calculated for each of the ten variations and the standard deviation is taken as the systematic uncertainty due to the Dalitz model. The resulting uncertainties for each (p_T, y) bin are shown in Table 4.14.

4.7.6 Tracking efficiency

Using results from previous measurements [20, 50] a fully correlated uncertainty of 3% per track is applied, resulting in an overall systematic uncertainty of 12% for the tracking efficiency.

Table 4.14: Systematic uncertainties resulting from the Dalitz model implementation in the Monte Carlo simulation.

p_t	y				
(GeV/c)	(2.0, 2.5)	(2.5, 3.0)	(3.0, 3.5)	(3.5, 4.0)	(4.0, 4.5)
(0, 1)	—	—	8.77	10.98	—
(1, 2)	—	1.79	3.35	2.61	—
(2, 3)	6.99	3.40	2.11	2.44	2.82
(3, 4)	3.61	2.72	2.06	1.63	1.28
(4, 5)	3.93	1.76	2.17	3.34	2.84
(5, 6)	3.21	2.02	2.67	2.25	3.44
(6, 7)	3.50	1.17	1.50	1.69	8.17
(7, 8)	4.49	2.27	2.72	3.35	3.88

4.7.7 Integrated luminosity

The uncertainty on the measurement of the integrated luminosity is determined to be 3.5% [51].

4.7.8 Branching fraction

The branching fraction value is taken from the PDG to be $\mathcal{B}(D^0 \to K^-\pi^+\pi^-\pi^+) = \left(8.07^{+0.21}_{-0.19}\right)$ % [52]. The average of the asymmetric errors is used as a systematic uncertainty.

4.7.9 Monte Carlo association failure

Occasionally the algorithm responsible for associating reconstructed tracks with MC particles will fail to identify a signal candidate and incorrectly classify it as a background event. This results in a small undercount for the number of MC signal candidates passing reconstruction and selection, which must be corrected for when calculating the cross-sections. The MC association failure rate is calculated using

$$F = \frac{N_F}{N_F + N_T} \tag{4.11}$$

and has an uncertainty

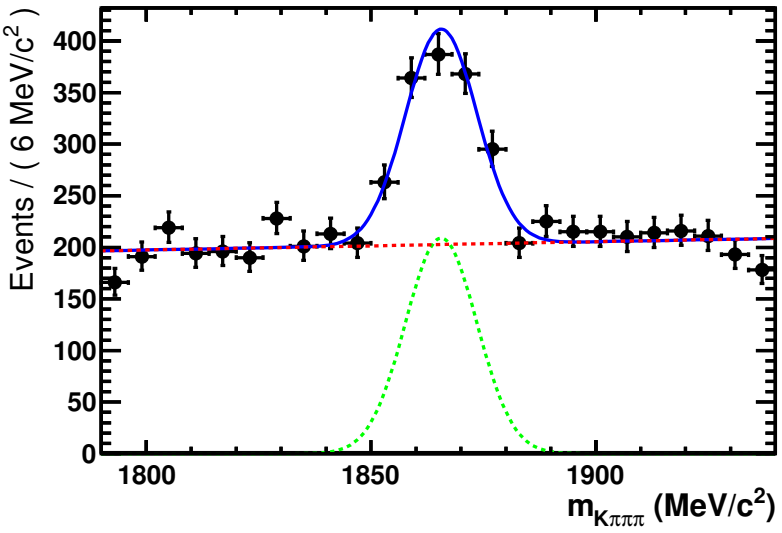

Figure 4.14: Invariant mass distribution for MC events which have been categorised as combinatorial background. The peak arises from signal candidates which fail MC association.

$$\sigma_F = \frac{1}{(N_T + N_F)^2}\sqrt{N_F^2\sigma_{N_T}^2 + N_T^2\sigma_{N_F}^2}. \tag{4.12}$$

Here, N_T is the number of truth-matched signal candidates and N_F is the number of signal candidates which fail MC association. After all reconstruction and selection requirements, $N_T = 20067 \pm 142$ within the full (p_T, y) range. To measure the number of association failures within the same MC sample, data identified as combinatorial background are fitted with the same signal and background PDFs used for the yield extraction (see Figure 4.14). The signal component of the fit yields $N_F = 696 \pm 52$. Inserting the numbers into Equations 4.11 and 4.12 gives $F = (3.25 \pm 0.24)\,\%$. To correct the results, cross-sections are multiplied by a factor of $(1 - F)$. The uncertainty σ_F is used as a systematic uncertainty.

The value of F is calculated separately in every (p_T, y) bin used in the analysis to check for any p_T or y dependence. The values show good consistency with the global value, therefore only the global value is used.

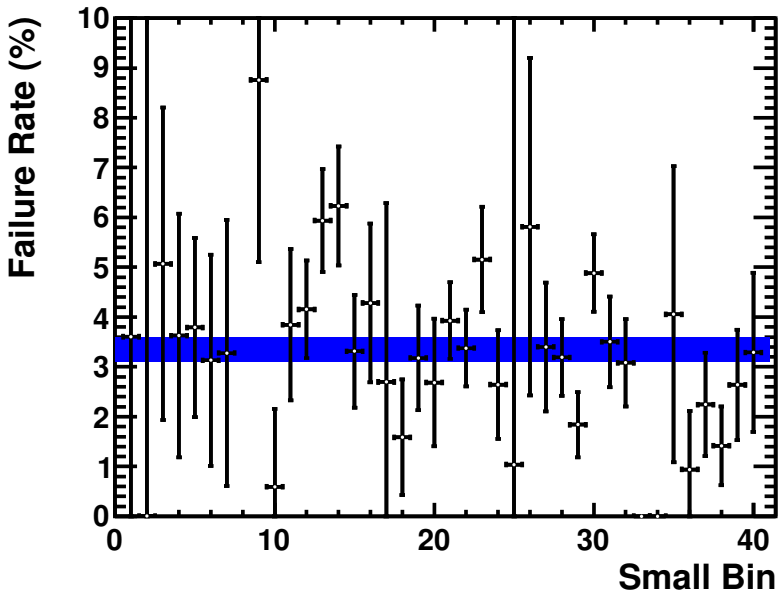

Figure 4.15: MC association failure rate calculated separately in each analysis bin. The blue band represents the value calculated for the entire (p_{T}, y) range along with its uncertainty.

4.7.10 Cut variable distributions

The efficiency of reconstruction and selection is calculated using Monte Carlo data, therefore any differences between the Monte Carlo and real data selection variable distributions need to be identified and corrected for. All variables that are used as selection criteria (see Table 4.2 for the full list) are examined, after applying all of the selection cuts except on the variable under examination, by comparing Monte Carlo signal distributions with sideband-subtracted data distributions. The majority of the variables do not lead to correction factors because either their Monte Carlo and real data distributions are similar enough or a cut is placed far enough from the peak of the distributions, both resulting in negligible differences between Monte Carlo and data efficiencies. Examples of these variables can be seen in Figure 4.16.

The stripping cuts placed on all of the daughter $IP\chi^2$ variables, as well as the largest of the daughter track fit χ^2/N_{dof} variables, prevent a direct determination of the efficiency for the real data. Instead, Monte Carlo and data distributions of those variables are fit with first order polynomials, which are extrapolated into the regions removed by the stripping cuts (see Figure 4.17 for examples). The ratio of efficiencies, $\varepsilon_{data}/\varepsilon_{MC}$, can

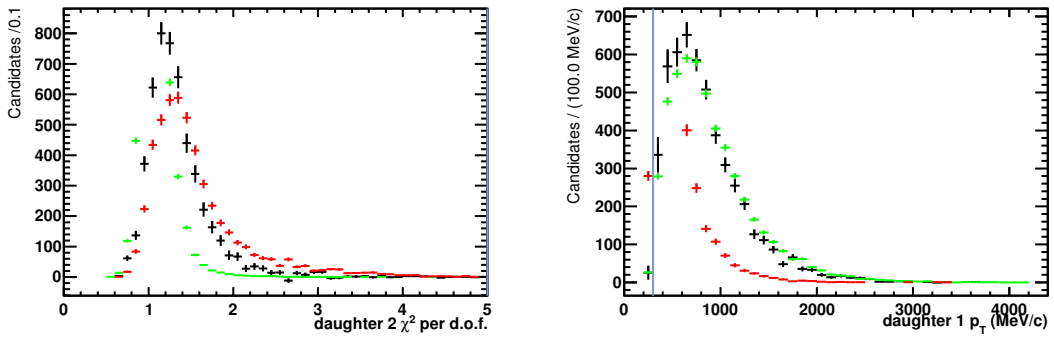

(a) (b)

Figure 4.16: Distributions of (a) the second largest daughter track fit χ^2/N_{dof} and (b) the second smallest daughter track p_{T}. Both figures show distributions from signal Monte Carlo (green), real data after background subtraction (black) and background (red). The blue line indicates where a cut is placed.

then be determined. For each variable the fit is performed within three different ranges. The median of the $\varepsilon_{data}/\varepsilon_{MC}$ ratios (which is very similar to the mean in each case) is used as a correction factor to the selection efficiency and the difference between the smallest and largest of the $\varepsilon_{data}/\varepsilon_{MC}$ ratios is used as a systematic uncertainty.

In the case of the smallest of the daughter momenta and the daughter p_{T} variables, the stripping cut is too tight to allow either of the techniques described above. Instead, the ratio of the real data to Monte Carlo distributions (both normalised) is plotted for each of the two variables up to the cut value and the resulting distributions are fit with first order polynomials (see Figure 4.18), which are extrapolated into the regions removed by the cuts. The Monte Carlo distributions without the cuts applied are then multiplied in each bin by the value of the fitted polynomial in the centre of the same bin to produce a simulated distribution for the real data. The correction factor $\varepsilon_{data}/\varepsilon_{MC}$ is then determined for each variable by measuring the fraction of the data and Monte Carlo distributions either side of the cut. A systematic uncertainty is calculated by varying the slope of the fitted polynomial within its errors. A summary of all correction factors and systematic uncertainties arising from differences between data and Monte Carlo distributions is shown in Table 4.15. The total correction factor is simply the product of all individual correction factors. Correlations between variables are taken into account when calculating the total systematic uncertainty using Pearson's correlation coefficient [53], which gives a measurement of the linear correlation between two

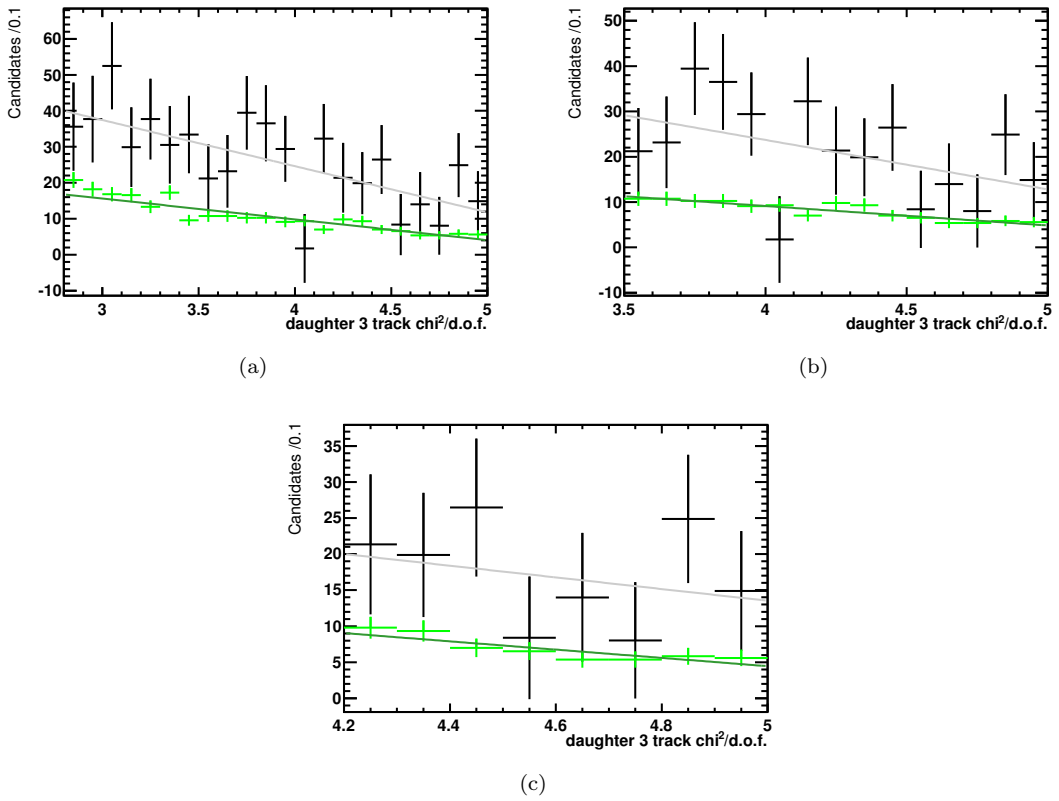

Figure 4.17: The largest daughter track fit χ^2/N_{dof} variable distribution shown for Monte Carlo signal events (green) and sideband-subtracted data (black) in three different ranges. First order polynomial fits are shown in dark green (Monte Carlo) and grey (real data).

variables.

4.7.11 Multiple candidates

Assuming that if one c quark from a $c\bar{c}$ pair is within fiducial acceptance then the other will be also, the probability for an event with a reconstructed $D^0 \to K^-\pi^+\pi^-\pi^+$ signal decay to contain another reconstructed $D^0 \to K^-\pi^+\pi^-\pi^+$ signal decay can be estimated by

$$\varepsilon_{\text{acc}} \cdot \varepsilon_{\text{sel|trig}} \cdot \varepsilon_{\text{PID|sel}} \cdot f\left(c \to D^0\right) \cdot \mathcal{B}(D^0 \to K^-\pi^+\pi^-\pi^+). \tag{4.13}$$

Here $f\left(c \to D^0\right)$ is the probability for a charm quark to hadronise into a D^0. At energies near the $\Upsilon(4S)$ resonance, $f\left(c \to D^0\right) = 0.565 \pm 0.032$ [54]. For the sake of this

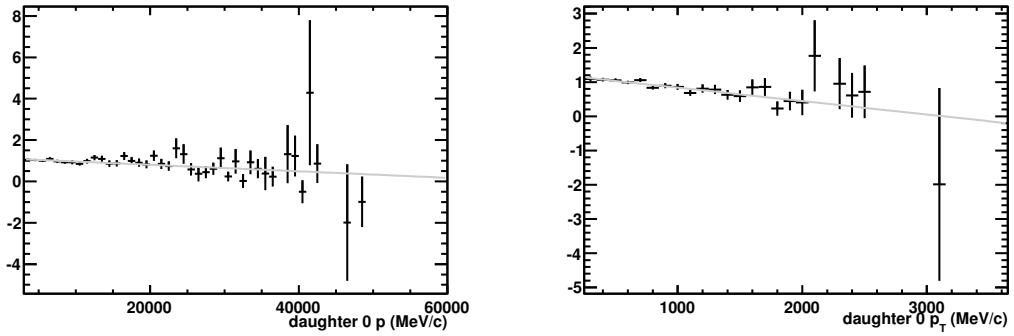

(a) (b)

Figure 4.18: Ratio of normalised data and Monte Carlo distributions as a function of (a) the lowest daughter track momentum, and (b) the lowest daughter track p_{T}. The grey lines show first order polynomial fits to the distributions.

Table 4.15: Correction factors to the selection efficiency and their corresponding systematic uncertainties. Uncertainties are quoted as absolute uncertainties on the correction factors.

	Variable name	Correction factor	Systematic uncertainty
D^0	vertex χ^2/N_{dof}	0.8828	0.0586
	DoCA	0.9532	0.0234
	DIRA	0.9684	0.0158
$h^{\pm}$	smallest *IP* χ^2	1.0113	0.0222
	3^{rd} largest *IP* χ^2	0.9772	0.0160
	2^{nd} largest *IP* χ^2	0.9915	0.0055
	largest *IP* χ^2	0.9944	0.0019
	largest track fit χ^2/N_{dof}	0.9906	0.0107
	smallest p_{T}	0.9849	0.0051
	smallest $\lvert\vec{p}\rvert$	0.9912	0.0041
	Total	0.7678	0.0880

calculation we will assume that this value is the same at $\sqrt{s} = 7\,\text{TeV}$. Over the ranges $0 < p_{\text{T}} < 8\,\text{GeV}$ and $2.0 < y < 4.5$, the efficiencies ε_{acc}, $\varepsilon_{\text{sel|trig}}$ and $\varepsilon_{\text{PID|sel}}$ are measured using Monte Carlo in the same way as described in Section 4.6. Their values are 0.857, 0.010 and 0.888 respectively. Combining all of these numbers with the branching fraction one obtains a probability of 0.035% for an event to contain two reconstructed signal candidates. Neglecting events which contain more than two reconstructed signal candidates, this corresponds to an expected average of 1.00035 candidates per event (note that the assumption that $f\left(c\to D^0\right) = 0.565$ at 7 TeV makes this a rough estimate, although there is evidence [55, 56] that fragmentation functions are independent of the collision energy). The number of candidates per event in the Monte Carlo signal sample is measured as 1.00065 ± 0.00017 which is close to the estimate. Since the deviation

from one is so small it is neglected in the cross-section measurements.

For the collision data the signal candidate multiplicity is calculated using

$$M = \frac{c_s - c_b}{e_s - e_b} \tag{4.14}$$

with an uncertainty

$$\sigma_M = \frac{\sqrt{c_s + c_b}}{e_s - e_b} \tag{4.15}$$

where c_s and c_b are the number of candidates inside signal and background search windows, and e_s and e_b are the number of events inside the same windows. The search windows are defined in the D^0 invariant mass distribution so that their total widths are the same and the number of signal events inside the background window is negligible. Because the background shape is assumed to be linear, we are effectively performing a linear background subtraction. Using Equations 4.14 and 4.15 the candidate multiplicity in the collision data sample is calculated to be 1.04044 ± 0.04052. The value is used as a correction factor to the cross-section calculation and the error is treated as a systematic uncertainty.

The value of M is calculated in each individual (p_T, y) bin to check for any p_T or y dependance. The result (shown in Figure 4.19) shows that there are no obvious trends. Consequently the correction factor is applied uniformly to all analysis bins.

4.7.12 Peaking background

To assess any contribution to the signal yields arising from background which peaks in the invariant mass distributions, a sample of inclusive $c\bar{c}$ Monte Carlo events is passed through the same reconstruction and selection algorithms as the data and signal Monte Carlo. Any background that passes all selection criteria and contributes towards the fitted signal yield needs to be taken into account when extracting the final corrected yields. The invariant mass distributions of signal and different categories of background

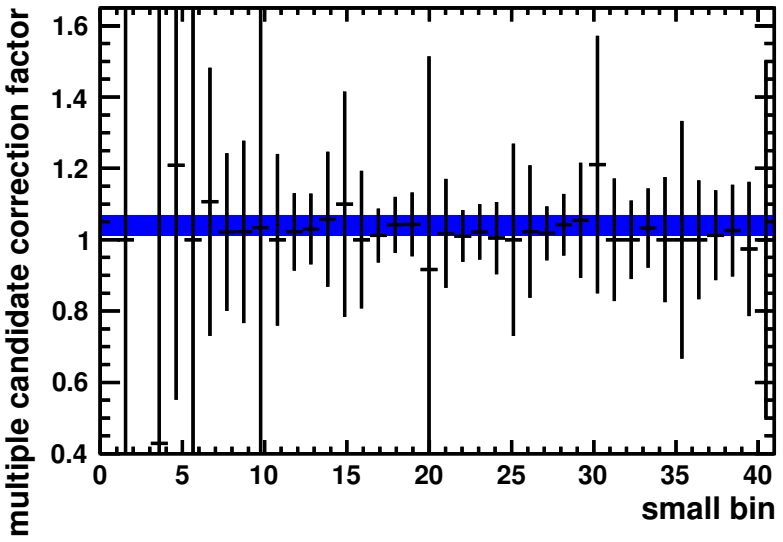

Figure 4.19: Multiple candidate correction factor for each small (p_{T}, y) bin. The global value calculated for all data within $0 < p_{\text{T}} < 8\,\text{GeV}$ and $2.0 < y < 4.5$ is shown with its uncertainty as the solid blue band.

are shown in Figure 4.20. The only type of background event that appears to peak anywhere in the distribution is classified as "low mass" background (see Section 2.2.9.1) which appears to collect around the same location as the left tail of the signal peak. Fits to the invariant mass distribution with and without the sources of potentially peaking background are performed using the same signal and background PDFs as for the yield extraction. The fit finds 2404 ± 69 "signal" candidates before including the peaking background (consistent with the 2395 true signal events in the sample) and 2488 ± 97 after. Within uncertainty the difference is consistent with the 55 low mass background events shown in Figure 4.20(b). The fitted distributions are shown in Figure 4.21 where one can see that the difference is largely attributable to a more prominent tail in the Crystal Ball function which is consistent with the distribution of the low mass background events.

Studying the low mass background events in more detail reveals that only two of the 55 events are true background events. These are the decays $D^0 \to \overline{K}^{*0}(892)\,\eta$ where $\overline{K}^{*0}(892) \to K^-\pi^+$ and $\eta \to \pi^+\pi^-\gamma$, and $D^0 \to K^-\pi^+\eta'$ where $\eta' \to \rho^0\gamma$. The other 53 are $D^0 \to K^-\pi^+\pi^-\pi^+$ decays where one or more photons have been emitted in the final state, which have been wrongly identified as background. Because the efficiency of reconstruction and selection is computed with these events classified as background, it is an underestimate. Therefore a correction factor is applied to compensate.

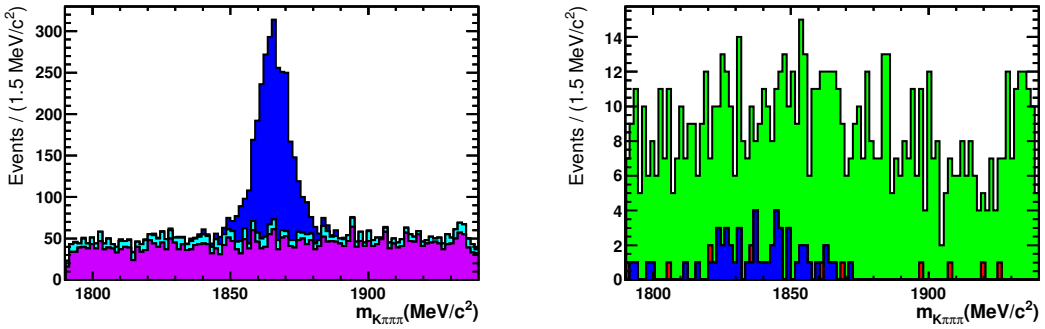

(a) (b)

Figure 4.20: Stacked histograms for invariant mass distributions from reconstructed inclusive $c\bar{c}$ Monte Carlo data. Signal (blue), combinatorial background (violet) and potentially peaking background (cyan) are shown in (a). The potentially peaking background is further split into categories in (b), showing low mass background (blue), reflections (red) and partially reconstructed physics background (green).

Based on this study the correction factor is calculated using

$$P = \frac{N_s + N_b}{N_s} \tag{4.16}$$

where N_s is the number of correctly identified signal events and N_b is the number of signal events categorised as low mass background. Assuming that the uncertainty on $N_{s,b}$ is simply $\sqrt{N_{s,b}}$, the uncertainty on P is given by

$$\sigma_P = \sqrt{\frac{N_b\,(N_s + N_b)}{N_s^3}}\,. \tag{4.17}$$

Inserting the numbers into Equations 4.16 and 4.17, one obtains a correction factor of 1.022 with a systematic uncertainty of 0.003.

4.7.13 Summary

A summary of all systematic uncertainties and correction factors can be found in Table 4.16.

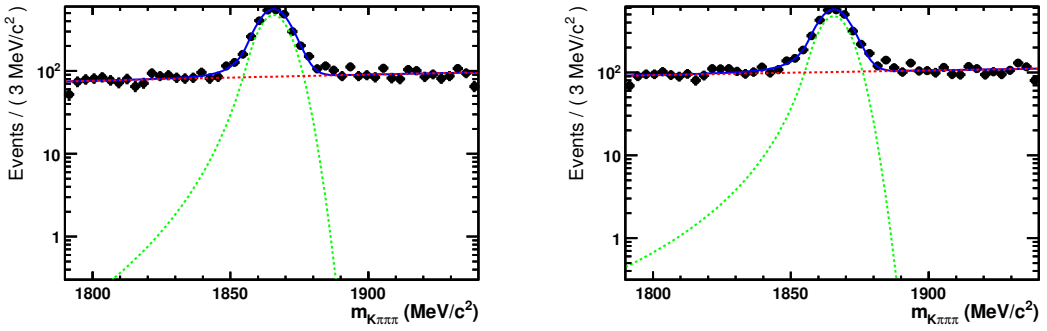

(a) (b)

Figure 4.21: Fits to the reconstructed D^0 invariant mass distributions from inclusive $c\bar{c}$ Monte Carlo data without (a) and with (b) the events classified as potentially peaking background. The dashed green line shows the signal component of the fit.

Table 4.16: Correction factors and systematic uncertainties for the cross section measurement. The correction factors are shown here as multiplicative corrections to the cross sections. The top section of the table shows the systematics that are calculated separately for individual (p_T, y) bins. The other two sections show systematic uncertainties that are applied globally.

Measurement	Correction factor	Systematic uncertainty (%)
Yield extraction	—	$1.04 - 35.49$
Fiducial acceptance	—	$0.00 - 3.21$
Selection/reconstruction efficiency	—	$0.24 - 2.89$
PID	—	$1.87 - 11.99$
Dalitz model	—	$1.17 - 10.98$
Multiple Candidates	0.961	2.74
MC association	0.966	0.25
Peaking background	0.978	0.31
MC variable distributions	1.302	11.46
Tracking efficiency	—	12.00
Integrated luminosity	—	3.50
Branching ratio	—	2.47

4.8 Results

Starting with Equation 4.3 and inserting all of the correction factors one obtains

$$\sigma_i\left(D^0\right) = \frac{N_i\left(D^0 \to K^-\pi^+\pi^-\pi^+\right)}{\varepsilon_{i,\text{acc}} \cdot \varepsilon_{i,\text{sel|trig}} \cdot \varepsilon_{i,\text{PID|sel}} \cdot \mathcal{B}\left(D^0 \to K^-\pi^+\pi^-\pi^+\right) \cdot \mathcal{L}_\text{eff}} \cdot \frac{(1-F)}{P \cdot M \cdot C}. \quad (4.18)$$

This formula is used to calculate the cross-section in each of the (p_T, y) bins which contain a sufficient number of signal events (bins with a statistical error larger than the

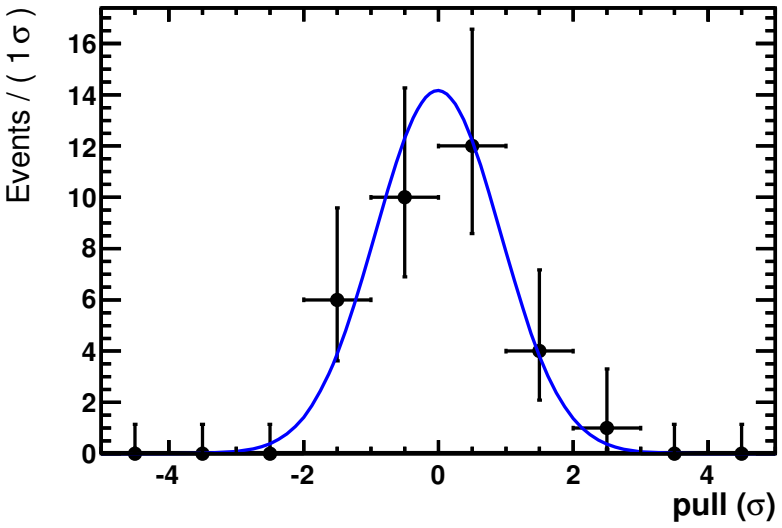

Figure 4.22: Pull distribution for the comparison between the cross-section results for the modes $D^0 \to K^-\pi^+$ and $D^0 \to K^-\pi^+\pi^-\pi^+$. The blue line is a Gaussian fit to the pulls with a mean of -0.007 ± 0.162 and a width of 0.929 ± 0.114. The χ^2/N_{dof} of the fit is 0.165.

measured yield are removed from the analysis). The cross-section results can be found in Table 4.17

4.8.1 Comparison with $D^0 \to K^-\pi^+$

The cross-section results are compared with the values obtained with the higher statistics mode $D^0 \to K^-\pi^+$ by producing a pull distribution. The difference between the two cross-section values in each (p_{T}, y) bin is divided by the total uncorrelated error for that bin. The total uncorrelated error is defined as the sum under quadrature of the statistical uncertainties from each analysis, as well as the bin-uncorrelated systematic uncertainties (listed for the $D^0 \to K^-\pi^+\pi^-\pi^+$ analyses in the top section of Table 4.16). The distribution for all of the bins in which there is a cross-section measurement in both analyses is shown in Figure 4.22. A Gaussian fit to this distribution yields a mean of -0.007 ± 0.162 and a width of 0.929 ± 0.114, with a χ^2 per degree of freedom of 0.165, showing excellent agreement between the two analyses. Pulls in individual (y, p_{T}) bins are shown in Figure 4.23.

Table 4.17: Binned production cross-section results for $D^0 \to K^+\pi^-\pi^+\pi^-$ in units of μb, shown with the statistical uncertainties coming from the yield extraction and the total systematic uncertainties.

p_t	y				
(GeV/c)	(2.0, 2.5)	(2.5, 3.0)	(3.0, 3.5)	(3.5, 4.0)	(4.0, 4.5)
(0, 1)	—	—	$240.3 \pm 63.5 \pm 58.9$	$278.9 \pm 97.0 \pm 118.8$	—
(1, 2)	—	$192.3 \pm 54.3 \pm 52.7$	$119.2 \pm 18.8 \pm 22.5$	$147.2 \pm 24.9 \pm 30.0$	—
(2, 3)	$145.2 \pm 32.1 \pm 32.3$	$70.2 \pm 6.9 \pm 13.6$	$68.7 \pm 5.3 \pm 14.0$	$47.4 \pm 5.2 \pm 10.3$	$68.6 \pm 13.6 \pm 23.1$
(3, 4)	$38.1 \pm 6.6 \pm 8.2$	$37.9 \pm 2.7 \pm 7.1$	$30.1 \pm 1.8 \pm 5.7$	$24.9 \pm 2.0 \pm 5.0$	$8.7 \pm 2.0 \pm 2.4$
(4, 5)	$17.6 \pm 2.3 \pm 4.5$	$17.9 \pm 1.2 \pm 3.5$	$13.2 \pm 0.9 \pm 2.6$	$10.2 \pm 0.8 \pm 1.8$	$5.1 \pm 1.1 \pm 1.1$
(5, 6)	$9.5 \pm 1.6 \pm 2.1$	$9.5 \pm 0.7 \pm 1.8$	$6.3 \pm 0.5 \pm 1.2$	$3.8 \pm 0.4 \pm 0.7$	$2.2 \pm 0.6 \pm 0.7$
(6, 7)	$3.8 \pm 0.6 \pm 0.8$	$3.9 \pm 0.4 \pm 0.8$	$2.9 \pm 0.3 \pm 0.6$	$2.0 \pm 0.3 \pm 0.4$	$1.7 \pm 0.5 \pm 0.6$
(7, 8)	$2.8 \pm 0.5 \pm 0.6$	$2.4 \pm 0.3 \pm 0.4$	$1.8 \pm 0.2 \pm 0.4$	$1.0 \pm 0.2 \pm 0.2$	$0.5 \pm 0.3 \pm 0.1$

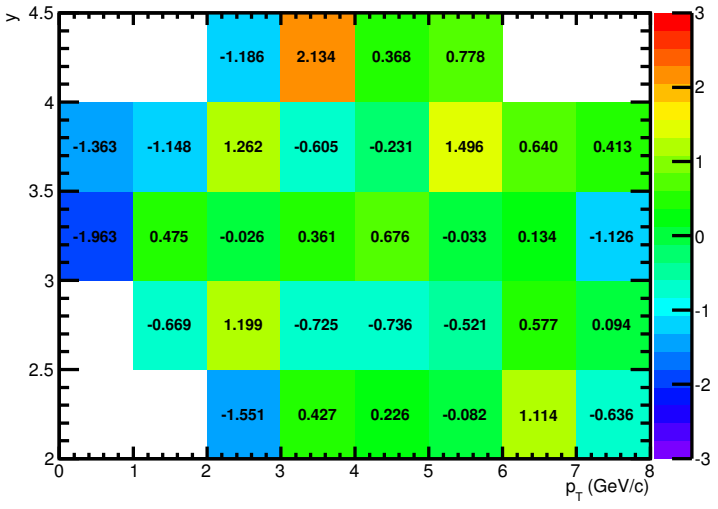

Figure 4.23: Two dimensional pull distribution comparing the $D^0 \to K^-\pi^+$ results with the $D^0 \to K^-\pi^+\pi^-\pi^+$ in each of the $(y, p_{\rm T})$ bins.

4.8.2 Comparison with theoretical predictions

The cross-section results are compared with NLO theoretical predictions calculated with the Generalized Mass Variable Flavour Number Scheme (GMVFNS) [57] and the Fixed Order Next to Leading Logarithm (FONNL) approach [58, 59]. The comparisons are shown in Figure 4.24.

In addition, the measurements are compared to different tunes of Pythia [22, 60]. These comparisons are shown in Figure 4.25.

4.9 Conclusions

Using $15.0\,\text{nb}^{-1}$ of pp collision data collected with the LHCb detector at an energy of $\sqrt{s} = 7\,\text{TeV}$, the production cross-section of prompt D^0 mesons is measured with $D^0 \to K^-\pi^+\pi^-\pi^+$ decays in two-dimensional $(y, p_{\rm T})$ bins, in the range $2.0 < y < 4.5$ and $0 < p_{\rm T} < 8\,\text{GeV}/c$. In the majority of bins, the systematic uncertainty dominates. The cross-section results are compared to those obtained using the more abundant mode $D^0 \to K^-\pi^+$, and excellent agreement is found. This is a powerful cross check which validates the analysis techniques and demonstrates that track reconstruction efficiencies are well understood.

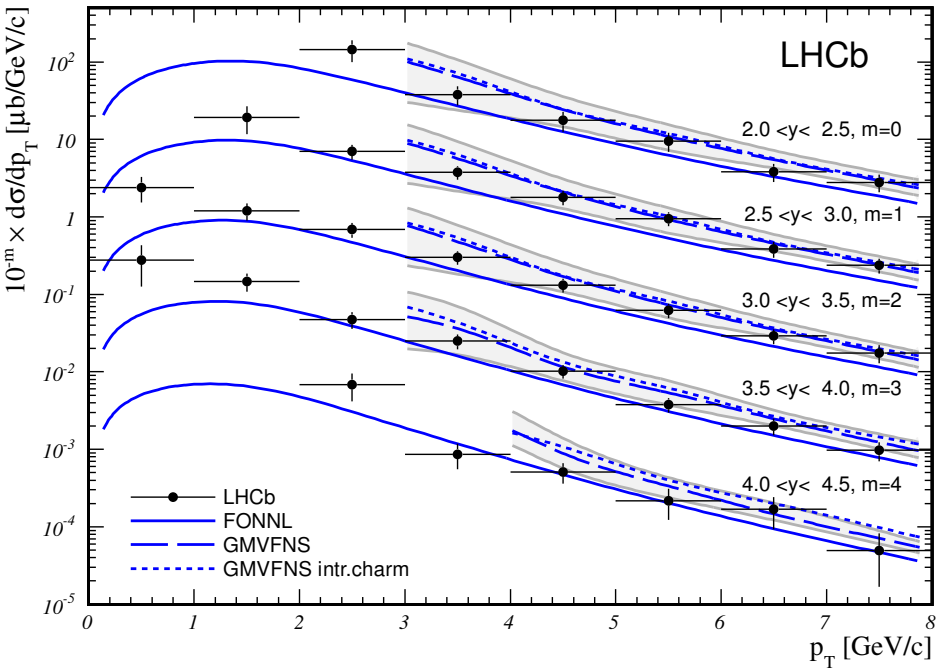

Figure 4.24: Differential cross-section results, compared with theoretical predictions. To display the results on one plot, the different rapidity ranges are scaled by factors of 10^{-m} (the values of m are shown next to the rapidity ranges). The grey shaded regions represent the theoretical uncertainties associated with the GMVFNS predictions. Data points in the first $p_{\rm T}$ bin belong to the bins $3.0 < y < 3.5$ and $3.5 < y < 4.0$.

Cross-section measurements can be used to test QCD predictions. The LHCb detector provides unique access to high rapidity and low $p_{\rm T}$ regions, where the other LHC experiments are unable to make measurements. Here we compare the results with theoretical predictions using two different NLO approaches. The predictions show reasonable agreement with the measurements, with the data points generally lying between the two different approaches. The results are also compared with different Monte Carlo predictions, and are found to agree best with the LHCb tune of Pythia.

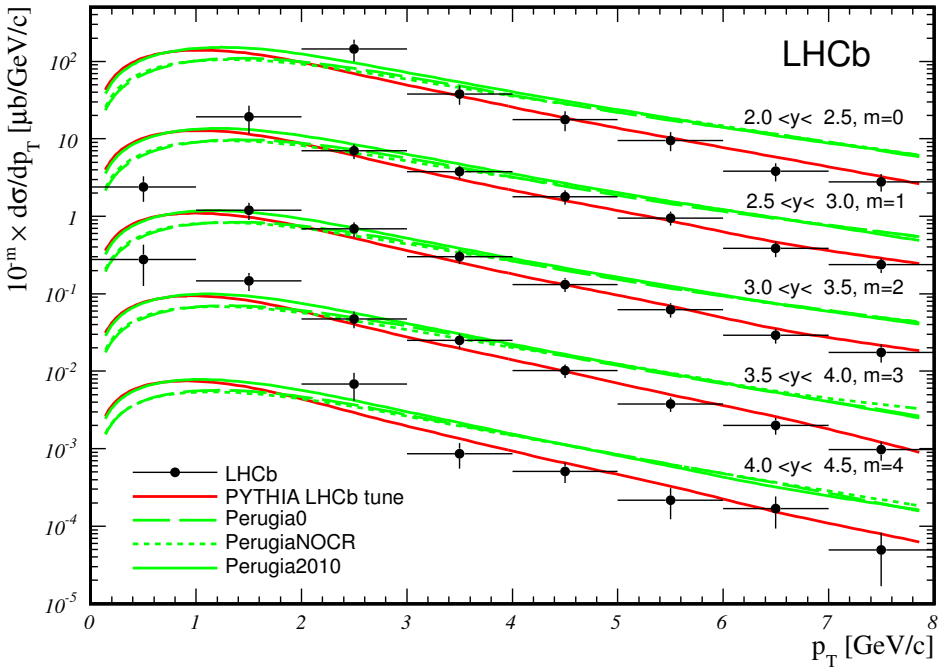

Figure 4.25: Differential cross-section results, compared with different Monte Carlo predictions. To display the results on one plot, the different rapidity ranges are scaled by factors of 10^{-m} (the values of m are shown next to the rapidity ranges). Data points in the first $p_{\rm T}$ bin belong to the bins $3.0 < y < 3.5$ and $3.5 < y < 4.0$.

Chapter 5

Search for $D^0 - \overline{D}^0$ oscillations and a measurement of the doubly Cabibbo suppressed decay $D^0 \to K^+\pi^-\pi^+\pi^-$

5.1 Introduction

Flavour mixing in neutral mesons occurs because their mass eigenstates are different to their flavour eigenstates. Mixing in down-type neutral mesons is a well established phenomenon, first discovered in 1956 in the neutral kaon system [61]. Since then it has also been observed with B^0 [62] and B_s^0 [63] mesons. The first observation of $D^0 - \overline{D}^0$ oscillations has only very recently been reported [64], using the WS decay $D^0 \to K^+\pi^-$. In the most recent measurement by the Belle collaboration involving the decay $D^0 \to K^+\pi^-\pi^+\pi^-$ [65], only a time-integrated analysis is carried out. More recently, the BABAR collaboration has used $D^0 \to K^+\pi^-\pi^+\pi^-$ decays to measure the time-integrated mixing rate [66], R_M, using the formalism shown in Section 1.7. Here we use the WS decay $D^0 \to K^+\pi^-\pi^+\pi^-$ to perform a time dependent analysis with $1.0\,\text{fb}^{-1}$ of data collected in 2011 with the LHCb detector at an energy $\sqrt{s} = 7\,\text{TeV}$.

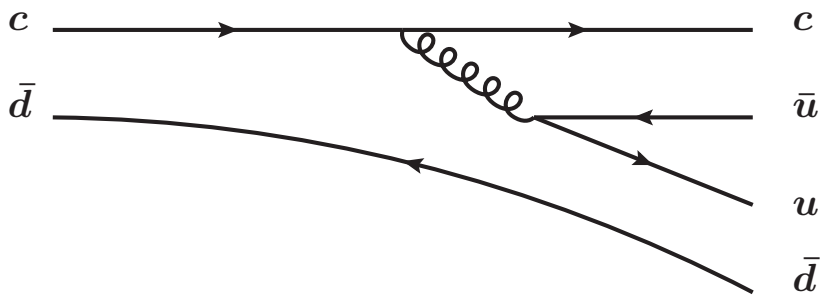

Figure 5.1: Feynman diagram for the strong decay $D^{*+} \to D^0\pi^+$.

Amongst the results presented are: a first measurement of the ratio of DCS/CF decay rates, the significance of $D^0 - \overline{D}^0$ oscillations, and a measurement of R_M.

5.2 Analysis strategy

Measuring the ratio of WS/RS $D \to K3\pi$ decays as a function of the D^0 decay time allows the extraction of physical parameters that appear in Equation 1.77. Any deviation of the time dependent ratio from a zeroth order polynomial would be clear indication of $D^0 - \overline{D}^0$ oscillations. However, the initial flavour of the D must be known in order to distinguish between WS and RS decays. The flavour of the D is determined by reconstructing strong decays of the excited resonant state $D^*(2010)^{\pm}$. The charge of the pion "tags" the flavour of the D (see Figure 5.1). Because the mass difference $\Delta m = m_{D^*(2010)^+} - m_{D^0}$ is so close to the pion mass ($\Delta m = 145.421 \pm 0.010\,\mathrm{MeV}/c^2$ [52]), the pion is always produced with a low momentum and is referred to as a "slow pion", or $\pi_s^{\pm}$.

Separating the sample of $D \to K3\pi$ events into their four categories (WS or RS decays from either a D^0 or $\overline{D}^0$), one can construct the ratios of event yields with the same initial state but different final states

$$\frac{N_{\overline{D}^0 \to K^+\pi^-\pi^+\pi^-}}{N_{\overline{D}^0 \to K^-\pi^+\pi^-\pi^+}} = \frac{1}{R\,(t)} \cdot \frac{\varepsilon_{K^+\pi^-}}{\varepsilon_{K^-\pi^+}} \cdot \frac{\varepsilon_{\mathrm{RS}}}{\varepsilon_{\mathrm{WS}}} \tag{5.1}$$

and

$$\frac{N_{D^0 \to K^-\pi^+\pi^-\pi^+}}{N_{D^0 \to K^+\pi^-\pi^+\pi^-}} = \frac{1}{R\,(t)} \cdot \frac{\varepsilon_{K^-\pi^+}}{\varepsilon_{K^+\pi^-}} \cdot \frac{\varepsilon_{\mathrm{RS}}}{\varepsilon_{\mathrm{WS}}} \tag{5.2}$$

where $R(t)$ is the time dependent ratio of WS to RS decay rates, $\frac{\varepsilon_{K^+\pi^-}}{\varepsilon_{K^-\pi^+}}$ is the ratio of the detection efficiencies of $K^+\pi^-$ and $K^-\pi^+$, and $\frac{\varepsilon_{\rm RS}}{\varepsilon_{\rm WS}}$ accounts for any difference in detection asymmetry due to the resonant substructure of WS and RS decays, leading to subtle differences in the kinematics of the daughters[1]. The detection asymmetry ratio can be eliminated by multiplying Equations 5.1 and 5.2, leaving

$$\frac{N_{\overline{D}^0\to K^+\pi^-\pi^+\pi^-}}{N_{\overline{D}^0\to K^-\pi^+\pi^-\pi^+}} \times \frac{N_{D^0\to K^-\pi^+\pi^-\pi^+}}{N_{D^0\to K^+\pi^-\pi^+\pi^-}} = \frac{1}{R(t)^2} \cdot \left(\frac{\varepsilon_{\rm RS}}{\varepsilon_{\rm WS}}\right)^2 . \tag{5.3}$$

Deviations of $\frac{\varepsilon_{\rm RS}}{\varepsilon_{\rm WS}}$ from one are expected to be very small (considered in Section 5.8.4). Therefore setting $\frac{\varepsilon_{\rm RS}}{\varepsilon_{\rm WS}} = 1$ and rearranging Equation 5.3 gives

$$R(t) = \sqrt{\frac{N_{\overline{D}^0\to K^+\pi^-\pi^+\pi^-}}{N_{\overline{D}^0\to K^-\pi^+\pi^-\pi^+}} \times \frac{N_{D^0\to K^-\pi^+\pi^-\pi^+}}{N_{D^0\to K^+\pi^-\pi^+\pi^-}}} , \tag{5.4}$$

which means $R(t)$ can be extracted from data simply by measuring the yields while ignoring any efficiencies. Note that the $D^{*+} - D^{*-}$ production asymmetry and $\pi_s^+ - \pi_s^-$ detection asymmetry do not appear in Equation 5.1 (and Equation 5.2) because the numerator and denominator both contain the same D flavour.

This analysis is performed by measuring the WS/RS ratio, $R(t)$, in bins of lifetime and fitting the resulting lifetime distribution to extract the physical parameters. In addition, the significance of $D^0 - \overline{D}^0$ oscillations is measured by comparing the results of fitting the data with two different models: a mixing hypothesis and a no-mixing hypothesis. The lifetime bin boundaries are chosen by using a toy Monte Carlo study so that each bin contains at least 100 WS signal events of each D flavour. The binning can be seen in Figure 5.7, for example, and the boundaries are listed in Table 5.3.

[1]Even if the differences are large in the D^0 rest frame, they become small in the centre-of-mass frame because of the boost of the D^0.

5.3 Trigger

5.3.1 L0 and HLT1 requirements

All candidates are required to contain at least one track that has been selected by the HLT1 1-track line [33]. This HLT1 line accepts events that contain at least one high-p_{T} track with a large IP with respect to the PV, and which pass any of the L0 triggers (*i.e.* there is no specific L0 requirement).

5.3.2 HLT2 selection

All reconstructed $D \to K3\pi$ candidates are required to have been triggered by the HLT2CharmHadD02HHHH trigger line. This trigger algorithm is designed to reconstruct $D^*(2010)^+ \to D^0\pi_s^+$ candidates where the D^0 decays to any neutral combination of four charged kaons and pions (except for the kinematically forbidden decay $D^0 \to K^-K^+K^-K^+$). The standard HLT2 track reconstruction requires tracks to have $p_{\mathrm{T}} > 500\,\mathrm{MeV}/c$ and $|\vec{p}| > 5\,\mathrm{GeV}/c$. This is very inefficient for four-body D decays, and affects the five-dimensional Dalitz space in a non-uniform way. For this reason, the HLT2CharmHadD02HHHH line takes advantage of a "second loop" to recover low momentum tracks discarded by the HLT2 track reconstruction. First, every possible two-body track combination is formed with the standard HLT2 tracks, and a set of strict criteria are applied (for example, good track fit χ^2 and high $IP\chi^2$). Then two more tracks are added to the combination to form a reconstructed D^0, followed by another pion for the D^* decay, before the final set of criteria are applied. These extra tracks are taken either from the standard HLT2 track reconstruction or the second loop reconstruction. The second loop tracks benefit the selection in two ways:

1. D^0 candidates with one or two low momentum daughter tracks are recovered, which increases the efficiency of the trigger and more uniformly populates the five-dimensional Dalitz space. This has been studied in detail for the $D^+ \to h^+h^-h^+$ HLT2 algorithm [67].

2. The addition of the pion to form the D^* part of the decay chain is only made possible by using the low momentum tracks from the second reconstruction loop. This is because the mass of the D^* is so close to the mass of the D^0 that the D^* daughter pion is always produced with a low momentum.

Table 5.1: Selection criteria used in the HLT2CharmHadD02HHHH trigger line.

	Variable name	two-body	four-body/D^*
$h^\pm$	Track χ^2/N_{dof}	< 3	< 5
	IP χ^2	> 10.0	> 1.7
	p_{T}	$> 500\,\text{MeV}/c$	$> 250\,\text{MeV}/c$
	$\lvert\vec{p}\rvert$	$> 5\,\text{GeV}/c$	$> 2\,\text{GeV}/c$
	$\sum p_{\text{T}}$	$> 2\,\text{GeV}/c$	$> 2\,\text{GeV}/c$
D^*	Δm	—	$< 180\,\text{MeV}/c^2$
π_s	p_{T}	—	$> 300\,\text{MeV}/c$
	$\lvert\vec{p}\rvert$	—	$> 3\,\text{GeV}/c$
D^0	Vertex χ^2/N_{dof}	—	< 20
$h_i h_j$ pair	*DoCA*	$< 0.1\,\text{mm}$	$< 0.5\,\text{mm}$
	FD	$> 3\,\text{mm}$	—
	FD χ^2	> 40	> 100
	$IP\chi^2$	—	< 25
	DIRA		> 0.9995
	Mass window	$\lvert m - m_{\text{PDG}}\rvert < 65\,\text{MeV}/c^2$	—
	$m_{\text{corrected}}$	$< 3.5\,\text{GeV}/c^2$	$< 3.5\,\text{GeV}/c^2$
GEC	N_{tracks}	< 110	

The selection criteria are shown for both the two-body and four-body stages of the trigger algorithm in Table 5.1. The variables used are largely the same as in Section 4.4, with a few additions:

- the scalar sum of the daughter track transverse momenta;
- the corrected mass[2], which approximately accounts for the missing daughters at the two-body combination stage [68];
- an upper limit is placed on the measured Δm to control the rate of the trigger, but which is far enough from the signal peak to have no effect on the signal efficiency;
- a Global Event Cut (GEC) is placed on the number of forward tracks in the event in order to remove high multiplicity events which take a long time to process.

[2]defined as $m_{\text{corrected}} = \sqrt{m^2 + |p_{\text{T}}^{\text{miss}}|^2} + |p_{\text{T}}^{\text{miss}}|$, where $p_{\text{T}}^{\text{miss}}$ is the missing momentum of the trigger candidate, transverse to the direction of flight

Because of the high charm production rate, this requirement is chosen to be fairly strict to reduce the rate of the trigger, instead of using a pre-scale.

Of the events selected by the HLT1 1-track line, the HLT2 line is 68% efficient for the offline selected $D^0 \to K^+K^-\pi^+\pi^-$ Monte Carlo sample used for testing.

5.4 Event selection

A good event selection is of vital importance to provide background rejection, especially for the WS decay mode, which has a branching fraction ~ 300 times smaller than the RS mode. A genetic algorithm is used to optimise the selection criteria, as described in Section 4.4 but with a few differences. Firstly, since no selection efficiencies need to be measured, the variable ranges are completely relaxed, allowing the algorithm more freedom to choose a solution. Secondly, because the stripping selection (see Table 5.2) is much tighter than in the case of the cross-section measurement, more data (both signal and background) is required for the optimisation. Finally, a few more variables are added because of the longer decay chain (now that the D^0 is reconstructed from a D^* decay), and to increase discriminating power between signal and background (the full list can be found in Table 5.2).

Optimisation is performed using a sample of 10 million Monte Carlo signal events to model the signal distributions, while the background distributions are taken directly from the D^0 mass sidebands of $\sim 37\,\text{pb}^{-1}$ of collision data collected in 2010 at an energy $\sqrt{s} = 7\,\text{TeV}$. The sidebands begin at $35\,\text{MeV}/c^2$ either side of the D^0 mass, and are $30\,\text{MeV}/c^2$ wide. After the stripping selection is applied, $\sim$ 30k signal and $\sim$ 120k background candidates remain. Although there will be a small fraction of signal decays within the data sidebands, the only effect will be a sub-optimal event selection (*i.e.* there will be no bias to the analysis results, only the sensitivity will be affected).

The signal significance, $\frac{\text{signal}}{\sqrt{\text{signal+background}}}$, is used as the figure of merit for the optimisation. It is vital that the numbers of signal and background events are scaled so that their ratio matches that found in data. To find the ratio of signal and background yields, a

two-dimensional fit to the m_{D^0} vs. Δm distribution is performed on a sample ($\sim 10\%$) of the 2010 dataset. The data are fitted with a PDF consisting of the following four components:

- **Signal:** Events that peak in both the m_{D^0} and Δm projections.
- **Random $\boldsymbol{\pi_s}$ background:** Events that peak in the m_{D^0} projection but not the Δm projection. These are true D^0s which have been paired with random background pions to produce a false D^* vertex.
- **Fake $\boldsymbol{D^0}$ background:** Events that peak only in the Δm projection. These are predominantly events where two of the D^0 daughter tracks have been misidentified.
- **Combinatorial background:** Events which peak in neither the D^0 projection nor the Δm projection.

The signal distribution in the m_{D^0} projection is modelled by the sum of a Gaussian and a Crystal Ball function, where the two functions share a common mean. A similar function is used to model the signal distribution in the Δm projection, except that the Crystal Ball tail is on the opposite (right-hand) side. Background in the m_{D^0} projection is described by a first order polynomial, while the background in the Δm projection is modelled by the *RooDstD0BG* PDF, defined as

$$P\left(\Delta m\right) \propto \begin{cases} \left(1 - e^{-\frac{\Delta m - \Delta m_0}{C}}\right)\left(\frac{\Delta m}{\Delta m_0}\right)^A + B\left(\frac{\Delta m}{\Delta m_0} - 1\right) & \text{if } \Delta m > \Delta m_0 \\ 0 & \text{if } \Delta m < \Delta m_0 \end{cases} \tag{5.5}$$

where A, B and C are free parameters, and Δm_0 is the threshold mass, which should be equal to the pion mass, although it is allowed to float in the fit.

The result of the fit[3], with all components, is shown in Figure 5.2. The fitted yields of signal and background are used to scale the number of signal and background events used in the optimisation so that the ratio of signal to background is consistent with the

[3]Note that the fit performed here is for the purpose of the event selection optimisation. The main fit procedure used for the signal yield extraction is detailed in Section 5.5.

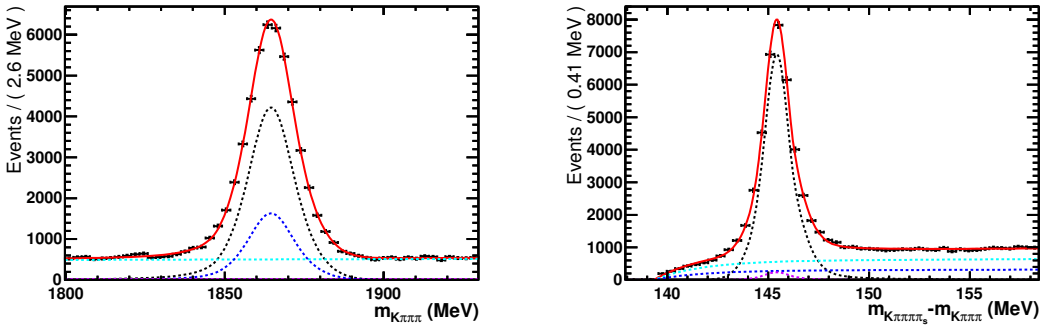

(a) (b)

Figure 5.2: (a) m_{D^0} and (b) Δm projections of the two-dimensional fit to 2010 collision data. The total PDF is represented by the solid red line. Dashed lines show the four individual components: signal (black), random π_s background (blue), fake D^0 background (magenta), and combinatorial background (cyan).

ratio measured using the collision data. A further factor of 0.323% is used to scale the number of signal events, which is the ratio of WS to RS branching fractions [52]. This allows optimisation for the WS mode, instead of the RS mode, and forces the genetic algorithm to choose a much tighter set of criteria. The list of selection criteria chosen by the genetic algorithm can be found in Table 5.2.

Table 5.2: $D^0 \to K^-\pi^+\pi^-\pi^+$ selection criteria used in the stripping selection, and in the genetic algorithm selection.

	Variable name	Stripping	Genetic algorithm
$h^\pm$	Track χ^2/N_{dof}	< 4	—
	IP χ^2	> 3.0, —, —, 30	$> 3.1, 6, 8, 35$
	p_{T}	$> 350\,\text{MeV}/c$	$> 360, 450, 620, 800\,\text{MeV}/c$
	$\lvert\vec{p}\rvert$	$> 3\,\text{GeV}/c$	$> 3.1, 3.2, 4.2, 4.8\,\text{GeV}/c$
K^-	$\log(\mathcal{L}_K/\mathcal{L}_\pi)$	> 0	—
$\pi^\pm$	$\log(\mathcal{L}_K/\mathcal{L}_\pi)$	< 3	—
D^*	Vertex χ^2/N_{dof}	< 20	< 8.5
	DoCA	$< 0.22\,\text{mm}$	$< 0.15\,\text{mm}$
	p_{T}	$> 3\,\text{GeV}/c$	—
π_s	p_{T}	$> 120\,\text{MeV}/c$	$> 180\,\text{MeV}/c$
D^0	Vertex χ^2/N_{dof}	< 10	< 2
h_ih_j pair	*DoCA*	$< 0.12\,\text{mm}$	$< 0.10\,\text{mm}$
	p_{T}	$> 3.0\,\text{GeV}/c$	$> 3.1\,\text{GeV}/c$
	FD χ^2	> 48	> 56
	$IP\chi^2$	< 30	—
	DIRA	> 0.99980	> 0.99997
	Mass window	$\lvert m - m_{\text{PDG}}\rvert < 65\,\text{MeV}/c^2$	—

In addition to the genetic algorithm, further selection requirements are imposed. Charm mesons that originate from decays of $b-$hadrons, instead of the primary vertex, are likely

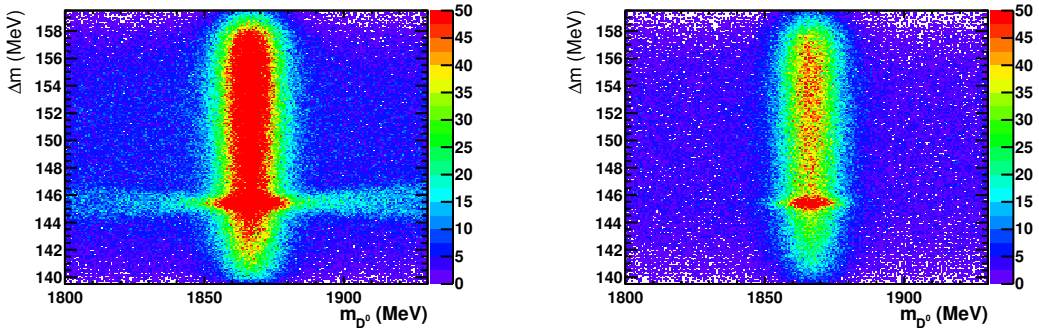

(a) (b)

Figure 5.3: Two dimensional Δm vs. m plane for wrong sign events (a) before and (b) after the double misidentification veto and tightened PID cuts for the 2011 dataset. The colour axis is capped at 50 entries per bin to improve the contrast between bins with lower populations.

to have a biasing effect on the measured time dependent ratio $R(t)$. To minimise the impact of this so-called "secondary background", a tighter cut is placed on the D^0 $\log_{10}(IP\chi^2)$ (see Section 5.6.1 for more details).

A RS decay may be wrongly identified as a WS decay if the kaon is misidentified as a pion and one of the pions is misidentified as a kaon (called a double mis-ID). This is the predominant source of peaking background in the Δm projection, and without any suppression it overwhelms the WS signal peak. The majority of double mis-IDs are removed by imposing tighter PID requirements on the three D^0 daughter pions ($\log(\mathcal{L}_K/\mathcal{L}_\pi) < 0$), as well as vetoing any candidates that lie within a $24\,\text{MeV}/c^2$ window about the D^0 mass peak when the mass hypothesis of the kaon is swapped with any of the three pions (discussed in Section 5.6.2). A Monte Carlo study reveals that the veto leaves only 0.68% of double- mis-IDs and is 70% efficient for signal events. Figure 5.3 shows the Δm vs. m plane before and after the tighter PID requirements and the double mis-ID veto. After the requirements, the double mis-ID component (which peaks in Δm but not m_{D^0}) is no longer visible.

Finally, for the small number of events that contain multiple signal candidates, all candidates in each event are discarded except the one with the lowest D^0 vertex χ^2/N_{dof} (or the lowest D^* vertex χ^2/N_{dof} if the candidates share the same D^0 vertex).

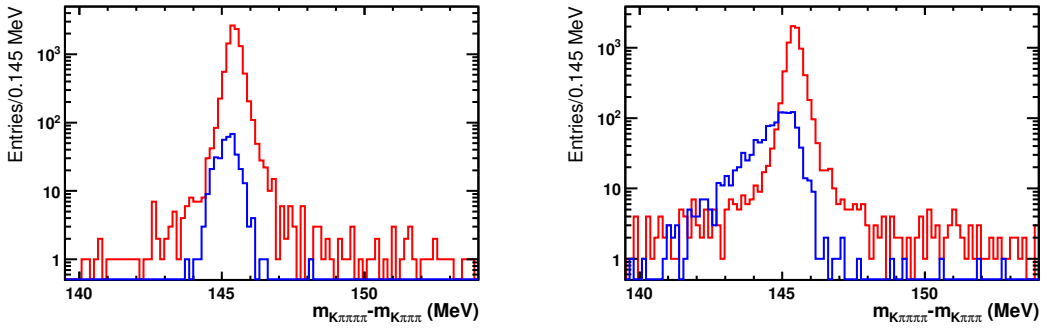

(a) (b)

Figure 5.4: Monte Carlo Δm distributions for (a) D^0 lifetimes below 0.8 ps and (b) above 0.8 ps. Prompt charm decays are shown in red and secondary charm decays are shown in blue.

5.5 Yield extraction

After the selection, the data is split into the four different decays in order to measure the double ratio shown in Equation 5.4. To measure the yield of each decay mode, we perform a one-dimensional unbinned maximum likelihood fit to the Δm distributions, after making a 24 MeV/c^2 mass window (slightly larger than 3σ) cut about the D^0 mass. The mass window requirement removes more of the double mis-ID events, as well as a large proportion of the combinatorial background.

To improve the resolution of the Δm peak, the Decay Tree Fitter (DTF) algorithm is used, which is similar to software used by the BABAR collaboration [69]. Instead of first reconstructing the D^0, followed by the D^*, the DTF algorithm takes into account the whole decay chain and fits all of the parameters (vertex positions, momenta and decay lengths) simultaneously, with the added constraint that the D^* must originate from a primary vertex. While this significantly improves the Δm resolution, because of the primary vertex constraint, Δm values from secondary decays are systematically shifted to lower values, especially at large values of measured D^0 lifetime[4]. This so-called "secondary shoulder" is shown in Figure 5.4 for Monte Carlo signal events.

The Δm signal distribution is modelled by the sum of a Johnson function [70] and three Gaussians, each with independent means and widths. The Johnson function is defined as

[4]The lifetime of the D^0 is always measured as if it originated from a primary vertex.

$$J\left(\Delta m\right) \propto \frac{\exp\left(-\frac{1}{2}\left[\gamma + \delta \sinh^{-1}\left(\frac{\Delta m - \mu}{\sigma}\right)\right]\right)}{\sqrt{1 + \left(\frac{\Delta m - \mu}{\sigma}\right)^2}} \tag{5.6}$$

where γ, δ, μ and σ are floating parameters. The background is modelled with

$$B\left(\Delta m\right) \propto \left(\left(\Delta m - \Delta m_0\right) + a\left(\Delta m - \Delta m_0\right)^2\right)^b \tag{5.7}$$

where the parameters a and b are allowed to float, but Δm_0 is fixed to the pion mass. Peaking background is ignored in the fit, and is instead treated as a systematic uncertainty (see Section 5.6.2). The signal and background PDFs can be seen in Figures 5.5 and 5.6.

Because the RS samples are completely dominated by signal events, the tails of the signal make it difficult to fit the background component. Conversely in the WS samples, because the WS signal peak is so small, it is difficult to constrain the tails of the signal shape. Therefore, we fit each of the four samples simultaneously, sharing all parameters of the signal and background PDFs, but allowing the yields of signal and background to float. This means that the signal shape is well constrained from the RS samples, and the WS samples help to constrain the background shape. The ratios of components within the signal PDF (the Johnson function and the three Gaussians) are also shared between the four different samples, so that the total signal PDF remains the same for each decay mode.

First, the entire dataset in the range $0.5\tau < t < 10.0\tau$ is fit[5], where $\tau = 0.4101\,\text{ps}$ is the mean D^0 lifetime [52] (fits to the RS and WS modes can be found in Figures 5.5 and 5.6). Then the fit is repeated in each of the τ bins (shown in Appendix B). All of the parameters of the Gaussian that peaks furthest to the right are Gaussian constrained to their values from the fit to the total data sample (including the mean, width and signal fraction) to improve the stability of the fits in each of the lifetime bins. The parameters of the other two Gaussians are allowed to float to account for the variation of the secondary shoulder. A list of measured signal yields for the four different decays

[5]Below 0.5τ the detector acceptance is too low, and above 10.0τ there are too few events.

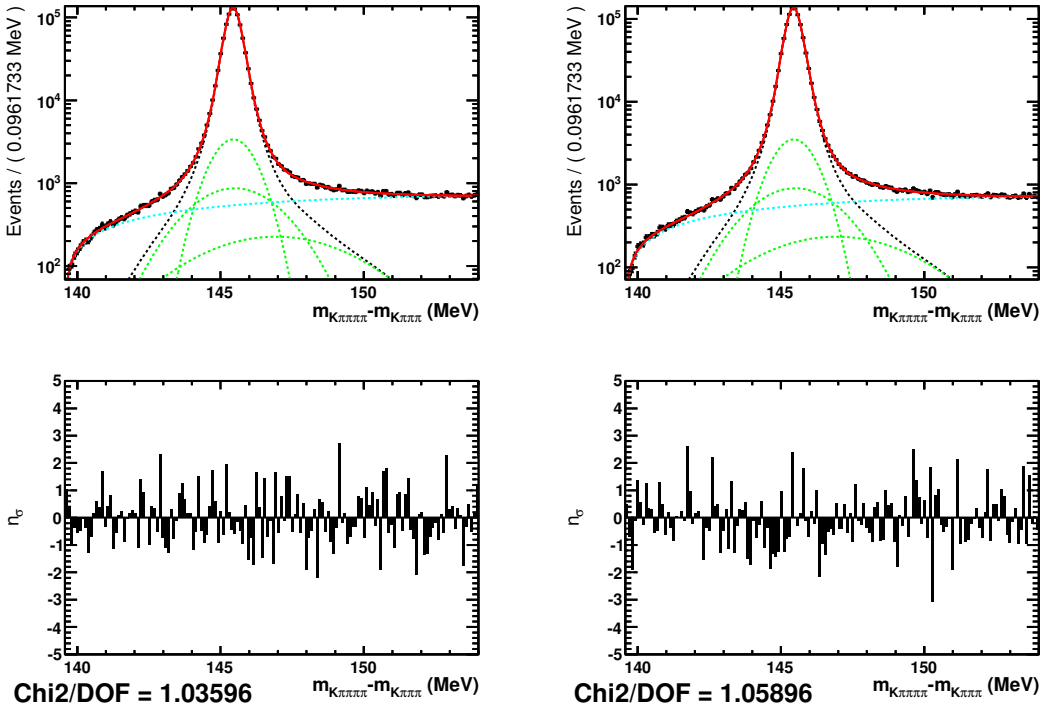

Figure 5.5: Fits for the RS decay modes $D^0 \to K^-\pi^+\pi^-\pi^+$ (top left), and $\overline{D}^0 \to K^+\pi^-\pi^+\pi^-$ (top right). The total PDF is shown in solid red. The dashed lines represent the background (cyan), the total signal component (black) and the three individual Gaussian signal components (green). Underneath each of the fits is the corresponding pull distribution.

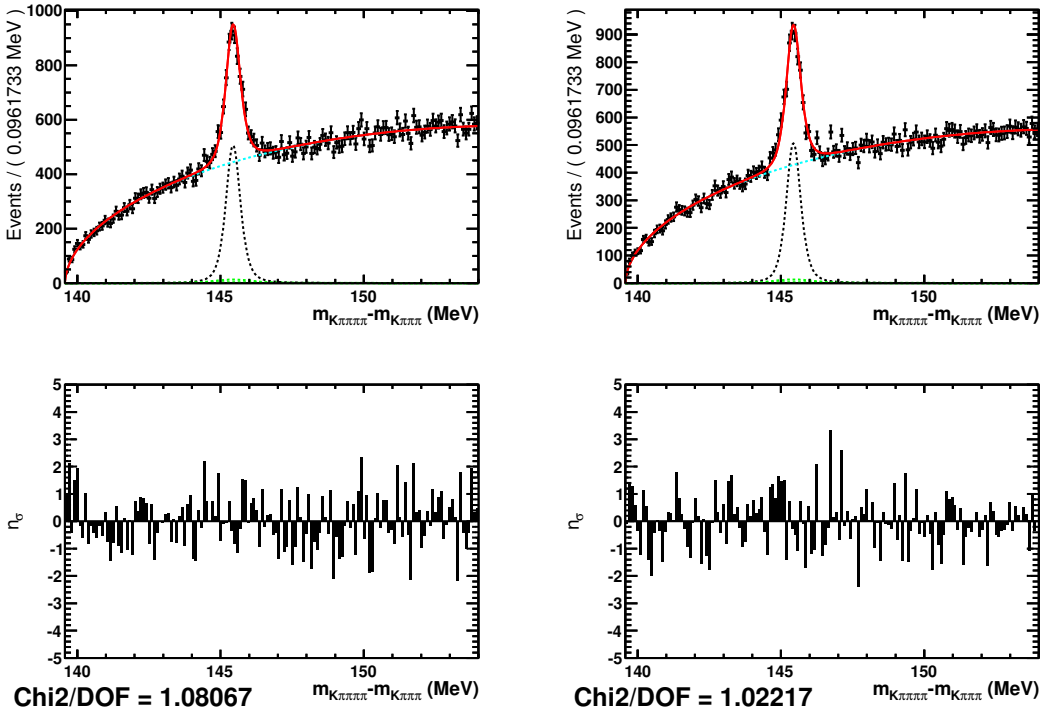

Figure 5.6: Fits for the WS decay modes $D^0 \to K^+\pi^-\pi^+\pi^-$ (top left), and $\overline{D}^0 \to K^-\pi^+\pi^-\pi^+$ (top right), shown above their pull distributions.

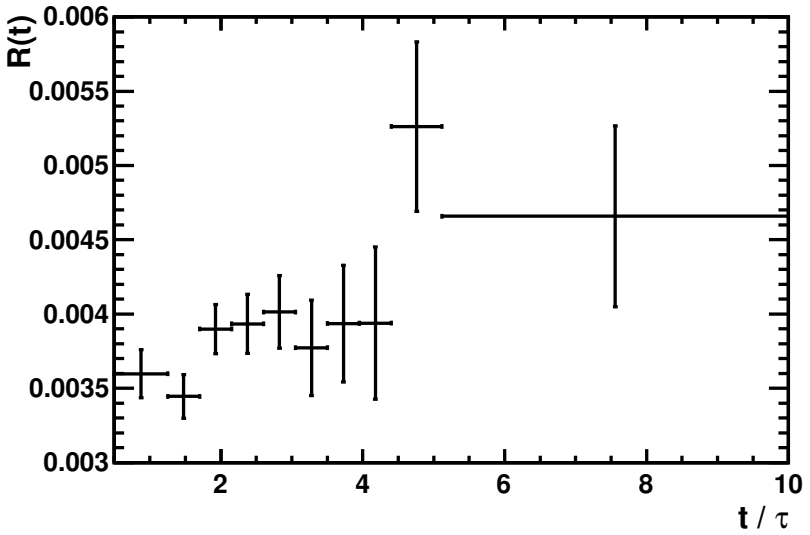

Figure 5.7: The measured WS/RS ratio as a function of D^0 lifetime.

modes is shown in Table 5.3. The yields are used to produce the time dependent WS/RS ratio $R(t)$, using Equation 5.4, which is shown in Figure 5.7.

Table 5.3: Signal yields for the four different decay modes in bins of D^0 lifetime. The yields from the fit to the entire lifetime range are shown at the bottom.

t/τ range	RS D^0	WS D^0	RS $\overline{D}^0$	WS $\overline{D}^0$
$(0.50, 1.25)$	164781 ± 426	651 ± 38	169832 ± 432	557 ± 37
$(1.25, 1.70)$	224304 ± 508	732 ± 47	233499 ± 520	850 ± 47
$(1.70, 2.15)$	193502 ± 475	801 ± 46	200327 ± 484	736 ± 45
$(2.15, 2.60)$	138839 ± 402	587 ± 40	144707 ± 411	530 ± 39
$(2.60, 3.05)$	93917 ± 334	405 ± 34	98334 ± 342	367 ± 32
$(3.05, 3.50)$	61406 ± 287	195 ± 27	64385 ± 295	288 ± 28
$(3.50, 3.95)$	39051 ± 218	148 ± 22	41004 ± 224	168 ± 22
$(3.95, 4.40)$	25121 ± 178	83 ± 17	25964 ± 182	121 ± 19
$(4.40, 5.12)$	22364 ± 164	126 ± 18	23271 ± 168	114 ± 18
$(5.12, 10.00)$	20026 ± 155	90 ± 17	20830 ± 158	100 ± 18
$(0.50, 10.00)$	983091 ± 1288	3818 ± 106	1021931 ± 1322	3825 ± 104

5.6 Corrections to the lifetime distribution

During the signal yield extraction, peaking background and contamination from secondary D decays are ignored, both of which are potential sources of bias. To account for this, the lifetime distribution of the measured WS/RS ratio must be corrected. A measurement of the expected number of peaking background events is used to correct

the value of the ratio in each lifetime bin, while the secondary contamination correction is applied to the PDF used to fit the lifetime dependence of the WS/RS ratio. Both procedures are described in the following sections.

5.6.1 Secondary background

Because the D^0 lifetime is computed with respect to the primary vertex, any that originate from decays of $b-$hadrons will have incorrectly measured lifetimes. This may introduce a bias to the time dependent WS/RS ratio. Without any correction, the measured ratio of WS/RS can be written as [71]

$$\begin{aligned} R^m(t) &= \frac{N^{WS}(t) + N_B^{WS}(t)}{N^{RS}(t) + N_B^{RS}(t)} && (5.8) \\ &= R(t)\left[1 + f_B^{RS}(t)\left(\frac{R_B(t)}{R(t)}\right)\right] && (5.9) \\ &= R(t)\left[1 - \Delta_B(t)\right] && (5.10) \end{aligned}$$

where $N^{WS}(t)$ and $N^{RS}(t)$ are the time dependent number of promptly produced WS and RS decays, $N_B^{WS}(t)$ and $N_B^{RS}(t)$ are the number of WS and RS decays originating from a secondary vertex, $R(t) = \frac{N^{WS}(t)}{N^{RS}(t)}$ is the time dependent ratio of prompt charm decays (the value we are ultimately interested in), $R_B(t) = \frac{N_B^{WS}(t)}{N_B^{RS}(t)}$ is the time dependent ratio of secondary charm decays,

$$f_B^{RS}(t) = \frac{N_B^{RS}(t)}{N^{RS}(t) + N_B^{RS}(t)} \tag{5.11}$$

is the time dependent secondary fraction in the RS sample, and

$$\Delta_B(t) = f_B^{RS}(t)\left(1 - \frac{R_B(t)}{R(t)}\right) \tag{5.12}$$

is the time dependent bias, arising from the secondary contamination. Calculation of $R_B(t)$ involves measuring the secondary fraction in WS decays, which is incredibly difficult because of the level of background. However, it is possible to bound $\Delta_B(t)$ on both sides, without $R_B(t)$.

Because the reconstructed D^0 lifetime for secondary events is always an overestimation, at time t the value of $R_B(t)$ must be within the range of values of $R(t)$ up to time t. It follows that

$$R_{\min}(t) \leq R_B(t) \leq R_{\max}(t) \tag{5.13}$$

where $R_{\min}(t)$ and $R_{\max}(t)$ are the minimum and maximum values of $R(t)$ up to time t. Multiplying Equation 5.13 by $\frac{f_B^{RS}(t)}{R(t)}$ and rearranging gives

$$f_B^{RS}(t)\left[1-\frac{R_{\max}(t)}{R(t)}\right] \leq \Delta_B(t) \leq f_B^{RS}(t)\left[1-\frac{R_{\min}(t)}{R(t)}\right]. \tag{5.14}$$

We take the upper limit as the systematic correction to the measured ratio.

To calculate $f_B^{RS}(t)$, we use the D^0 $\log_{10}(IP\chi^2)$ variable to measure the yield of prompt and secondary events in each of the lifetime bins. The ${}_s\mathcal{P}lot$ technique is used to extract the signal $\log_{10}(IP\chi^2)$ distributions from unbinned maximum likelihood fits to the Δm distribution of all RS events (both flavours) in each lifetime bin, before the tighter $\log_{10}(IP\chi^2)$ cut is applied. The resulting distributions are fit with two components, one for the prompt contribution, and one for the secondary contribution.

The prompt component is modelled with a sum of two bifurcated Gaussians[6], each with a common mean. Because prompt charm mesons originate from the primary vertex (by definition), it can be assumed that their $\log_{10}(IP\chi^2)$ distribution does not depend on the D^0 lifetime. Therefore all of the bifurcated Gaussian parameters are fixed from a fit to the $\log_{10}(IP\chi^2)$ distribution in the first D^0 lifetime bin (Figure 5.9(a)), in which the secondary fraction is assumed to be negligible. This assumption is considered in Section 5.8.1.

The secondary component is modelled as follows. A sample of $B^+ \to \overline{D}^0\pi^+$ events is reconstructed, and selected with the same criteria as for the prompt sample (except for the removal of cut on the D^0 $IP\chi^2$). An unbinned maximum likelihood fit is performed on the B^+ invariant mass distribution of the whole sample, with three components:

- a Gaussian for the signal

[6] A bifurcated Gaussian has a different width either side of the peak.

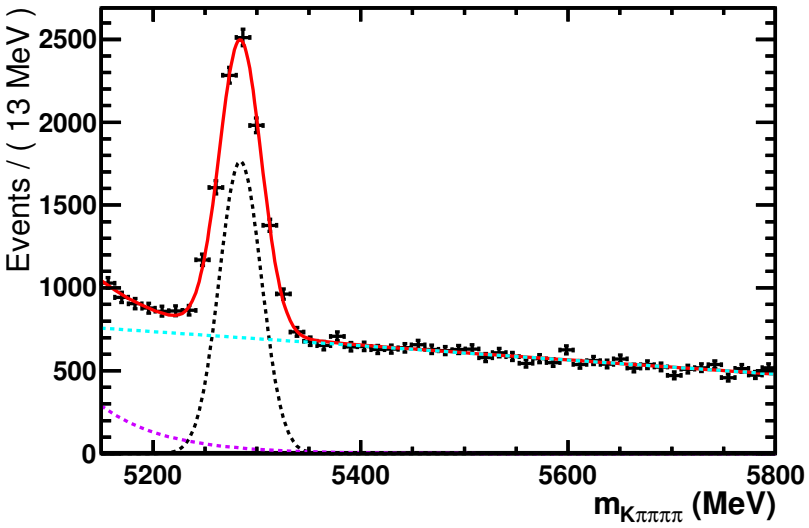

Figure 5.8: Fit to the $B^+ \to \overline{D}^0\pi^+$ invariant mass spectrum. The total PDF is shown by the solid red line. The dashed lines represent: signal (black), partially reconstructed physics background (magenta), and combinatorial background (cyan).

- an exponential function for partially reconstructed physics background (see Section 2.2.9.1)
- a first order polynomial for combinatorial background.

The fit is shown in Figure 5.8. All of the shape parameters are then fixed, before fitting the B^+ mass distribution in each lifetime bin, again using the ${}_s\mathcal{P}lot$ technique to extract the signal D^0 $\log_{10}(IP\chi^2)$ distributions. A single bifurcated Gaussian is used to fit the resulting secondary $\log_{10}(IP\chi^2)$ distributions. Unlike the prompt $\log_{10}(IP\chi^2)$ distribution, we expect the secondary distribution to shift to the right in the high D^0 lifetime bins.

Finally, using the prompt $\log_{10}(IP\chi^2)$ shape (fixed from the first lifetime bin), and the secondary shapes (fixed from the fits to the $B^+ \to \overline{D}^0\pi^+$ data), the secondary fraction (f_B^{RS}) can be measured in each lifetime bin by floating the yields of the prompt and secondary components, using Equation 5.11, with an uncertainty

$$\sigma_B = \frac{1}{\left(N^{RS} + N_B^{RS}\right)^2}\sqrt{\left(N_B^{RS}\right)^2\sigma^2_{N^{RS}} + \left(N^{RS}\right)^2\sigma^2_{N_B^{RS}}}. \tag{5.15}$$

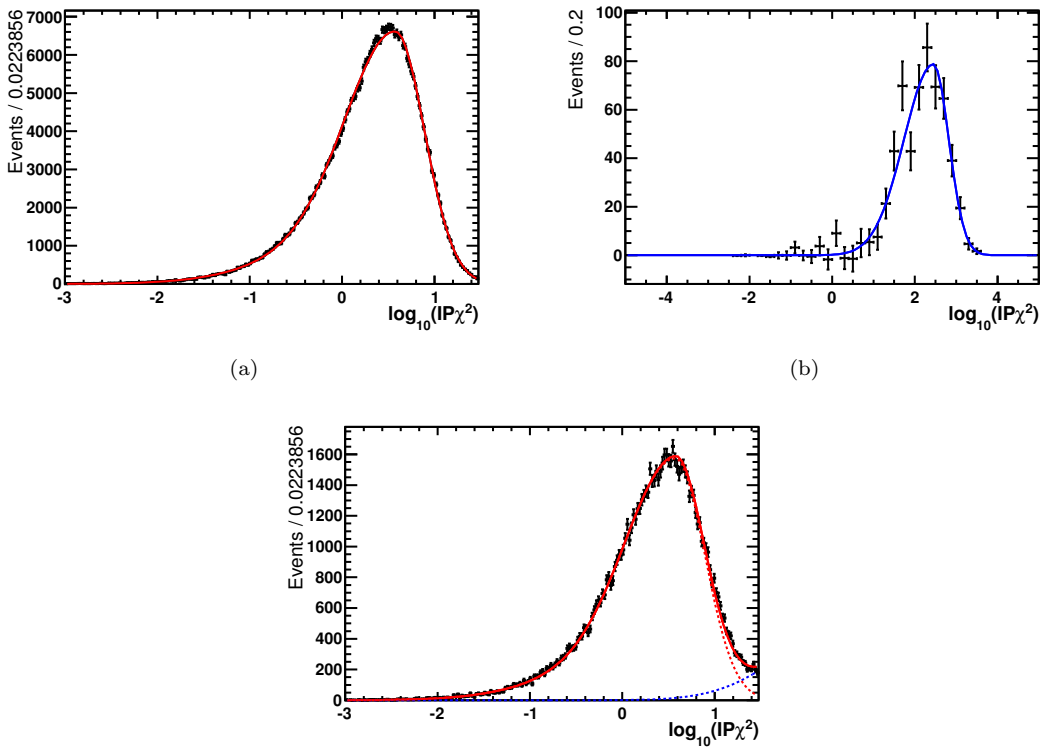

Figure 5.9: An example of the $\log_{10}(IP\chi^2)$ fits used to extract the fraction of secondary decays in lifetime bin $3.50 < t/\tau < 3.95$. (a) shows a fit to data in the first lifetime bin, which is used to model the prompt shape; (b) is a fit to $B^+ \to \overline{D}^0\pi^+$ events in the bin $3.50 < t/\tau < 3.95$, used as the secondary shape; and (c) is the fit to measure the secondary fraction in the RS D^* sample, using the fit parameters from (a) and (b), but allowing the prompt and secondary yields to float.

The fit to the $\log_{10}(IP\chi^2)$ distribution in the first lifetime bin of the D^* sample is shown in Figure 5.9(a), followed by an example fit to the $\log_{10}(IP\chi^2)$ distribution from the $B^+ \to \overline{D}^0\pi^+$ sample in one of the higher lifetime bins ($3.50 < t/\tau < 3.95$). These two fits provide the shape parameters for a fit to the $\log_{10}(IP\chi^2)$ distribution in the range $3.50 < t/\tau < 3.95$ (see Figure 5.9(c)). The resulting secondary fractions for all lifetime bins are shown in Figure 5.10(a). All fits in bins of lifetime including the B^+ mass fits, the secondary $\log_{10}(IP\chi^2)$ fits, and the $\log_{10}(IP\chi^2)$ fits for the D^* sample, can be found in Appendix B.

In order to minimise the secondary correction, Δ_B, a tighter cut is placed on the D^0 $\log_{10}(IP\chi^2)$ variable to remove a significant fraction of secondary events. However, cutting too tightly will result in the loss of a large fraction of prompt events too, increasing the fractional statistical uncertainty. To find the optimum value, the total fractional

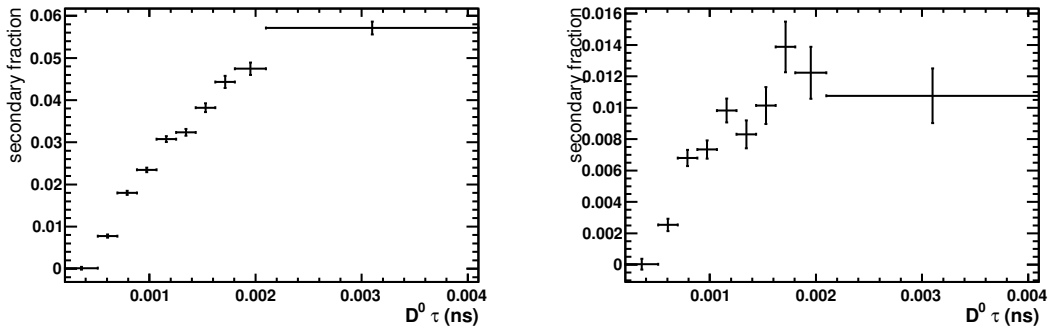

(a) (b)

Figure 5.10: Measured secondary fractions (a) before, and (b) after the tighter $\log_{10}(IP\chi^2)$ cut.

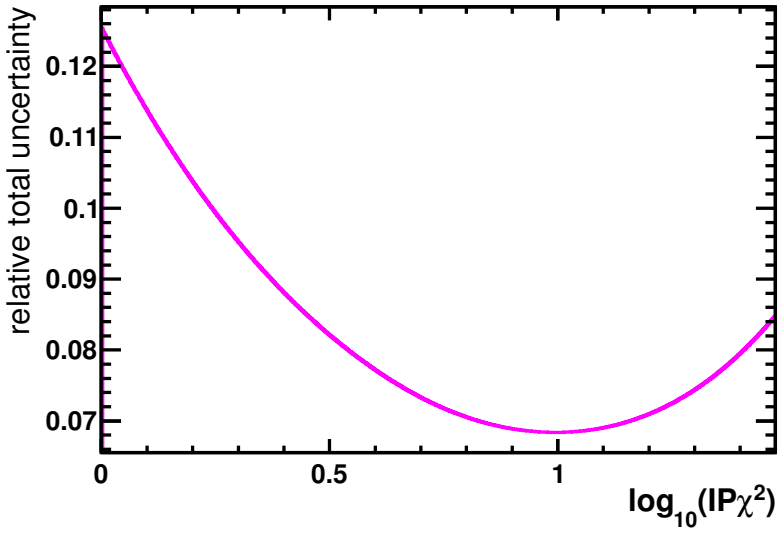

Figure 5.11: The total uncertainty arising from the statistical uncertainty due to the number of WS events, and the systematic uncertainty due to secondary contamination, as a function of a cut on the D^0 $\log_{10}(IP\chi^2)$. The units on the vertical axis arbitrary.

uncertainty is estimated for a large range of possible cut values, for the highest lifetime bin, considering only the secondary systematic and assuming the statistical uncertainty is dominated by the number of WS events. The resulting distribution, shown in Figure 5.11, reveals that the cut should be tightened to D^0 $\log_{10}(IP\chi^2) < 1.0$. The tighter cut is applied before the final yields are extracted.

The final values of f_B^{RS}, shown in Figure 5.10(b), are used to modify the χ^2 of the lifetime fit (see Section 5.7 for details).

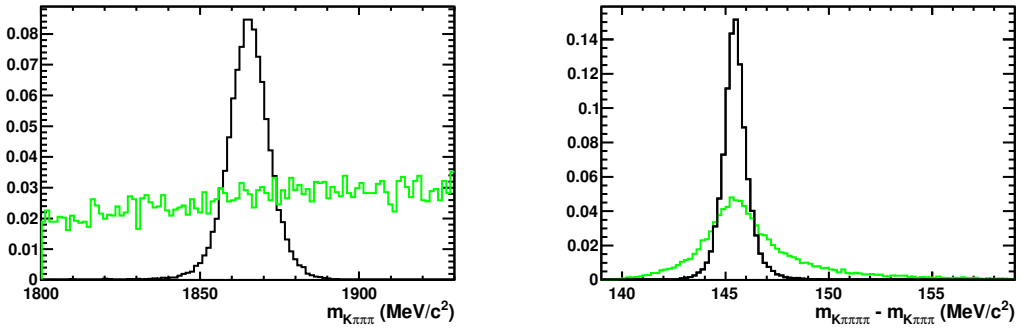

(a) (b)

Figure 5.12: Normalised (a) m_{D^0} and (b) Δm distributions of Monte Carlo signal (black) and double mis-ID events (green). The double mis-ID distribution is scaled by a factor of ten in the m_{D^0} distribution so that it is more easily visible.

5.6.2 Peaking background

The dominant source of peaking background in the Δm distribution of WS events arises from RS events in which two of the D^0 daughters are misidentified. If the kaon is mistaken for a pion, and one of the pions of opposite charge is misidentified as a kaon, a RS decay will be incorrectly reconstructed as a WS candidate, and vice versa. Although the mis-ID rate is low, and consequently the double mis-ID is even lower, the RS branching fraction is two orders of magnitude higher than the WS branching fraction, so double mis-ID background cannot be ignored when measuring the WS signal yield. The background has an almost flat distribution in m_{D^0} but peaks in Δm (see Figure 5.12), which is the variable used in the yield extraction.

The double mis-ID distributions are simulated using a sample of Monte Carlo $D^0 \to K^-\pi^+\pi^-\pi^+$ signal events. First the kaon energy is recalculated under the pion mass hypothesis, then the energy of one of the pions is recomputed under the kaon mass hypothesis, and finally the invariant mass of the D^0 is determined. This is shown over a much wider mass range in Figure 5.13(b). To study the effect of single mis-ID background, $D^0 \to K^+K^-\pi^+\pi^-$ and $D^0 \to \pi^+\pi^-\pi^+\pi^-$ Monte Carlo signal decays are used. In each case one daughter track mass hypothesis is changed before recalculating the D^0 invariant mass, in order to simulate a single mis-ID. The resulting distributions are shown in Figure 5.13(a).

To minimise the double mis-ID background, three steps are taken:

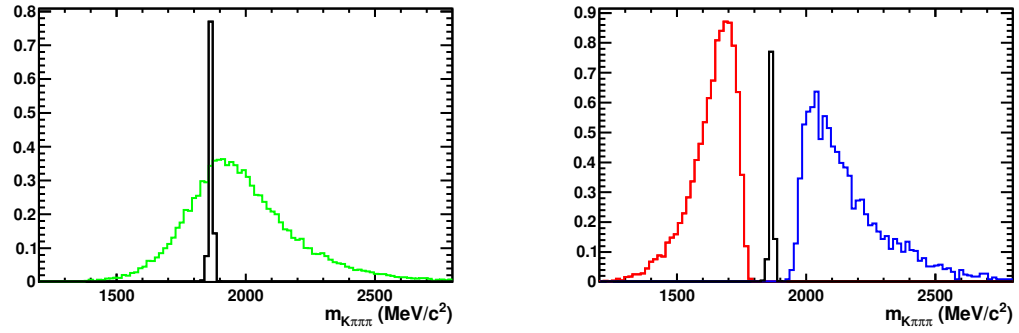

(a) (b)

Figure 5.13: Normalised invariant mass distributions, shown over a wide mass range, when misidentifying (a) two daughter tracks, and (b) one daughter track. The green line shows the effect of swapping the hypothesis of a kaon and a pion, using $D^0 \to K^-\pi^+\pi^-\pi^+$ Monte Carlo signal decays. The red and blue lines represent $D^0 \to K^+K^-\pi^+\pi^-$ and $D^0 \to \pi^+\pi^-\pi^+\pi^-$ Monte Carlo signal decays that are reconstructed as $D^0 \to K^-\pi^+\pi^-\pi^+$ decays. In both plots the $D^0 \to K^-\pi^+\pi^-\pi^+$ signal distribution is shown in black, and the mis-ID distributions are scaled by a factor of ten so they are more easily visible.

1. PID requirements on each of the three D^0 daughter pions is made more strict. This reduces the probability of a pion being misidentified as a kaon, and therefore reduces the double mis-ID probability.

2. D^0 candidates are deliberately doubly misidentified and vetoed if their reconstructed D^0 mass lies within a $24\,\text{MeV}/c^2$ window of the nominal D^0 mass. By swapping the mass hypotheses of a kaon and a pion, signal events become very broadly distributed in D^0 invariant mass, whereas double mis-ID background events peak very sharply (which is exactly opposite to how they are both distributed before the mass hypothesis switch). Therefore, the veto is extremely efficient at removing double mis-ID background while retaining the majority of signal events. The efficiencies are measured as 0.68% for the background and 70% for the signal, using Monte Carlo events.

3. A tight D^0 mass window of $\pm 24\,\text{MeV}/c^2$ (slightly larger than 3σ) is imposed before the yields are extracted from the fits to the Δm distributions. This removes approximately 60% of the remaining double mis-ID background, and all of the single mis-ID background, which peaks far from the mass of the D^0.

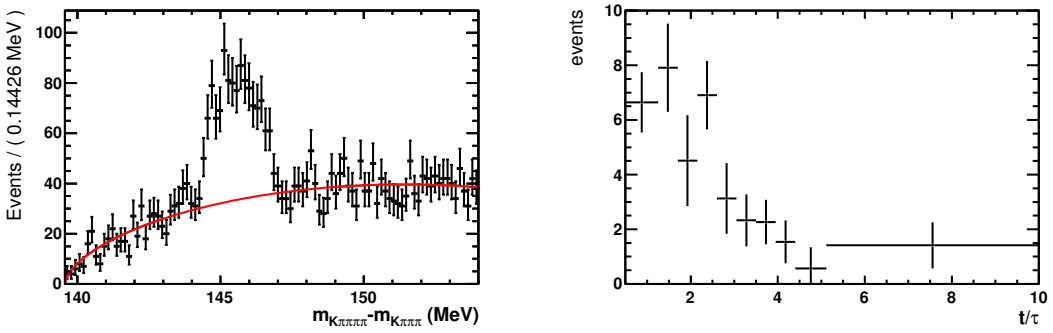

(a) (b)

Figure 5.14: (a) A fit to determine the number of mis-ID events in the second bin of the WS sample. (b) The expected number of mis-ID events remaining in each lifetime bin, after all of the selection criteria.

Although the majority of double mis-ID events are removed, a small fraction remain in the WS sample (the remaining fraction in the RS sample from doubly misidentified WS decays can be safely neglected). Because they are ignored in the Δm fits, they are accounted for by applying a correction factor to the measured number of WS events in each lifetime bin.

To measure the expected number of double mis-ID events, we use events (after the tightened PID criteria are applied) from the right-hand side of the WS D^0 mass distribution ($m_{D^0} > 1900.0\,\mathrm{MeV}/c^2$). This is far enough from the D^0 peak to contain a negligible number of signal events. The Δm distribution for these events is fit with the background PDF (Equation 5.7), while excluding the data in the peak region, $143.0 < \Delta m < 149.0\,\mathrm{MeV}/c^2$, from the fit. An example fit is shown in Figure 5.14(a), where the peaking background is much wider than the signal peak, as expected (compare to Figure 5.6). The number of events is then calculated by subtracting the integral of the PDF from the number of entries in the histogram. This number is multiplied by 0.68% (the veto background rejection efficiency), and scaled to take account of the mass window cut, assuming the mis-IDs are flatly distributed in the $\mathrm{m_{D^0}}$ distribution. The process is repeated in each of the lifetime bins.

The number of expected double mis-ID events in each of the lifetime bins is shown in Figure 5.14(b). This number is used to correct the ratio of WS/RS events in each bin using

$$\frac{N^{WS}}{N^{RS}} = \frac{N_m^{WS}}{N^{RS}} - \frac{N^{\text{misID}}}{N^{RS}} \tag{5.16}$$

where N_m^{WS} is the number of measured WS events, and N^{misID} is the number of expected mis-ID events remaining after all selection criteria. The uncertainty is propagated from the uncertainty on the integral of the PDF, and is added in quadrature with the statistical uncertainty. The corrections are found to be between 0.2% and 0.8%.

5.7 Fitting the lifetime distribution

Once the WS/RS ratio is measured in each of the ten lifetime bins, a fit to the lifetime distribution is performed by minimising the following χ^2

$$\chi^2 = \sum_i \left(\frac{r_i - R\left(t_i\right)\left[1 - \Delta_B\left(t_i\right)\right]}{\sigma_i} \right)^2 + \chi_B^2 + \chi_{x,y}^2 \tag{5.17}$$

where r_i and σ_i are the measured value and uncertainty of the mis-ID corrected WS/RS ratio in lifetime bin i, and Δ_B is the secondary background correction factor, given by the upper limit of Equation 5.14. The penalty term χ_B^2 comes from constraining the measured secondary fractions within their uncertainties,

$$\chi_B^2 = \sum_i \left(\frac{f_B^{RS}\left(t_i\right) - f_B^i}{\sigma_B\left(t_i\right)} \right)^2 \tag{5.18}$$

where $f_B^{RS}\left(t_i\right)$ is the RS secondary fraction measured in lifetime bin i, with an uncertainty σ_B, and f_B^i are fit parameters. The second penalty term, $\chi_{x,y}^2$, arises from constraining the mixing parameters x and y to their PDG values [72], and is given by

$$\chi_{x,y}^2 = \begin{pmatrix} \Delta x & \Delta y \end{pmatrix} \begin{pmatrix} \frac{1}{\sigma_x^2} & \frac{\rho_{x,y}}{\sigma_x \sigma_y} \\ \frac{\rho_{x,y}}{\sigma_x \sigma_y} & \frac{1}{\sigma_y^2} \end{pmatrix} \begin{pmatrix} \Delta x \\ \Delta y \end{pmatrix} \tag{5.19}$$

where

$$\Delta x = x - x_{\text{PDG}}\,, \quad \Delta y = y - y_{\text{PDG}} \tag{5.20}$$

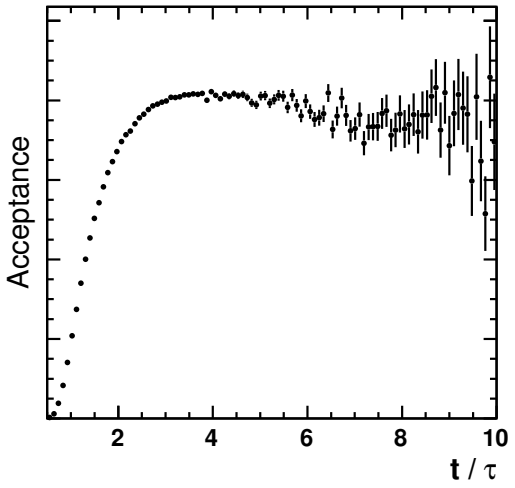

Figure 5.15: Acceptance as a function of D^0 lifetime, measured with RS events. The vertical scale is not important because it cancels in the expression for $R(t_i)$.

and

$$\rho(x,y) = \frac{\mathrm{cov}(x,y)}{\sigma_x \sigma_y}. \tag{5.21}$$

The uncertainties and correlations are taken from the Heavy Flavour Averaging Group (HFAG) [73].

$R(t_i)$ is the WS/RS ratio integrated over lifetime bin i. Because the decay time acceptance is not flat, and we have to assume that the D^0 lifetime distributions are different for WS and RS decays, $R(t_i)$ is given by the expression

$$R(t_i) = \frac{\int_{t_i} R'(t)\, A(t)\, e^{-\Gamma t} \mathrm{d}t}{\int_{t_i} A(t)\, e^{-\Gamma t} \mathrm{d}t}. \tag{5.22}$$

Here $\Gamma = 1/\tau$, $A(t)$ is the decay time acceptance, and $R'(t)$ is given by

$$R'(t) = r_D^2 + r_D b \Gamma t + \frac{x^2 + y^2}{4} (\Gamma t)^2 \tag{5.23}$$

where r_D and b are allowed to float in the fit. The decay time acceptance is measured by dividing the RS lifetime distribution by $e^{-\Gamma t}$, and is shown in Figure 5.15. Note that the vertical scale is not important because it is a constant term that cancels in Equation 5.22.

In total, there are 14 fit parameters: r_D, b, x, y, and the ten secondary fractions, f_B^i. Only r_D and b are allowed to float fully, while x, y, and f_B^i are Gaussian constrained.

To measure the D^0-$\overline{D}^0$ mixing significance, the WS/RS lifetime distribution is fit with two different functions. Each fit minimises the same χ^2 as in Equation 5.17, but with the removal of the penalty terms for the mixing parameters x and y, and with different forms of $R'(t)$. For the no-mixing hypothesis, the form is

$$R'(t) = A \tag{5.24}$$

while for the mixing hypothesis, it takes the form

$$R'(t) = A + B\Gamma t + C(\Gamma t)^2 . \tag{5.25}$$

5.8 Systematic uncertainties

Because of the efficiency cancellations in the double ratio (Equation 5.4), there are very few sources of systematic uncertainty. We have identified three potential sources of uncertainty which may affect the time dependence of the WS/RS ratio. These are uncertainties that may arise from the corrections described in Section 5.6, and an uncertainty from the choice of signal PDF. In addition, we consider two sources of uncertainty that will have an effect on the measurement of the branching fraction of $D^0 \to K^+\pi^-\pi^+\pi^-$ via the DCS amplitude. These are differences between the resonant substructure of DCS and CF decays, and the uncertainty on the branching fraction of $D^0 \to K^-\pi^+\pi^-\pi^+$.

5.8.1 Secondary background

When measuring the fraction of secondary events in each of the bins, the prompt component of the $\log_{10}(IP\chi^2)$ distribution is assumed to be independent of the D^0 lifetime. To test this assumption, the fits are repeated while floating the prompt component shape parameters. The resulting secondary fractions are compared to those measured with

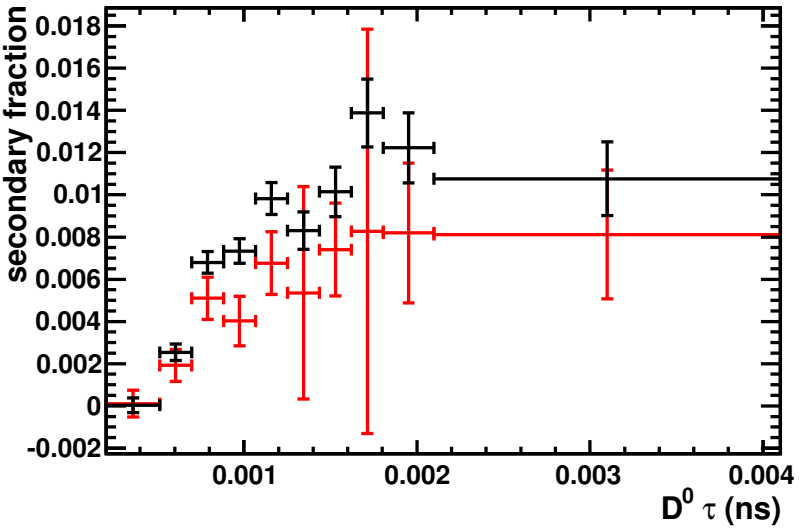

Figure 5.16: Secondary background fractions measured with (red) and without (black) floating the prompt component shape parameters.

those measured using a constant prompt shape in Figure 5.16. Although the agreement between the two sets of results is good, the fractions measured using floating prompt shape parameters are systematically lower. This may be expected because the prompt shape is free to overlap more with the secondary shape, and reduce the size of the secondary component.

To calculate the size of the uncertainty arising from secondary background, the fit to the WS/RS lifetime distribution is performed both with and without the secondary background correction. The difference between the fit results are used as the systematic uncertainties, which are found to be 0.05% of the measured value of r_D, and 2.74% of the value of b. Note that because the maximum value of Δ_B is used in the correction factor, the systematic uncertainty is conservative.

5.8.2 Peaking background

To asses the systematic uncertainties for r_D and b, the fit to the lifetime distribution is performed both with and without the correction for peaking background. The differences between the two results are used as the systematic uncertainties, and are measured as 0.21% of r_D, and 1.52% of b.

5.8.3 Signal model

Because the PDF used to describe the signal component of the Δm fit is fairly arbitrary, we test the robustness of the signal yield extraction by removing one of the three Gaussians from the model and repeating the analysis to extract the parameters r_D and b. The differences between the fit results are 0.56% for r_D, and 66.0% for b.

5.8.4 Dalitz model

Because the amplitude model of the DCS decay $D^0 \to K^+\pi^-\pi^+\pi^-$ is presently unknown, we cannot assume that the distribution of events over the five-dimensional phase space is the same for CF and DCS events. Therefore, a systematic uncertainty is calculated for the $y-$intercept (r_D^2) of the $R(t)$ distribution. Unlike the secondary contamination, the size of the systematic is expected to decrease as a function of D^0 lifetime. This is because, at later times the WS events are more likely to have come from an oscillation, followed by a CF decay. Therefore, at later times, the phase space distributions of RS and WS events will become more similar.

To calculate the uncertainty, the Mark III Dalitz model [48] is used, along with ten random variations of it. For each of the variations, the amplitudes of the resonances are multiplied by a uniformly generated random number between 0 and 2, and their phases are chosen at random between 0 and 2π. The ratio

$$\frac{\varepsilon^{\mathrm{M}}_{\mathrm{gen}}}{\varepsilon^{\mathrm{v}}_{\mathrm{gen}}} \cdot \frac{\varepsilon^{\mathrm{M}}_{\mathrm{sel}}}{\varepsilon^{\mathrm{v}}_{\mathrm{sel}}} \tag{5.26}$$

is measured for each of the ten random variations, where $\varepsilon^{\mathrm{M}}_{\mathrm{gen}}$ and $\varepsilon^{\mathrm{M}}_{\mathrm{sel}}$ are the generator level and selection efficiencies measured using the Mark III model, and $\varepsilon^{\mathrm{v}}_{\mathrm{gen}}$ and $\varepsilon^{\mathrm{v}}_{\mathrm{gen}}$ are the efficiencies measured using one of the random variations of the model.

The standard deviation of the ten values is 1.4%, which is used as a systematic uncertainty on r_D^2, and subsequently, the DCS branching fraction. The large variation of randomly generated models means that the systematic uncertainty is conservative.

Table 5.4: Summary of systematic uncertainties, shown as percentages. The statistical uncertainty is shown for comparison.

Source of uncertainty	r_D	r_D^2	b
Secondary correction	0.05	0.10	2.74
Peaking background	0.21	0.43	1.52
Δm fit model	0.56	1.12	66.0
Dalitz model	—	1.43	—
Total	0.60	1.90	66.0
Statistical	2.54	5.08	81.5

Table 5.5: Results of the fit to the time dependent WS/RS ratio, including all corrections.

Parameter	result (%)
r_D	5.842 ± 0.149
b	-0.1800 ± 0.1467
x	0.6180 ± 0.1868
y	0.7444 ± 0.1191

5.8.5 Branching fraction

Converting the measured value of r_D^2 into a DCS branching fraction requires multiplication by the CF branching fraction. The value is taken from the PDG to be $\mathcal{B}(D^0 \to K^-\pi^+\pi^-\pi^+) = \left(8.07^{+0.21}_{-0.19}\right)$ % [52]. The average of the asymmetric errors gives an uncertainty of 2.5%.

5.8.6 Summary

A summary of the systematic uncertainties can be found in Table 5.5. The branching fraction uncertainty of 2.5% is quoted separately to the other sources of systematic uncertainty.

5.9 Results

The fit to the time dependent WS/RS ratio using Equation 5.23 in the χ^2 is shown in Figure 5.17(a). Results are shown in Table 5.4, and the correlation matrix can be found

Table 5.6: Correlations between the fit parameters for the WS/RS lifetime distribution fit.

	r_D	b	x	y
r_D	1.000	0.895	0.204	0.152
b	0.895	1.000	0.370	0.276
x	0.204	0.370	1.000	−0.055
y	0.152	0.276	−0.055	1.000

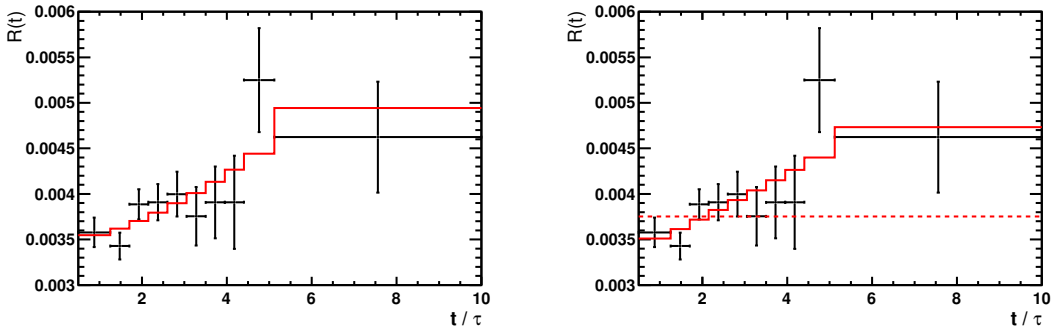

(a) (b)

Figure 5.17: (a) The fit to the WS/RS ratio as a function of D^0 lifetime, performed to extract the parameters r_D and b. (b) The data is fit with the mixing hypothesis (solid red line), and the no-mixing hypothesis (dashed red line) to measure the mixing significance.

in Table 5.6. Squaring r_D gives the ratio of DCS to CF decay rates:

$$r_D^2 = (0.341 \pm 0.017 \pm 0.006)\,\%$$

where the first uncertainty is statistical and the second is systematic. This is a previously unmeasured quantity, and can be used to calculate the branching fraction of $D^0 \to K^+\pi^-\pi^+\pi^-$ via DCS decays:

$$\mathcal{B}\left(D^0 \to K^+\pi^-\pi^+\pi^-\right) \text{ via DCS } = (2.75 \pm 0.14 \pm 0.05 \pm 0.07) \times 10^{-4}$$

where the first uncertainty is statistical, the second is systematic, and the third is from the uncertainty on the branching fraction of the CF decay $D^0 \to K^-\pi^+\pi^-\pi^+$. Including the systematic uncertainty, the value of $b = (-0.180 \pm 0.147 \pm 0.119)\,\%$. Discussion of this parameter is left until Section 5.10.

To measure the significance of $D^0 - \overline{D}^0$ oscillations, the parameters x and y are removed from the χ^2 and Equation 5.23 is replaced by either Equation 5.24 for the no-mixing

hypothesis, or Equation 5.25 for the mixing hypothesis. Both fits are shown in Figure 5.17(b). The χ^2/N_{dof} is 6.9/9 for the mixing hypothesis and 17.5/7 for the no-mixing hypothesis. This corresponds to a p-value of 0.0052 for the no-mixing hypothesis, which means that it is excluded at 2.8 standard deviations. The parameter C is often referred to as the mixing rate (but divided by two), R_M, which is measured as

$$R_M = (0.04 \pm 0.88) \times \ 10^{-4}.$$

5.10 Conclusions

To summarise, with $1.0\,\text{fb}^{-1}$ of data collected by the LHCb detector in 2011, we measure the ratio of DCS/CF decay rates as

$$r_D^2 = (0.341 \pm 0.017\,(\text{stat}) \pm 0.006\,(\text{syst}))\,\%$$

and when combining with the world average value of $\mathcal{B}(D^0 \to K^-\pi^+\pi^-\pi^+) = \left(8.07^{+0.21}_{-0.19}\right)\,\%$ [52], this gives

$$\mathcal{B}\left(D^0 \to K^+\pi^-\pi^+\pi^-\right) \text{ via DCS } = (2.75 \pm 0.14\,(\text{stat}) \pm 0.05\,(\text{syst}) \pm 0.07\,(\mathcal{B})) \times 10^{-4}.$$

For each measurement the uncertainty is dominated by its statistical component. The analysis is systematically very robust because of the efficiency cancellations in the double ratio (Equation 5.4). Any remaining systematics have been calculated in a conservative way. When the analysis is updated with the full 2012 data set, the statistical and systematic uncertainties will be comparable, so a much more detailed treatment will be required.

The parameter b appears in the first order term in the time dependent WS/RS rate equation. Referring back to Equation 1.77 reveals that

$$b = R_D y'_+ \quad \text{with} \quad y'_+ = y\cos(\delta_D) - x\sin(\delta_D)\,. \tag{5.27}$$

Although it is possible to extract a constraint for the coherence factor, R_D, and average strong phase, δ_D, significant further work is required. This is because the coherence factor and strong phase are only meaningful when the efficiency over the five-dimensional phase space is flat. Therefore, events need to be re-weighted in a way that compensates for the Dalitz space bias introduced in the many stages of event selection. Only then can a combination be made with the most recent result, measured by the CLEO collaboration [74]. Furthermore, re-weighting events to flatten the Dalitz space efficiency will remove the need for a Dalitz model systematic. These parameters will provide valuable constraints when measuring the CP violating phase γ using $B^- \to DK^-$ decays.

Using WS $D^0 \to K^+\pi^-\pi^+\pi^-$ decays, the no-mixing hypothesis is excluded at 2.8 Gaussian standard deviations. In light of the recent $D^0 \to K^+\pi^-$ measurement [64], this is expected to increase significantly when the full 2012 data set is added, which will increase the sample size by a factor of almost four. The mixing rate is measured as $R_M = (0.04 \pm 0.88) \times 10^{-4}$. This result is consistent with the most recent $D^0 \to K^+\pi^-\pi^+\pi^-$ measurement reported by the BABAR collaboration [66], $R_M = \left(1.9^{+1.6}_{-1.5}\,(\text{stat}) \pm 0.2\,(\text{syst})\right) \times 10^{-4}$, although it suggests a smaller value. The measurement is also consistent with the world average [73] of $R_M = (0.476 \pm 0.152) \times 10^{-4}$, which combines results from a wide range of different D^0 decay modes. A comparison of these results is shown in Figure 5.18

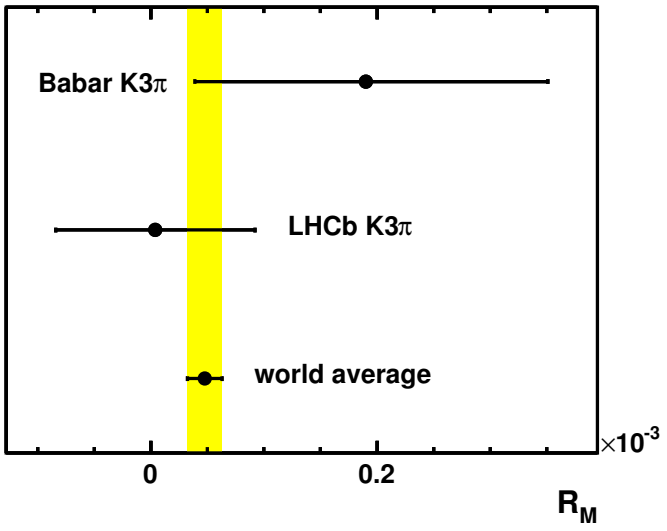

Figure 5.18: A comparison of R_M results from BABAR and LHCb, both using the decay mode $D^0 \to K^+\pi^-\pi^+\pi^-$. The world average combines results from many different decay modes, and does not include the two $D^0 \to K^+\pi^-\pi^+\pi^-$ results shown here.

Chapter 6

Conclusions

Flavour physics provides a mechanism for precision tests of the SM with high sensitivity to physics beyond the SM, including mass scales beyond those directly accessible via production at the LHC. Neutral charm mesons are up-type neutral mesons, and could be affected by new physics in a different way to the neutral B and K meson systems. Furthermore, because B mesons decay predominantly to charm, the study of charm mesons provides vital input for the study of CP violation in B decays.

The LHCb experiment has been designed to exploit the copious production of heavy flavour hadrons provided by the LHC. In this thesis, an optimisation of the LHCb RICH optical alignment is presented, which is vital for obtaining large, clean data samples needed for precision flavour physics. The RICH detector is particularly important for distinguishing between kaons and pions, which is essential for separating the DCS decay $D^0 \to K^+\pi^-\pi^+\pi^-$ from the CF mode $D^0 \to K^-\pi^+\pi^-\pi^+$, which has a branching fraction ~ 300 times larger, as measured in this thesis. Using a time-dependent analysis, charm meson mixing is confirmed at 2.8σ, and a mechanism is set up for measuring the coherence factor and average strong phase between the decays $D^0 \to K^\pm\pi^\mp\pi^+\pi^-$, which are key inputs for a precision measurement of the CKM angle γ using $B^- \to DK^-$ decays. The mode $D^0 \to K^-\pi^+\pi^-\pi^+$ is also used to measure the D^0 production cross section at LHC energies. Using the LHCb detector allows measurements up to a rapidity of 4.5, and down to $p_{\mathrm{T}} < 1\,\mathrm{GeV}/c$; ranges that are not accessible to the other LHC experiments.

Alignment of the RICH mirrors plays a crucial role in their Cherenkov angle resolution, which has a significant effect on the PID performance. The alignment procedure has been used on data collected in 2011 to improve the resolution from 13.96 mrad to 1.60 mrad in RICH1, and from 0.73 mrad to 0.63 mrad in RICH2. The resolutions are now very close to their Monte Carlo predicted limits. An event selection has been used to select events that populate the outer regions of the RICH mirror planes, in order to reduce the number of events required for the alignment procedure. A reduction factor of ~ 50 is achieved.

Production of promptly produced D^0 mesons is measured using $15.0\,\text{nb}^{-1}$ of pp collisions with a centre-of-mass energy of $\sqrt{s} = 7\,\text{TeV}$, collected by the LHCb detector in 2010. The cross-section is measured in two-dimensional bins of (y, p_T) in the range $2.0 < y < 4.5$ and $0 < p_\text{T} < 8\,\text{GeV}/c$. The decay mode $D^0 \to K^-\pi^+\pi^-\pi^+$ is used, and results are compared with those obtained using the much more abundant mode $D^0 \to K^-\pi^+$. Excellent agreement is found, which gives confidence in the analysis techniques used, and demonstrates a well understood track reconstruction efficiency. The results are also compared with NLO QCD predictions, which are found to have reasonable agreement. Now that data has been collected with a higher energy of $\sqrt{s} = 8\,\text{TeV}$, there is the potential for new cross-section measurements, which would provide a further testing ground for QCD predictions.

With $1.0\,\text{fb}^{-1}$ of data collected in 2011, a time dependent analysis is performed using ~ 7500 wrong sign $D \to K3\pi$ decays and $\sim 2\,\text{M}$ right sign $D \to K3\pi$ decays. The ratio of DCS/CF decay rates is measured as

$$r_D^2 = (0.341 \pm 0.017\,(\text{stat}) \pm 0.006\,(\text{syst}))\,\%$$

which is a previously unmeasured quantity. When combining with the world average value of $\mathcal{B}(D^0 \to K^-\pi^+\pi^-\pi^+) = \left(8.07^{+0.21}_{-0.19}\right)\,\%$ [52], this gives

$$\mathcal{B}\left(D^0 \to K^+\pi^-\pi^+\pi^-\right) \text{ via DCS } = (2.75 \pm 0.14\,(\text{stat}) \pm 0.05\,(\text{syst}) \pm 0.07\,(\mathcal{B})) \times 10^{-4}.$$

Both measurements are limited by their statistical uncertainties. A future analysis using

both the 2011 and 2012 datasets is expected to increase the sample size by a factor of almost four.

In addition, the time dependent ratio of wrong sign to right sign decays is used to measure the significance of $D^0 - \overline{D}^0$ oscillations. The no-mixing hypothesis is excluded at 2.8 Gaussian standard deviations, and using the mixing hypothesis the mixing rate is measured as $R_M = (0.04 \pm 0.88) \times 10^{-4}$, which is independent of the D^0 decay mode. This is consistent with the world average [73] of $R_M = (0.476 \pm 0.152) \times 10^{-4}$. Updating the analysis with the 2012 dataset is an exciting prospect, especially in light of the recent 9.1σ observation of $D^0 - \overline{D}^0$ oscillations using $D^0 \to K^+\pi^-$ decays [64].

Appendix A

Charm cross-section fits in (y, p_{T}) bins

Contained within this Appendix are the projections of fits used to extract the yields for the measurement of the prompt charm production-cross section (see Chapter 4). The fits to data within each (y, p_{T}) bin are grouped with their "big bins" (see Figure 4.9). For each bin the fits to Monte Carlo prompt and secondary $\log_{10}(IP\chi^2)$ distributions, along with the fit to the $\log_{10}(IP\chi^2)$ distribution of data taken from the D^0 mass sideband are shown. These fits are used to set initial parameter values (some of which are then fixed) for the two-dimensional fit to the D^0 mass - $\log_{10}(IP\chi^2)$ plane. Projections of the two-dimensional fit are also shown.

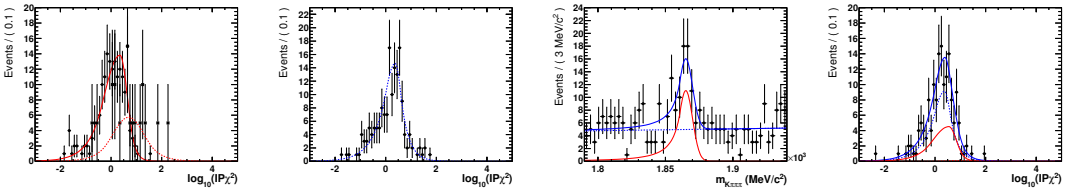

(a) (b) (c) (d)

Figure A.1: Fits to the $\log_{10}(IP\chi^2)$ distributions of (a) prompt and secondary Monte Carlo, and (b) data mass sidebands; and the (c) mass, and (d) $\log_{10}(IP\chi^2)$ projections of the two-dimensional fit to data, in the bin $2.5 < y < 3.0$ and $1 < p_{\mathrm{T}} < 2\,\mathrm{GeV}/c$. In (a) the solid red line is a fit to the prompt Monte Carlo (circular markers), and the dashed red line is a fit to the secondary Monte Carlo (square markers), which has been scaled by a factor of five. In (c) the red line represents the prompt signal and secondary background components, and the blue dashed line is the combinatorial background component. In (d) the prompt signal component is a solid red line, the secondary background component is a red dashed line and the combinatorial background is shown as a blue dashed line.

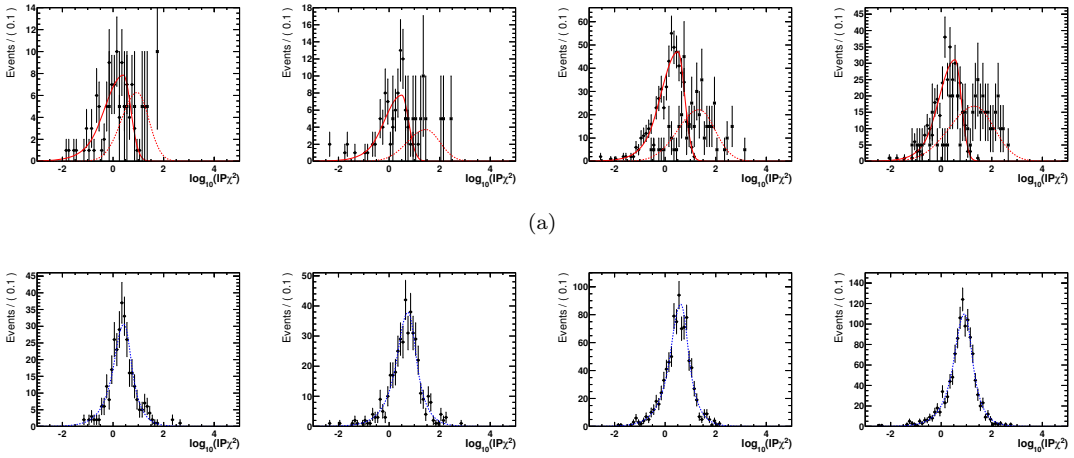

(a)

(b)

Figure A.2: Fits to the $\log_{10}(IP\chi^2)$ distributions of (a) prompt (red solid line and circular markers) and secondary Monte Carlo (red dashed line and square markers, scaled by a factor of five), and (b) data mass sidebands for bins between $3.0 < y < 4.0$ and $0 < p_{\mathrm{T}} < 2\,\mathrm{GeV}/c$.

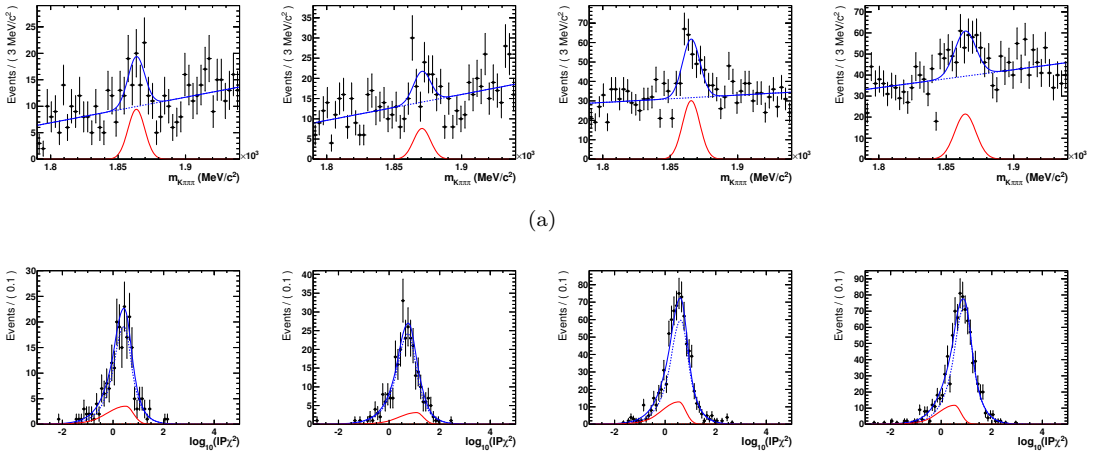

(a)

(b)

Figure A.3: The (a) mass, and (b) $\log_{10}(IP\chi^2)$ projections of the two-dimensional fit to data for bins between $3.0 < y < 4.0$ and $0 < p_{\mathrm{T}} < 2\,\mathrm{GeV}/c$. The solid red line in (a) represents the contribution from D^0 signal decays (either prompt or secondary), combinatorial background is shown in dashed blue in both (a) and (b), and the prompt and secondary D^0 $\log_{10}(IP\chi^2)$ contributions are shown in (b) by red solid and dashed lines respectively.

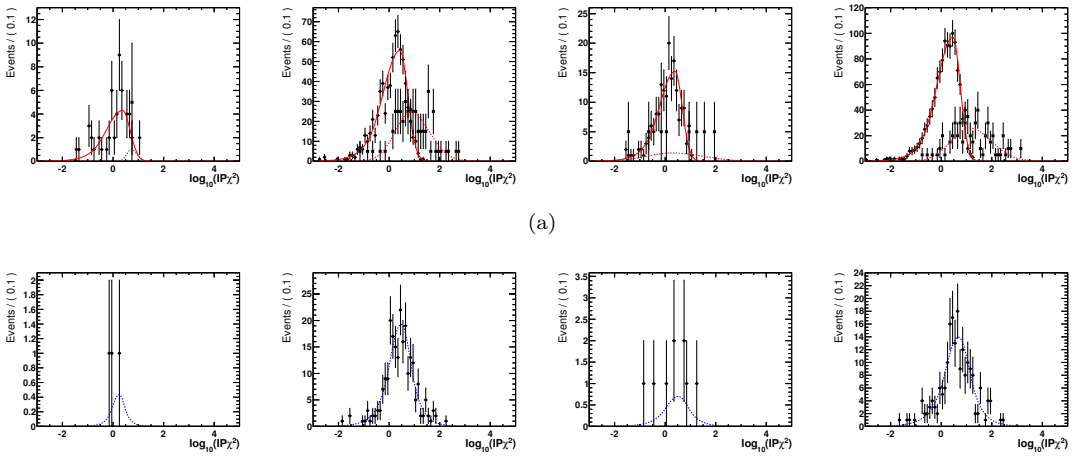

(a)

(b)

Figure A.4: Fits to the $\log_{10}(IP\chi^2)$ distributions of (a) prompt (red solid line and circular markers) and secondary Monte Carlo (red dashed line and square markers, scaled by a factor of five), and (b) data mass sidebands for bins between $2.0 < y < 3.0$ and $2 < p_{\mathrm{T}} < 4\,\mathrm{GeV}/c$.

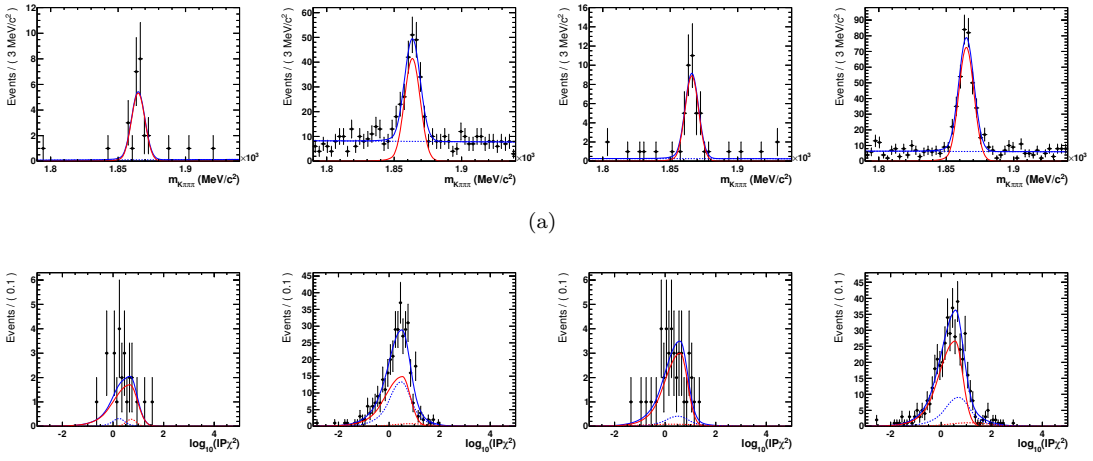

(a)

(b)

Figure A.5: The (a) mass, and (b) $\log_{10}(IP\chi^2)$ projections of the two-dimensional fit to data for bins between $2.0 < y < 3.0$ and $2 < p_{\mathrm{T}} < 4\,\mathrm{GeV}/c$. The solid red line in (a) represents the contribution from D^0 signal decays (either prompt or secondary), combinatorial background is shown in dashed blue in both (a) and (b), and the prompt and secondary D^0 $\log_{10}(IP\chi^2)$ contributions are shown in (b) by red solid and dashed lines respectively.

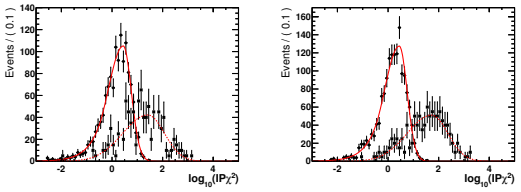

(a)

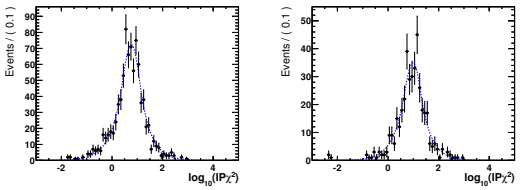

(b)

Figure A.6: Fits to the $\log_{10}(IP\chi^2)$ distributions of (a) prompt (red solid line and circular markers) and secondary Monte Carlo (red dashed line and square markers, scaled by a factor of five), and (b) data mass sidebands for bins between $3.0 < y < 3.5$ and $2 < p_{\mathrm{T}} < 4\,\mathrm{GeV}/c$.

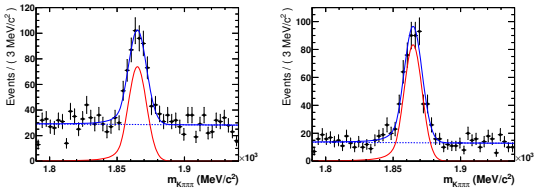

(a)

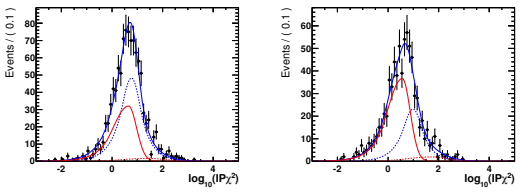

(b)

Figure A.7: The (a) mass, and (b) $\log_{10}(IP\chi^2)$ projections of the two-dimensional fit to data for bins between $3.0 < y < 3.5$ and $2 < p_{\mathrm{T}} < 4\,\mathrm{GeV}/c$. The solid red line in (a) represents the contribution from D^0 signal decays (either prompt or secondary), combinatorial background is shown in dashed blue in both (a) and (b), and the prompt and secondary D^0 $\log_{10}(IP\chi^2)$ contributions are shown in (b) by red solid and dashed lines respectively.

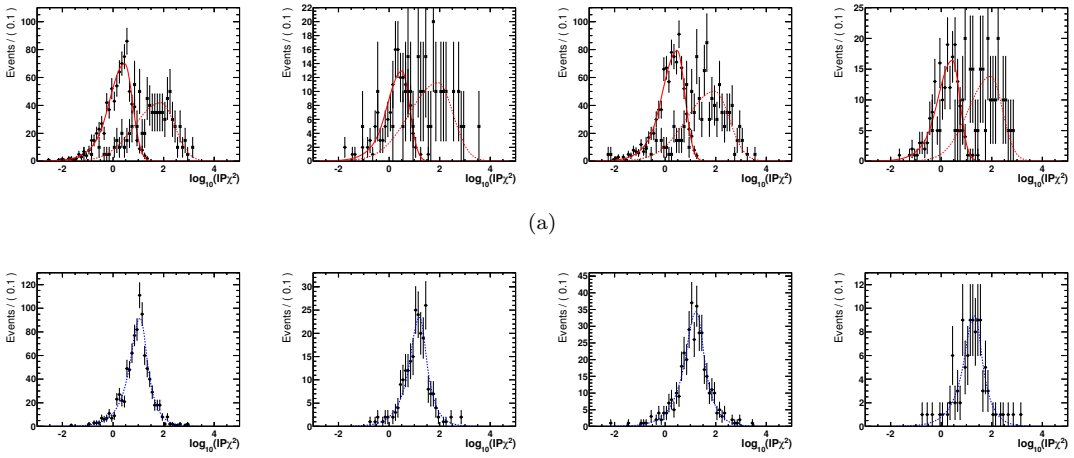

(a)

(b)

Figure A.8: Fits to the $\log_{10}(IP\chi^2)$ distributions of (a) prompt (red solid line and circular markers) and secondary Monte Carlo (red dashed line and square markers, scaled by a factor of five), and (b) data mass sidebands for bins between $3.5 < y < 4.5$ and $2 < p_{\mathrm{T}} < 4\,\mathrm{GeV}/c$.

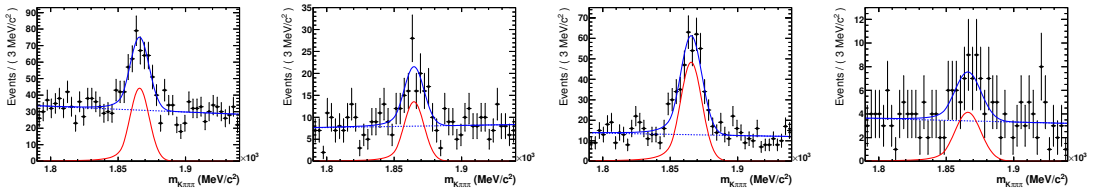

(a)

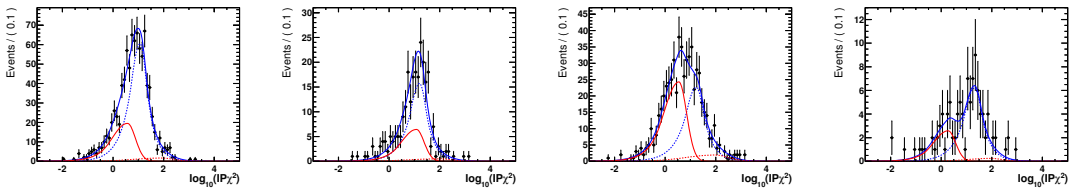

(b)

Figure A.9: The (a) mass, and (b) $\log_{10}(IP\chi^2)$ projections of the two-dimensional fit to data for bins between $3.5 < y < 4.5$ and $2 < p_{\mathrm{T}} < 4\,\mathrm{GeV}/c$. The solid red line in (a) represents the contribution from D^0 signal decays (either prompt or secondary), combinatorial background is shown in dashed blue in both (a) and (b), and the prompt and secondary D^0 $\log_{10}(IP\chi^2)$ contributions are shown in (b) by red solid and dashed lines respectively.

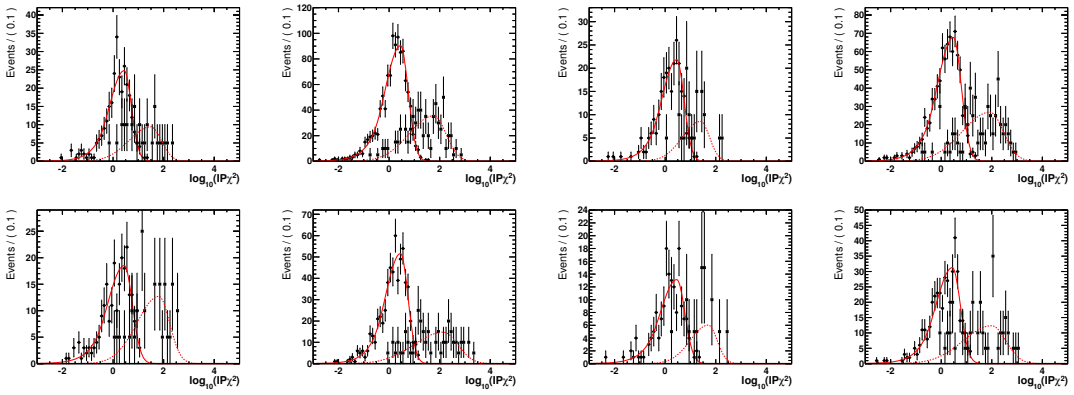

(a)

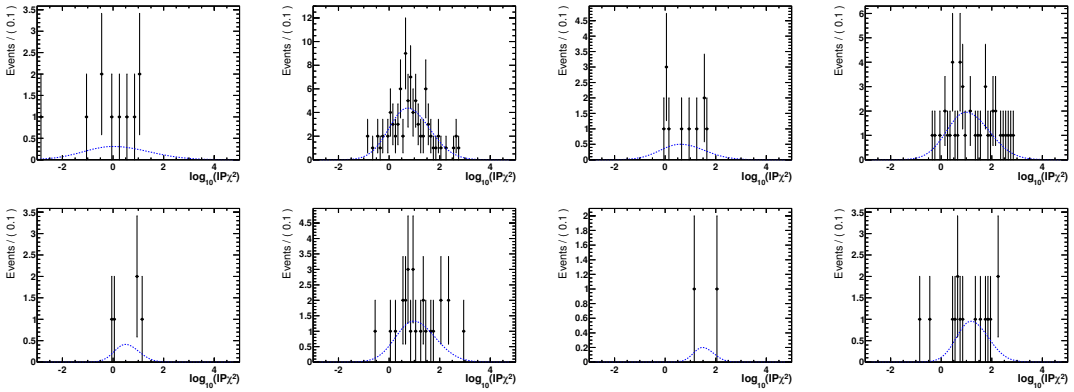

(b)

Figure A.10: Fits to the $\log_{10}(IP\chi^2)$ distributions of (a) prompt (red solid line and circular markers) and secondary Monte Carlo (red dashed line and square markers, scaled by a factor of five), and (b) data mass sidebands for bins between $2.0 < y < 3.0$ and $4 < p_{\mathrm{T}} < 8\,\mathrm{GeV}/c$.

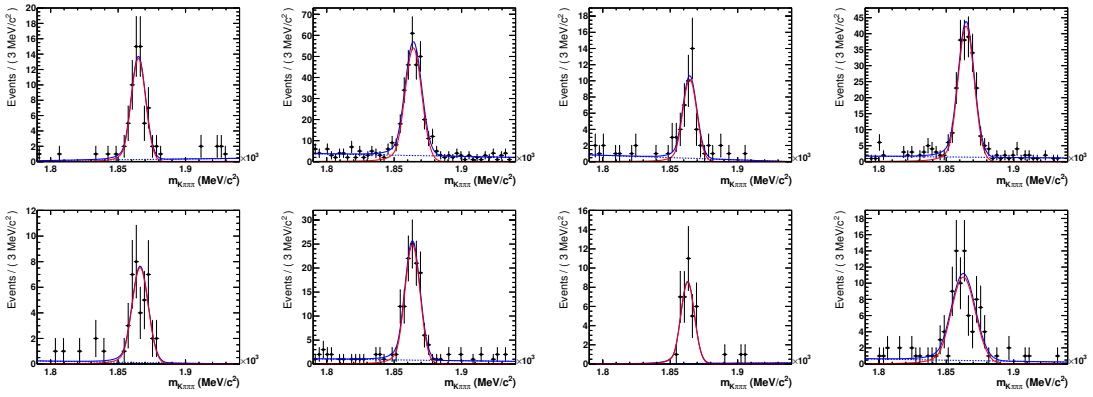

(a)

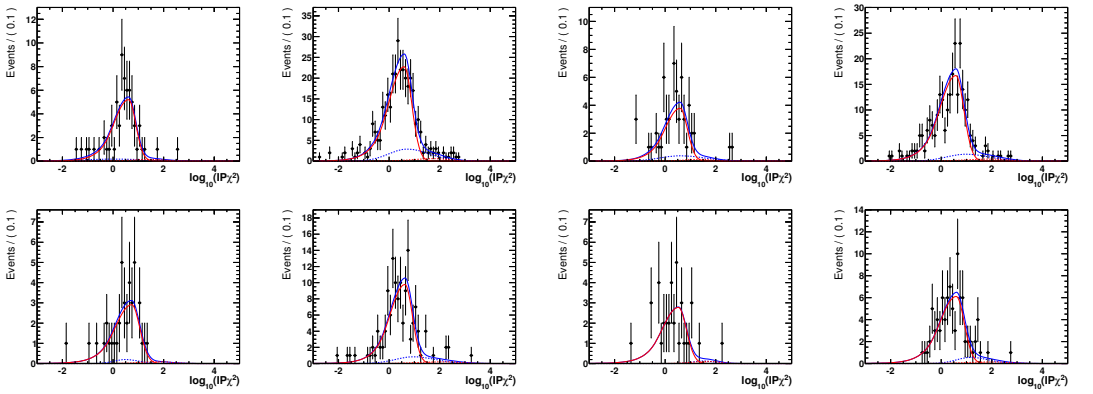

(b)

Figure A.11: The (a) mass, and (b) $\log_{10}(IP\chi^2)$ projections of the two-dimensional fit to data for bins between $2.0 < y < 3.0$ and $4 < p_{\mathrm{T}} < 8\,\mathrm{GeV}/c$. The solid red line in (a) represents the contribution from D^0 signal decays (either prompt or secondary), combinatorial background is shown in dashed blue in both (a) and (b), and the prompt and secondary D^0 $\log_{10}(IP\chi^2)$ contributions are shown in (b) by red solid and dashed lines respectively.

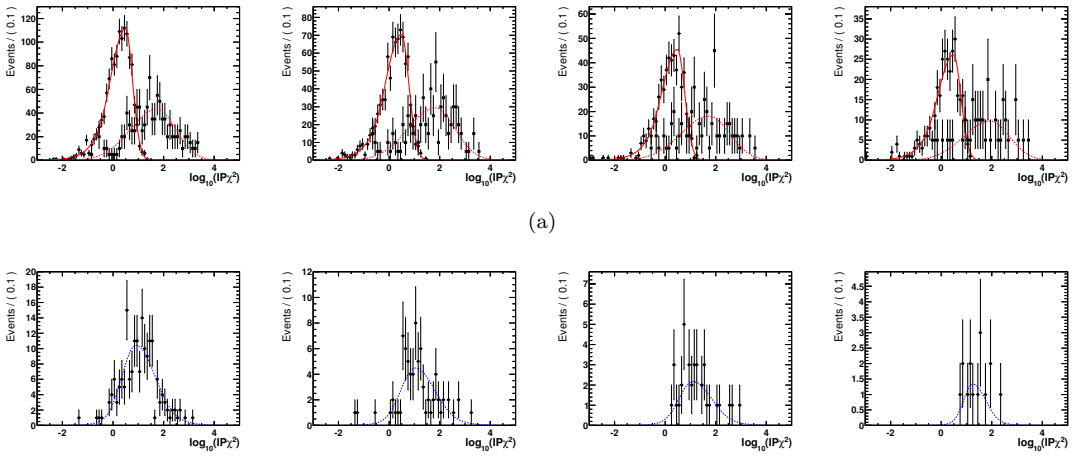

(a)

(b)

Figure A.12: Fits to the $\log_{10}(IP\chi^2)$ distributions of (a) prompt (red solid line and circular markers) and secondary Monte Carlo (red dashed line and square markers, scaled by a factor of five), and (b) data mass sidebands for bins between $3.0 < y < 3.5$ and $4 < p_{\mathrm{T}} < 8\,\mathrm{GeV}/c$.

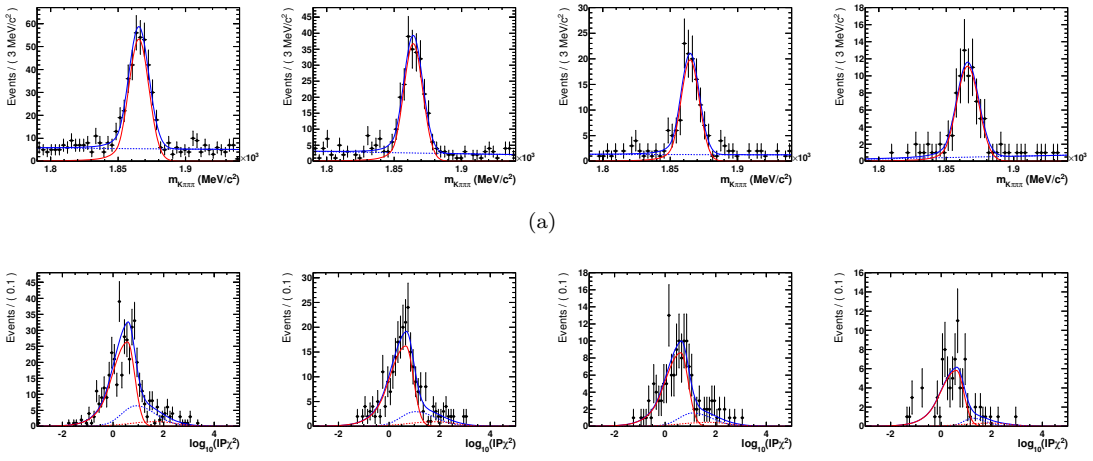

(a)

(b)

Figure A.13: The (a) mass, and (b) $\log_{10}(IP\chi^2)$ projections of the two-dimensional fit to data for bins between $3.0 < y < 3.5$ and $4 < p_{\mathrm{T}} < 8\,\mathrm{GeV}/c$. The solid red line in (a) represents the contribution from D^0 signal decays (either prompt or secondary), combinatorial background is shown in dashed blue in both (a) and (b), and the prompt and secondary D^0 $\log_{10}(IP\chi^2)$ contributions are shown in (b) by red solid and dashed lines respectively.

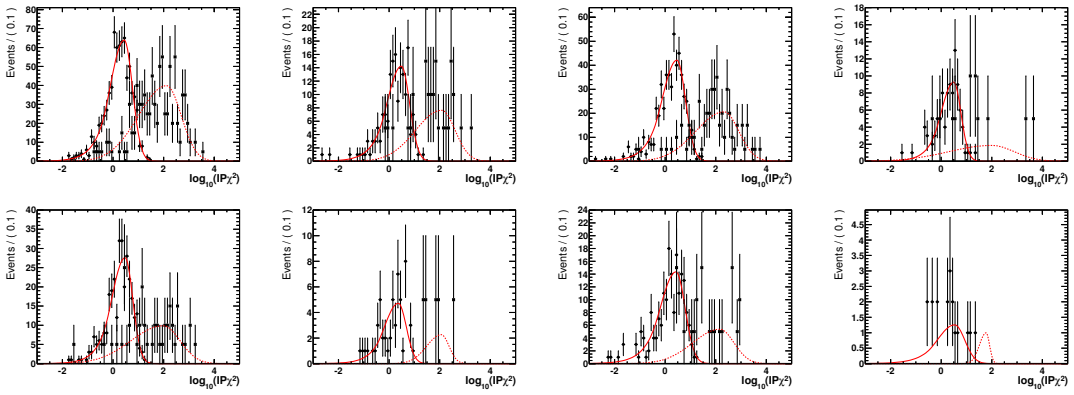

(a)

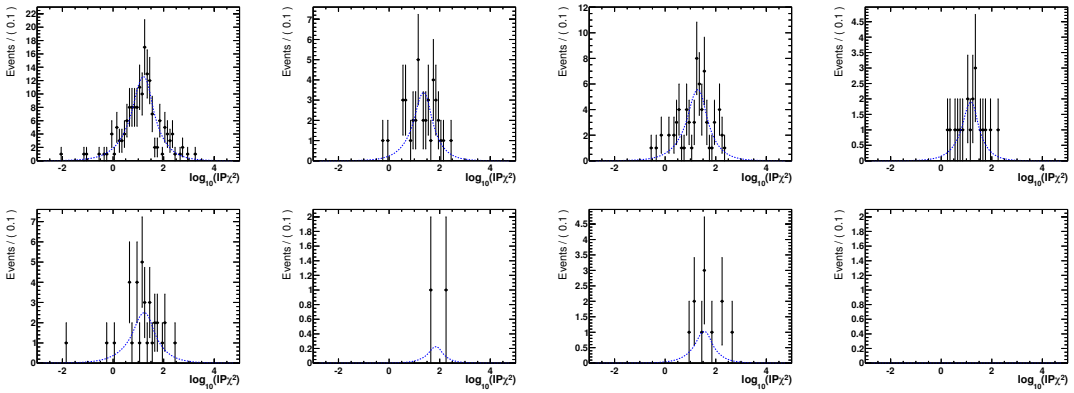

(b)

Figure A.14: Fits to the $\log_{10}(IP\chi^2)$ distributions of (a) prompt (red solid line and circular markers) and secondary Monte Carlo (red dashed line and square markers, scaled by a factor of five), and (b) data mass sidebands for bins between $3.5 < y < 4.5$ and $4 < p_{\mathrm{T}} < 8\,\mathrm{GeV}/c$.

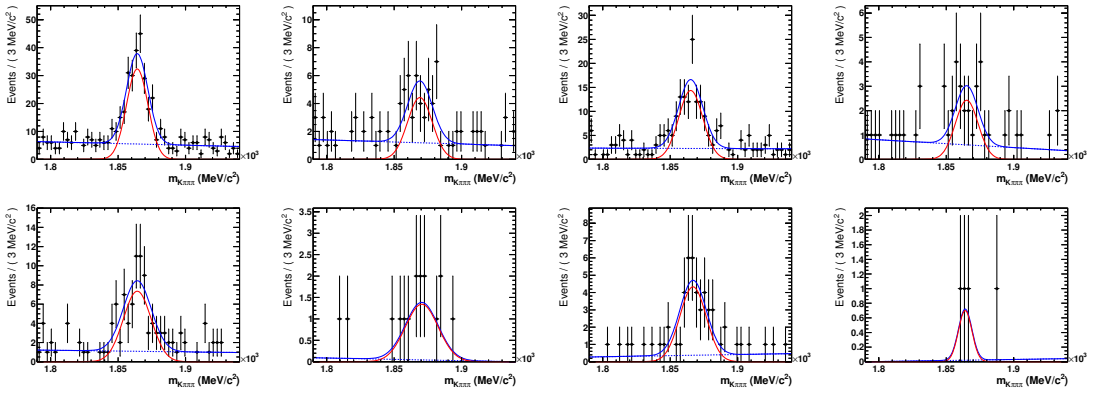

(a)

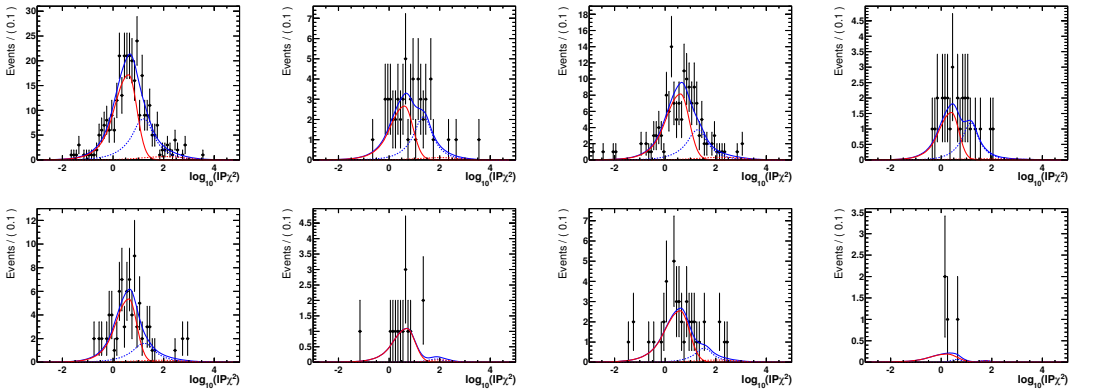

(b)

Figure A.15: The (a) mass, and (b) $\log_{10}(IP\chi^2)$ projections of the two-dimensional fit to data for bins between $3.5 < y < 4.5$ and $4 < p_{\mathrm{T}} < 8\,\mathrm{GeV}/c$. The solid red line in (a) represents the contribution from D^0 signal decays (either prompt or secondary), combinatorial background is shown in dashed blue in both (a) and (b), and the prompt and secondary D^0 $\log_{10}(IP\chi^2)$ contributions are shown in (b) by red solid and dashed lines respectively.

Appendix B

Mass and $\log_{10}(IP\chi^2)$ fits in bins of D^0 lifetime

This Appendix contains material relevant to Chapter 5. Each of the Figures contains plots in different bins of D^0 lifetime. They are arranged so that the lifetime increases form left to right and from top to bottom, as one would expect.

Figures B.1 – B.8 show the fits to Δm distributions used to extract the yields of the four different decay modes, along with their pull distributions.

Figure B.9 shows fits to the B^+ invariant mass in individual lifetime bins (the pulls are in Figure B.10). These are use to extract signal distributions using the ${}_s\mathcal{P}lot$ technique. The resulting $\log_{10}(IP\chi^2)$ distributions are shown in Figure B.11, each of which is fit with a bifurcated Gaussian.

Figure B.12 shows the $\log_{10}(IP\chi^2)$ distributions obtained from using the ${}_s\mathcal{P}lot$ technique on the D^* sample. The prompt shape is modelled by the sum of two bifurcated Gaussians with common means, and is fixed from a fit to the first lifetime bin, assuming a 0% secondary fraction. Using this shape, and the secondary shapes (fixed after the fits to the $B^+ \to \overline{D}^0\pi^+$ sample), the secondary fraction in each lifetime bin is measured by floating the yields of the prompt and secondary components.

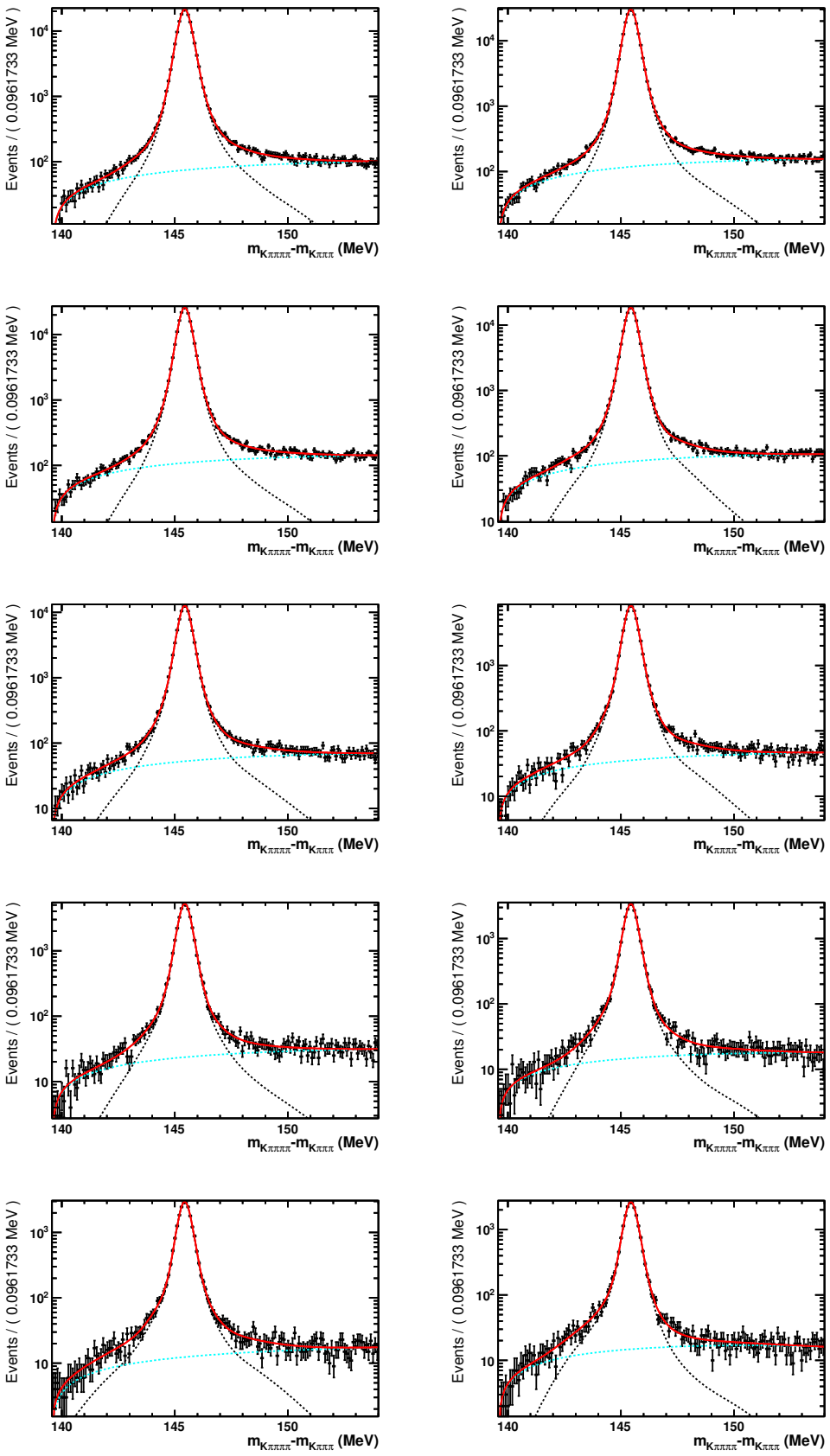

Figure B.1: RS D^0 fits in bins of lifetime. The dashed lines represent the signal (black) and background (cyan) components.

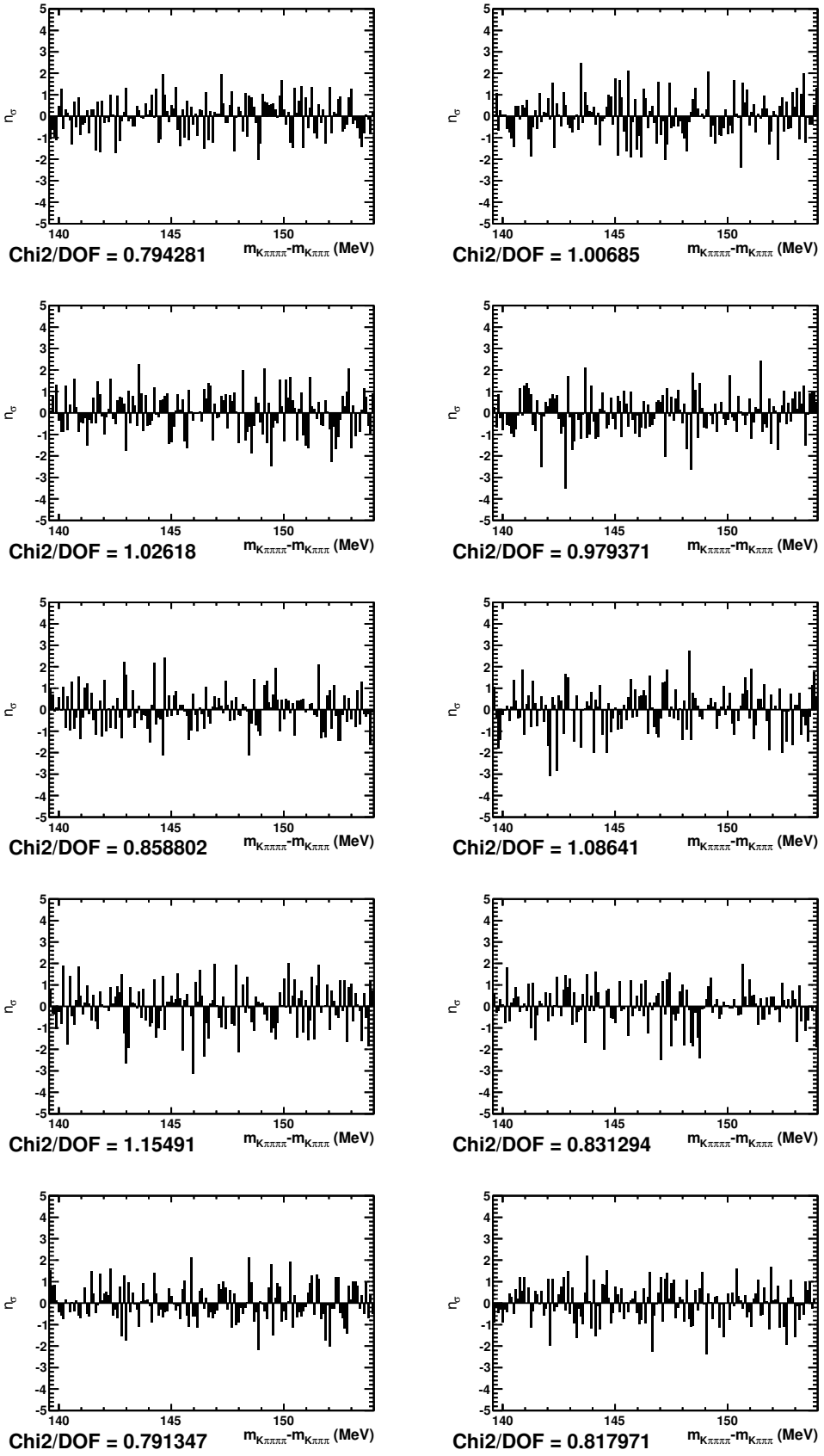

Figure B.2: RS D^0 pulls distributions in lifetime bins.

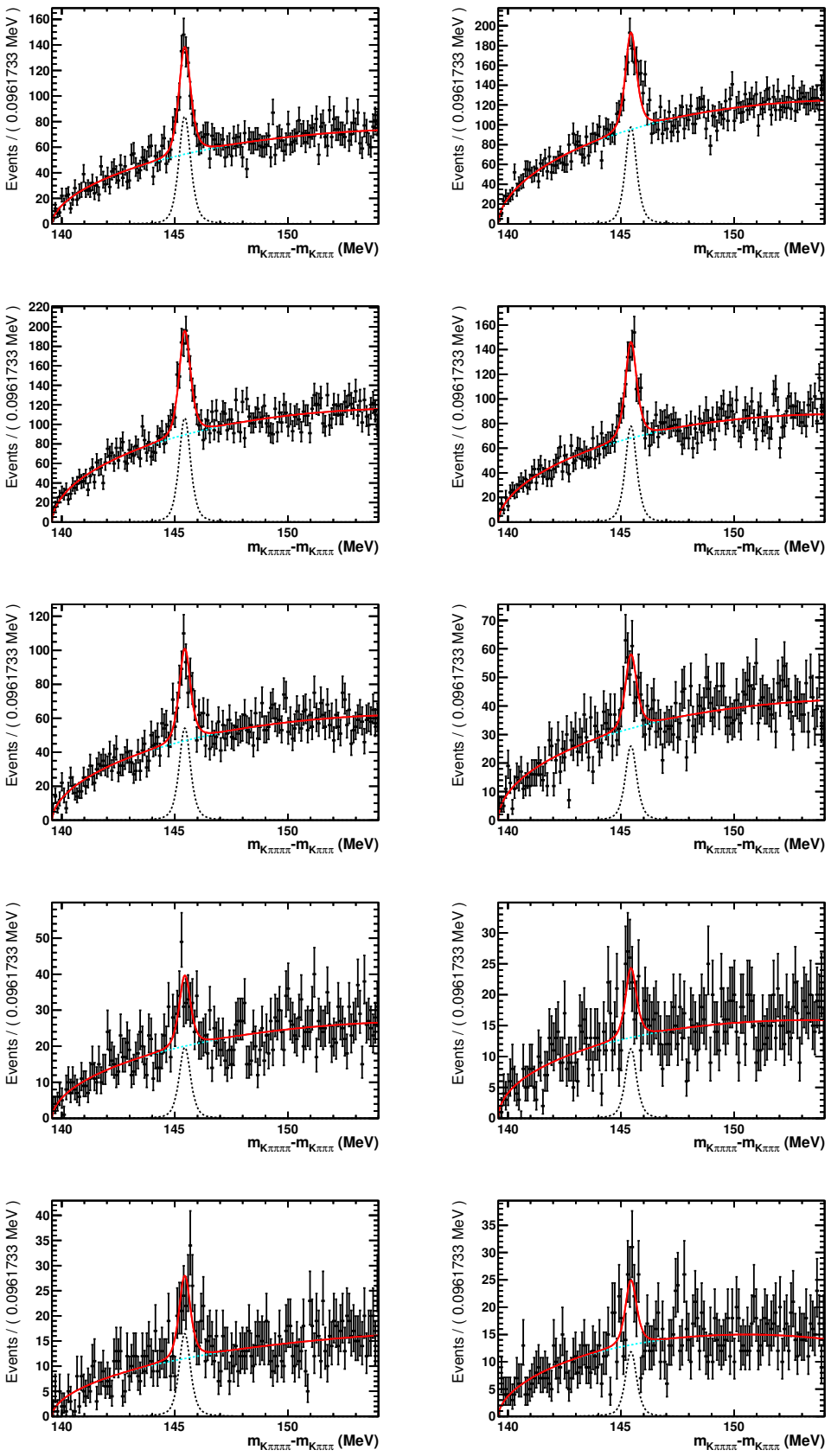

Figure B.3: WS D^0 fits in lifetime bins. The dashed lines represent the signal (black) and background (cyan) components.

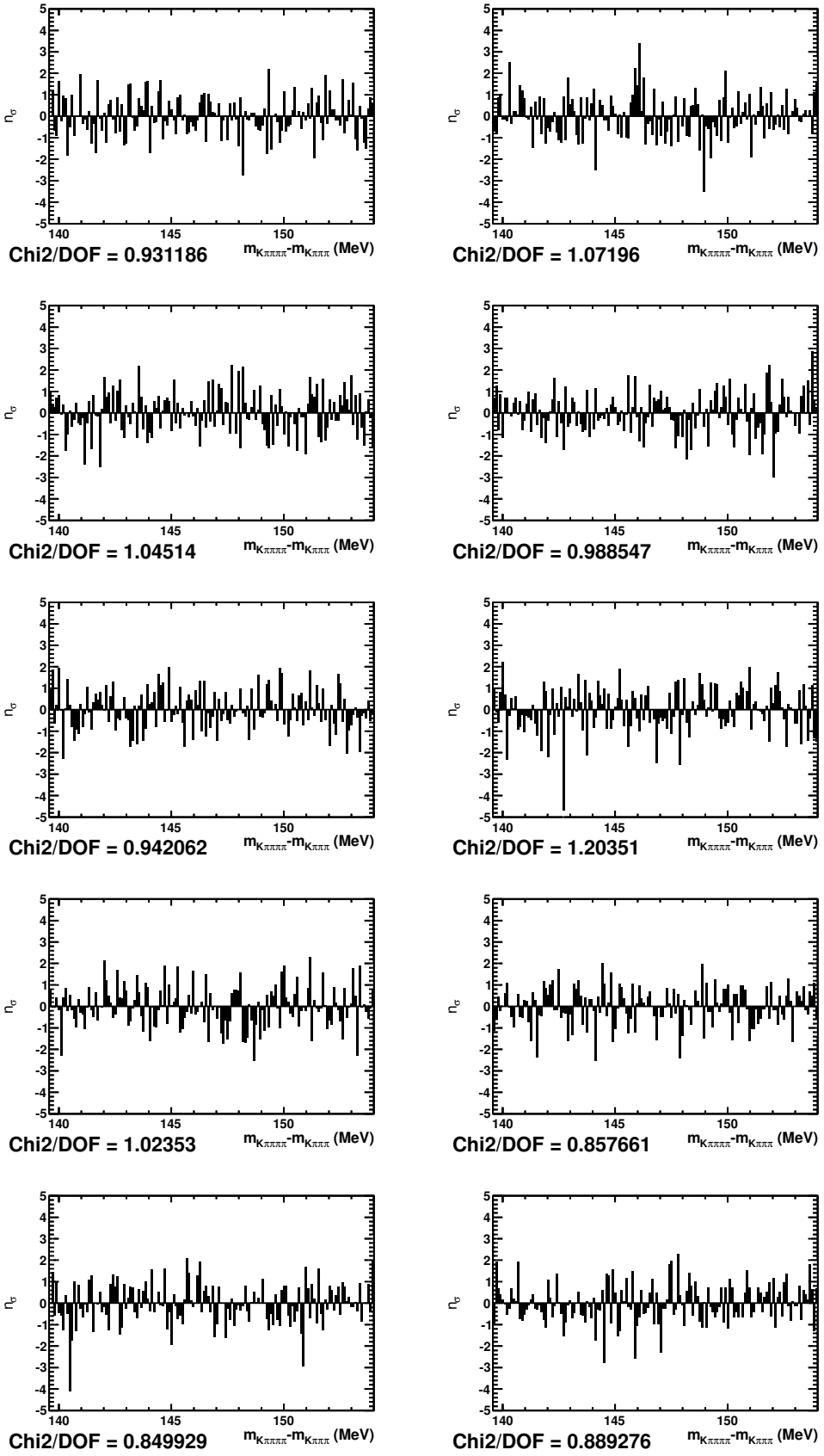

Figure B.4: WS D^0 pulls in lifetime bins.

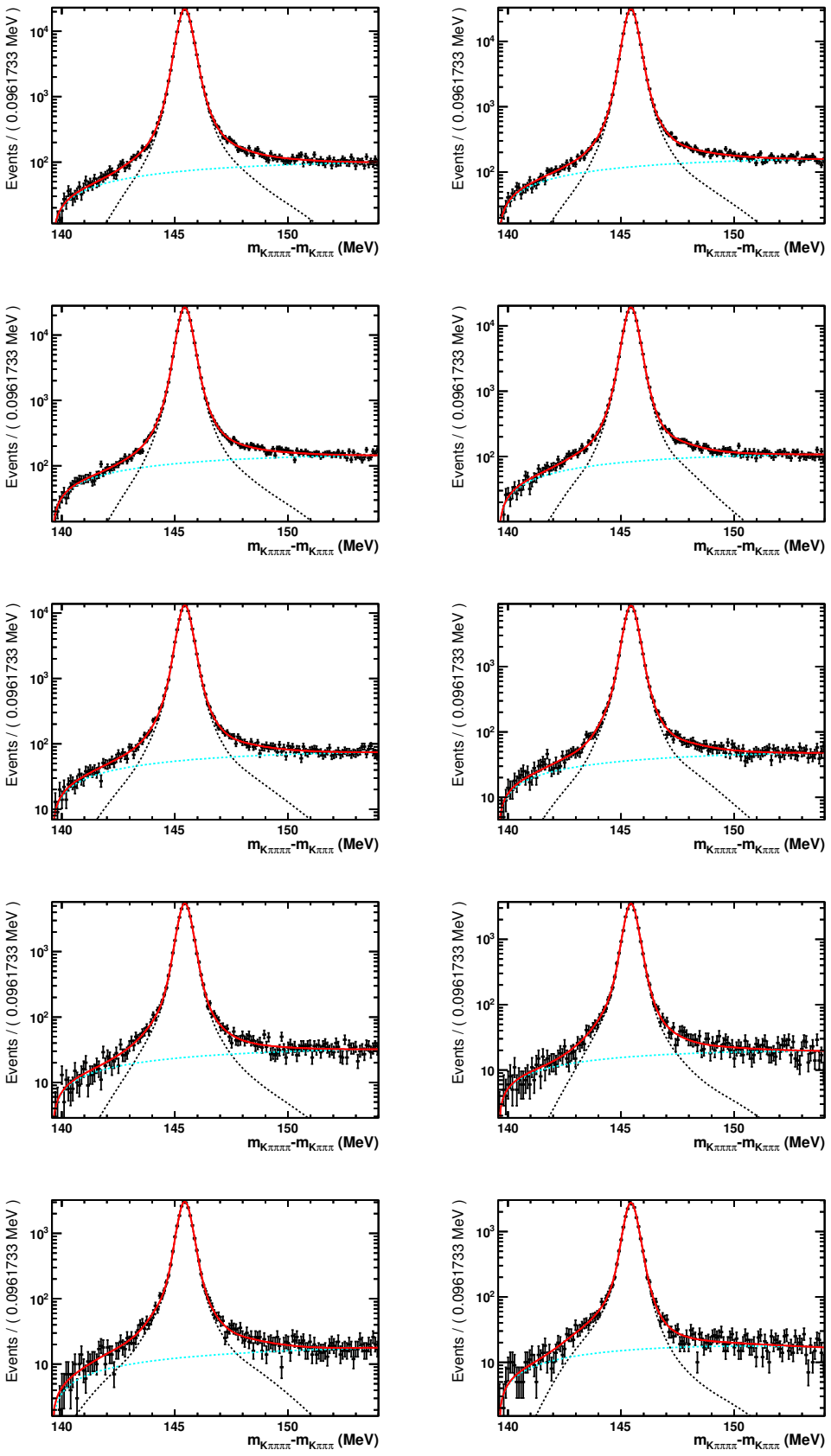

Figure B.5: RS $\overline{D}^0$ fits in lifetime bins. The dashed lines represent the signal (black) and background (cyan) components.

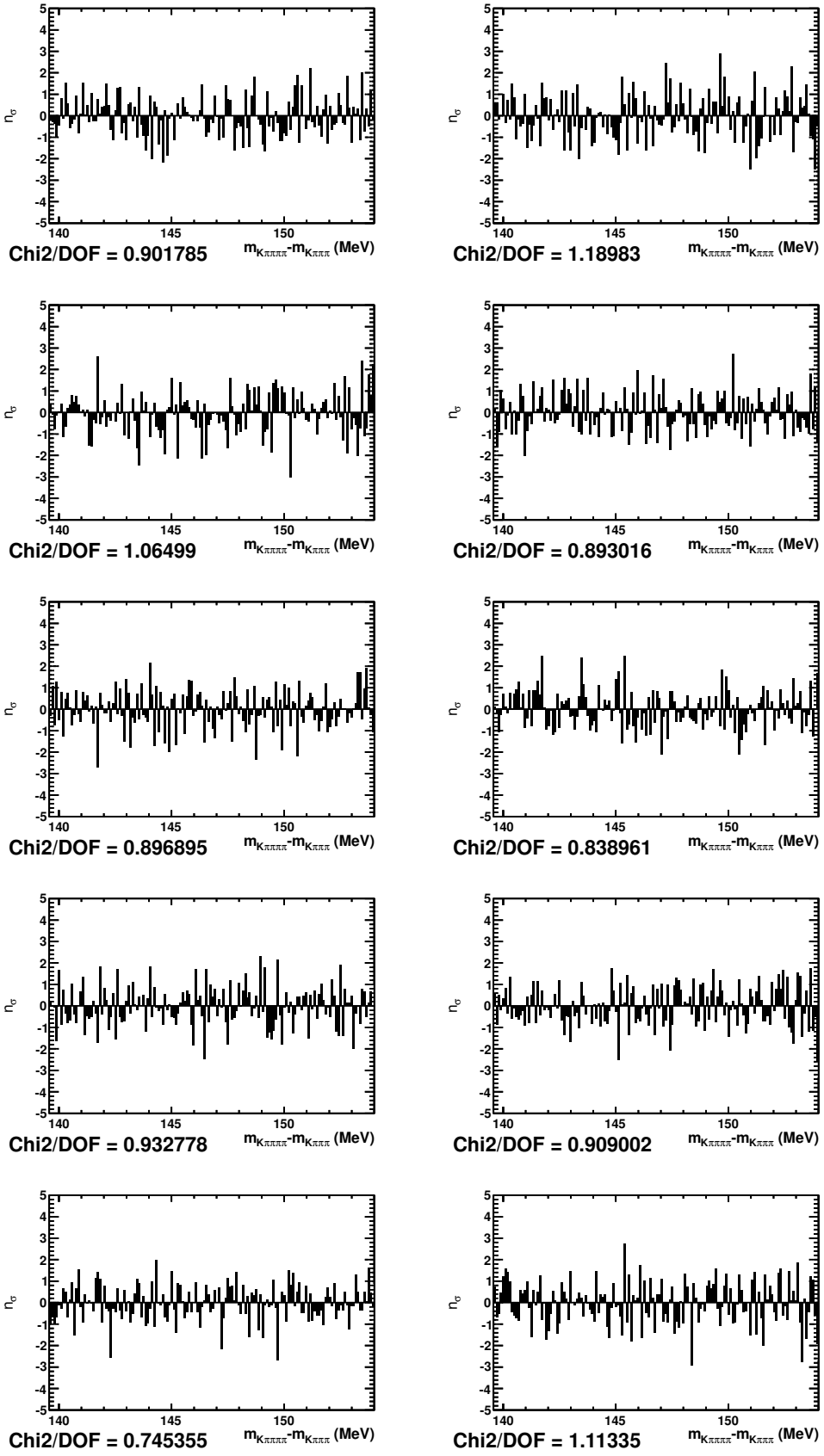

Figure B.6: RS $\overline{D}^0$ pulls in lifetime bins.

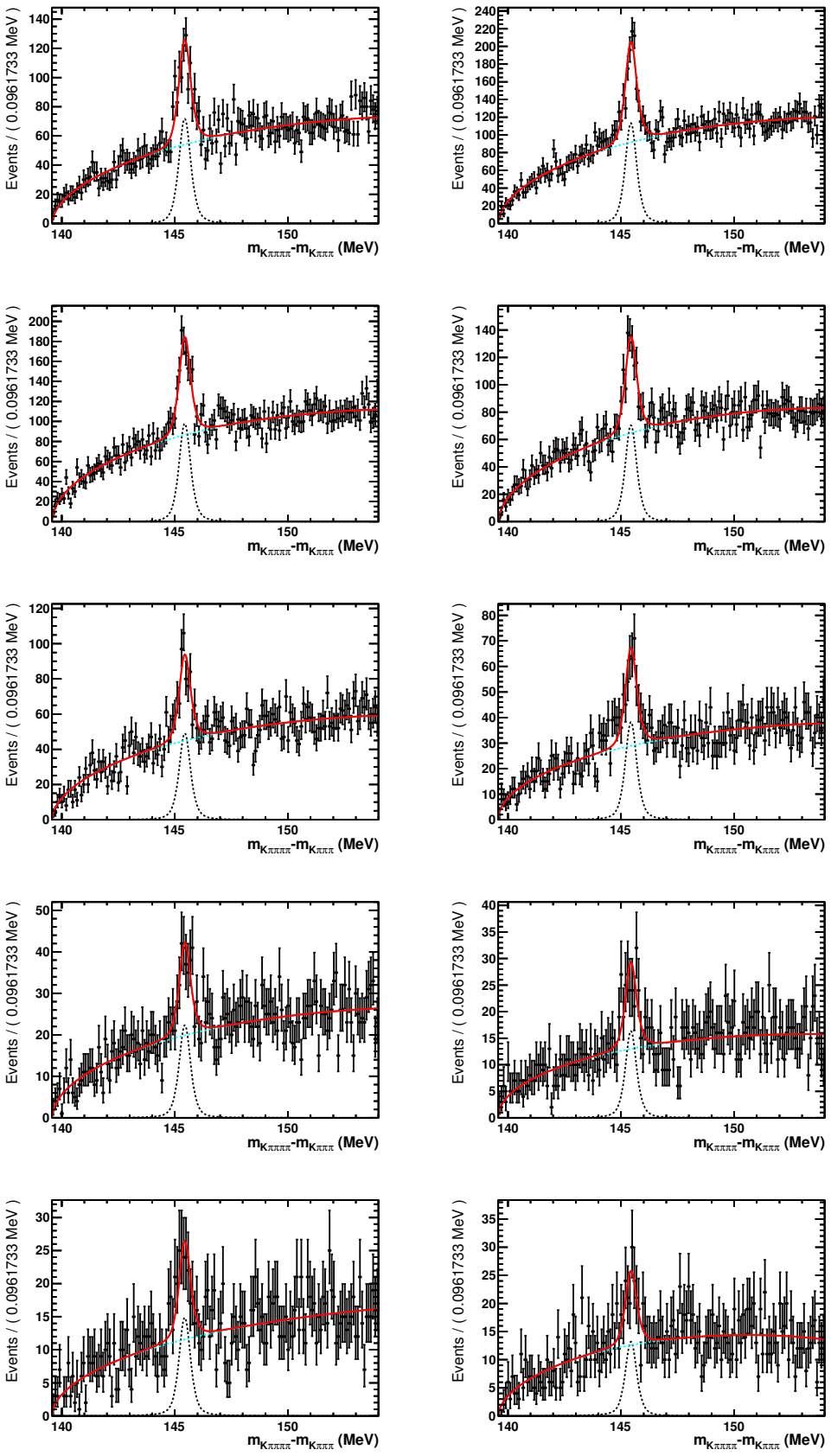

Figure B.7: WS $\overline{D}^0$ fits in lifetime bins. The dashed lines represent the signal (black) and background (cyan) components.

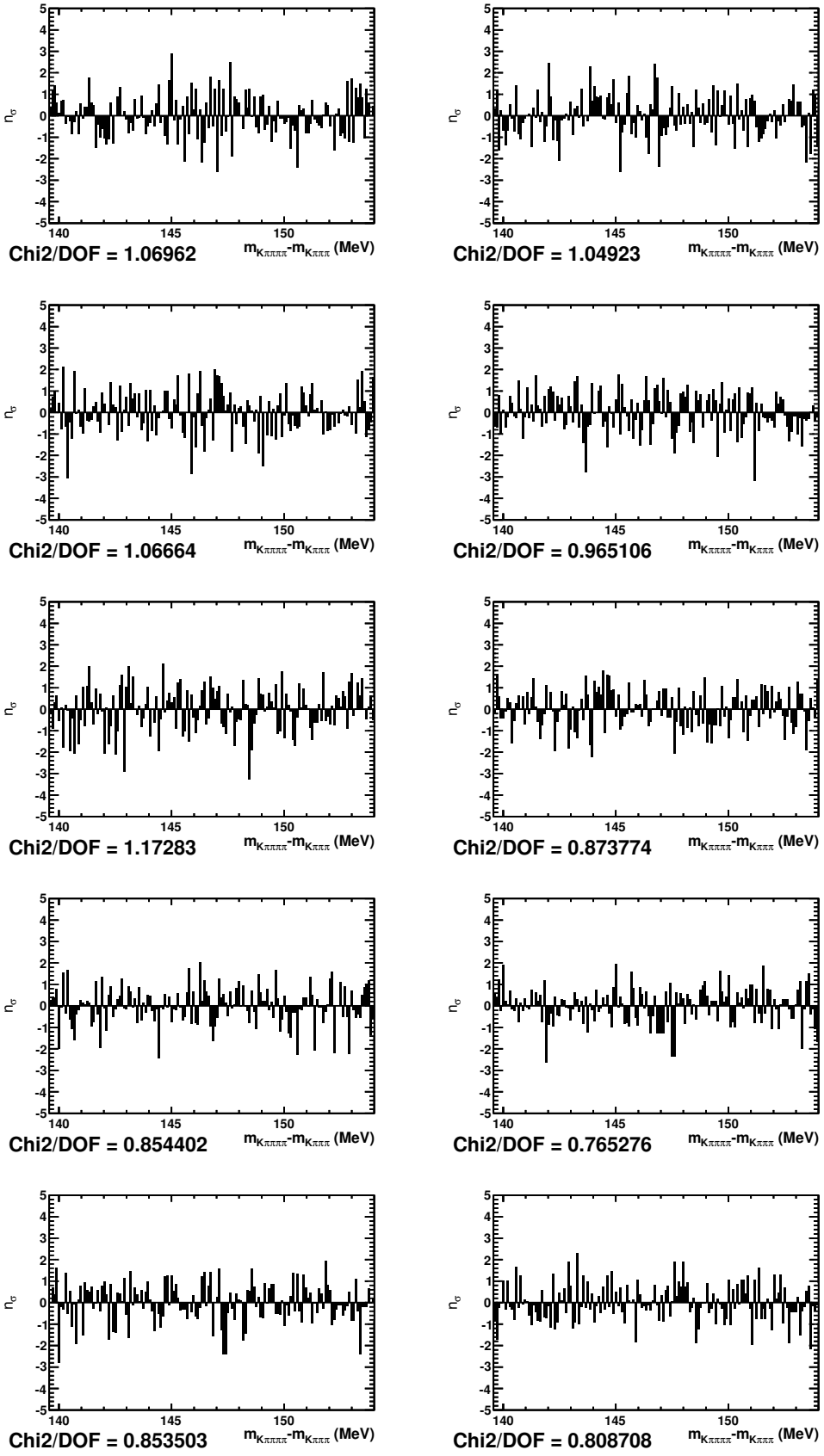

Figure B.8: WS $\overline{D}^0$ pulls in lifetime bins.

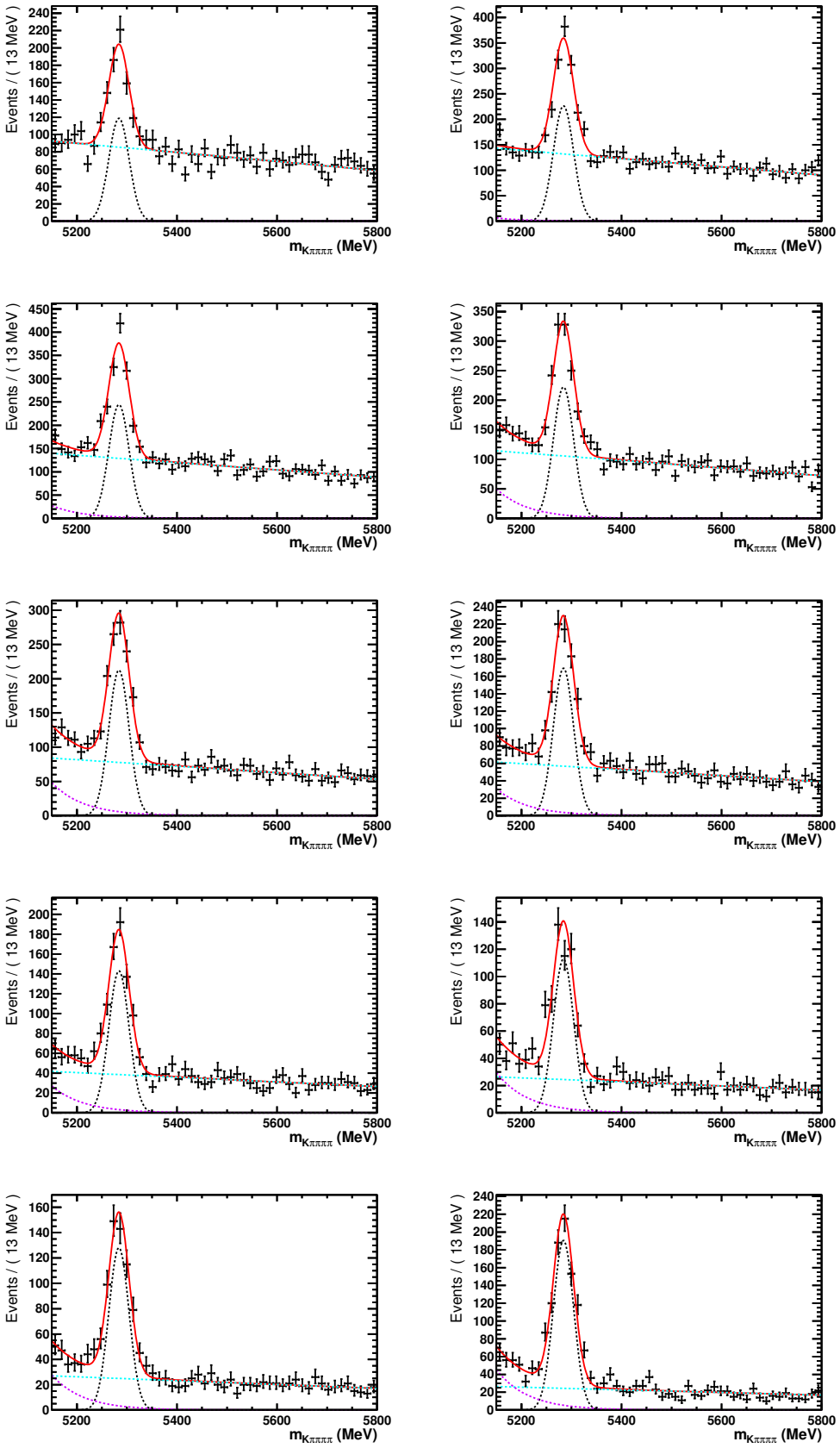

Figure B.9: Fits to the B^+ mass in lifetime bins. The dashed lines represent signal (black), partially reconstructed physics background (magenta), and combinatorial background (cyan) components.

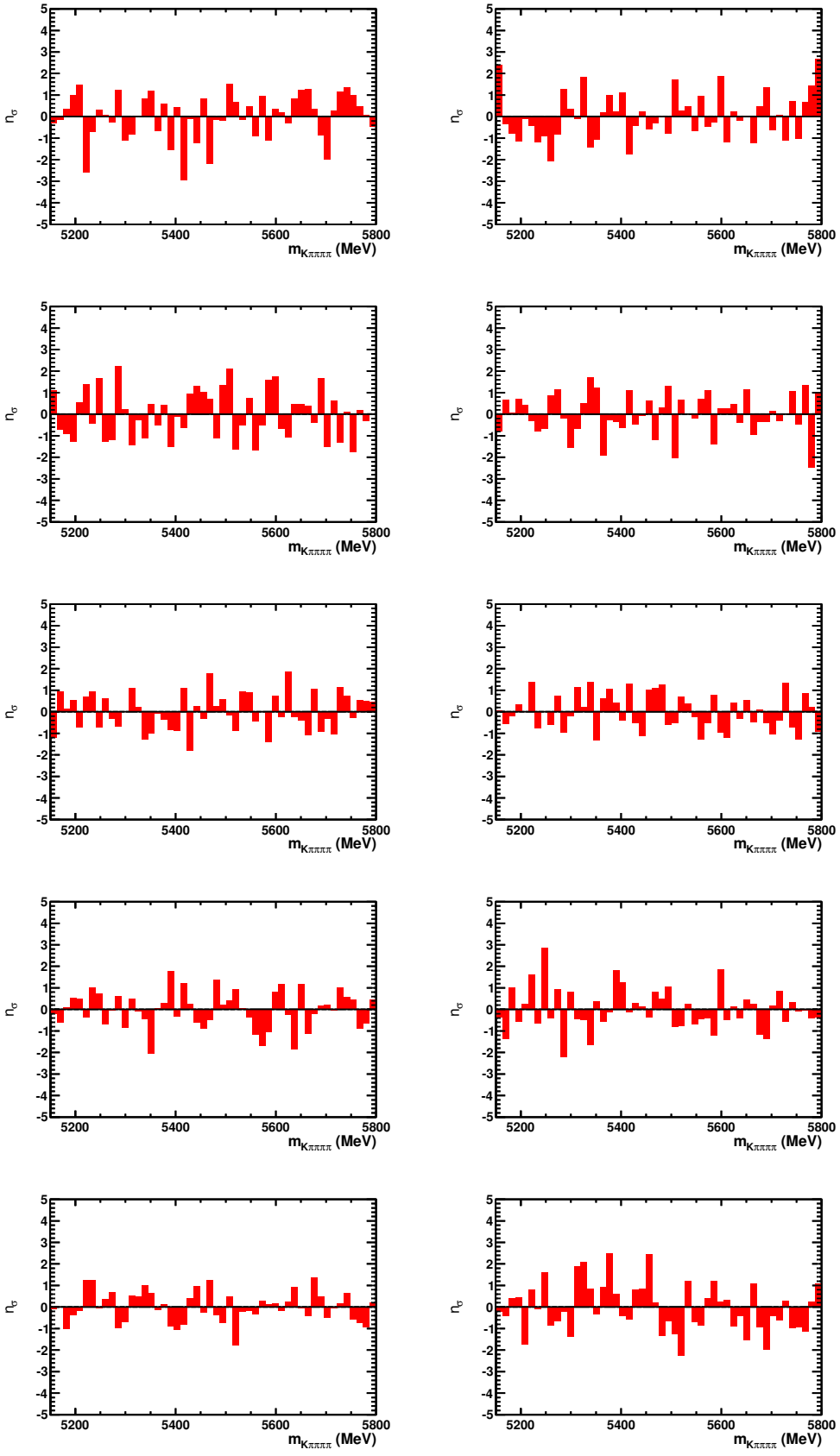

Figure B.10: Pulls for the B^+ fits in bins of D^0 lifetime.

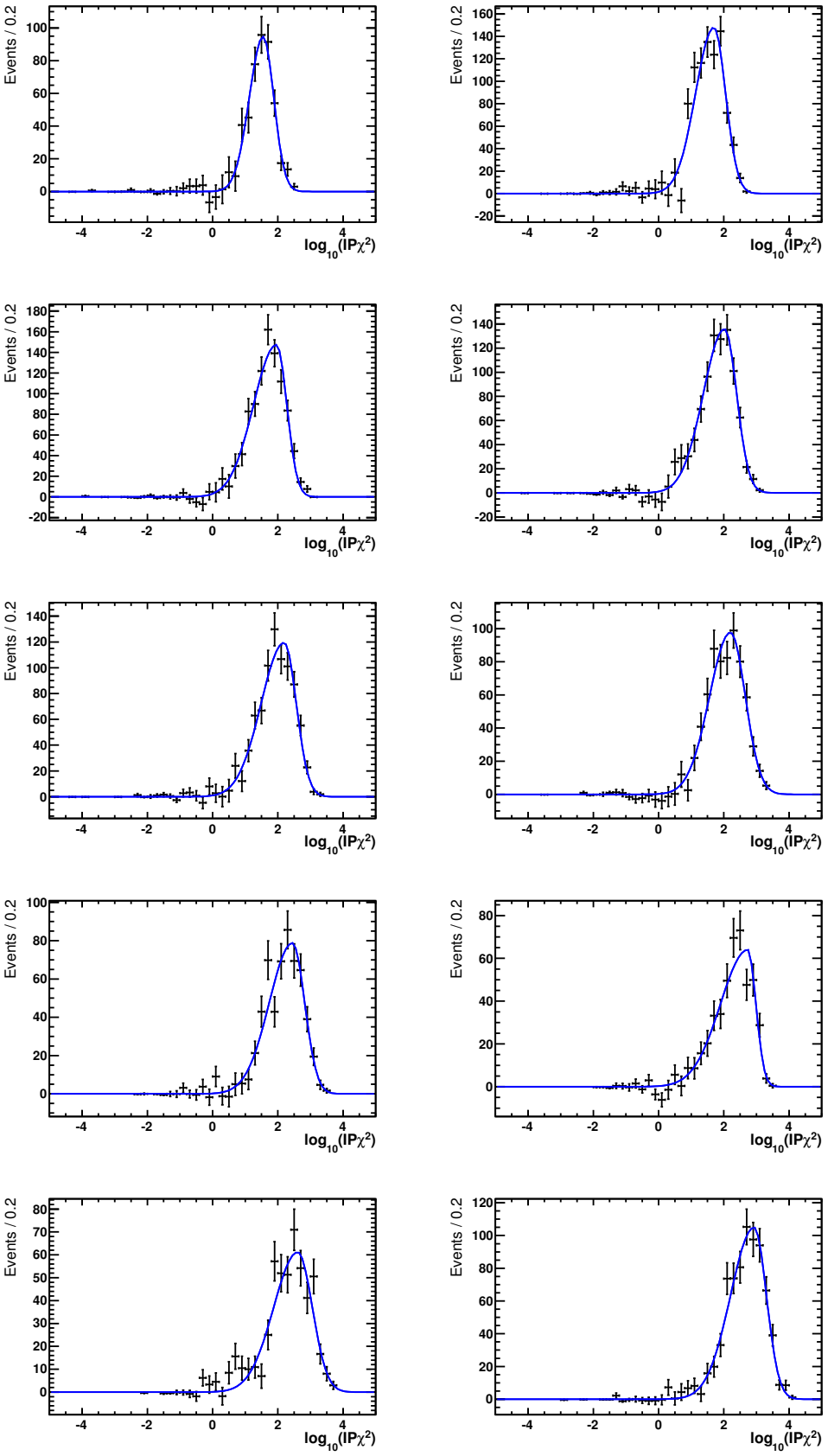

Figure B.11: Secondary $\log_{10}(IP\chi^2)$ distributions, each fit with a bifurcated Gaussian.

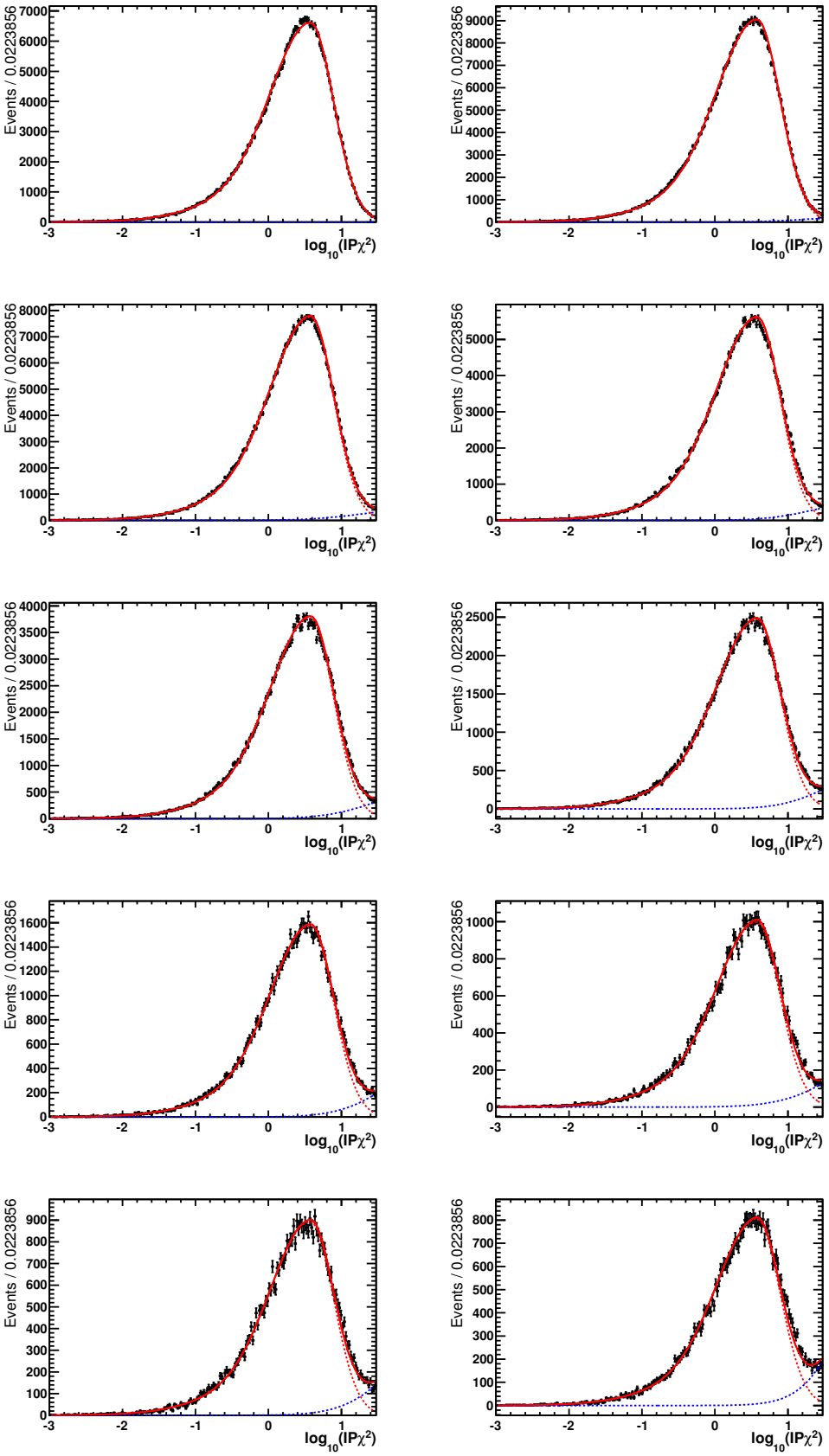

Figure B.12: Fits to the $\log_{10}(IP\chi^2)$ distributions from the D^* sample in bins of D^0 lifetime. The solid red line shows the total PDF. The dashed lines show the prompt (red) and secondary (blue) components.

Bibliography

[1] C. Fitzpatrick, *A measurement of the CP-violating phase ϕ_s in the decay $B_s^0 \to J/\psi\phi$*. PhD thesis, Edinburgh University, Edinburgh, 2012.

[2] **Particle Data Group** Collaboration, C. Amsler *et al.*, "Particle physics summary tables," *Phys. Lett.* **B667** (2008) 31 – 100.

[3] **CMS** Collaboration, S. Chatrchyan *et al.*, "Observation of a new boson at a mass of 125 GeV with the CMS experiment at the LHC," *Phys. Lett.* **B716** (2012) 30–61, `arXiv:1207.7235 [hep-ex]`.

[4] **ATLAS** Collaboration, G. Aad *et al.*, "Observation of a new particle in the search for the Standard Model Higgs boson with the ATLAS detector at the LHC," *Phys. Lett.* **B716** (2012) 1 – 29, `arXiv:1207.7214 [hep-ex]`.

[5] D. Griffiths, *Introduction to elementary particles*. John Wiley & Sons, 1987.

[6] S. Weinberg, "A model of leptons," *Phys. Rev. Lett.* **19** (1967) 1264–1266.

[7] **UA1** Collaboration, G. Arnison *et al.*, "Experimental observation of isolated large transverse energy electrons with associated missing energy at $\sqrt{s} = 540\,\text{GeV}$," *Phys. Lett.* **B122** (1983) no. 1, 103 – 116.

[8] **UA1** Collaboration, G. Arnison *et al.*, "Experimental observation of lepton pairs of invariant mass around 95 GeV/c^2 at the CERN SPS collider," *Phys. Lett.* **B126** (1983) no. 5, 398 – 410.

[9] S. Weinberg, "General theory of broken local symmetries," *Phys. Rev.* **D7** (1973) 1068–1082.

[10] J. Goldstone, "Field theories with superconductor solutions," *Il Nuovo Cimento* **19** (1961) no. 1, 154–164.

[11] L. Wolfenstein, "Parametrization of the Kobayashi-Maskawa matrix," *Phys. Rev. Lett.* **51** (1983) 1945–1947.

[12] A. Powell, *Measuring the CKM Angle γ with $B^\pm \to DK^\pm$ Decays at LHCb and a Determination of the $D \to K\pi\pi\pi$ Coherence Factor at CLEO-c*. PhD thesis, Oxford University, Oxford, 2009.

[13] D. Atwood and A. Soni, "Role of a charm factory in extracting CKM-phase information via $B \to DK$," *Phys. Rev.* **D68** (2003) 033003.

[14] S. Harnew, J. Rademacker, and T. Hampson, "D mixing formalism for multi-body final states," Tech. Rep. CERN-LHCb-INT-2012-024, CERN, Geneva, 2012.

[15] L. Evans and P. Bryant, "LHC machine," *JINST* **3** (2008) S08001.

[16] **ATLAS** Collaboration, G. Aad *et al.*, "The ATLAS experiment at the CERN Large Hadron Collider," *JINST* **3** (2008) S08003.

[17] **CMS** Collaboration, S. Chatrchyan *et al.*, "The CMS experiment at the CERN LHC," *JINST* **3** (2008) S08004.

[18] **ALICE** Collaboration, K. Aamodt *et al.*, "The ALICE experiment at the CERN LHC," *JINST* **3** (2008) S08002.

[19] **LHCb** Collaboration, A. A. Alves *et al.*, "The LHCb Detector at the LHC," *JINST* **3** (2008) S08005.

[20] **LHCb** Collaboration, R. Aaij *et al.*, "Measurement of $\sigma(pp \to b\bar{b}X)$ at $\sqrt{s} = 7$ TeV in the forward region," *Phys. Lett.* **B694** (2010) 209–216, `arXiv:1009.2731 [hep-ex]`.

[21] **CDF** Collaboration, T. Aaltonen *et al.*, "Measurement of the b-hadron production cross section using decays to $\mu^- D^0 x$ final states in $p\overline{p}$ collisions at $\sqrt{s} = 1.96$ TeV," *Phys. Rev.* **D79** (2009) 092003.

[22] T. Sjostrand, S. Mrenna, and P. Z. Skands, "PYTHIA 6.4 Physics and Manual," *JHEP* **0605** (2006) 026, `arXiv:hep-ph/0603175 [hep-ph]`.

[23] **LHCb** Collaboration, *LHCb VELO (VErtex LOcator): Technical Design Report.* CERN, Geneva, 2001.

[24] **LHCb** Collaboration, *LHCb reoptimized detector design and performance: Technical Design Report.* CERN, Geneva, 2003.

[25] **LHCb** Collaboration, *LHCb RICH: Technical Design Report.* CERN, Geneva, 2000.

[26] **LHCb** Collaboration, *LHCb calorimeters: Technical Design Report.* CERN, Geneva, 2000.

[27] **LHCb** Collaboration, *LHCb magnet: Technical Design Report.* CERN, Geneva, 2000.

[28] **LHCb** Collaboration, *LHCb inner tracker: Technical Design Report.* CERN, Geneva, 2002.

[29] **LHCb** Collaboration, *LHCb outer tracker: Technical Design Report.* CERN, Geneva, 2001.

[30] **LHCb** Collaboration, R. Aaij *et al.*, "First evidence for the decay $B_s^0 \to \mu^+\mu^-$," `arXiv:1211.2674 [hep-ex]`.

[31] **LHCb** Collaboration, *LHCb muon system: Technical Design Report.* CERN, Geneva, 2001.

[32] **LHCb** Collaboration, *LHCb trigger system: Technical Design Report.* CERN, Geneva, 2003.

[33] V. V. Gligorov, "A single track HLT1 trigger," Tech. Rep. LHCb-PUB-2011-003, CERN, Geneva, 2011.

[34] G. Barrand *et al.*, "GAUDI - A software architecture and framework for building HEP data processing applications," *Comput.Phys.Commun.* **140** (2001) 45–55.

[35] D. Lange, "The EvtGen particle decay simulation package," *Nucl. Instrum. Meth.* **A462** (2001) 152–155.

[36] P. Golonka and Z. Was, "PHOTOS Monte Carlo: a precision tool for QED corrections in Z and W decays," *Eur. Phys. J.* **C45** (2006) 97–107.

[37] **GEANT4** Collaboration, S. Agostinelli *et al.*, "GEANT4 - a simulation toolkit," *Nucl. Instrum. Meth.* **A506** (2003) no. 3, 250 – 303.

[38] V. V. Gligorov, "Reconstruction of the channel $B_d^0 \to D^+\pi^-$ and background classification at LHCb (revised)," Tech. Rep. LHCb-2007-044, CERN, Geneva, 2007.

[39] J. Rademacker, *Evaluation of the LHCb RICH detectors and a measurement of the CKM angle γ.* PhD thesis, Oxford University, Oxford, 2001.

[40] N. Brook, M. Coombes, T. Hampson, and A. Solomin, "The software framework and method for the alignment of the LHCb RICH optical system using proton-proton collisions," Tech. Rep. CERN-LHCb-INT-2013-007, CERN, Geneva, 2013.

[41] C. G. Blanks, *V^0 production ratios at LHCb and the alignment of its RICH detectors.* PhD thesis, Imperial College, London, 2011.

[42] A. Gorisek, P. Krizan, S. Korpar, and M. Staric, "Alignment of the HERA-B RICH optical system with data," *Nucl. Instrum. Meth.* **A433** (1999) 408–412.

[43] M. Adinolfi *et al.*, "Performance of the LHCb RICH detector at the LHC," `arXiv:1211.6759 [physics.ins-det]`.

[44] **CDF** Collaboration, D. Acosta *et al.*, "Measurement of the B^+ total cross section and B^+ differential cross section $\mathrm{d}\sigma/\mathrm{d}_{p_\mathrm{T}}$ in $p\overline{p}$ collisions at $\sqrt{s} = 1.8\,\mathrm{TeV}$," *Phys. Rev.* **D65** (2002) 052005.

[45] M. Needham, "Clone track identification using the Kullback-Liebler distance,". CERN-LHCB-2008-002.

[46] T. Skwarnicki, *A study of the radiative cascade transitions between the upsilon-prime and upsilon resonances*. PhD thesis, Institute of Nuclear Physics, Krakow, 1986. DESY-F31-86-02, Appendix E.

[47] T. Bauer *et al.*, "Prompt charm production in pp collisions at $\sqrt{s} = 7\,\mathrm{TeV}$ in 2010 data: Λ_c^+." LHCb-ANA-2011-018-Lambdac, 2011.

[48] **Mark-III** Collaboration, J. Adler *et al.*, "Resonant substructure in $K^-\pi^+\pi^+\pi^-$ decays of D^0 mesons," *Phys. Rev. Lett.* **64** (1990) 2615–2618.

[49] M. Pivk and F. R. Le Diberder, "sPlot: a statistical tool to unfold data distributions," *Nucl. Instrum. Meth.* **A555** (2005) 356–369, `arXiv:physics/0402083`.

[50] **LHCb** Collaboration, R. Aaij *et al.*, "Prompt K^0_S production in pp collisions at $\sqrt{s} = 0.9$ TeV," *Phys. Lett.* **B693** (2010) 69–80, `arXiv:1008.3105 [hep-ex]`.

[51] Y. Amhis, V. Balagura, C. Barschel, M. Ferro-Luzzi, P. Hopchev, S. Oggero, R. Matev, B. Pietrzyk, J. Panman, and S. Redford, "Absolute luminosity measurements at $\sqrt{s} = 7$ TeV," Tech. Rep. CERN-LHCb-INT-2011-018, CERN, Geneva, 2011.

[52] **Particle Data Group** Collaboration, K. Nakamura *et al.*, "Review of particle physics," *J. Phys.* **G37** (2010) 075021.

[53] R. J. Barlow, *Statistics: a guide to the use of statistical methods in the physical sciences*. John Wiley & Sons, 1989.

[54] **Particle Data Group** Collaboration, C. Amsler *et al.*, "Review of particle physics," *Phys. Lett.* **B667** (2008) 1–. and 2009 partial update for the 2010 edition.

[55] **CDF** Collaboration, T. Affolder *et al.*, "Measurement of b-quark fragmentation fractions in $p\overline{p}$ collisions at $\sqrt{s} = 1.8\,\mathrm{TeV}$," *Phys. Rev. Lett.* **84** (2000) 1663–1668.

[56] **ZEUS** Collaboration, S. Chekanov *et al.*, "Measurement of charm fragmentation ratios and fractions in photoproduction at HERA," *Eur. Phys. J.* **C44** (2005) 351–366. `http://eprints.gla.ac.uk/28317/`.

[57] B. A. Kniehl, G. Kramer, I. Schienbein, and H. Spiesberger, "Inclusive Charmed-Meson Production at the CERN LHC," `arXiv:1202.0439 [hep-ph]`.

[58] M. Cacciari, S. Frixione, M. Mangano, M. Nason, and G. Ridolfi, "private communication," (2010) .

[59] M. Cacciari, M. Greco, and P. Nason, "The $p_{\rm T}$ spectrum in heavy-flavour hadroproduction," *JHEP* **05** (1998) 007, `arXiv:hep-ph/9803400`.

[60] P. Z. Skands, "Tuning Monte Carlo generators: The Perugia tunes," *Phys.Rev.* **D82** (2010) 074018, `arXiv:1005.3457 [hep-ph]`.

[61] K. Lande, E. T. Booth, J. Impeduglia, L. M. Lederman, and W. Chinowsky, "Observation of long-lived neutral V particles," *Phys. Rev.* **103** (1956) 1901–1904.

[62] **ARGUS** Collaboration, H. Albrecht *et al.*, "Observation of $B^0 - \overline{B}^0$ mixing," *Phys. Lett.* **B192** (1987) no. 1-2, 245 – 252.

[63] **CDF** Collaboration, A. Abulencia *et al.*, "Observation of $B_s^0 - \overline{B}_s^0$ oscillations," *Phys. Rev. Lett.* **97** (2006) 242003.

[64] **LHCb** Collaboration, R. Aaij *et al.*, "Observation of $D^0 - \overline{D}^0$ oscillations," `arXiv:1211.1230 [hep-ex]`.

[65] **Belle** Collaboration, X. C. Tian *et al.*, "Measurement of the wrong-sign decays $D^0 \to K^+\pi^-\pi^0$ and $D^0 \to K^+\pi^-\pi^+\pi^-$, and search for CP violation," *Phys. Rev. Lett.* **95** (2005) 231801.

[66] **BABAR** Collaboration, B. Aubert *et al.*, "Search for $D^0 - \overline{D}^0$ mixing in the decays $D^0 \to K^+\pi^-\pi^+\pi^-$," `arXiv:hep-ex/0607090 [hep-ex]`.

[67] S. Amato *et al.*, "HLT2 open charm triggers, 2010-2011," Tech. Rep. CERN-LHCb-INT-2011-031, CERN, Geneva, 2011.

[68] M. Williams, V. V. Gligorov, C. Thomas, H. Dijkstra, J. Nardulli, and P. Spradlin, "The HLT2 topological lines," Tech. Rep. CERN-LHCb-PUB-2011-002, CERN, Geneva, 2011.

[69] W. D. Hulsbergen, "Decay chain fitting with a kalman filter," *Nucl. Instrum. Meth.* **552** (2005) no. 3, 566 – 575.

[70] N. L. Johnson, "Systems of frequency curves generated by methods of translation," *Biometrika* **36** (1949) 149 – 176.

[71] S. Bachman, M. Bessner, R. Borchardt, A. Di Canto, J. Marks, U. Uwer, and A. Weiden, "Measurement of $D^0 - \bar{D}^0$ oscillations with "wrong-sign" $D^{*+} \to D^0(\to K + \pi^-)\pi^+$ decays." LHCb-ANA-2012-088, 2012.

[72] **Particle Data Group** Collaboration, J. Beringer *et al.*, "Review of particle phyiscs," *Phys. Rev.* **D86** (2012) 010001.

[73] Heavy Flavour Averaging Group, "D mixing results allowing for CPV," 2012. `www.slac.stanford.edu/xorg/hfag/charm/March12/results_mix+cpv.html`.

[74] **CLEO** Collaboration, N. Lowrey *et al.*, "Determination of the $D^0 \to K^-\pi^+\pi^0$ and $D^0 \to K^-\pi^+\pi^-\pi^+$ coherence factors and average strong-phase differences using quantum-correlated measurements," *Phys. Rev.* **D80** (2009) 031105.